The Dissertation Committee for Juliana Yuk Wing Leung certifies that this is the approved version of the following dissertation:

Reservoir Modeling Accounting for Scale-Up of Heterogeneity and Transport Processes

Committee:

Sanjay Srinivasan, Supervisor

Chun Huh

Larry W. Lake

Kamy Sepehrnoori

Alexander Sun

Reservoir Modeling Accounting for Scale-Up of Heterogeneity and Transport Processes

by

Juliana Yuk Wing Leung, B.Sc.; M.S.

Dissertation

Presented to the Faculty of the Graduate School of
The University of Texas at Austin
in Partial Fulfillment
of the Requirements
for the Degree of

Doctor of Philosophy

The University of Texas at Austin
December 2009

Dedication

To my ever loving and devoting parents, Louis Leung and Cecilia Lee

Acknowledgements

I would like to express my most sincere gratitude to my supervising professor, Dr. Sanjay Srinivasan. I always feel extremely fortunate to have the opportunity to study with him. When I took his undergraduate reservoir engineering class in my junior year, I would never have anticipated that a seemingly innocent technical elective could lead to a doctorate degree in a place far from home almost a decade later. I thank him for the fascinating research ideas, the interesting discussions, the steady encouragement and mentorship, the guidance for better erudition, the inspiration to be a stellar researcher, and the friendship. I learnt from him to see the "fun" in research. I know I could be headstrong at times and must have given him much grief over the years, but his unwavering patience makes me feel free to express my ideas and even to disagree.

I would also like to express my special thanks to my committee for their mentorship, questions, and suggestions. I thank Dr. Chun Huh for his expert advice and enthusiasm for the polymer flow scale-up project. I thank Dr. Larry Lake for his insightful comments and his constant emphasis on "seeing the big picture". I thank Dr. Kamy Sepehrnoori for his useful suggestions related to the numerical aspects of this work. I truly appreciate Dr. Alexander Sun for serving as an external member on my committee; his remarks of the practical implications of this research and his thoughtful comments regarding various stochastic algorithms have been very helpful.

My appreciation is extended towards my colleagues in the research group, especially Cesar Mantilla (my essential research buddy), Selin Erzybek, Alvaro Barrera, Kiomars Eskandaridalvand, Nnamdi Azom, Ankesh Anupam, Sayantan Bhowmik, Yonghwee Kim, Louis Forster, Aviral Sharma, Pradeep Govind, Donovan Kilmartin, and the rest of GAMMA team. Their helpful ideas, discussions, and encouragement are my constant sources of support. I truly treasured the times we worked together as a group.

The Department of Petroleum and Geosystems Engineering at the University of Texas at Austin has provided me with the most resourceful environment for the research. I would like to thank the knowledgeable faculty members, the friendly staff, especially Jin Lee for her help with the administrative work, Dr. Roger Terzian, Cheryl Kruzie, and most importantly, my fellow graduate students and friends.

I need to thank my dearest friend, Tan, for his love and all the sacrifice he has made. The confidence he places in me gives me hope even at tough times. I also wish to express my greatest gratitude to my wonderful sister and best friend, Teresa. Finally, I must thank my parents, to whom I owe absolutely everything in life. They have always stressed the importance of education, and their endless faith in me helps me in every endeavor.

Reservoir Modeling Accounting for Scale-Up of Heterogeneity and Transport Processes

Publication No._____________

Juliana Yuk Wing Leung, Ph.D.
The University of Texas at Austin, 2009

Supervisor: Sanjay Srinivasan

Reservoir heterogeneities exhibit a wide range of length scales, and their interaction with various transport mechanisms control the overall performance of subsurface flow and transport processes. Modeling these processes at large-scales requires proper scale-up of both heterogeneity and the underlying transport mechanisms. This research demonstrates a new reservoir modeling procedure to systematically quantify the scaling characteristics of transport processes by accounting for sub-scale heterogeneities and their interaction with various transport mechanisms based on the volume averaging approach.

Although treatments of transport problems with the volume averaging technique have been published in the past, application to real geological systems exhibiting complex heterogeneity is lacking. A novel procedure, where results from a fine-scale numerical flow simulation reflecting the full physics of the transport process albeit over a small sub-volume of the reservoir, can be integrated with the volume averaging technique to provide effective description of transport at the coarse scale. In a volume averaging

procedure, scaled up equations describing solute transport in single-phase flow are developed. Scaling characteristics of effective transport coefficient corresponding to different reservoir heterogeneity correlation lengths as well as different transport mechanisms including convection, dispersion, and diffusion are studied. The method is subsequently extended to describe transport in multiphase systems to study scaling characteristics of processes involving adsorption and inter-phase transport.

Key conclusions drawn from this dissertation show that 1) variance of reservoir properties and flow responses generally decrease with scale; 2) scaling of recovery processes can be described by the scaling of effective mass transfer coefficient (K_{eff}); in particular, mean and variance of K_{eff} decrease with length scale, similar in the fashion of recovery statistics (e.g., variances in tracer breakthrough time and recovery); 3) the scaling of K_{eff} depends on the underlying heterogeneity and is influenced by the dominant transport mechanisms. To show the versatility of the approach for studying scale-up of other transport mechanisms, it is also applied to derive scaled up formulations of non-Newtonian polymer flow to investigate the scaling characteristics of the apparent viscosity and effective shear rate in porous media.

Table of Contents

List of Tables

List of Figures

Chapter 1: Introduction

1.1 PROBLEM DESCRIPTION

Mass transfer associated with multiphase flow in porous media is frequently encountered in various aspects of science and engineering. Multiple mechanisms, such as diffusion, convection (viscous), capillary, gravity, and chemical reactions together influence the overall mass transfer process. Since heterogeneity in porous media, which manifest itself in a wide range of length scales, interact differently with these various types of mechanisms, accurate prediction of flow performance on large scales requires understanding of 1) the scaling characteristics of the underlying heterogeneity, 2) their impacts on fluid flow, 3) how these impacts can be coupled with transport mechanisms at a range of scales, and 4) prediction of effective transport coefficients at large scales. Together, these aspects of fluid flow in heterogeneous reservoirs translate into scaling characteristics of different recovery processes. During the implementation of hydrocarbon recovery or groundwater flow processes, discrepancy between core floods, pilot tests, and field-scale recovery are often observed. This change in recovery with scale is illustrated in Figure 1-1. This is mostly because heterogeneity length scales exhibited in the field are significantly different from those observed in cores. Proper representation of multi-scale heterogeneity and its interaction with various transport processes is fundamental to understanding the scale-up of recovery performance at the field scale.

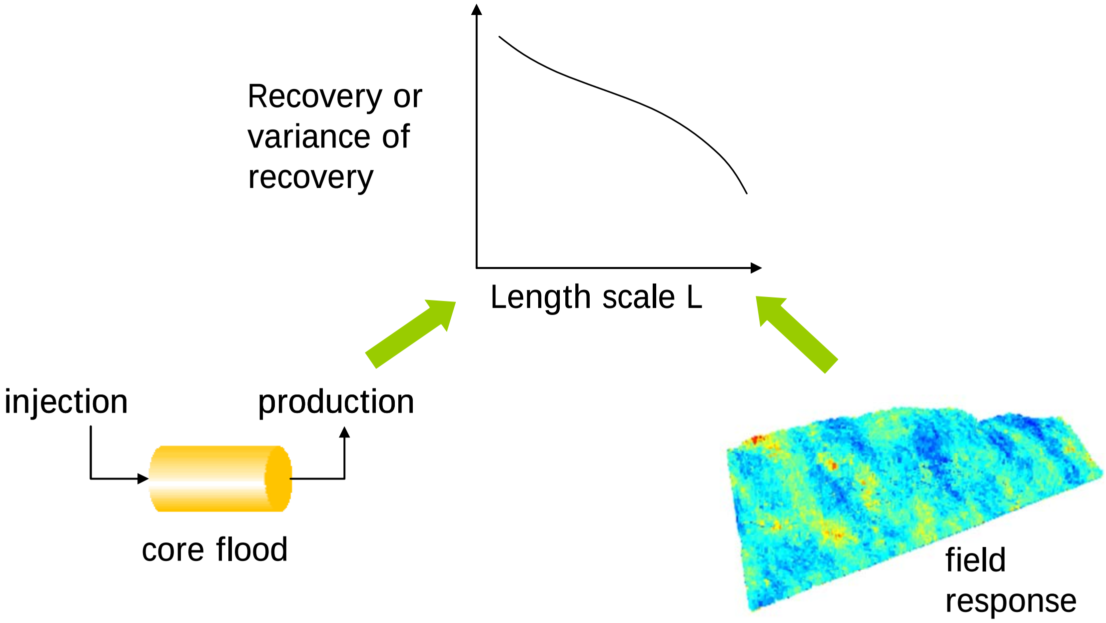

Figure 1-1: A schematic illustrating the scaling characteristics of recovery.

1.2 RESEARCH OBJECTIVES

Reservoir heterogeneities exhibit a wide range of length scales, and their interaction with various transport mechanisms control the performance of subsurface flow and transport processes. Modeling these processes at large scales requires proper representation of multi-scale heterogeneity taking into account its interaction with underlying transport mechanisms. *Therefore, it is hypothesized that predicting reservoir flow performance at large scales depends on the uncertainty introduced due to scale-up of reservoir properties compounded with the influence of heterogeneity on transport processes. Hence the scaling characteristics of a given recovery process can be understood by studying the effective transport as a function of scale.* The primary research objective is to develop a framework for quantifying the scaling characteristics of flow responses accounting for heterogeneity in the underlying reservoir model. This objective can be split into two parts:

1. Scale-up of flow-related reservoir attributes such as porosity and permeability – There is likely to be uncertainty introduced by scaling up from the measurement scale to the model scale even at data locations – this sub-scale uncertainty has to be propagated to un-sampled locations within the reservoir. Subsequently, the relationship between reservoir attributes and flow response (e.g., in the form of a flow transfer function) can be used to propagate the uncertainty due to sub-scale variability to flow performance uncertainty.
2. Scale-up of flow processes in the presence of reservoir heterogeneities using the techniques of volume averaging – Despite application of volume averaging to study averaging characteristics of transport processes is available in several research publications, application to real geological systems exhibiting complex heterogeneity is lacking. The research objective is to develop a new procedure where results from a fine-scale numerical flow simulation reflecting the full physics of the transport process performed over a small volume of the reservoir can be integrated with the volume averaging technique to provide effective description of transport at the coarse scale. Spatial averaging of the fine-scale governing equations is performed to derive scaled-up transport coefficients and effective contribution of each transport mechanism. These can be computed at a range of scales and thereby provide insights into the scaling characteristics/relationship of effective mass transfer coefficients corresponding to different transport mechanisms. These relationships can in turn be used to describe the scaling characteristics of recovery responses.

Application of the concept of volume averaging to flow processes with transport mechanisms such as convection, dispersion, diffusion, reaction, inter-phase transport, and adsorption in both single-phase and multi-phase systems are presented in subsequent chapters. The volume averaging method is also applied to derive scaled up formulations of polymer flow to study the scaling characteristics of the apparent viscosity and effective shear rate of the polymer solution flowing in porous media.

1.3 DISSERTATION OUTLINE

Chapter 2 presents a review of the literature pertinent to scale-up of reservoir properties and flow. Chapter 3 utilizes some concepts from Chapter 2 in a series of case studies and numerical examples to analyze uncertainty introduced by scale-up of reservoir properties and flow response. Chapter 4 discusses the mathematical formulations and concepts of volume averaging techniques for solute transport in single-phase flow; it also explains the modifications made to study scale-up of various transport mechanisms on realistic geologic models exhibiting different spatial correlation models. Chapter 5 demonstrates the method developed in Chapter 4 on a series of case studies with different heterogeneity models and dominant transport mechanisms. Chapter 6 extends the techniques to two-phase flow; in particular mechanisms such as adsorption and inter-phase transport are studied. Chapter 7 illustrates how the volume averaging techniques can be used to study scale-up of apparent viscosity and effective shear rate in single phase polymer flow. In Chapter 8, key observations and findings of the research are presented, along with ideas for future work.

Chapter 2: Literature Review

2.1 OVERVIEW

In this chapter, relevant literature relating to scale-up of fluid flow in porous media is reviewed. We begin with a discussion of scale-up and upscaling where we attempt to differentiate between these two important concepts. Next, we focus on a review of previous works on scale-up of reservoir attributes. This is followed by a review of the popular methods for scale-up of flow: using dimensionless groups and by stochastic perturbation and volume averaging of flow equations. A brief introduction to the methodology of volume averaging and some key limitations with current implementations of that method are also presented.

2.2 SCALE-UP AND UPSCALING

Upscaling is a process in reservoir simulation which aims to replace a fine-scale detailed description of reservoir properties with a coarser scale description that has equivalent properties (Christie, 2001); Upscaling techniques can generally be classified in terms of the types of parameters being upscaled: single or multi-phase flow parameters (Durlofsky, 2003). Single-phase upscaling produces effective reservoir properties such as absolute permeability. Two-phase upscaling derives effective flow parameters such as relative permeability and capillary pressure curve. Qi and Hesketh (2005) provide a descriptive summary of several upscaling techniques and the challenges to obtaining representative effective parameters corresponding to complex flow and boundary conditions. Pickup et al. (2005) discuss the use of multi-stage methods to two-phase upscaling. In this method, the upscaling from models with millimeter-sized grid cells to full-field models with grid cells of several tens of meters in length is carried out in stages, which are defined by geologically based length scales (e.g., laminae size, bed size etc.). Many other authors have written reviews of upscaling methods; for example, Christie (1996), Wen and Gomez-Hernandez (1996), Barker and Thibeau (1997), Renard and de Marsily (1997), Miller et al. (1998).

Scale-up, on the other hand, is a process of relating phenomena observable at one scale to another scale. Upscaling forces a correspondence between fine and coarse scale flow response (pressure drop or flow rate). No such correspondence is assumed in scale-up and in fact the challenge is to describe the coarse scale flow behavior, given observations at the fine scale. Predicting pilot scale response using core flood data is a typical example of scale-up. This becomes challenging because heterogeneities occur at a range of scales and their impacts on transport mechanisms are different at various scales. However, both processes entail accounting for sub-scale variability in geological characteristics. Since scale-up is the focus of this research, in the remaining of this chapter, a literature review related to scale-up of reservoir attributes and flow responses is presented.

2.3 SCALE-UP OF RESERVOIR ATTRIBUTES

Scale-up of reservoir properties is often performed for two reasons. First, measurement scales are usually different for data from different sources; for example, seismic data has a different resolution than log or core data. Second, the modeling scales are also disparate; flow simulation scale is generally larger than geo-modeling scale. These changes in scale or volume support lead to additional uncertainty, due to *sub-scale variability*. Sub-scale variability is particularly significant in heterogeneous reservoirs. It should be properly accounted for in scale-up of reservoir models and be carried forward to flow simulations, introducing additional uncertainty in our flow prediction.

The following thought-experiment serves to illustrate this crucial point. Imagine taking a small piece of rock and measuring its average porosity. This process of porosity measurement is repeated with larger and larger pieces of rock. A schematic of average porosity as a function of the size of rock or scale is shown in Figure 2-1 (Bear, 1972). At the very small scale, there are significant fluctuations due to microscopic effects. The averaged quantity starts to stabilize at a length scale referred to as *Representative Elementary Volume* or REV. REV is the volume at which the averaging becomes stable. At the extremely small scale, there is either a grain (zero porosity) or a pore (100% porosity), hence the extreme fluctuations can be observed. Figure 2-1 explains the scaling characteristics of pore-level heterogeneity very well. At the reservoir scale however, heterogeneity occurs at many scales. The same plot as in Figure 2-1 can be conceptualized for this case, except the initial scale would already be at the REV of the pore-scale phenomena (e.g., size of a core plug) and the average porosity range would not as wide. The REV in some cases (where reservoir features exhibit long range correlation) could be larger than the inter-well distance. For this research, the focus is on reservoir-scale heterogeneity.

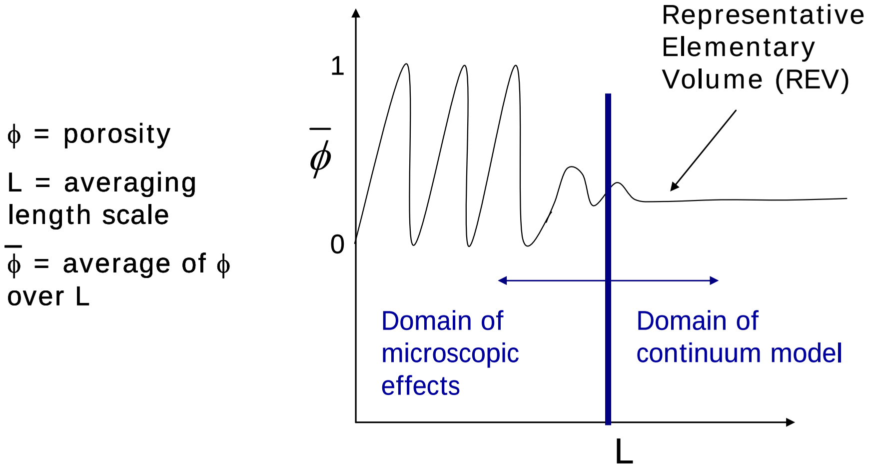

Figure 2-1: Variability of spatial average as a function of scale and its stabilization at the representative elementary volume (adapted from Bear, 1972).

Moreover, in most cases, we are dealing with reservoir attributes that have significant uncertainty associated with them i.e. these attributes have to be modeled as random variables. This uncertainty refers to ensemble variance and should not be confused with heterogeneity, which is related to spatial variance. Furthermore, the average of a set of outcomes of a random variable is also a random variable. The variance of the mean of the attribute can be interpreted as the fluctuation that is seen in the mean of porosity in Figure 2-1. Together with a plot of the variance of the mean with the length scale *L* would therefore be a good tool to evaluate the REV scale of an attribute. Figure 2-2 illustrates this variance of mean for different spatial correlation lengths. Several interesting features should be noted:

1. It is related to the REV representation in Figure 2-1. Significant fluctuations are observed at small scales, and the corresponding variance of mean is also large.
2. This variance of mean decreases slowly with *L* when *L* is small, as it reaches the REV length scale, it decreases drastically. In fact, the plot reaches a constant

negative unit slope on a log-log plot. This negative slope originates from the law of large number, which states that the variance of sample equals fine-scale variance divided by the number of samples. At the REV threshold, the samples act independent of each other, and consequently the mean of sample values and the variance of that mean follow the law of large numbers.

3. This variance of mean is directly related to sub-scale variability – when the averaging scale is large, the sub-scale variability within the averaging scale might be high, but the process of averaging dampens the influence of that variability, causing the variability of the mean (across different samples) to be small; therefore, both the variance of mean and the sub-scale variability are small at large scales. On the other hand, averages computed over tiny blocks would still show the influence of sub-scale variability. The impact of sub-scale variability on the effective/average property decreases as the averaging scale increases.
4. As the correlation length of heterogeneity increases, REV becomes larger. For a given length scale, the variance of the mean increases with correlation length; in other words, it takes a much larger averaging volume for the mean or the variance of mean to stabilize.

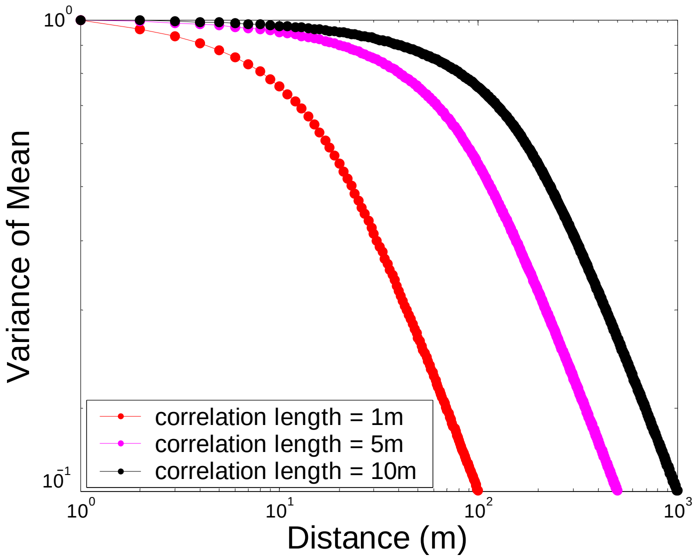

Figure 2-2: Variance of mean as a function of scale for different correlation lengths.

In order to compute the variance of mean for a given autocorrelation model, one can refer to the formulation given in Lake and Srinivasan (2004), let Z be a continuous, Gaussian random variable. The variances of the *linear average* of Z ($\bar{Z}$) over a distance L in 1-D and over a volume V in 3-D are given by the following:

$$Var\left(\bar{Z}\right)=\frac{2\sigma^2}{L^2}\left(\int_{\xi=0}^{\xi=L}\int_{\eta=0}^{\eta=\xi}\rho_{corr}\left(\eta\right)d\eta d\xi\right) \tag{2-1}$$

$$Var\left(\bar{Z}\right)=\frac{2\sigma^2}{V^2}\left(\int_V\int_\eta\rho_{corr}\left(\eta\right)d\eta d\xi\right) \tag{2-2}$$

where σ^2 is the variance of Z, ρ_{corr} is the spatial autocorrelation function, and η represents all the possible spatial lags within *L or V*. As *L or V* increases, the variance of mean ($\bar{Z}$) decreases, while as L approaches zero, the variance of mean becomes the population mean at the point-scale. Another interpretation of this variance of mean is in terms of Krige's relation (Journel and Hujbregts, 1978):

$$Var\left(\overline{Z}\right)=\sigma_{L/D}^{2}=\sigma_{O/D}^{2}-\sigma_{O/L}^{2} \qquad (2\text{-}3)$$

In the above equation, $\sigma_{O/D}^{2}=\sigma^{2}$ is the variance of the attribute computed over points (*O*) embedded in a large domain *D*; $\sigma_{O/L}^{2}$ is the variance of points within a length or volume *L* smaller than *D*, and $\sigma_{L/D}^{2}$ is the same as the variance at the support of $\overline{Z}$. The variance of the mean referred to in the earlier discussion is exactly $\sigma_{L/D}^{2}$ and Krige's relation prescribes its limits. The general procedure for calculating the variance of the mean and the REV scale is to infer and model the variogram using data at the point support and then compute the variance of mean numerically by summing the model $\rho_{corr}(\eta)$ over all possible lag distances within a given length scale *L*.

Another alternative is to generate multiple spatial realizations of the chosen attribute for a given correlation function and compute the mean of each averaging block. The variance of mean can be obtained from these block averages directly. Repeating this calculation by systematically changing the block size would yield a plot similar to Figure 2-2. This same procedure can also be repeated by replacing the arithmetic average of point scale attributes with a more general power average:

$$\overline{Z}^{*}=\left[\frac{1}{n}\sum_{i=1}^{n}\left(Z_{i}\right)^{\varpi}\right]^{1/\varpi} \qquad (2\text{-}4)$$

Figure 2-3 shows the comparison of variance of mean calculated using different correlation lengths and averaging schemes. As ω decreases, the variance of mean increases. Recall that $\omega=-1$ corresponds to a harmonic average; $\omega=0.5$ to a geometric average; and $\omega=1$ to an arithmetic average.

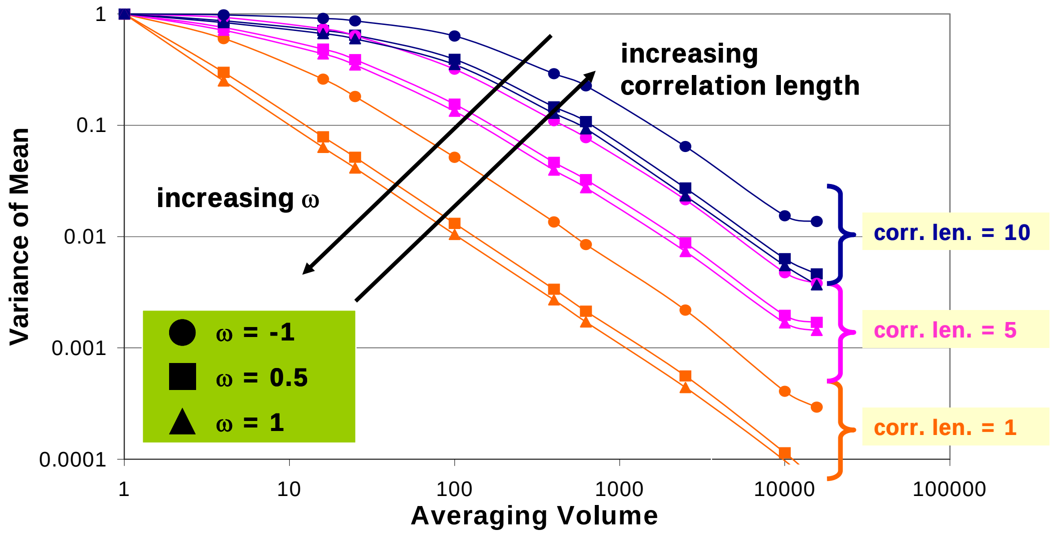

Figure 2-3: Variance of mean calculated using several correlation lengths and averaging schemes.

As discussed previously, REV can be determined from a plot of variance of mean vs. *L* on log-log scale (Lake and Srinivasan, 2004). Such a plot exhibits a diagnostic negative unit slope at scales larger than REV. This REV has important implications in scale-up. When the model length scale is smaller than the measurement REV, additional variance due to sub-scale variability must be accounted for when assigning data values to the model. For example, if a porosity measurement is obtained at the REV scale of the field phenomena, the variance associated with that measurement is small; however, a porosity measurement observed at the core scale (much smaller than the REV scale), the associated variance could be much higher, and that additional variance must be carried forward as uncertainty in our reservoir models. In effect, this amounts to saying that the core scale porosity measurement is not representative of all the variability that can be expected at the model scale. These implications can be summarized in the form of the following cases:

- Case 1: grid size = data resolution → no scale-up
- Case 2: grid size > data resolution > REV → negligible sub-scale variability
- Case 3: data resolution < grid size < REV → sub-scale variability must be accounted for. This is the case in most practical applications because the cell size is generally much smaller than the reservoir-scale heterogeneity. Since the variance of mean represents sub-scale variability at the particular averaging scale, it can be utilized to account for additional uncertainty due to scale-up. Details are discussed in Chapter 3.

Unfortunately, most reservoir attributes such as permeability or fracture porosity do not average linearly. Simple relationships for variance of mean and REV are not readily available. In the case where permeability is log-normally distributed, we can perform a logarithmic transform to a space where linear averaging is permissible. In general, the aforementioned concepts can be used to analyze scaling characteristics of any variables provided that the variables are transformed into a space where linear averaging is applicable. An example of fracture porosity that is non-linearly averaged is described in Chapter 3.

The aforementioned theories are valid with the assumption that a REV can be defined in the absence of large-scale non-stationarity. In the case of permeability, it is widely observed that lateral (horizontal or bed parallel) permeability increases while vertical (bed normal) permeability decreases with scale (Neuman, 1994; Rovey and Cherkauer, 1995; Corbett et al., 1998). These scale effects of permeability or hydraulic conductivity are illustrated in the following two figures.

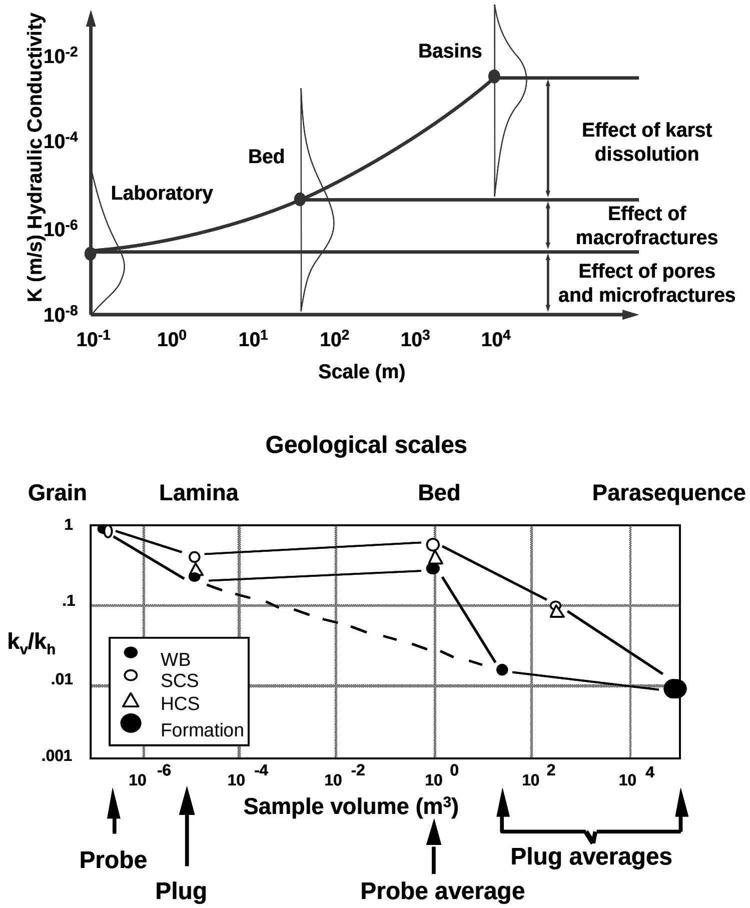

Figure 2-4: Top: Effect of scale on lateral permeability and its distribution (adapted from Kiraly, 1975). Bottom: Variation of vertical to horizontal permeability ratio with scale (adapted from Corbett et al., 1996).

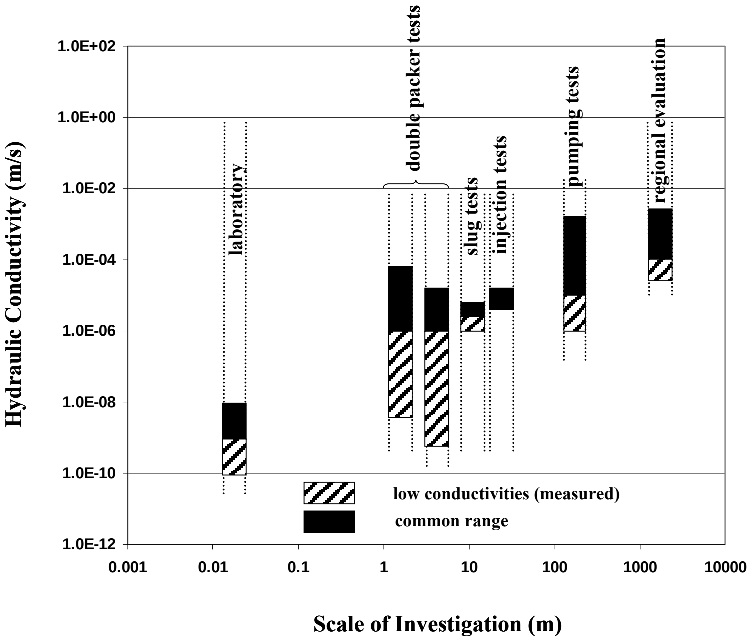

Figure 2-5: Hydraulic conductivity as a function of scale (adapted from Sauter, 1991).

Scale dependency of dispersivity has also been reported in numerous works such as Mahadevan et al. (2003). Gelhar et al. (1992) reported that field-scale dispersivity increases with length scale and begins to plateau at some very large scale (Figure 2-6). John et al. (2008) performed flow reversal tests for tracer transport in permeability realizations of different correlation lengths using particle-tracking simulations to study large-scale dispersion. Their results showed the following: 1) dispersivity increases with scale mainly because of increase in correlation in permeability field; 2) in the case of uncorrelated or short correlation length (e.g., range << size of the medium), dispersivity grows and reaches an asymptotic value; 3) in the presence of long correlated features (e.g., range is comparable to the size of the medium), higher dispersivity values are observed without reaching an asymptotic value. Dispersivity was computed from particle velocities and positions of the particle cloud; therefore, as the correlation length increases, the variance of particle velocities and position of the particle cloud also increases. The authors also showed that longer correlation length enhances local mixing.

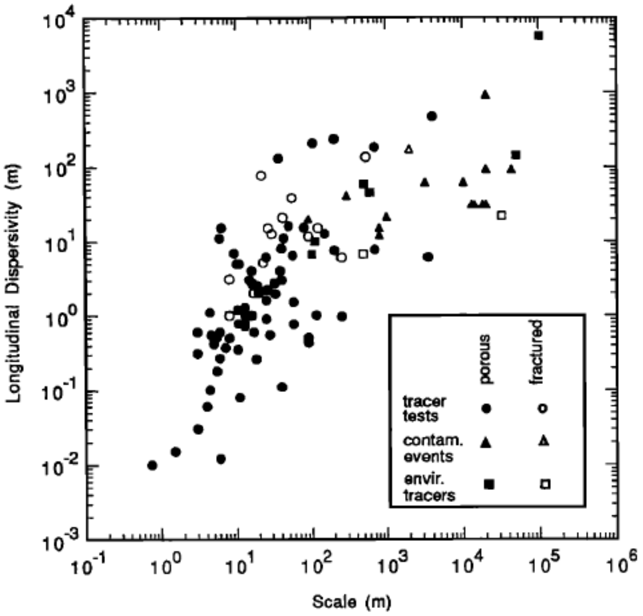

Figure 2-6: Scale dependency of field measured dispersivity for various formation types (reprinted with permission from Gelhar et al., 1992).

Nonlinearity of flow functions also leads to some interesting scale-up characteristics of relative permeability. Scale dependency of flow properties are well documented in literature. It is widely observed that the curvature of relative permeability curves decreases, capillary pressure decreases, and residual saturations increase with scale (Ringrose et al., 1993; Kumar and Jerauld, 1996). Figure 2-7 illustrates the scale effects of relative permeability. The cross-over saturation and endpoints of the oil relative permeability are also significantly impacted by the averaging.

Given that the scale dependency of all these flow related properties, it should not be surprising to discover that permeability and dispersivity are the most common parameters to be increased to match field performance data during a history matching procedure.

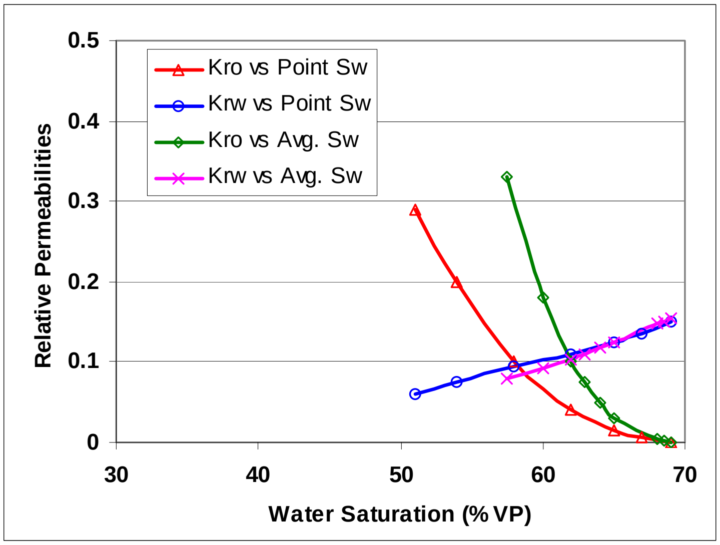

Figure 2-7: A comparison of point and average relative permeability (adapted from Crotti and Cobeñas, 2001). It is observed that relative permeability curves straighten and residual saturations increase with averaging.

2.4 SCALE-UP OF FLOW RESPONSE

As in the case of linear or non-linear averaged variables, we would expect a plot of variance of recovery factor (RF) vs. *L* to decrease with increasing scale, as seen in Figure 2-8. In other words, we expect the recovery from several core samples subject to laboratory core floods to exhibit more variability than recovery from pilot or field scale process implementations for similar geological settings. However, REV for flow response variable such as recovery factor could be in most general cases much larger than that for a "static" reservoir parameter such as permeability. In the case of RF, a negative unit slope, similar to that observed in the scale-up of static attributes, might not exist, as RF scales in a very non-linear fashion. My research objective is to develop a framework for investigating RF and its variance as a function of length scale, given that we know the underlying heterogeneity and the dominating transport mechanisms. We would like to do this without having to repeatedly perform reservoir simulations on hundreds of fine-scale reservoir models (e.g., porosity and permeability). For example, if at a certain scale of experiment, a particular recovery is observed, we can determine what would be the corresponding variance, and more importantly, what uncertainty should be attached to that core flood result. Recovery obtained from a core flood experiment might be high, but since the core scale is much smaller than the REV, significant uncertainty may be associated with the core flood result and this should be taken into account when designing a pilot scale implementation.

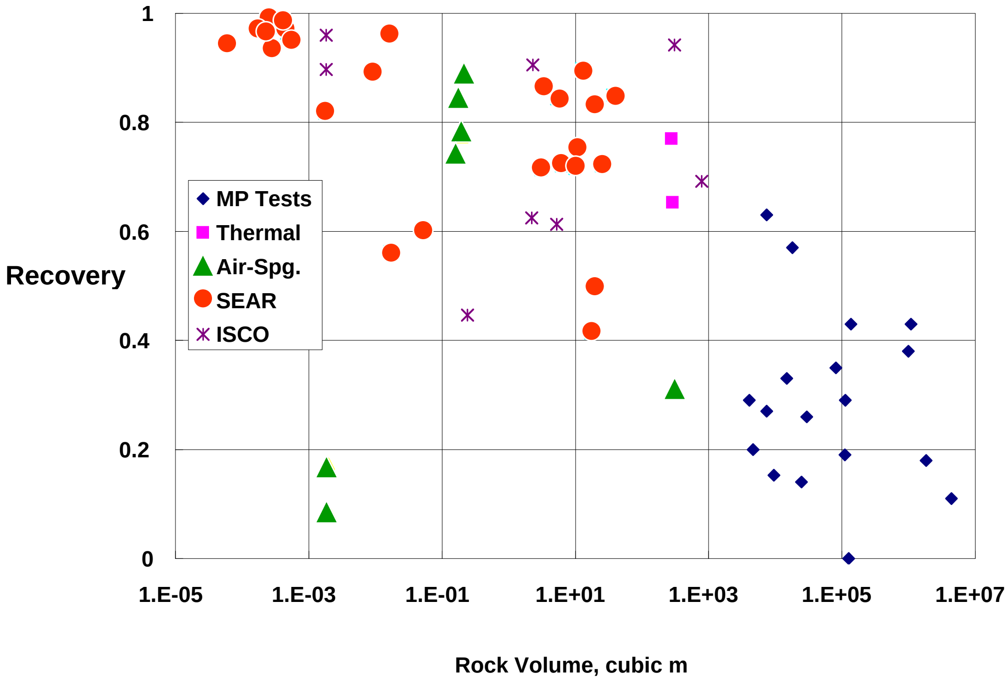

Figure 2-8: Plot of ultimate recoveries versus scale based on data collected from various enhanced oil recovery and remediation processes, including micellar polymer (MP), thermal recovery (thermal), air sparging (Air-Spg.), surfactant flushing (SEAR), and in-situ chemical oxidation (ISCO) (adapted from Lake et al., 2005).

There are two major approaches to understanding the scale-up characteristics of recovery responses. One way is to utilize dimensionless groups that assess the relative magnitudes of different transport mechanisms based on mean reservoir parameters. Recovery performance is assumed to scale according to these dimensionless groups (Peters, 1983; Shook et al., 1992; Wood et al., 2006). Li and Lake (1995) have collected these dimensionless groups into *flow scaling groups* and *heterogeneity scaling groups*. Flow scaling groups include effective aspect ratio, end-point mobility ratio, buoyancy number (gravity vs. viscous forces), and capillary number (capillary vs. viscous forces), whereas the various heterogeneity scaling groups capture some statistical measures of spatial correlation of permeability in three main scales: local, global, and zonal. The authors have generated "type curves" of oil recovery as a function of each flow scaling group for different values of the heterogeneity scaling factors. The major drawback with dimensionless group approach is that detailed information regarding spatial correlation of reservoir parameters is not incorporated; all fine-scale geologic models are lumped into a single dimensionless number that is used within the scaling groups.

Another approach is to evaluate the scale-up characteristics by deriving the full set of flow/mass transfer equations at the macroscopic scale as averages of fine scale quantities. The effective transport parameters at the coarse scale are then averages of fine scale quantities. The two main classes of such techniques are 1) Stochastic Perturbation Methods and 2) Volume Averaging Methods. These methods are useful for describing effective transport parameters or variance of effective transport parameters (provided that we account for reservoir heterogeneity) as a function of length scale. This information could subsequently be translated to understanding recovery as a function of length scale. It should be noted that these techniques are generally used in the application of upscaling to derive effective transport parameters at the coarse scale; however, since these techniques also produce a set of equations at coarse scale describing the macroscopic response, they can be used to study the scale-up of flow response as well, which is the focus of this research.

In the stochastic formalism, uncertainty is represented by probability or other related quantities like statistical moments. Boundary conditions, initial conditions, and parameters are treated as random fields depicted by probability distributions. Sequentially, dependent variables like pressure (or hydraulic head) and flux are also modeled as random fields, and the governing equations describing the transport become stochastic differential equations (SDEs), whose solutions are probability distributions of pressure and flux. Generally speaking, we cannot solve a SDE exactly, as we can only estimate the first few moments of the corresponding probability distribution (e.g., its mean, variance, and covariances). Fortunately, these first few moments would suffice to describe most of the systems of interest. These ensemble or moment statistics can be used subsequently to describe average transport in a scaled-up medium and to define the corresponding effective transport coefficients.

In the framework of volume averaging, instead of working with ensemble statistics, spatial average is employed. Applying the spatial averaging theorem (Cushman, 1982; Howes and Whitaker, 1985), fine-scale governing equations are spatially averaged over a particular volume to produce scaled-up equations that are valid everywhere in the volume. These scaled-up equations describe the effective transport and can be used to obtain scaled-up transport coefficients at the averaging length scale of interest.

2.4.1 Stochastic Perturbation Methods

Stochastic Perturbation or Ensemble Averaging Methods are approaches based on the statistical moment equations governing transport phenomena. Significant research efforts have been made in the area of statistical moment equation approaches over the past two decades. The majority of this work has been done by subsurface hydrologists, who are interested in relating statistical moments of flow and transport quantities to those of permeability field and mean flow characteristics (Zhang, 1999). Some of the work was done by Gelhar et al. (1979), Gelhar and Axness (1983), Dagan (1984, 1987 and 1989), Neuman et al. (1987), Dagan et al. (1992), Cvetkovic et al. (1992), Rubin and Dagan (1992), Gelhar (1993), Newman and Orr (1993), Cvetkovic and Dagan (1994), Zhang and Neuman (1995), and Zhang (1998).

Much of the earlier work was based on numerous assumptions such as unbounded domains, uniform mean flow, stationarity of the flow medium, and these assumptions have greatly restricted the applicability of the stochastic models. Unbounded or infinite-acting reservoirs imply that the flow never experiences the influence of boundary effects, and it is valid only during early flow period or if there is unlimited supply of oil or gas in the reservoirs. Uniform mean flow suggests that there are no pumping or injection effects. Finally, the assumption about stationarity of the reservoir medium is valid when there is absence of geological layers, zones, or faults (Zhang 1999). Zhang and Winter (1999) have relaxed all the aforementioned assumptions for single-phase steady-state flow. They developed a numerical moment differential equation approach that 1) includes a forcing term (sink/source function) in the mass balance; 2) handles complex boundary conditions, various covariance functions of the independent variables, and moderately irregular geometries; and 3) incorporates an additional second order correction term for the mean head, which is otherwise identically zero for uniform mean flow in unbounded domains in a stationary medium. The authors validated their results by comparing with solutions obtained from traditional Monte Carlo simulations. Zhang (1999) then extended their work to transient flow. Sun and Zhang (2000) studied solute spreading in bounded media with flow nonstationarity. Zhang et al. (2000) later extended the method for two-phase fluid flow. By following Vereecken's (2007) approach and notation, we can derive the general mathematical statements for unsaturated flow with the following assumptions:

1. Darcy's law applies
2. Isothermal
3. Ignore interaction of solids
4. Complete immiscibility
5. Density of air is negligible

6. Incompressible water phase

The following nomenclature is used in the ensuing discussion:

$\boldsymbol{x}$ = spatial coordinate of the location

t = time

$\mathbf{u}(\boldsymbol{x},t)$ = flow flux

$\Sigma(\psi, \mathbf{x})$ = specific capacity

$\theta(\mathbf{x},t)$ = source/sink function

$\psi(\mathbf{x},t)$ = $p(\mathbf{x})/(\rho g)$, hydraulic head (p, ρ, and g are pressure, fluid density, and gravitational constant, respectively)

z = elevation

$\mathbf{K}(\psi, \boldsymbol{x})$ = $\mathbf{k}(\psi, \boldsymbol{x})\rho g/\mu$, hydraulic conductivity ($\mathbf{k}$ and μ are absolute permeability and fluid viscosity, respectively)

The equations for momentum and mass balance at the fine scale can be written as:

$$\mathbf{u}(\mathbf{x}) = -\mathbf{K}(\psi, \mathbf{x}) \cdot \nabla\left(\psi + z\right) \tag{2-5}$$

$$\Sigma(\psi, \mathbf{x})\frac{\partial \psi}{\partial t} + \nabla \cdot \mathbf{u}(\mathbf{x}) = \theta(\mathbf{x}, \psi, t) \tag{2-6}$$

Assuming **K** (a random function) to be isotropic locally and dependent on a spatial parameter $\alpha(\boldsymbol{x})$:

$$K\left(\psi, \mathbf{x}\right) = K_s(\mathbf{x})\exp\left[\alpha\left(x\right)\psi\left(\mathbf{x}, t\right)\right] \tag{2-7}$$

If we further assume that α and $ln(K_s)$ are Gaussian random functions, each parameter can be expressed as the sum of their mean (uppercase symbols: K_s, F, A, H, Γ, U) and a perturbation (lowercase symbols: f, a, h, γ, u):

$$\ln K_s(\mathbf{x}) = F\left(\mathbf{x}\right) + f \tag{2-8}$$

$$\alpha = A + a \tag{2-9}$$

$$\psi = H + h \tag{2-10}$$

$$\Sigma(\psi) = \Gamma(\psi) + \gamma(\psi) \tag{2-11}$$

$$\mathbf{u} = \mathbf{U} + \mathbf{u}' \tag{2-12}$$

To obtain a linearized perturbation equation (i.e. an equation that is linear in the perturbation terms), the following steps are then implemented.

1. Substitute equations (2-8) – (2-12) into equations (2-5) and (2-6).
2. Neglect higher order perturbation terms (i.e. nonlinear perturbation terms).
3. Subtract the expected value of the equation from the original fine-scale equations (2-5) and (2-6).
4. Assume steady state (i.e. ignore the transient term in equation (2-6)) and constant *A* and *F* (i.e. not a function of spatial position or **x**). Since *A* and *F* together define the mean of *K* in equations (2-7) –(2-9), this assumption essentially represents the stationarity of the mean of *K*.

$$\begin{aligned}
&\nabla^2 h(\mathbf{x}) + A\left[2J(\mathbf{x}) - \nabla z(\mathbf{x})\right]^T \nabla h(\mathbf{x}) - A\frac{\theta(\mathbf{x},H)}{K_m(H)} h(\mathbf{x}) \\
&= -J^T(\mathbf{x})\left[\nabla f(\mathbf{x}) + H(\mathbf{x})\nabla a(\mathbf{x})\right] + \frac{\theta(\mathbf{x},H)}{K_m(H)} f(\mathbf{x}) \\
&+ \left[\frac{\theta(\mathbf{x},H)}{K_m(H)} H(\mathbf{x}) - J^T(\mathbf{x})\nabla H(\mathbf{x})\right] a(\mathbf{x})
\end{aligned} \tag{2-13}$$

Note that equation (2-13) is an example of a linear perturbation equation, since the expected value has been subtracted (in a linear fashion) from the complete equation for the head ψ. To obtain the moments equations, we multiply the linear perturbation

Equation (2-13) with a perturbation $h(\chi)$ at a location χ, and take the ensemble mean. Cov_{ij} represents the covariance between variable i and j.

$$\begin{aligned}
&\nabla_x{}^2 Cov_{hh}(\mathbf{x},\boldsymbol{\chi}) + A\left[2J(\mathbf{x}) - \nabla_x z(\mathbf{x})\right]^T \nabla_x Cov_{hh}(\mathbf{x},\boldsymbol{\chi}) - A\frac{\theta(\mathbf{x},H)}{K_m(H)}Cov_{hh}(\mathbf{x},\boldsymbol{\chi}) \\
&= -J^T(\mathbf{x})\left[\nabla_x Cov_{fh}(\mathbf{x},\boldsymbol{\chi}) + H(\mathbf{x})\nabla_x Cov_{ah}(\mathbf{x},\boldsymbol{\chi})\right] \\
&+ \frac{\theta(\mathbf{x},H)}{K_m(H)}Cov_{fh}(\mathbf{x},\boldsymbol{\chi}) + \left[\frac{\theta(\mathbf{x},H)}{K_m(H)}H(\mathbf{x}) - J^T(\mathbf{x})\nabla H(\mathbf{x})\right]Cov_{ah}(\mathbf{x},\boldsymbol{\chi})
\end{aligned} \qquad (2\text{-}14)$$

Similarly, we can also multiply the linear perturbation equation with $f(\chi)$ and $a(\chi)$ and later take the expected value of the product to come up with the moment equation in terms of covariances $Cov_{fh}()$ and $Cov_{ah}()$. Note that J is the gradient of hydraulic head.

$$\begin{aligned}
&\nabla_x{}^2 Cov_{fh}(\mathbf{x},\boldsymbol{\chi}) + A\left[2J(\mathbf{x}) - \nabla_x z(\mathbf{x})\right]^T \nabla_x Cov_{fh}(\mathbf{x},\boldsymbol{\chi}) - A\frac{\theta(\mathbf{x},H)}{K_m(H)}Cov_{fh}(\mathbf{x},\boldsymbol{\chi}) \\
&= -J^T(\mathbf{x})\left[\nabla_x Cov_{ff}(\mathbf{x},\boldsymbol{\chi}) + H(\mathbf{x})\nabla_x Cov_{fa}(\mathbf{x},\boldsymbol{\chi})\right] \\
&+ \frac{\theta(\mathbf{x},H)}{K_m(H)}Cov_{ff}(\mathbf{x},\boldsymbol{\chi}) + \left[\frac{\theta(\mathbf{x},H)}{K_m(H)}H(\mathbf{x}) - J^T(\mathbf{x})\nabla H(\mathbf{x})\right]Cov_{fa}(\mathbf{x},\boldsymbol{\chi})
\end{aligned} \qquad (2\text{-}15)$$

$$\begin{aligned}
&\nabla_x{}^2 Cov_{ah}(\mathbf{x},\boldsymbol{\chi}) + A\left[2J(\mathbf{x}) - \nabla_x z(\mathbf{x})\right]^T \nabla_x Cov_{ah}(\mathbf{x},\boldsymbol{\chi}) - A\frac{\theta(\mathbf{x},H)}{K_m(H)}Cov_{ah}(\mathbf{x},\boldsymbol{\chi}) \\
&= -J^T(\mathbf{x})\left[\nabla_x Cov_{af}(\mathbf{x},\boldsymbol{\chi}) + H(\mathbf{x})\nabla_x Cov_{aa}(\mathbf{x},\boldsymbol{\chi})\right] \\
&+ \frac{\theta(\mathbf{x},H)}{K_m(H)}Cov_{af}(\mathbf{x},\boldsymbol{\chi}) + \left[\frac{\theta(\mathbf{x},H)}{K_m(H)}H(\mathbf{x}) - J^T(\mathbf{x})\nabla H(\mathbf{x})\right]Cov_{aa}(\mathbf{x},\boldsymbol{\chi})
\end{aligned} \qquad (2\text{-}16)$$

Cov_{hh} can be obtained from Equation (2-14) if Cov_{ah} and Cov_{fh} can be solved from Equations (2-15) and (2-16). Recall that knowledge of the covariance is a pre-requisite to calculating volume-variance relationships. Cov_{hh} can be calculated if we know:

1. Cov_{aa}, Cov_{af}, Cov_{ff}

2. Boundary conditions
3. *H(x)*, which can be obtained by solving Equation (2-6) using the expected values of all the parameters; however, such an approach neglects the effects of spatial variability of hydraulic parameters on the mean flow variables.

Knowledge of these covariances is used to obtain the ensemble water flux, the effective hydraulic conductivity, and the upscaled mass balance. It should not be surprising that analytical solutions to these moment equations are extremely difficult without further simplifications or assumptions. It is also possible to solve such equations numerically. Further details about the derivations and solution strategies can be found in the references cited. There are still certain challenges that remain active areas for research:

1. Assumption of Gaussian statistics: it is assumed that the variability of the phenomena in both space and time are completely described by the first two orders of moment (mean and variances).
2. Assumption of ergodicity (the equivalence of spatial mean and ensemble mean): this is valid only if the length scale of interest is much larger than correlation length. This assumption is not valid when we have sharp interfaces within the averaging volume, such as reaction fronts or flow fingering, which act as point sources of instability and propagates continuously throughout the system. In a Lagrangian framework, Dagan and Cvetkovic (1996) have obtained closed form solutions for the expected values of the spatial and temporal moments of a nonlinearly reacting solute plume, or of two immiscible fluids. Given that the one-dimensional solutions to various transport processes such as mineral dissolution and oil-water displacement have been studied extensively using the method of characteristics, the authors proposed to model reactive transport along three-

dimensional flow paths in a transformed one-dimensional Lagrangian domain. In other words, one-dimensional solutions are obtained along the streamlines, and the moment equations are written in terms of τ and t (τ is the travel time) instead of $\mathbf{x}$ and t. To obtain τ, a set of equations defining the streamlines are solved separately.

3. Data conditioning: formulations such as those derived in this chapter are applicable when the permeability field $K(\mathbf{x})$ is "unconditional". In most cases, the correlation structure of the random field is modeled in the presence of sparse data using expert judgment. This implies that there is likely to be a slight discrepancy between the specified correlation structure and that exhibited by the data. This slight non-stationarity may cause the basis for the stochastic PDE to be violated. Some authors such as Rubin and Gomez-Hernandez (1990) have proposed approaches for upscaling block conductivities conditional to lognormally-distributed point conductivities. Rubin et al. (1999) present an approach for modeling block effective macrodispersivity in spatially variable velocity fields conditioned to measured data.

2.4.2 Volume Averaging Methods

As opposed to the ensemble averaging methods, volume averaging methods deal with the spatial mean. Since spatial heterogeneity influences that spatial mean, the concepts of volume averaging dovetail closely with our objectives. Volume averaging is a rigorous mathematical technique to derive continuum equations for multiphase systems. Equations that are valid within a particular phase are spatially averaged to produce equations that are valid everywhere in the system (Whitaker, 1999).

General treatments of various types of transport problems using the volume averaging techniques can be found in Whitaker (1999). The most common types of transport problems studied with this method are solute transport (Zanotti and Carbonell, 1984; Plumb and Whitaker, 1988), fluid flow (Quintard and Whitaker, 1988; 1996; 1996; 1998), and heat transfer, from which scaled-up versions of various transport parameters such as dispersivity, mass or heat transfer coefficients, permeability tensor can be derived. Wood et al. (2003) compares effective dispersivity tensor using volume averaging with periodic unit cells with results obtained from stochastic perturbation. Their results show that when second-order spatial stationarity is imposed on the velocity field, the two methods yield the same solution in the limit as the period of the unit cell approaches infinity. The same study also shows that as the size of the averaging volume increases, the variation in the effective dispersion tensor components decreases.

Specific applications relating to reaction-transport processes in single phase flow are available in Quintard and Whitaker (1994) and Kechagia et al. (2002), in which they focus on systems with fast kinetics (the limit at which thermodynamic equilibrium applies) and derived effective mass transfer coefficient.. Coutelieris et al. (2006) extended the algorithm to multiphase mass transfer with partitioning and interface transport. Detailed description of the approach will be provided in subsequent chapters; however, it is appropriate to briefly discuss here some key assumptions and concepts related to the volume averaging approach.

A schematic representation of various averaging volumes in a heterogeneous medium is shown in Figure 2-9, describing the four typical scales encountered in most transport problems (Ahmadi et al., 1998):

1. Macropore scale with averaging volume V_σ
2. Darcy (or continuum) scale with averaging volume V
3. Local heterogeneity scale with averaging volume V_∞
4. Reservoir-scale heterogeneities with a length scale L_H with no associating average volume because governing equations are solved numerically at this scale.

The most important assumption invoked is that the length scale of heterogeneity has to be less than the averaging volume. We can represent this length scale constraint as follows (see Figure 2-9 for explanation of each symbol):

$$\begin{aligned} &l_\kappa, l_\gamma \ll r_\sigma \ll l_\beta, l_\sigma \\ &l_\beta, l_\sigma \ll r_o \ll l_\eta, l_\varpi \\ &l_\eta, l_\varpi \ll R_o \ll L_H \le L \end{aligned} \qquad (2\text{-}17)$$

In the above constraint, r_s, r_o, R_o, L represent the averaging scale, and $l_\kappa, l_\gamma, l_\beta, l_\sigma, l_\eta, l_\varpi, L_H$ are the corresponding length scales of heterogeneity. This assumption is invoked in the existing volume averaging approaches to ensure the average quantities vary smoothly in space, a property that is needed to solve for the deviation equation when fine-scale solutions are not available. This assumption will be relaxed in the proposed formulations because solutions from fine-scale simulations are integrated. Furthermore, most studies begin at the continuum scale, where the governing equations are assumed to be a volume averaged representation of the macropore scale. In order to obtain the volume averaged equations at the scale of local heterogeneities, we perform volume averaging again on the continuum scale equations. The following is a brief outline of the approach:

1. Derive point-scale governing transport equations
2. Apply spatial averaging to the point-scale equations
3. Re-write fine-scale quantity (e.g., velocity, concentration, pressure) with a sum of coarse scale average and a fine-scale deviation to obtain the *averaged equation*.
4. Subtract the averaged equation from the original point-scale equation to attain the *deviation equation*.
5. The averaged equation provides the description of effective transport; however, since it is written in terms of both average and deviation quantities, both the averaged and deviation equations must be solved simultaneously.

Although much of the research in the literature focused on single-phase flow, some authors have extended this approach to two phase system for both solute transport and flow problems. The main difference is that the averaged and deviation equations are derived for each phase, and these equations are all coupled. For example, in the case of solute transport, the concentrations of all phases are coupled through the inter-phase mass transfer coefficients, which could be a function of injection phase concentration, velocity, or pressure. Although this method appears to be mathematically sound and sophisticated, there are some major drawbacks:

1. Volume averaged equations can be derived only if the internal heterogeneities have a length scale much smaller than the averaging volume.
2. The formulation is very complex, hence applications of this technique is generally limited to system with simple geometry such as a unit cell with periodic properties.

This research aims to alleviate these drawbacks such that the volume averaging techniques can be applied to investigate scale-up of flow accounting for heterogeneity at different scales. First, we derive averaged and deviation equations that are valid at the geocellular scale, such that geocellular models (already at the REV of pore scale) can be used, assuming that the pore to fine grid scale-up has been done. Second, flow simulations are performed with these reservoir models to obtain all the fine-scale quantities; this information allows the length scale constraint to be relaxed and helps to constrain the simultaneous solutions of the average and deviation equations so that original material balance is satisfied. Since fine-scale flow simulations are computationally expensive, it is proposed that flow simulations to be performed over only a sub-section of the reservoir to capture the fine-scale physics.

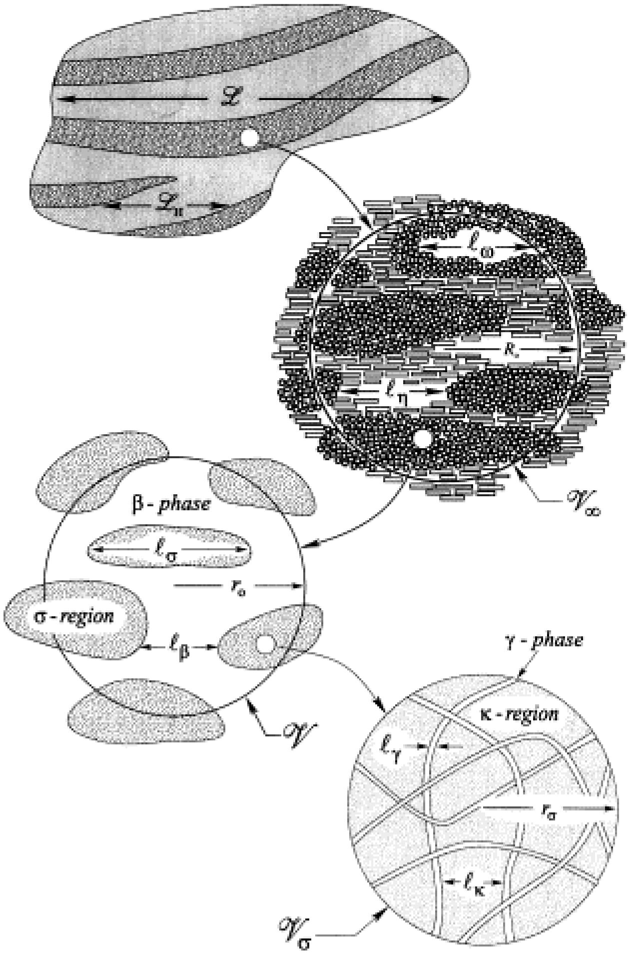

Figure 2-9: Averaging volumes in a hierarchical porous medium (reprinted with permission from Ahmadi et al., 1998).

Chapter 3: Analysis of Uncertainty Introduced by Scale-Up of Reservoir Attributes and Flow Response

3.1 OVERVIEW

Proper scale-up of petrophysical properties that are autocorrelated or heterogeneously distributed in space is necessary in order to make reliable predictions of reservoir recovery. A methodology is proposed to investigate and quantify the uncertainty in reservoir models introduced by scale-up. It is demonstrated that when the volume support of the measurement is smaller than the REV scale of the attribute to be modeled, there is uncertainty in the conditioning data due to scale-up and that uncertainty has to be propagated to spatial models for the attribute. This methodology for uncertainty assessment is demonstrated for mapping total porosity and secondary (fracture) porosity for a carbonate reservoir in the Gulf of Mexico. The results demonstrate that in most cases, the uncertainty distributions obtained by accounting for the scale-up procedure bracket the actual core and log data observed along new wells. Conventional reservoir models considering the well data as "hard" conditioning data fail to bracket the "true" values.

Following this discussion on scaling of reservoir attributes, a conceptual understanding of the scaling characteristics of flow responses such as recovery factor (RF) is provided in the form of numerical simulation results at different scales. Relationships of mean and variance of RF versus length scale depicts its scaling characteristics, which are specific to the underlying heterogeneity model and the dominating transport mechanisms. The overall research objective is to provide a tool to generate these scaling relationships for RF without having to perform detailed compositional reservoir simulations over hundreds of fine-scale reservoir models.

3.2 SCALE-UP OF RESERVOIR ATTRIBUTES

In reservoir modeling, relevant information about model parameters is available from a wide range of data sources that sample different volumes of the reservoir. In order to incorporate all these different types of information into a single model, a procedure termed “scale-up” is necessary to integrate information at the relevant volume support. Since reservoir properties are heterogeneously distributed in space, scale-up of the underlying heterogeneity is crucial for capturing the overall uncertainty in reservoir properties at the scale of interest (Lake and Srinivasan, 2004). Scale-up of petrophysical properties such as porosity is generally accomplished by linear averaging of fine-scale log data to the appropriate geocellular model. Unfortunately, this change in volume support often leads to a loss of information and additional uncertainty in the reservoir models. In the case of secondary porosity that is induced by chemical dissolution and micro-fractures, the averaging process is non-linear and therefore requires analyses to be performed taking into consideration a nonlinear-transformation procedure. The focus of this section is to illustrate a methodology to scale-up reservoir properties. The technique is applied to a case study where we investigate and quantify the uncertainty in both total and secondary porosity introduced by scale-up for a carbonate reservoir located in the Gulf of Mexico.

3.2.1 Method

In order to model the effect of additional variability due to scale-up, the variance of block mean is computed corresponding to a given spatial correlation model for a particular length scale (Chapter 2). This variance characterizes the uncertainty in property value for that particular length scale. When that calculation is performed at a conditioning data location using the support volume of the geo-cellular grid, the uncertainty in the conditioning value is obtained. We sample from these uncertainty distributions of data values using spatially correlated probability values and generate multiple sets of conditioning data. Using a linearly-averaged scaled-up semi-variogram, conditional simulation is performed on all sets of conditioning data in order to establish the uncertainty estimates at locations away from conditioning data (Leung and Srinivasan, 2008). The uncertainty in attribute value at any location away from the data location therefore has compounded uncertainty due to sparse data and due to uncertainty in the available data.

In order to apply this method for a non-linearly averaged attribute such as secondary porosity due to micro-fractures, a transformation to a linear space using Archie's exponent is employed. The premise for such a transformation is that if secondary porosity is nonlinearly related to the linearly averaged total porosity via an Archie's exponent, a transformation into the linear space using Archie's exponent should be feasible, and subsequently, the procedure for establishing the variance of the mean can be readily implemented. The work plan of scale-up can be outlined as follows:

1. 3-D variogram analysis based on fine-scale data.
2. Calculations of representative elementary volume and variance of mean using the 3-D point-scale variogram from Step #1 and equations (2-1) and (2-2) from Chapter 2.
3. Computation of up-scaled variogram via linear volume averaging.
4. Sample multiple sets of up-scaled conditioning data values from distributions whose mean is the block-average of the actual measured values and the variance is the previously calculated variance of the mean. A Gaussian assumption is implicit in this step.

5. Use the up-scaled variogram from Step #3 along with one sampled set of conditioning data to perform conditional simulations at the coarse scale.
6. Repeat Step #5 for other sets of conditioning data obtained in Step #4.

3.2.2 Case Studies – Scale-Up in a Carbonate Reservoir

Consider a field example of a carbonate reservoir, where available information includes total porosity logs (neutron porosity) and secondary porosity logs that are inferred based on facies and total porosity calculations (Sharma et al., 2008). The log resolution is 0.15m, while the geocellular grid resolution is 50m x 50m x 6m. It is obvious that data resolution is much smaller than the reservoir model resolution. Our task is to generate scaled-up reservoir models for total and secondary porosity that accurately portray the uncertainty due to sparse information and disparities between the measurement and modeling scale.

3.2.2.1 – Linear Averaging of Total Porosity

Total porosity is generally up-scaled assuming linear averaging because porosity mostly follows a normal distribution. For a random sample of *n* observations from a normally distributed population $N\{\mu, \sigma^2\}$, the sample mean distribution is described as:

$$\overline{X} \sim N\left\{\mu, \frac{\sigma^2}{n}\right\} \qquad (3\text{-}1)$$

$\overline{X}$ is the sample mean computed via arithmetic averaging. The above expression suggests that $\overline{X}$ is the unbiased estimator of μ. Assuming that total porosity can be averaged linearly, the procedure outlined above is readily applicable. Variogram analysis of well porosity (neutron porosity, NPHI) data revealed a non-stationarity trend in the 135^{o} direction (Figure 3-1). This is also corroborated by geological studies regarding a SE-NW trend in the area. On the other hand, the experimental variogram in the vertical direction (Figure 3-2) shows a range of approximately 30m.

In order to construct a composite 3-D variogram, the following decomposition of total porosity is adopted: $Z(\mathbf{x}) = m(\mathbf{x}) + R(\mathbf{x})$, where $R(\mathbf{x})$ is the isotropic residual added to a directional trend $m(\mathbf{x})$. Since no auxiliary data such as seismic impedance is available to infer the trend, a trend map is synthesized using a variogram with an exaggerated long range in the direction of the trend. Note that the trend map is computed on the coarse scale, whereas the residuals are computed on the fine scale. The variogram parameters for the trend model can be summarized as follows:

- Nugget = 0.05
- One Structure: exponential
    - Sill contribution = 0.95
    - Azimuth angle = 135 degrees
    - Range = 6000m (major) & 3000m (minor)
    - Vertical range = 30m

Given the trend model $m(\mathbf{x})$, the residuals $R(\mathbf{x})$ are now computed as $[Z(\mathbf{x}) - m(\mathbf{x})]$, and the experimental residual variogram in the horizontal direction is shown in Figure 3-3. An isotropic variogram is fitted to the point-scale residual variogram in 3-D as follows:

- Nugget = 0.05
- One Structure: exponential
    - Sill contribution = 0.95
    - Horizontal range = 2000m (isotropic)
    - Vertical range = 30m

The logs show a great deal of vertical variability as shown in Figure 3-4. The first step is therefore to determine the REV scale in the vertical direction and to determine the additional variance (uncertainty) introduced by using a sub-REV scale grid resolution. This can be achieved by plotting the variance of mean as a function of length scale in the vertical direction as described in the previous section (Figure 3-5). In this case, the REV calculations show that the minimum averaging length scale should be approximately 60-100m. In other words, a vertical averaging window of a minimum size of 60-100m is required to average out sub-scale variance. When the scale is smaller than this REV, additional variance due to sub-scale variability of total porosity has to be accounted for. The coarse grid that is used to model porosity in this real-field example has a vertical resolution of 6m. This resolution is smaller than the REV scale in the vertical direction and therefore results in additional variance (uncertainty) that has to be carried forward in stochastic simulations. It can be seen that a length scale of 6m translates into a variance of 0.0008 (i.e. standard deviation of 0.028 porosity unit).

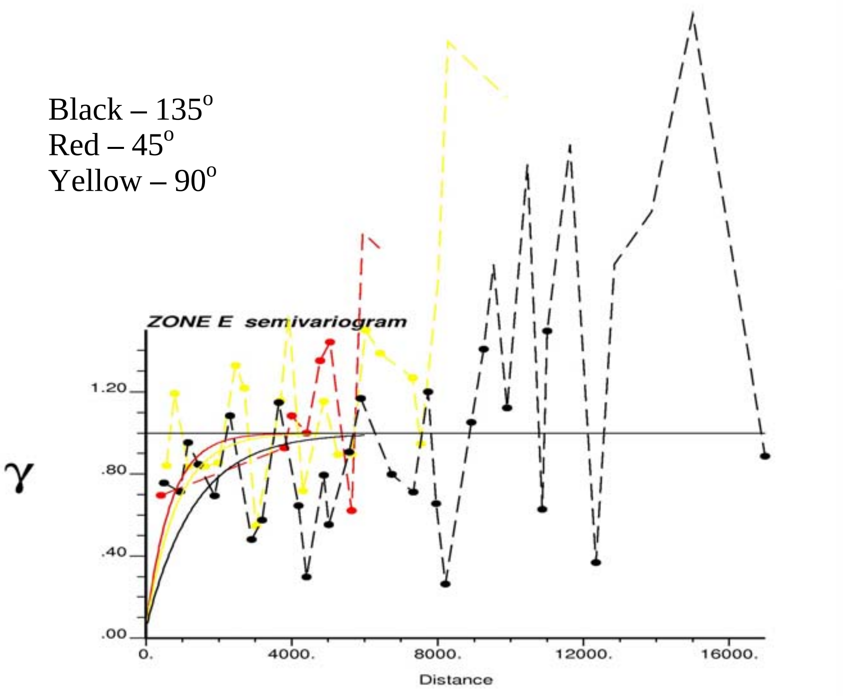

Figure 3-1: Experimental variogram in the horizontal direction computed along various azimuth angles.

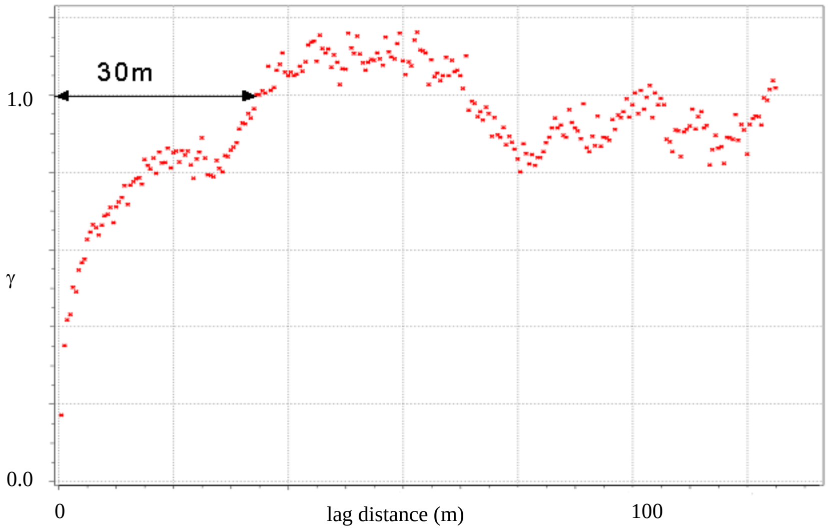

Figure 3-2: Experimental variogram in the vertical direction.

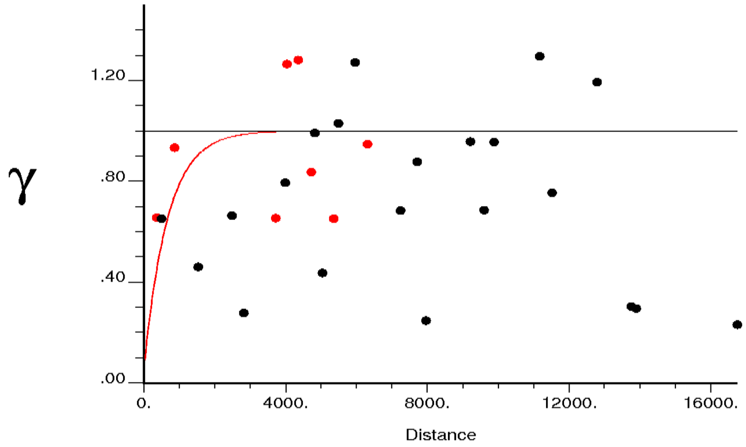

Figure 3-3: Horizontal residual variograms along 45° (red) and 135° (black) azimuth directions. An isotropic variogram is fitted.

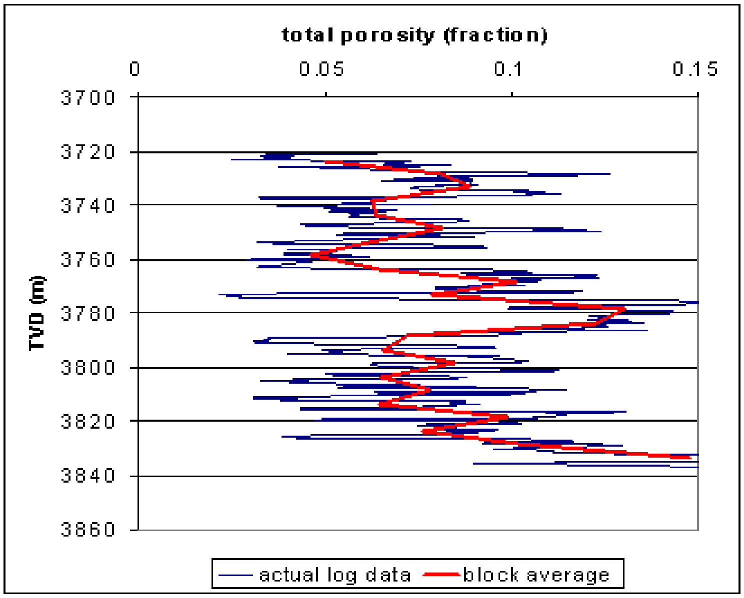

Figure 3-4: Typical section of the total porosity log. Significant vertical variability can be observed.

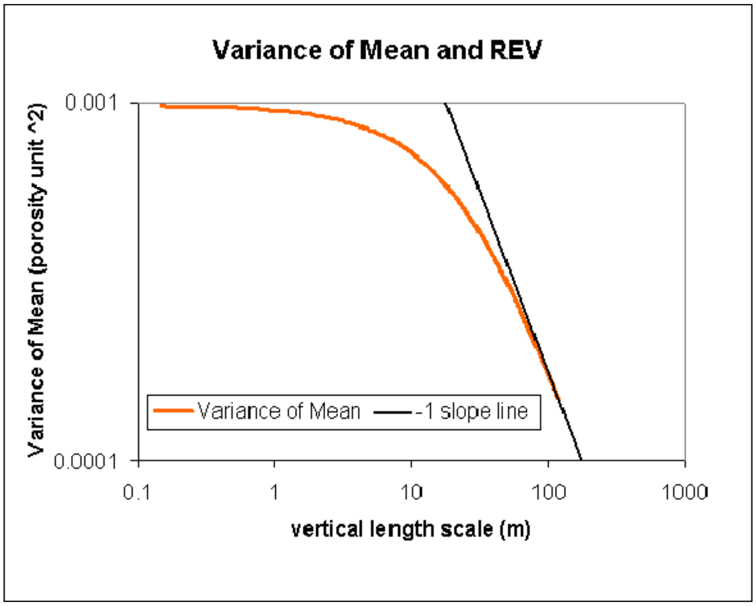

Figure 3-5: Variance of mean as a function of vertical length scale corresponding to the vertical variogram. The diagnostic negative unit slope line shows a REV scale of ~60-100m. At the vertical length scale of 6m (geocellular grid resolution), the corresponding variance of the mean is approximately 0.0008.

The 3-D variogram model and the variance of mean calculations can now be used to perform sequential simulation that accounts for sub-scale variability. Since we are now working with residuals, $R(\mathbf{x})$, instead of the actual variable, $Z(\mathbf{x})$, slight modifications to the steps outlined in the previous section (3.2.1) are required:

1. Steps 1-3 are performed with the residual variogram
2. In Steps 4-6, up-scaled conditioning data are obtained from distributions whose mean is the block-average of residuals. Block conditional simulation results must be added to the trend map to obtain the final simulated values.

The next step is to perform the conditional simulations accounting for the uncertainty in the “hard” data. But prior to doing the simulation, it has to be recognized that variograms of $R(\mathbf{x})$ inferred on the basis of logs have to be scaled up in order to reflect the spatial variability of the average quantities on the geocellular grid. For this reason, average variograms (gamma-bar $\bar{\gamma}$, Journel and Hujbregts (1978)) are calculated and modeled on the basis of the variogram at log-support (shown in Figure 3-6). These gamma-bar models are specified for the conditional simulations as follows:

- Nugget = 0
- Structure #1: spherical
    - Sill contribution = 0.3
    - Horizontal range = 1600m (isotropic)
    - Vertical range = 40m
- Structure #2: exponential
    - Sill contribution = 0.7
    - Horizontal range = 2600m (isotropic)
    - Vertical range = 40m

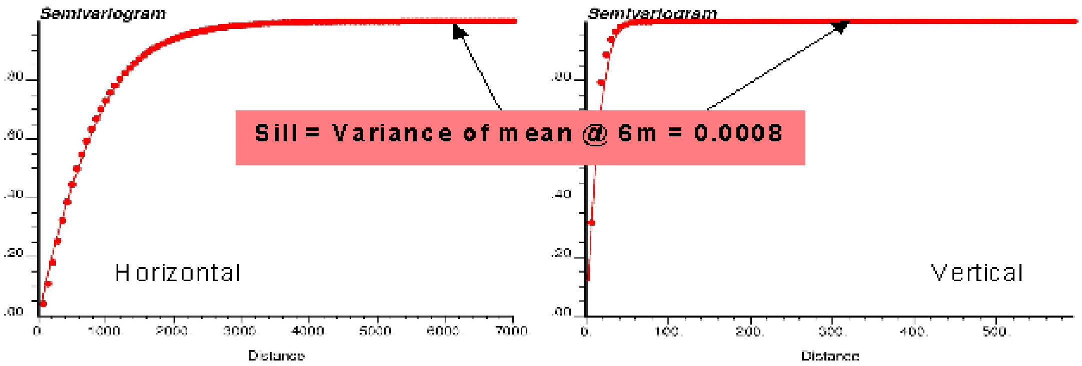

Sill = Variance of mean @ 6m = 0.0008

Figure 3-6: Averaged or scaled-up variograms (gamma bar) of the residuals *R*(**x**).

Results from three different cases are shown in Figure 3-7 and Figure 3-8: (1) Sequential Gaussian simulation (SGSIM) using the log data as conditioning data, combined with the residual variogram inferred at the log-scale. (2) SGSIM using the point-scale data as conditioning data, combined with linear volume averaged variogram (gamma-bar). (3) SGSIM using 10 sets of conditioning block data (representing the uncertainty in hard data value), combined with linear volume averaged variogram and trend map. It is evident from Figure 3-8 that uncertainty is subsided near the conditioning (well) locations, but increased uncertainty is observed when uncertainty in "hard" conditioning data due to scale-up is accounted for (Case 3).

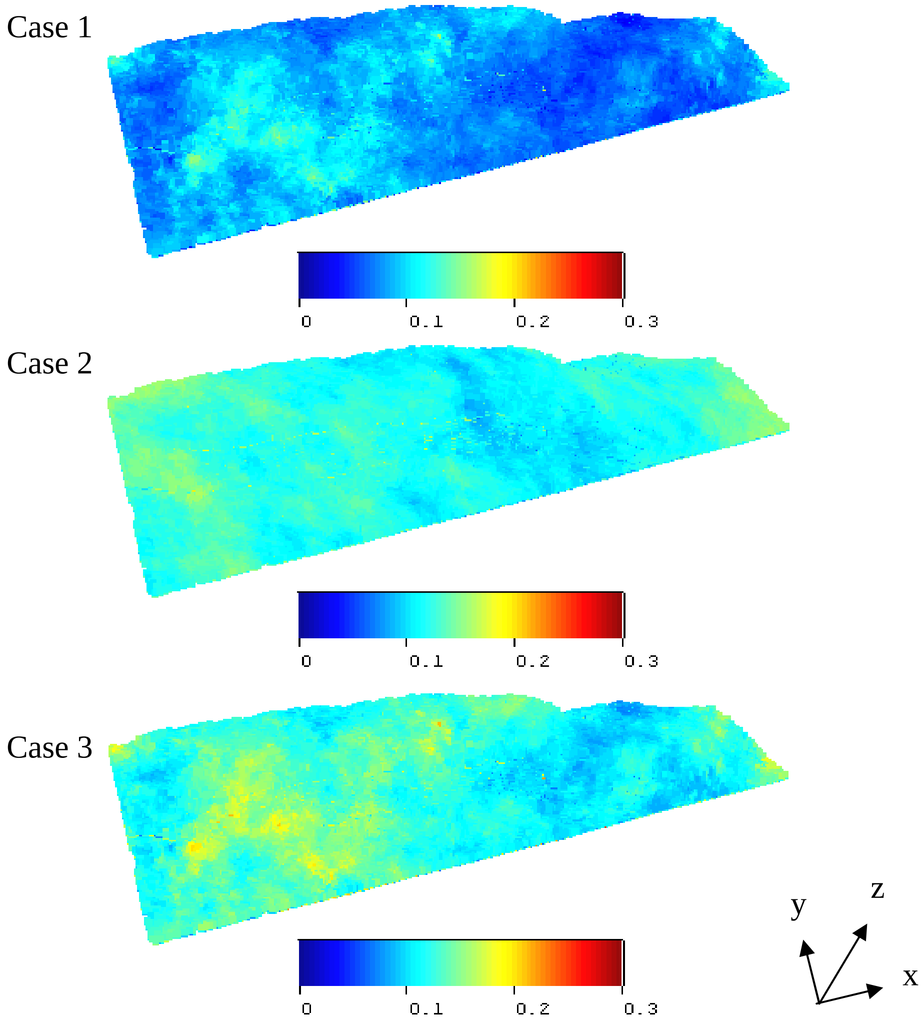

Figure 3-7: Comparison of mean realizations for: point-scale simulation (Case 1); point-scale data with volume-averaged variogram (Case 2); block simulation (Case 3).

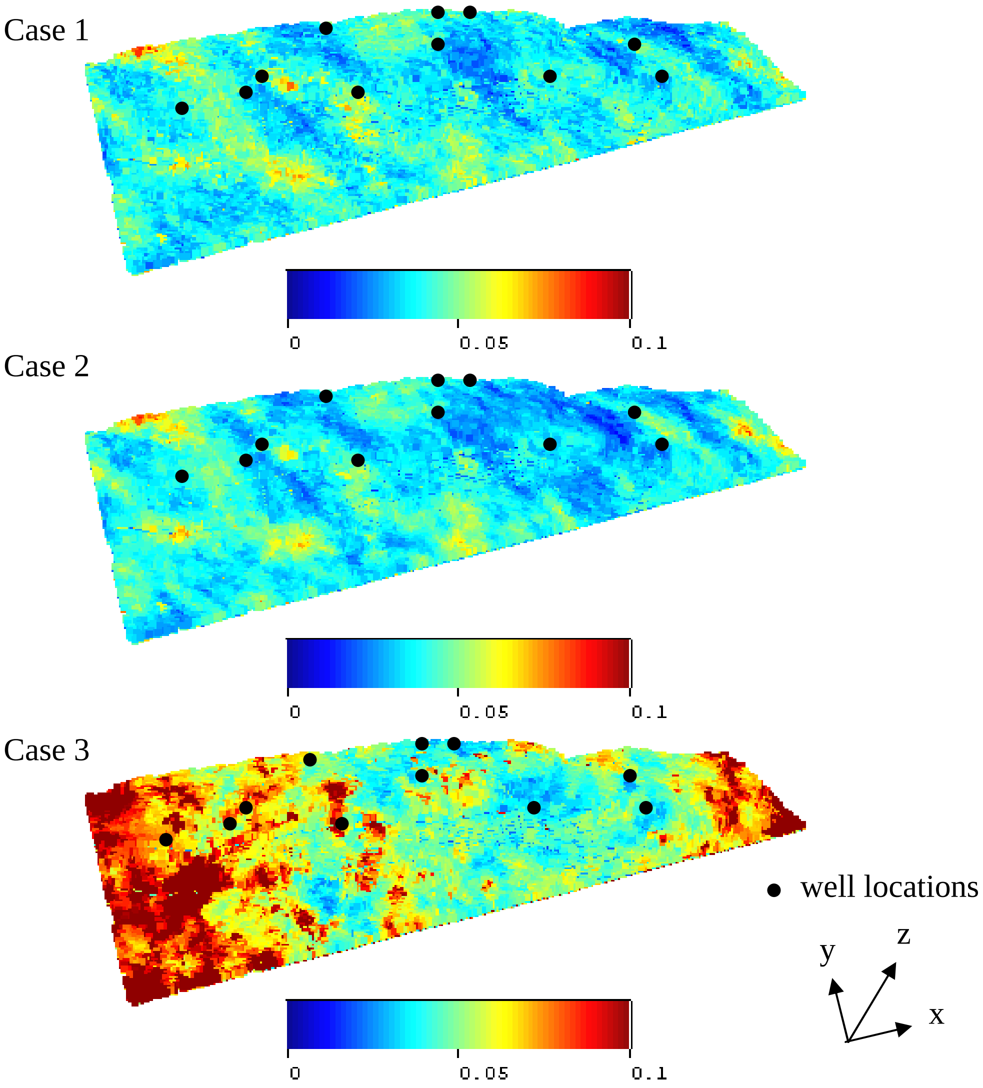

Figure 3-8: Comparison of standard deviation maps from the three cases. Case 3 is all encompassing, representing the uncertainty due to scale-up and scarcity of conditioning data. Increased uncertainty is observed when sub-scale variability in "hard" conditioning data is accounted for.

Total porosity values from core analysis were obtained from two new wells and compared against results obtained from the 3-D conditional block simulation (Case 3). For Well #1, both values obtained from core analysis and the NPHI logs are bracketed by the probability distribution obtained from conditional block simulation. The average of the log and core value is 0.044, while the probability distribution has a mean of 0.05, with a 95% confidence interval of 0.033-0.067. Similar results are obtained for Well #2. The average of core values is 0.072, while the probability distribution has a mean of 0.09, with a 95% confidence interval of 0.072-0.107 based on a sample size of 10. For the purpose of comparison, in the case where scale-up is not performed (i.e. Case #1), the probability distribution has a mean of 0.044, with a 95% confidence interval of 0.040-0.048 for Well #1 (which, incidentally, is a rather good match with the core average), while for Well #2, the probability distribution has a mean of 0.11, with a 95% confidence interval of 0.104-0.117, which is much higher than the core average. Furthermore, the confidence interval is also much narrower than in case #3 because the variability due to scale-up has not been accounted for. Results are illustrated in Figure 3-9.

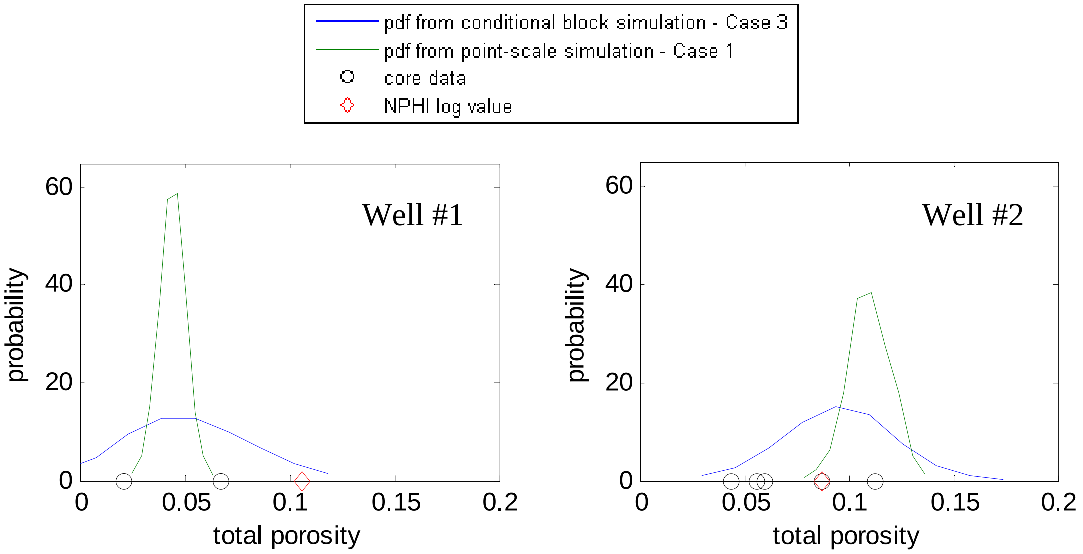

Figure 3-9: Comparison of simulation results with core and log data at two new wells. Results show that values obtained from core analysis and the NPHI logs are bracketed by the probability distribution obtained from conditional block simulation (Case 3), but not by the point-scale simulation (Case 1).

3.2.2.1 – Non-Linear Averaging of Secondary Porosity

The relationship between total porosity (ϕ_t), and secondary porosity (ϕ_f) is given by (Elkewidy and Tiab, 1998):

$$\phi_f = \phi_t^m \left(\phi_t - 1\right) / \left(\nu\phi_t - 1\right) \propto \phi_t^{m+1} \qquad (3\text{-}2)$$

In the above equation, *m* is the Archie exponent and ν is the partition coefficient representing the proportioning of total porosity between matrix and secondary porosity. This means that if total porosity averages linearly, secondary porosity raised to the power of 1/(*m*+1) also averages linearly (Deutsch, 1992; Srinivasan and Journel, 1998). Therefore, we postulate that we can work in the 1/(*m*+1) transformed space for secondary porosity and follow the same procedure as in the total porosity case. We first transform ϕ_f to $\phi_f^{1/(m+1)}$ and infer variograms in the transformed space. This is followed by calculation of variance of mean and gamma-bar. Block conditional simulations are performed by sampling conditioning data sets as described in the previous section. Finally, we transform the results back to the actual variable space and assess the uncertainty at each location in the reservoir over all realizations. Results over 100 reservoir models (10 sets of conditioning data x 10 realizations) are shown in Figure 3-10. To check whether results of the conditional block simulation bracket the actual log response, data from one well (Well #3) was intentionally excluded during the simulation step, and it was compared against the simulated response at the well location (Figure 3-11). It is evident that the actual secondary porosity log exhibits significant variability vertically, but the simulated responses appear to bracket the uncertainty in most intervals. Finally, unbiasedness of the transform is checked by comparing the mean of all simulated values over 100 realizations (0.035) to the mean of block-averaged conditioning data (0.028).

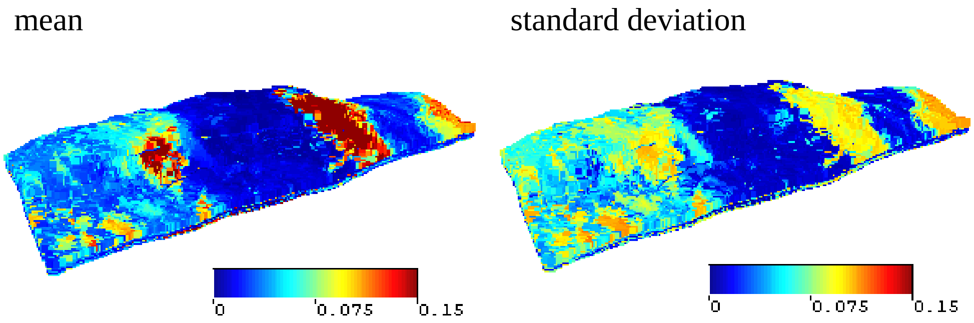

Figure 3-10: Results of the conditional block simulation of secondary porosity over 100 reservoir models (10 sets of conditioning data x 10 realizations) are shown.

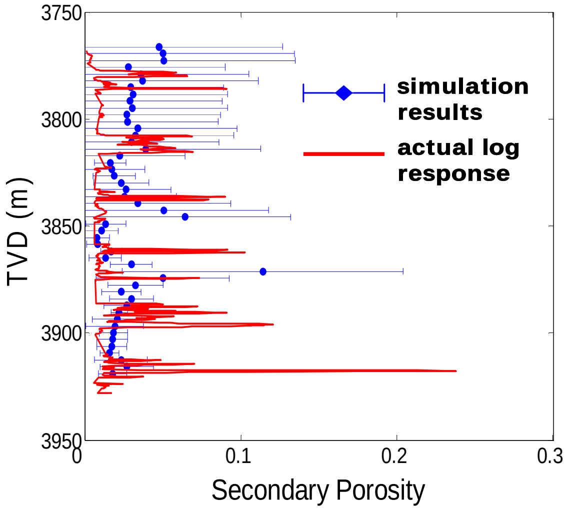

Figure 3-11: Comparison between results from conditional block simulation (excluding Well #3) and the interpreted secondary porosity log values at Well #3. The error bar indicates the mean plus/minus a standard deviation.

3.2.3 Discussion

3-D block simulation has to be performed to quantify the uncertainty in block property values in the simulation grid. Since the variograms of the petrophysical properties exhibit variability from one zone to the next, the uncertainty due to scale will be different depending on the properties of the zone. For the case of secondary porosity, a transformation has to be performed prior to performing the volume-variance calculations. Our results reveal the following: (1) ideally if the grid resolution of the reservoir model is at the REV scale of the phenomenon, no additional variance due to the sub-scale variability needs to be taken into account; (2) if the grid-resolution is at the sub-REV scale, additional variance (uncertainty) due to sub-scale variability needs to be taken into account; (3) generally, when one moves from point scale to volume scale, the average variogram exhibits smoothing characteristics, but it is offset by the increase in uncertainty due to scale-up, hence the increase in overall uncertainty (Case 3 in Figure 3-8). A fundamental result presented in this section is that conditioning data in most practical cases of reservoir modeling are in fact “soft”. A scheme to directly propagate uncertainty from “soft” data locations to unsampled locations is therefore necessary. This will eliminate the need to sample multiple sets of conditioning data and generate multiple realizations conditioning to each data set. A technique for such direct propagation of uncertainty is discussed in Leung and Srinivasan (2008) and in Appendix A.

3.3 SCALE-UP OF FLOW RESPONSE

The preceding section provides some insights into the scaling characteristics of static reservoir attributes. That, in some fashion has to be translated to the scaling of dynamic reservoir responses. A simplified case study is presented in this section that serves to demonstrate how flow response (recovery factor, RF, in this example) scales with the volume of investigation.

Consider a two dimensional grid with 500 grid blocks in the x and z directions. The fine-grid dimensions are 4m x 4m x 4m. Fifty fine-scale permeability realizations were generated via unconditional SGSIM using an isotropic spherical variogram structure with a correlation length of 20m (equivalent to 5 grid blocks). Ratio of vertical to horizontal permeability is assumed to be 0.1. Next, we choose a particular size (smaller than 500 grid blocks) and randomly select a sub-model of that size from each of the fifty realizations generated previously. All sub-models have an aspect ratio of 10:1 (x- to z-direction). This procedure is illustrated in Figure 3-12. Next, flow simulations of unit-mobility displacement with constant rate injection occurring into a well at the left edge of the cross-section and production at constant pressure on the right edge are performed on each sub-model. Recovery factor (RF) is calculated from cumulative oil production when water cut reaches 95%.

Statistics such as the variance of the mean are calculated using the value for recovery and average permeability. This process is repeated for other sub-model size such that plots of variance of mean of recovery and average permeability as a function of sub-model size can be obtained (Figure 3-13). For comparison purposes, the mean of permeability is calculated based on power averaging with exponent (ω) equals 1 (arithmetic average) and also for the harmonic average ($\omega = -1$). The variance and mean of recovery are also shown in Figure 3-13. Injection rates are adjusted proportional to the total volume of each sub-model to preserve the local pressure gradient/velocity ratio and the breakthrough time.

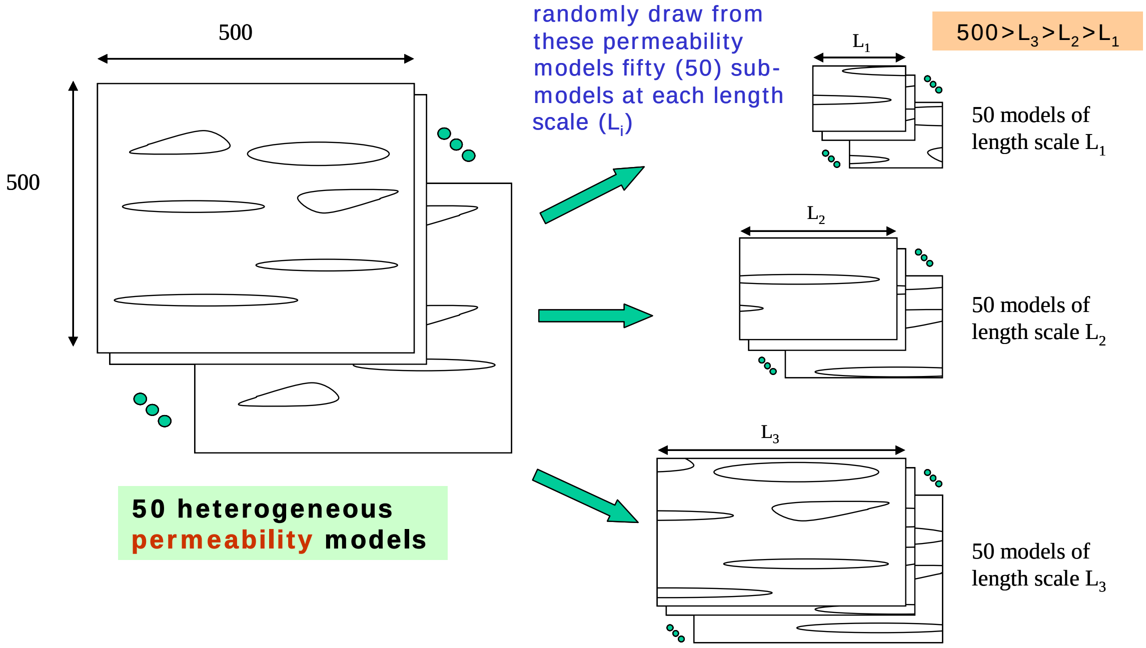

Figure 3-12: Schematic of the numerical flow simulation experiment, where repeated simulations are performed at increasing length scale (reservoir volume) to characterize the scale-up of flow response.

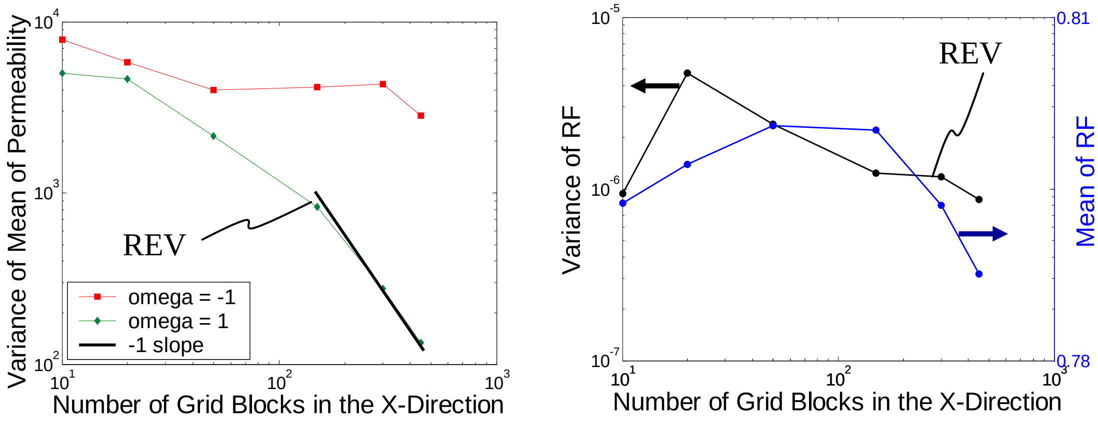

Figure 3-13: Scaling of permeability and recovery factor. The diagnostic -1 slope indicates the REV for permeability based on linearly averaging is ~100 grid blocks, while the REV for recovery factor is ~ 200 grid blocks.

It can be observed that both the mean and variance of RF exhibit a slight increase at small scales and decrease gradually at large scales. This initial increase might be due to boundary effects when model sizes are too small. The scaling characteristic for RF does not resemble that of arithmetic averaging. In fact, it appears to be similar to the case of power averaging with $\omega < 0$. A negative unit slope is not reached for either cases, but the variance decreases after stabilizing at some intermediate scales. The length scale at which the variance of RF starts to decline is much greater than the REV for permeability. This length scale might be used to define the REV for dynamic flow response parameters such as velocity.

It is reasonable to postulate that the variance of RF is a function of the underlying heterogeneity. Therefore, in this next example, the numerical flow simulations are repeated for different model sizes as well as different heterogeneity. Consider three two-dimensional grids in the x and z directions of different sizes (50x10, 100x20, and 200x40), keeping the same aspect ratio. For each of the three sizes, fifty porosity realizations are generated via unconditional SGSIM for two different porosity models: 1) isotropic with a correlation length of 5 blocks; 2) anisotropic with a horizontal correlation of 50 blocks and a vertical correlation length of 5 blocks. Permeability (in mD) is related to porosity as $10^5\phi^4$ and ranges from 1 to 2000mD (mean = 400mD), while ϕ ranges from 0.05 to 0.38 (mean = 0.23). Ratio of vertical to horizontal permeability is assumed to be 1.0. Flow simulations of a water-oil displacement with constant bottom-hole pressures at both the injection and production ends are performed. Oil viscosity is approximately 10 times higher than water viscosity, resulting in an unfavorable mobility. Recovery factor (RF) is again calculated from cumulative oil production when water cut reaches 95%. Results of scaling of RF are shown in Figure 3-14. The unfavorable mobility has resulted in a more drastic decline in RF with scale, as compared to Figure 3-

13. Furthermore, in the case of an anisotropic reservoir (more heterogeneous), significantly higher uncertainty in RF is observed.

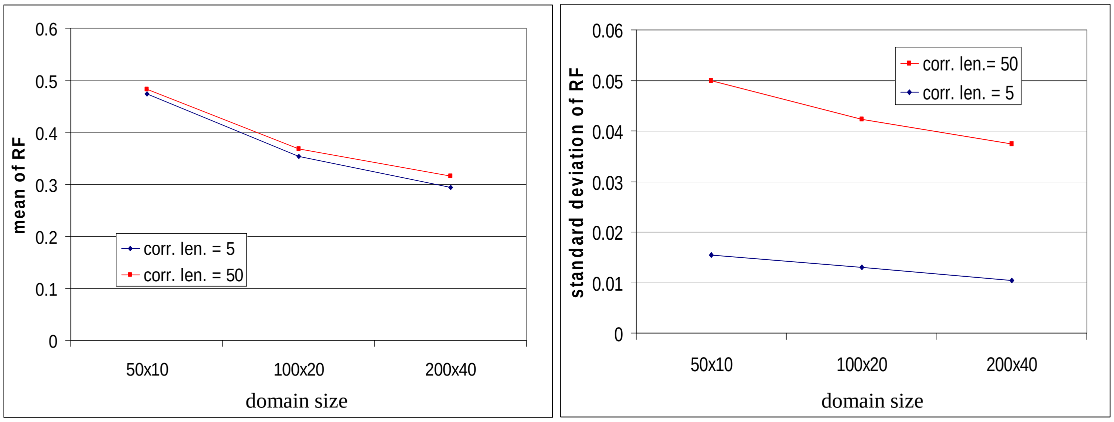

Figure 3-14: Scaling of recovery factor as a function of heterogeneity for a water-oil displacement with an unfavorable mobility ratio.

In addition to the underlying heterogeneity, the variance of RF plot is also impacted by the dominating transport mechanisms. As a result, for each spatial correlation structure of permeability, it is possible for us to generate a corresponding variance of RF plot for a given recovery process (provided that we can identify the dominating transport mechanisms). These plots can be used as type curves for understanding empirical scaling relationships between flow responses and heterogeneity. My research objective is to provide a general framework to generate these scaling relationships for RF without having to perform detailed full-physics reservoir simulations over hundreds of fine-scale reservoir models.

The previous case study illustrates the scaling characteristics of flow response, but another question arises: what is the uncertainty in flow response prediction that is introduced by scale-up of reservoir attributes? In other words, for a fixed domain size, how much additional uncertainty is introduced in the prediction of RF due to sub-scale variability in reservoir models? In order to gain an insight into these issues, let us consider the process of bitumen recovery via solvent-assisted gravity drainage. Nenniger and Dunn (2008) calibrated an empirical correlation that relates steady-state mass flux of bitumen to average reservoir and fluid properties.

$$\dot{m} = 43550\left(k\phi / \mu\right)^{0.51} \tag{3-3}$$

where $\dot{m}$ = mass flux (g oil/m^2 hour)
k = average permeability (Darcy)
μ = initial oil viscosity (cP)
ϕ = average porosity (fraction)

The authors demonstrated excellent agreement between much of their experimental data and this correlation. This suggests that it can be used as a simple flow-transfer function for evaluating recovery of bitumen. Two questions are of particular interest:

1. What is the scaling of flow response, in this case, mass flux $\dot{m}$?
2. How does scale-up of porosity and permeability impact the prediction of $\dot{m}$?

To study these two issues, consider a two-dimensional single layered reservoir in the x and y directions with the following porosity model: correlation lengths that are 40 and 20 grid blocks along E-W and N-S directions, respectively. Permeability is related to porosity through the same relationship $k(mD) = 10^5\phi^4$. Just as in the unit mobility displacement example (Figure 3-12), fifty realizations of porosity and permeability are generated at different length scales. Next, average porosity for each realization is obtained via linear averaging, and average permeability is obtained by substituting the average porosity into the same porosity-permeability relationship: $\bar{k}(mD) = 10^5\left(\bar{\phi}\right)^4$. Using the average porosity and permeability, a corresponding value of $\dot{m}$ can be obtained from the empirical correlation for realization. Figure 3-15 shows the scaling of $\dot{m}$ in terms of its coefficient of variation (standard deviation normalized by the mean), which is a measure of uncertainty in $\dot{m}$, as a function of domain size. It can be seen that the variability in $\dot{m}$ decreases with model size.

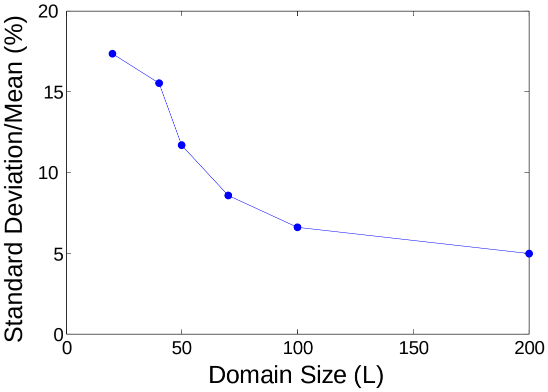

Figure 3-15: Uncertainty (coefficient of variation) in mass flux with domain size.

To understand the impact of scale-up of porosity and permeability on $\dot{m}$, we perform the following experiment: for a fixed domain size, namely 200 grid blocks by 200 grid blocks (the largest size in Figure 3-15), instead of performing the above calculations to characterize the flow response with fifty 200x200 models, what if fifty scaled-up models with various degree of coarsening are used?

The procedure is illustrated in Figure 3-16. First, we randomly select 50 points from one of the previously generated 200x200 realization as the "conditioning data". Next, following the conditioning block simulation algorithm outlined in section 3.2.1, fifty realizations at each coarsening level are generated. Once again, $\overline{\phi}$, $\overline{k}$, and $\dot{m}$ are computed for each realization. The statistics are presented in Figure 3-17, which shows the uncertainty in $\dot{m}$ as a function of coarse grid size. It should be reminded that all data points in Figure 3-17 are obtained with models that have a total domain size of 200x200, the difference lies in the level of coarsening: the red data point is taken from the last data point (domain size = 200) in Figure 3-15, as it represents the case where no scale-up of porosity and permeability is performed; the blue data points represent cases of different level of coarsening. A few important features can be observed:

1. Scale-up generally has a smoothing effect, as it is evident in the reduction of variance with coarse grid size.
2. Accounting for sub-scale variability in scaled-up models introduces additional variance, especially when the averaging block size is smaller than REV.
3. Uncertainty in reservoir models due to both heterogeneity and scale-up manifests itself as additional uncertainty in flow responses. As a result, flow prediction that neglects uncertainty in reservoir models due to both heterogeneity and sub-scale variability might introduce significant errors.

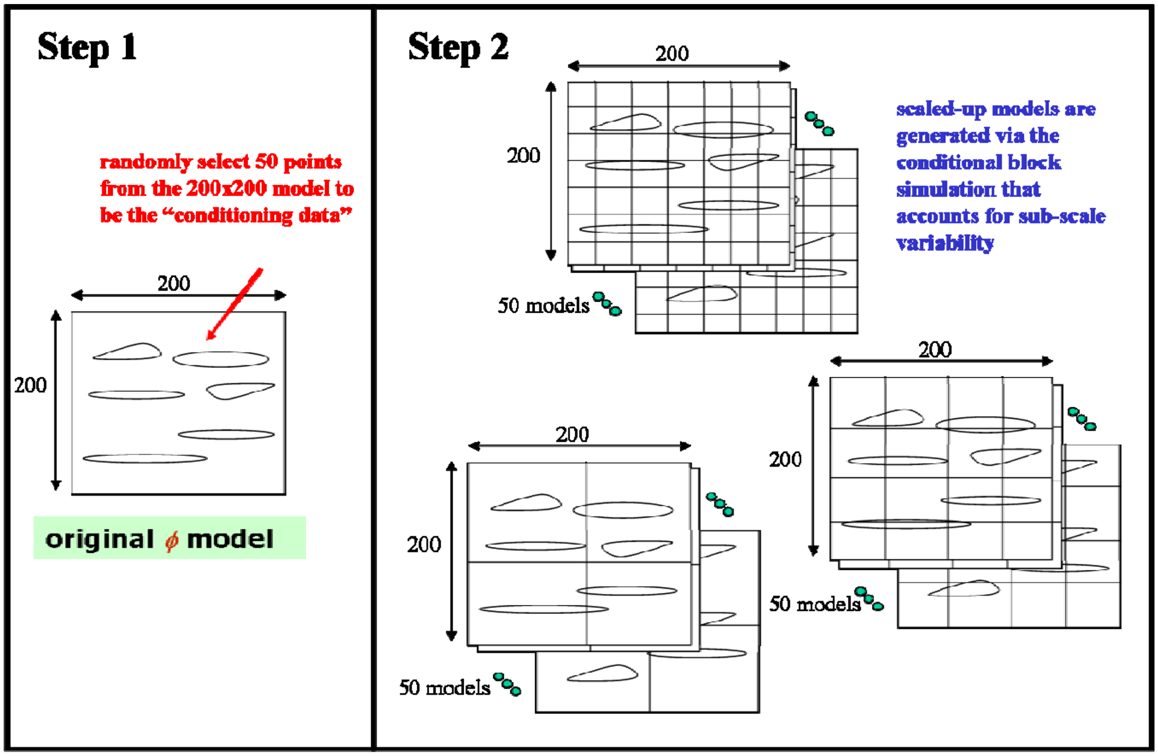

Figure 3-16: Schematic of the numerical flow simulation experiment, where repeated simulations are performed at increasing coarse grid size to investigate the impacts of scale-up of reservoir properties.

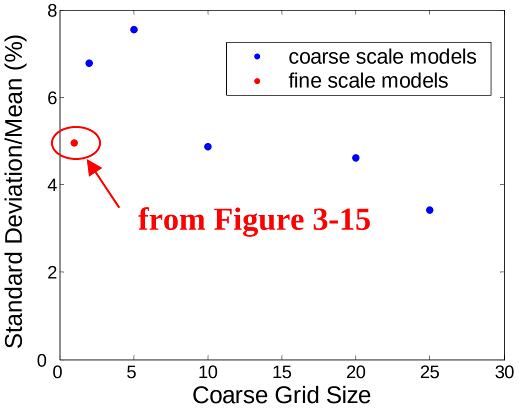

Figure 3-17: Uncertainty (coefficient of variation) in mass flux with scale-up of reservoir properties.

3.4 SUMMARY

Uncertainty due to sub-scale variability decreases as the averaging scale increases and becomes negligible at scale greater than the REV. A procedure has been proposed such that the variance of mean concept is used to represent this decrease in uncertainty due to sub-scale variability for linearly-averaged reservoir properties. In order to extend the algorithm to non-linearly averaged properties, a transformation to a space where linear averaging is permissible is required.

Similar to the case of reservoir attributes, the magnitude of the flow response as well as its variability decreases with length scale/domain size, and this observation is illustrated with several numerical examples in this chapter. Furthermore, the effect of scale-up of static reservoir attributes and heterogeneity on flow response is also demonstrated.

A major implication resulting from these observations is that as one compares flow responses obtained at different scales (e.g., core floods, pilot tests, and field recovery), it is important to remember that decrease in recovery with scale is expected due to the averaging of small scale phenomena. However, the uncertainty in prediction of that recovery factor may increase over length scales smaller than the REV for that process and then decrease for larger length scales. Given that the scaling relationship of recovery is a strong function of heterogeneity, the focus of this research is to propose a new procedure integrating the volume averaging techniques with numerical simulation results to derive this scaling relationship accounting for the underlying heterogeneity.

Chapter 4: A Numerical Approach to Scale-Up of Mass Transfer Equations in Single-Phase Flow Using Volume Averaging

4.1 OVERVIEW

This chapter begins with the formulations of volume averaged transport equations for single phase flow. Detailed derivations of volume averaged mass transfer coefficient accounting for dispersion, diffusion, convection, rock-fluid interactions, and reactions will be presented. The mass transfer coefficients will be expressed as a function of the averaging length scale. A brief description of the general numerical treatment of these volume averaged equations and effective transport coefficients will be discussed. In order to apply the volume averaging technique to real geological systems exhibiting complex heterogeneity, a new procedure is proposed where results from a fine-scale numerical flow simulation reflecting the full physics of the transport process albeit over a small sub-volume of the reservoir can be integrated. A detailed outline of the numerical scheme will be presented.

4.2 MATHEMATICAL FORMULATION

4.2.1 Scale-Up of Transport Equations

We will begin with the pore-scale formulation of the governing equations that describe the transport over an aggregation of pores and fluid distribution among them. The following major assumptions are made:

1. Constant temperature

2. β = aqueous phase; σ = solid phase; γ = non-aqueous phase; the σ, γ phases are assumed to be immobile: $\mathbf{u}_\sigma$ & $\mathbf{u}_\gamma = 0$ (**u** indicates velocity). This is equivalent to oil at residual saturation.
3. Incompressible aqueous phase and no-slip $\mathbf{u}_\beta = 0$ at $A_{\beta\gamma}$ and $A_{\beta\sigma}$ (A_{ij} represents the interface between phases i and j)
4. Fast kinetics such that equilibrium concentration is quickly established at the β-γ interface.

The governing equation, boundary and initial conditions become (Quintard and Whitaker, 1994):

$$\frac{\partial C_{i\beta}}{\partial t} + \nabla \cdot \left(\mathbf{u}_\beta C_{i\beta} \right) = \nabla \cdot \left(\overline{\overline{D}} \cdot \nabla C_{i\beta} \right) \tag{4-1}$$

B.C. 1: $C_{i\beta} = C_{eq}$ at $A_{\beta\gamma}$

B.C. 2: at $A_{\beta\sigma}$, $\mathbf{n}_{\beta\sigma} \cdot D \nabla C_{i\beta} = 0$ (no diffusion across the solid interface)

I.C. $C_{i\beta} = C_{i\beta o}(\mathbf{x})$ at $t = 0$ and $\mathbf{x} \in \Omega$

where C_i is the concentration of component i, $\overline{\overline{D}}$ is the molecular diffusion tensor, and the subscript eq indicates equilibrium condition. The subscript β indicates that the equations are written for the moving phase. The notation $C_{i\beta o}(\mathbf{x})$ represents the initial conditions for $C_{i\beta}$, which can vary spatially. For convenience, we drop the subscript i, assume isotropic $\overline{\overline{D}}$ (i.e. $\overline{\overline{D}} = D$), apply no-slip boundary conditions ($\mathbf{u}_\beta = 0$ at the solid interface), and ignore variations of molecular diffusivity (i.e. D is constant). This yields the following simplified form of the transport equation.

$$\frac{\partial C_\beta}{\partial t} + \nabla \cdot \left(\mathbf{u}_\beta C_\beta \right) = \nabla \cdot \left(D \nabla C_\beta \right) \tag{4-2}$$

It should be noted that the governing equation can also be formulated at the continuum scale by defining quantities scaled-up from the pore scale as $\langle \mathbf{u}_\beta \rangle_\varpi$, $\langle \mathbf{u}_\beta \rangle_\eta$, $\langle C_\beta \rangle_\eta^\beta = \langle C_\eta \rangle^\eta$, and $\langle C_\beta \rangle_\varpi^\beta = \langle C_\varpi \rangle^\varpi$, The notations ω and η represent different regions of local heterogeneity, with $\mathbf{D}_\eta$ and $\mathbf{D}_\varpi$ being the *effective dispersion tensors* for the corresponding regions.

$$\frac{\partial \langle C_\eta \rangle^\eta}{\partial t} + \nabla \cdot \left(\langle \mathbf{u}_\beta \rangle_\eta \langle C_\eta \rangle^\eta \right) = \nabla \cdot \left(\mathbf{D}_\eta \cdot \nabla \langle C_\eta \rangle^\eta \right)$$

$$\frac{\partial \langle C_\varpi \rangle^\varpi}{\partial t} + \nabla \cdot \left(\langle \mathbf{u}_\beta \rangle_\varpi \langle C_\varpi \rangle^\varpi \right) = \nabla \cdot \left(\mathbf{D}_\varpi \cdot \nabla \langle C_\varpi \rangle^\varpi \right) \tag{4-3}$$

B.C. 1: $\langle C_\eta \rangle^\eta = \langle C_\varpi \rangle^\varpi$ at $A_{\eta\omega}$

B.C. 2: $-\mathbf{n}_{\eta\varpi} \cdot \left(\langle \mathbf{u}_\beta \rangle^\eta \langle C_\eta \rangle^\eta - \mathbf{D}_\eta \cdot \nabla \langle C_\eta \rangle^\eta \right) = -\mathbf{n}_{\eta\varpi} \cdot \left(\langle \mathbf{u}_\beta \rangle^\varpi \langle C_\varpi \rangle^\varpi - \mathbf{D}_\varpi \cdot \nabla \langle C_\varpi \rangle^\varpi \right)$ at $A_{\eta\omega}$

In order to follow the derivations commonly found in literature such as Quintard and Whitaker (1994), we temporarily revert back to pore-scale formulations. Modifications for continuum scale representations will be discussed in subsequent sections of this chapter.

Performing the process of spatially smoothing by forming superficial volume average using the spatial averaging theorem (Cushman, 1982; Howes and Whitaker, 1985):

Define:

ψ_j = function value in phase j

V_j = volume of phase j

V = averaging volume

$\langle \psi_j \rangle = \varepsilon_j \langle \psi_j \rangle^j$ and $\varepsilon_j = \frac{V_j}{V}$

Superficial volume average: $\left\langle \psi_j \right\rangle = \frac{1}{\mathrm{V}} \int_{V_j} \psi_j dV$

Intrinsic volume average: $\left\langle \psi_j \right\rangle^j = \frac{1}{\mathrm{V_j}} \int_{V_j} \psi_j dV$

Spatial average of scalar: $\left\langle \nabla \cdot \psi_j \right\rangle = \nabla \cdot \left\langle \psi_j \right\rangle + \frac{1}{\mathrm{V}} \sum_{k=1;k\neq j}^{n} \int_{A_{jk}} \mathbf{n}_{jk} \cdot \psi_j dA$

Spatial average of vector: $\left\langle \nabla \psi_j \right\rangle = \nabla \left\langle \psi_j \right\rangle + \frac{1}{\mathrm{V}} \sum_{k=1;k\neq j}^{n} \int_{A_{jk}} \mathbf{n}_{jk} \psi_j dA$

n = total number of interfaces (4-4)

We get:

$$\begin{aligned}
&\underbrace{\frac{\partial \left\langle C_\beta \right\rangle}{\partial t}}_{\text{accum}} + \underbrace{\nabla \cdot \left\langle \mathbf{u}_\beta C_\beta \right\rangle}_{\text{convection}} = \underbrace{\nabla \cdot \left[D \left(\nabla \left\langle C_\beta \right\rangle + \frac{1}{V} \int_{A_{\beta\gamma}} \mathbf{n}_{\beta\gamma} C_\beta dA + \frac{1}{V} \int_{A_{\beta\sigma}} \mathbf{n}_{\beta\sigma} C_\beta dA \right) \right]}_{\text{diffusion}} \\
&\underbrace{+ \frac{1}{V} \int_{A_{\beta\gamma}} \mathbf{n}_{\beta\gamma} \cdot \left(D \nabla C_\beta \right) dA + \frac{1}{V} \int_{A_{\beta\sigma}} \mathbf{n}_{\beta\sigma} \cdot \left(D \nabla C_\beta \right) dA}_{\text{interfacial flux}}
\end{aligned} \tag{4-5}$$

The various transport mechanisms described by equation (4-5) are illustrated in Figure 4-1. The additional terms in the interfacial flux come from applying spatial averaging to the RHS of equation (4-2). The macroscopic quantity of interests, such as concentrations and velocities, can be expressed as a sum of their intrinsic average and a random fluctuation under the condition that they vary smoothly in space: $C_\beta = \left\langle C_\beta \right\rangle^\beta + C'_\beta$, where $\left\langle C_\beta \right\rangle = \varepsilon_\beta \left\langle C_\beta \right\rangle^\beta$ with ε_β = volume fraction (saturation) of phase β and $\mathbf{u}_\beta = \left\langle \mathbf{u}_\beta \right\rangle^\beta + \mathbf{u}'_\beta$. The superscript β indicates that it is an intrinsic average (i.e. an average over only the volume of β phase in the averaging volume), as opposed to the superficial average $\left\langle C_\beta \right\rangle$, which is the average over the entire averaging volume.

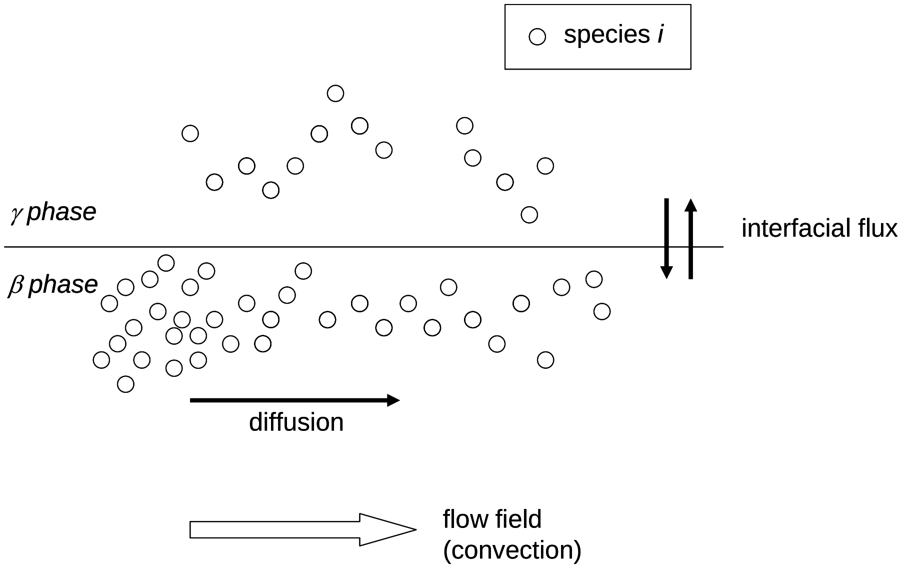

Figure 4-1: Illustration of various transport mechanisms described by equation (4-5).

The decomposition of concentration and velocity into an average and a fluctuation implies a *decomposition of length scales* – the spatial average represents large scale or low frequency variations, while the high frequency variations are represented by the perturbation term. An important assumption is that the summation of all deviation quantities over the average volume is approximately zero. The ***averaged equation*** becomes:

$$
\begin{aligned}
&\underbrace{\varepsilon_\beta \frac{\partial \left\langle C_\beta \right\rangle^\beta}{\partial t}}_{\text{accum}} + \underbrace{\nabla \cdot \left\langle \mathbf{u}'_\beta C'_\beta \right\rangle}_{\text{dispersion}} + \underbrace{\varepsilon_\beta \left\langle \mathbf{u}_\beta \right\rangle^\beta \cdot \nabla \left\langle C_\beta \right\rangle^\beta}_{\text{convection}} = \\
&\underbrace{\nabla \cdot \left[D_\beta \left(\varepsilon_\beta \nabla \left\langle C_\beta \right\rangle^\beta + \frac{1}{V} \int_{A_{\beta\gamma}} \mathbf{n}_{\beta\gamma} C'_\beta dA + \frac{1}{V} \int_{A_{\beta\sigma}} \mathbf{n}_{\beta\sigma} C'_\beta dA \right) \right]}_{\text{diffusion}} \\
&\underbrace{\begin{aligned}&+\frac{1}{V} \int_{A_{\beta\gamma}} \mathbf{n}_{\beta\gamma} \cdot D_\beta \nabla C'_\beta dA + \frac{1}{V} \int_{A_{\beta\sigma}} \mathbf{n}_{\beta\sigma} \cdot D_\beta \nabla C'_\beta dA + \frac{1}{V} \int_{A_{\beta\gamma}} \mathbf{n}_{\beta\gamma} \cdot D \nabla \left\langle C_\beta \right\rangle^\beta dA \\ &+\frac{1}{V} \int_{A_{\beta\sigma}} \mathbf{n}_{\beta\sigma} \cdot D \nabla \left\langle C_\beta \right\rangle^\beta dA\end{aligned}}_{\text{interfacial flux}}
\end{aligned}
\qquad (4\text{-}6)
$$

All the approximations are valid if the volume averaging length scale is large. In particular, the averaging volume has to be large enough so that smooth functions are obtained by the averaging process and average quantities $\left\langle C_\beta \right\rangle^\beta$ can be removed from all the interfacial area integrals (since they are spatially constant) that would arise in the intermediate steps (omitted here, see Appendix B for details). To obtain the ***deviation equation***, we subtract the averaged equation from the original governing equation and simplify:

$$
\begin{aligned}
&\frac{\partial C'_\beta}{\partial t} - \varepsilon_\beta{}^{-1} \nabla \cdot \left\langle \mathbf{u}'_\beta C'_\beta \right\rangle + \mathbf{u}_\beta \cdot \nabla C'_\beta + \mathbf{u}'_\beta \cdot \nabla \left\langle C_\beta \right\rangle^\beta = \nabla \cdot \left(D \nabla C'_\beta \right) \\
&-\varepsilon_\beta{}^{-1} \nabla \cdot \left[D \left(\frac{1}{V} \int_{A_{\beta\gamma}} \mathbf{n}_{\beta\gamma} C'_\beta dA + \frac{1}{V} \int_{A_{\beta\sigma}} \mathbf{n}_{\beta\sigma} C'_\beta dA \right) \right] \\
&-\varepsilon_\beta{}^{-1} \left(\begin{aligned} &\frac{1}{V} \int_{A_{\beta\gamma}} \mathbf{n}_{\beta\gamma} \cdot D \nabla C'_\beta dA + \frac{1}{V} \int_{A_{\beta\sigma}} \mathbf{n}_{\beta\sigma} \cdot D \nabla C'_\beta dA \\ &+\frac{1}{V} \int_{A_{\beta\gamma}} \mathbf{n}_{\beta\gamma} \cdot D \nabla \left\langle C_\beta \right\rangle^\beta dA + \frac{1}{V} \int_{A_{\beta\sigma}} \mathbf{n}_{\beta\sigma} \cdot D \nabla \left\langle C_\beta \right\rangle^\beta dA \end{aligned} \right)
\end{aligned}
\qquad (4\text{-}7)
$$

To use equation (4-6) to predict the coarse-scale $\left\langle C_\beta \right\rangle$ based on the fine scale C_β, we must first solve for the deviation concentrations C'_β at each spatial location using equation (4-7). In most volume averaging applications, the objective is to derive a closed form representation for some effective transport parameters; therefore, the fine-scale quantities are never explicitly solved for, as they are deemed unnecessary. The solution of C'_β is achieved by constructing a closure problem, in which we impose a "closure condition" such that the summation of the average and deviation quantities satisfies some global mass balance conditions. The closure condition involves representing the deviation quantities as a function of some closure variable(s) and the averaged quantities. The purpose is to impose a consistency between the deviation (noise) quantities that are introduced during the decomposition procedure and the average values, such that both the averaged and deviation equations satisfy the original governing equation.

Following the formulation by Kechagia et al. (2002), we substitute $C'_\beta = s_\beta \left(C_{eq} - \left\langle C_\beta \right\rangle^\beta \right)$, assuming linearity in deviations. The closure condition can thus be interpreted as the noise originating from the deviation of the averaged quantities from the equilibrium values. Substituting the closure condition into equations (4-6) and (4-7), and assuming the perturbation is added to the average quantities under quasi-steady state conditions (i.e. $\frac{\partial C'_\beta}{\partial t} \approx 0$), we obtain the final form of closure partial differential equation (or closure PDE) and the averaged equation at quasi-steady state:

$$
\begin{aligned}
&\left[\mathbf{u}_\beta - 2D\frac{\nabla\left(C_{eq}-\left\langle C_\beta\right\rangle^\beta\right)}{\left(C_{eq}-\left\langle C_\beta\right\rangle^\beta\right)}\right]\cdot\nabla s_\beta = -\mathbf{u}'_\beta\cdot\frac{\nabla\left\langle C_\beta\right\rangle^\beta}{\left(C_{eq}-\left\langle C_\beta\right\rangle^\beta\right)} + D\nabla^2 s_\beta \\
&+\left[-\mathbf{u}_\beta\cdot\frac{\nabla\left(C_{eq}-\left\langle C_\beta\right\rangle^\beta\right)}{\left(C_{eq}-\left\langle C_\beta\right\rangle^\beta\right)} + D\frac{\nabla^2\left(C_{eq}-\left\langle C_\beta\right\rangle^\beta\right)}{\left(C_{eq}-\left\langle C_\beta\right\rangle^\beta\right)}\right]s_\beta - \varepsilon_\beta{}^{-1}\frac{D}{V\left(C_{eq}-\left\langle C_\beta\right\rangle^\beta\right)}\cdot \\
&\left[\begin{aligned}
&\nabla\cdot\int_{A_{\beta\gamma}}\mathbf{n}_{\beta\gamma}s_\beta\left(C_{eq}-\left\langle C_\beta\right\rangle^\beta\right)dA+\nabla\cdot\int_{A_{\beta\sigma}}\mathbf{n}_{\beta\sigma}s_\beta\left(C_{eq}-\left\langle C_\beta\right\rangle^\beta\right)dA \\
&+\int_{A_{\beta\gamma}}\mathbf{n}_{\beta\gamma}\cdot\nabla\left[s_\beta\left(C_{eq}-\left\langle C_\beta\right\rangle^\beta\right)\right]dA+\int_{A_{\beta\sigma}}\mathbf{n}_{\beta\sigma}\cdot\nabla\left[s_\beta\left(C_{eq}-\left\langle C_\beta\right\rangle^\beta\right)\right]dA \\
&+\int_{A_{\beta\gamma}}\mathbf{n}_{\beta\gamma}\cdot\nabla\left\langle C_\beta\right\rangle^\beta dA+\int_{A_{\beta\sigma}}\mathbf{n}_{\beta\sigma}\cdot\nabla\left\langle C_\beta\right\rangle^\beta dA
\end{aligned}\right]
\end{aligned}
\tag{4-8}
$$

$$
\begin{aligned}
&\underset{\text{convection}}{\left\langle\mathbf{u}_\beta\right\rangle\cdot\nabla\left\langle C_\beta\right\rangle^\beta} = \underset{\text{dispersion}}{-\nabla\cdot\left\langle\mathbf{u}'_\beta s_\beta\left(C_{eq}-\left\langle C_\beta\right\rangle^\beta\right)\right\rangle} + \underset{\text{diffusion}}{D\varepsilon_\beta\nabla^2\left\langle C_\beta\right\rangle^\beta} \\
&\underbrace{\begin{aligned}
&+\nabla\cdot\left[\frac{D}{V}\int_{A_{\beta\gamma}}\mathbf{n}_{\beta\gamma}s_\beta\left(C_{eq}-\left\langle C_\beta\right\rangle^\beta\right)dA+\frac{D}{V}\int_{A_{\beta\sigma}}\mathbf{n}_{\beta\sigma}s_\beta\left(C_{eq}-\left\langle C_\beta\right\rangle^\beta\right)dA\right] \\
&+\frac{D}{V}\left[\begin{aligned}
&\int_{A_{\beta\gamma}}\mathbf{n}_{\beta\gamma}\cdot\nabla\left[s_\beta\left(C_{eq}-\left\langle C_\beta\right\rangle^\beta\right)\right]dA+\int_{A_{\beta\sigma}}\mathbf{n}_{\beta\sigma}\cdot\nabla\left[s_\beta\left(C_{eq}-\left\langle C_\beta\right\rangle^\beta\right)\right]dA \\
&+\int_{A_{\beta\gamma}}\mathbf{n}_{\beta\gamma}\cdot\nabla\left\langle C_\beta\right\rangle^\beta dA+\int_{A_{\beta\sigma}}\mathbf{n}_{\beta\sigma}\cdot\nabla\left\langle C_\beta\right\rangle^\beta dA
\end{aligned}\right]
\end{aligned}}_{\substack{\text{mass transfer (reaction,}\\ \text{interfacial transport)}}}
\end{aligned}
\tag{4-9}
$$

Rewriting equation (4-9) in the form of a general mass balance equation, we get:

$$\left\langle\mathbf{u}_\beta\right\rangle\cdot\nabla\left\langle C_\beta\right\rangle = K_{eff}\left(C_{\max}-\left\langle C_\beta\right\rangle\right) \tag{4-10}$$

where $K_{eff}\left(C_{\max}-\left\langle C_{\beta}\right\rangle\right)$ equals the RHS of equation (4-9). *K* K_{eff} is the effective *mass transfer coefficient*, representing the combined effects of mass transfer due to dispersion, diffusion, and interfacial transport. Hence the scaling characteristics of K_{eff} should be closely related to the scaling characteristics of recovery. The difference in concentration $\left(C_{\max}-\left\langle C_{\beta}\right\rangle\right)$ drives the mass transfer process. In the case of injection, we can take this $C_{\max}$ to be the solute concentration at injection conditions. It should be noted that K_{eff} is not defined if $\left(C_{\max}-\left\langle C_{\beta}\right\rangle\right)$ equals zero i.e. at equilibrium there is effectively no mass transfer occurring in the system.

It should be noted that the formulation derived so far is the most general case of single-phase solute transport. If there is no reaction at the interface between β and γ, the formulation could be simplified as follows:

1. The 1st B.C. in equation (4-1) would not exist. An important consequence would be the source term $\left(C_{eq}-\left\langle C_{\beta}\right\rangle^{\beta}\right)$ would be missing, so the only generator of the C'_{β}-field originates from $\nabla\left\langle C_{\beta}\right\rangle^{\beta}$ (i.e. there are terms involving $\nabla\left\langle C_{\beta}\right\rangle^{\beta}$ in the deviation equation and the 2nd B.C. that are considered as source terms for C'_{β}, see Appendix B for details). Therefore, the closure formulation becomes $C'_{\beta}=\mathbf{b}_{\beta}\cdot\nabla\left\langle C_{\beta}\right\rangle^{\beta}$.
2. All the interfacial flux involving $A_{\beta\gamma}$ or $A_{\gamma\beta}$ would disappear.

However, the solution of earlier equations poses a problem: the closure PDE (4-8) and the averaged equation (4-9) are coupled. In other words, the evaluation of closure variables requires simultaneous solution of $\left\langle C_{\beta}\right\rangle^{\beta}$ in the averaged equation. Under certain restrictive conditions (e.g., average concentration and its gradient are independent), one common approach is to decouple the system, and the closure PDE could be solved without the knowledge of $\left\langle C_{\beta}\right\rangle^{\beta}$. A brief summary of these simplifications will be presented next. In all cases, once the closure variables are solved, the averaged equation can be used directly to predict coarse-scale responses. There are still a few additional remarks. First, the velocity terms, $\left\langle \mathbf{u}_\beta \right\rangle^\beta$ and $\mathbf{u}'_\beta$, are generally obtained separately from the momentum balance (e.g., Stokes equation) which will be discussed in further details in subsequent sections. Next, a periodic external boundary condition is generally imposed on unit cell typed geometry. Furthermore, all the terms involving the interfacial integral are lumped together as α.

$$\begin{aligned}\alpha = \nabla \cdot \left[D_\beta \left(\frac{1}{V} \int_{A_{\beta\gamma}} \mathbf{n}_{\beta\gamma} C'_\beta dA + \frac{1}{V} \int_{A_{\beta\sigma}} \mathbf{n}_{\beta\sigma} C'_\beta dA \right) \right] + \frac{1}{V} \int_{A_{\beta\gamma}} \mathbf{n}_{\beta\gamma} \cdot D_\beta \nabla C'_\beta dA \\ + \frac{1}{V} \int_{A_{\beta\sigma}} \mathbf{n}_{\beta\sigma} \cdot D_\beta \nabla C'_\beta dA + \frac{1}{V} \int_{A_{\beta\gamma}} \mathbf{n}_{\beta\gamma} \cdot D \nabla \left\langle C_\beta \right\rangle^\beta dA + \frac{1}{V} \int_{A_{\beta\sigma}} \mathbf{n}_{\beta\sigma} \cdot D \nabla \left\langle C_\beta \right\rangle^\beta dA\end{aligned} \quad (4\text{-}11)$$

Finally, the deviation equation can be simplified substantially if we assume

a. Spatial average of the product of $\mathbf{u}'_\beta$ and C'_β are negligible:

$$\varepsilon_\beta^{-1} \nabla \cdot \left\langle \mathbf{u}'_\beta C'_\beta \right\rangle \approx 0$$

b. Gradient of $C_\beta{}'$ across the interface boundary is approximately zero:

$$-\varepsilon_\beta^{-1} \left(\frac{1}{V} \int_{A_{\beta\gamma}} \mathbf{n}_{\beta\gamma} \cdot D \nabla C'_\beta dA + \frac{1}{V} \int_{A_{\beta\sigma}} \mathbf{n}_{\beta\sigma} \cdot D \nabla C'_\beta dA \right) \approx 0$$

c. Constant volume fraction of β-phase and by averaging theorem:

$\nabla \varepsilon_\beta = -\frac{1}{V} \int_{A_{\beta\gamma}} \mathbf{n}_{\beta\gamma} dA - \frac{1}{V} \int_{A_{\beta\sigma}} \mathbf{n}_{\beta\sigma} dA$, we get:

$$-\varepsilon_\beta^{-1} \left(\frac{1}{V} \int_{A_{\beta\gamma}} \mathbf{n}_{\beta\gamma} \cdot D \nabla \left\langle C_\beta \right\rangle^\beta dA + \frac{1}{V} \int_{A_{\beta\sigma}} \mathbf{n}_{\beta\sigma} \cdot D \nabla \left\langle C_\beta \right\rangle^\beta dA \right) = 0$$

The simplified deviation equation becomes:

$$\mathbf{u}_\beta \cdot \nabla C'_\beta + \mathbf{u}'_\beta \cdot \nabla \left\langle C_\beta \right\rangle^\beta = \nabla \cdot \left(D \nabla C'_\beta \right) - \varepsilon_\beta^{-1} \nabla \cdot \left[D \left(\frac{1}{V} \int_{A_{\beta\gamma}} \mathbf{n}_{\beta\gamma} C'_\beta dA + \frac{1}{V} \int_{A_{\beta\sigma}} \mathbf{n}_{\beta\sigma} C'_\beta dA \right) \right] \quad (4\text{-}12)$$

There are two ways of handling the coupling of the closure variables and $\left\langle C_\beta \right\rangle^\beta$.

Technique #1

Replace the perturbation in terms of two closure variables, $\mathbf{b}_\beta$ and s_β (i.e. the perturbation is generated by the spatial gradient of the average concentration as well as the deviation of the average concentration from the equilibrium concentration), we get:

$$C'_\beta = \mathbf{b}_\beta \cdot \nabla \left\langle C_\beta \right\rangle^\beta - s_\beta \left(\left\langle C_\beta \right\rangle^\beta - C_{eq} \right) \quad (4\text{-}13)$$

This would create two closure equations. Upon substitution of the above expression into equation (4-12), it becomes equivalent to the summation of the following two equations:

$$\begin{aligned} &\mathbf{u}_\beta \cdot \nabla \left[\mathbf{b}_\beta \cdot \nabla \left\langle C_\beta \right\rangle^\beta \right] + \mathbf{u}'_\beta \cdot \nabla \left\langle C_\beta \right\rangle^\beta = \nabla \cdot \left(D \nabla \left[\mathbf{b}_\beta \cdot \nabla \left\langle C_\beta \right\rangle^\beta \right] \right) \\ &- \varepsilon_\beta^{-1} \nabla \cdot \left[D \left(\frac{1}{V} \int_{A_{\beta\gamma}} \mathbf{n}_{\beta\gamma} \mathbf{b}_\beta \cdot \nabla \left\langle C_\beta \right\rangle^\beta dA + \frac{1}{V} \int_{A_{\beta\sigma}} \mathbf{n}_{\beta\sigma} \mathbf{b}_\beta \cdot \nabla \left\langle C_\beta \right\rangle^\beta dA \right) \right] \end{aligned} \quad (4\text{-}14)$$

$$\begin{aligned} &\mathbf{u}_\beta \cdot \nabla \left[s_\beta \left(C_{eq} - \left\langle C_\beta \right\rangle^\beta \right) \right] = \nabla \cdot \left(D \nabla \left[s_\beta \left(C_{eq} - \left\langle C_\beta \right\rangle^\beta \right) \right] \right) \\ &- \varepsilon_\beta^{-1} \nabla \cdot \left[D \left(\frac{1}{V} \int_{A_{\beta\gamma}} \mathbf{n}_{\beta\gamma} \left[s_\beta \left(C_{eq} - \left\langle C_\beta \right\rangle^\beta \right) \right] dA + \frac{1}{V} \int_{A_{\beta\sigma}} \mathbf{n}_{\beta\sigma} \left[s_\beta \left(C_{eq} - \left\langle C_\beta \right\rangle^\beta \right) \right] dA \right) \right] \end{aligned} \quad (4\text{-}15)$$

This serves to effectively decouple $\nabla \left\langle C_\beta \right\rangle^\beta$ and $\left\langle C_\beta \right\rangle^\beta$, and assuming that one can factor out $\nabla \left\langle C_\beta \right\rangle^\beta$ and $\left(C_{eq} - \left\langle C_\beta \right\rangle^\beta \right)$ from equations (4-14) and (4-15), respectively, the solution to these two equations become dependent on the unit cell geometry only (Quintard and Whitaker, 1994; Whitaker, 1999), and they are shown below. The averaged quantities can be obtained from the averaged equation after the closure variables (deviation quantities) are computed.

Equation #1

$$\mathbf{u}_\beta \cdot \nabla \mathbf{b}_\beta + \mathbf{u}'_\beta = \nabla \cdot \left(D \nabla \mathbf{b}_\beta \right) - {\varepsilon_\beta}^{-1} \mathbf{d}_\beta \tag{4-16}$$

Where $\mathbf{d}_\beta = \left[\left(\frac{1}{V} \int_{A_{\beta\gamma}} \mathbf{n}_{\beta\gamma} \cdot \nabla D \mathbf{b}_\beta dA + \frac{1}{V} \int_{A_{\beta\sigma}} \mathbf{n}_{\beta\sigma} \cdot \nabla D \mathbf{b}_\beta dA \right) \right]$

B.C. 1: $\mathbf{b}_\beta = 0$ at $A_{\beta\gamma}$

B.C. 2: $\mathbf{n}_{\beta\sigma} \cdot \nabla \mathbf{b}_\beta = -\mathbf{n}_{\beta\sigma}$ at $A_{\beta\sigma}$

Equation #2

$$\mathbf{u}_\beta \cdot \nabla s_\beta = \nabla \cdot \left(D \nabla s_\beta \right) - {\varepsilon_\beta}^{-1} \kappa_\beta \tag{4-17}$$

Where $\kappa_\beta = \left[\left(\frac{1}{V} \int_{A_{\beta\gamma}} \mathbf{n}_{\beta\gamma} \cdot D \nabla s_\beta dA + \frac{1}{V} \int_{A_{\beta\sigma}} \mathbf{n}_{\beta\sigma} \cdot D \nabla s_\beta dA \right) \right]$

B.C. 1: $s_\beta = 1$ at $A_{\beta\gamma}$

B.C. 2: $\mathbf{n}_{\beta\sigma} \cdot \nabla s_\beta = 0$ at $A_{\beta\sigma}$

A unique solution can be obtained for each of the above two equations without the knowledge of $\langle C_\beta \rangle^\beta$. Although these problems are integro-differential equations, convenient procedures are available to solve for $\mathbf{b}_\beta$ and s_β (Quintard and Whitaker, 1994).

In summary, this traditional technique #1 aims to formulate the closure formulation using multiple closure variables and to generate numerous independent closure PDEs such that one can solve for the closure variables separately without the knowledge of $\langle C_\beta \rangle^\beta$. Once the closure variables are known, they can be substituted back into the averaged equation and $\left\langle C_\beta \right\rangle^\beta$ can be obtained as a function of time and space directly.

Technique #2

Represent deviation concentrations in terms of a single closure variable s_β, so solution of the closure variable requires the simultaneous solution of the averaged equation as well. Kechagia et al. (2002) simplified for various special cases and employing the substitution of $s_\beta = 1 + \alpha\zeta$, where α is the eigenvalue and ζ is the eigenfunction. The closure problem is therefore transformed into an eigenvalue problem. Once again, the closure variables are solved without the explicit knowledge of $\left\langle C_\beta \right\rangle^\beta$, and the averaged equation is solved once the closure variables are computed.

All these complicated procedures are necessary because the solutions of $\left\langle C_\beta \right\rangle^\beta$ and C'_β are coupled, while the fine-scale solution C_β is not explicitly known. Among all the assumptions and approximations that are invoked to decouple the solutions of these two quantities, the most important drawback is the constraint that the length scale of heterogeneity must be less than the size of the averaging volume, a necessary criterion for many of those assumptions to be valid. This constraint will be relaxed in a new proposed formulation where solutions from fine-scale simulations are integrated.

As mentioned earlier, a point to note in all the above derivations is that the averaging is performed over a certain representative pore volume consisting of an aggregation of pores (which is the quasi-point support). In the case of flow simulations, the scale we are interested is generally much larger. A similar averaging procedure can be performed over the scale of local heterogeneity with numerous regions (facies) within the averaging volume. We will show that the exact same averaged equation can be derived except 1) the average quantities are now defined over a larger representative volume and the corresponding fine scale is defined at the scale of the constituent regions (or facies), and 2) the interfacial integrals would now become inter-regional integrals (Plumb & Whitaker, 1988; Quintard and Whitaker, 1998; Ahmadi et. al., 1998) that are generally lumped together and referred to as α.

A practical formulation for scaling up to field scale quantities

Starting with the governing equation at the continuum scale, equation (4-3), we can obtain the following averaged equation for large-scale averaging by following the same spatial smoothing procedure and assuming constant effective dispersion tensors; recall that l_ϖ and l_η represent local heterogeneity length scale in an averaging volume V_∞ (see Figure 2-9).

$$\begin{gathered}
\underbrace{\varphi_\varpi \frac{\partial\left\{\left\langle C_\varpi\right\rangle^\varpi\right\}^\varpi}{\partial t}}_{\text{accum}} + \underbrace{\nabla\cdot\left(\varphi_\varpi\left\{\mathbf{u}'_{\beta\varpi}C'_\varpi\right\}^\varpi\right)}_{\text{dispersion}} + \underbrace{\varphi_\varpi\left\{\left\langle\mathbf{u}_\beta\right\rangle_\varpi\right\}^\varpi\cdot\nabla\left\{\left\langle C_\varpi\right\rangle^\varpi\right\}^\varpi}_{\text{convection}} = \\
\underbrace{\nabla\cdot\left[\mathbf{D}_\varpi\cdot\left(\varphi_\varpi\nabla\left\{\left\langle C_\varpi\right\rangle^\varpi\right\}^\varpi + \frac{1}{V_\infty}\int_{A_{\varpi\eta}}\mathbf{n}_{\varpi\eta}C'_\varpi dA\right)\right] + \frac{1}{V_\infty}\int_{A_{\varpi\eta}}\mathbf{n}_{\varpi\eta}\cdot\mathbf{D}_\varpi\cdot\nabla C'_\varpi dA}_{\text{large-scale diffusion}} \qquad (4\text{-}18) \\
-\underbrace{\frac{1}{V_\infty}\int_{A_{\varpi\eta}}\mathbf{n}_{\varpi\eta}\cdot\left(\left\langle\mathbf{u}_\beta\right\rangle_\varpi\left\langle C_\varpi\right\rangle^\varpi - \mathbf{D}_\varpi\cdot\nabla\left\langle C_\varpi\right\rangle^\varpi\right)dA}_{\text{inter-region flux}}
\end{gathered}$$

$$
\begin{gathered}
\underbrace{\varphi_\eta \frac{\partial \left\{\left\langle C_\eta\right\rangle^\eta\right\}^\eta}{\partial t}}_{\text{accum}} + \underbrace{\nabla\cdot\left(\varphi_\eta \left\{\mathbf{u}'_{\beta\eta} C'_\eta\right\}^\eta\right)}_{\text{dispersion}} + \underbrace{\varphi_\eta \left\{\left\langle \mathbf{u}_\beta\right\rangle_\eta\right\}^\eta \cdot \nabla\left\{\left\langle C_\eta\right\rangle^\eta\right\}^\eta =}_{\text{convection}} \\
\underbrace{\nabla\cdot\left[\mathbf{D}_\eta\cdot\left(\varphi_\eta\nabla\left\{\left\langle C_\eta\right\rangle^\eta\right\}^\eta + \frac{1}{V_\infty}\int\limits_{A_{\varpi\eta}} \mathbf{n}_{\eta\varpi} C'_\eta dA\right)\right] + \frac{1}{V_\infty}\int\limits_{A_{\varpi\eta}} \mathbf{n}_{\eta\varpi}\cdot\mathbf{D}_\eta\cdot\nabla C'_\eta dA}_{\text{large-scale diffusion}} \\
\underbrace{-\frac{1}{V_\infty}\int\limits_{A_{\varpi\eta}} \mathbf{n}_{\eta\varpi}\cdot\left(\left\langle\mathbf{u}_\beta\right\rangle_\eta\left\langle C_\eta\right\rangle^\eta - \mathbf{D}_\eta\cdot\nabla\left\langle C_\eta\right\rangle^\eta\right)dA}_{\text{inter-region flux}}
\end{gathered}
\tag{4-19}
$$

Where φ_ϖ and φ_η are the volume fraction of each region inside the averaging volume. These two equations are coupled, but if we assume large-scale mass equilibrium, i.e. $\left\{\left\langle C_\eta\right\rangle^\eta\right\}^\eta = \left\{\left\langle C_\varpi\right\rangle^\varpi\right\}^\varpi = \left\{\left\langle C\right\rangle\right\}$ then we can combine the two equations. Under the assumption of large-scale equilibrium, as we add the two equations together, the inter-region flux terms cancel out (because the normal vectors are in opposite directions):

$$
\begin{gathered}
\underbrace{\varphi_\eta \frac{\partial \left\{\left\langle C\right\rangle\right\}}{\partial t}}_{\text{accum}} + \underbrace{\nabla\cdot\left(\varphi_\eta \left\{\mathbf{u}'_{\beta\eta} C'_\eta\right\}^\eta + \varphi_\varpi \left\{\mathbf{u}'_{\beta\varpi} C'_\varpi\right\}^\varpi\right)}_{\text{dispersion}} + \underbrace{\left\{\left\langle\mathbf{u}_\beta\right\rangle\right\}\cdot\nabla\left\{\left\langle C\right\rangle\right\} =}_{\text{convection}} \\
\nabla\cdot\left[\underbrace{\left(\varphi_\eta\mathbf{D}_\eta + \varphi_\varpi\mathbf{D}_\varpi\right)\cdot\nabla\left\{\left\langle C\right\rangle\right\}}_{\text{diffusion}} + \frac{\mathbf{D}_\varpi}{V_\infty}\cdot\int\limits_{A_{\varpi\eta}} \mathbf{n}_{\eta\varpi} C'_\eta dA + \frac{\mathbf{D}_\eta}{V_\infty}\cdot\int\limits_{A_{\varpi\eta}} \mathbf{n}_{\varpi\eta} C'_\varpi dA\right] \\
+\frac{1}{V_\infty}\int\limits_{A_{\varpi\eta}} \mathbf{n}_{\eta\varpi}\cdot\mathbf{D}_\eta\cdot\nabla C'_\eta dA + \frac{1}{V_\infty}\int\limits_{A_{\varpi\eta}} \mathbf{n}_{\varpi\eta}\cdot\mathbf{D}_\varpi\cdot\nabla C'_\varpi dA \qquad \begin{array}{l}\text{mass transfer (reaction,}\\ \text{inter-regional transport)}\end{array}
\end{gathered}
\tag{4-20}
$$

Comparing this equation to the averaged equation derived at the pore scale:

$$
\begin{aligned}
&\underbrace{\varepsilon_\beta \frac{\partial \left\langle C_\beta \right\rangle^\beta}{\partial t}}_{\text{accum}} + \underbrace{\nabla \cdot \left\langle \mathbf{u}'_\beta C'_\beta \right\rangle}_{\text{dispersion}} + \underbrace{\left\langle \mathbf{u}_\beta \right\rangle \cdot \nabla \left\langle C_\beta \right\rangle^\beta}_{\text{convection}} = \\
&\nabla \cdot \left[\underbrace{D_\beta \left(\varepsilon_\beta \nabla \left\langle C_\beta \right\rangle^\beta}_{\text{diffusion}} + \frac{1}{V} \int_{A_{\beta\gamma}} \mathbf{n}_{\beta\gamma} C'_\beta \, dA + \frac{1}{V} \int_{A_{\beta\sigma}} \mathbf{n}_{\beta\sigma} C'_\beta \, dA \right) \right] \\
&+ \frac{1}{V} \int_{A_{\beta\gamma}} \mathbf{n}_{\beta\gamma} \cdot D_\beta \nabla C'_\beta \, dA + \frac{1}{V} \int_{A_{\beta\sigma}} \mathbf{n}_{\beta\sigma} \cdot D_\beta \nabla C'_\beta \, dA \qquad \text{mass transfer (reaction, interfacial transport)} \\
&+ \frac{1}{V} \int_{A_{\beta\gamma}} \mathbf{n}_{\beta\gamma} \cdot D_\beta \nabla \left\langle C_\beta \right\rangle^\beta dA + \frac{1}{V} \int_{A_{\beta\sigma}} \mathbf{n}_{\beta\sigma} \cdot D_\beta \nabla \left\langle C_\beta \right\rangle^\beta dA
\end{aligned}
\tag{4-21}
$$

It is observed that these two equations are practically identical with the same transport mechanisms: accumulation, dispersion, convection, diffusion, and some *interfacial* or *inter-region* flux terms. The similarity of the two equations also implies that the closure formulation would be identical as well. The interfacial or inter-region flux terms are never evaluated individually but rather computed as whole. For convenience, we will employ the nomenclature for the pore scale averaged equations in the subsequent discussion, keeping in mind the analogy between the pore scale and continuum scale equations.

The two techniques for simultaneous solution of $\left\langle C_\beta \right\rangle^\beta$ and closure variables suffer from some serious difficulties. Taking the volume average of fine-scale equation results in additional terms involving quantities such as $\mathbf{u}'$ and C'. Evaluation of the averaged equation and the effective transport parameters (K_{eff}, $\boldsymbol{D}^*$ etc.) would not be possible unless one can compute the deviation quantities that represent sub-grid effects.

In the conventional framework of volume averaging employing the spatial averaging theorem, fine-scale solution to the flow and transport problem are assumed to be unknown, and then the solution of deviation quantities C' is possible only if we 1) employ closure formulation that relate the perturbation terms to the averaged quantities, and 2) impose interfacial boundary conditions within the averaging volume to ensure continuity. Most importantly, <u>linear (arithmetic) averaging of **u** and *C* is assumed</u>, but it is well-understood that permeability in a reservoir and the resultant flow velocity cannot be linearly averaged. The periodic boundary condition implies applicability of the solution only to media that exhibit periodic heterogeneity characteristics (resembling self-similar characteristics). Implicit in all these closure formulations are assumptions such as $\langle C_\beta \rangle^\beta \rightarrow C_{eq}$, or $\nabla \langle C_\beta \rangle^\beta$ and $\langle C_\beta \rangle^\beta$ are independent. These restrictive assumptions and complicated mathematical formulations limit the application of this technique to mostly simple geometry such as a unit cell.

In lieu of all the assumptions made to derive the deviation quantities, in this work use is made of fine-scale solutions to obtain these deviation quantities. There are other studies in the upscaling literature that have demonstrated the viability of such an approach. A brief discussion of upscaling approaches and their relation to volume averaging is presented in Appendix C.

The volume averaged equation readily identifies the scaled-up contribution of each mechanism, whose magnitude is a function of the size of the averaging volume and the underlying heterogeneity (and velocity fields). Putting all this together, the central theme of this dissertation is *a new procedure where results from a fine-scale numerical flow simulation reflecting the full physics of the transport process albeit over a small sub-volume of the reservoir are integrated with the volume averaging technique to study the scaling characteristics of solute transport and recovery in complex stochastic geologic medium* (Leung and Srinivasan, 2009).

Numerical flow simulation is first performed over a representative small portion of the reservoir depicting the underlying heterogeneity; this provides the fine scale quantities $\mathbf{u}_\beta$ and C_β. In order to account for the correct averaging of velocity and concentration, a few flow simulations are performed at different coarse scales using reservoir models upscaled using flow-based upscaling techniques. These yield the coarse scale quantities $\langle \mathbf{u}_\beta \rangle$ and $\langle C_\beta \rangle^\beta$ eliminating the need to assume linear averaging of these quantities. Knowing these two quantities and solving the closure problem, the scaling characteristics of effective mass transfer coefficient can be computed. The deviation quantities can be readily computed from the fine- and coarse-scale solutions. However, since the boundary conditions in the flow-based upscaling might not be exactly identical to the fine-scale problem, if we were to substitute these average and deviation quantities back into equations (4-5) and (4-6) (closure PDE and averaged equation, respectively) directly, there will most likely be a slight mismatch between the two sides of the equations. Therefore, $\langle C_\beta \rangle^\beta$ is adjusted iteratively using a simulated annealing scheme such that the difference between the left and right hand sides of (4-5) and (4-6) are minimized.

A major advantage for incorporating flow simulation results is that it allows us to apply the volume averaging techniques to complex stochastic geologic medium that exhibits large-scale heterogeneity. Knowledge of the exact fine-scale solution relaxes many of the restrictive assumptions regarding periodicity of facies boundaries assumed in the traditional volume averaging formulations.

The scheme described above allows us to evaluate the coarse-scale response over different averaging scales. We can thus obtain the spatial distribution and statistics of the effective mass transfer coefficient (comprising of convection, dispersion, diffusion, inter-regional transport etc.) as a function of averaging scale. Furthermore, since the calculations are based on fine scale flow responses, the underlying spatial heterogeneity can be varied and its effect on the scale-up characteristics can be assessed. A fundamental result of this work is that effective mass transfer is a strong function of reservoir heterogeneity.

It should be noted that this application of the volume averaging method is different from the conventional upscaling technique. In the traditional upscaling approach, the coarse scale equations are usually applied over one or two coarse blocks at a time to compute some effective parameters – simple boundary conditions are specified between coarse blocks such that the same response as the fine-scale can be reproduced. In our approach, fine-scale responses are aggregated into numerous coarse grid blocks whose responses are now described by the averaged equations – boundary conditions are not fixed around each coarse block, instead the same global boundary conditions as for the fine scale problem, are specified.

There are still a few additional modifications to the conventional volume averaging formulations that need to be implemented before performing scale-up calculations. First, simulators output grid-block averaged quantities instead of intrinsic values; therefore, we need to replace intrinsic averages in our formulations with superficial averages. This is equivalent to resolving the quantities such as $\mathbf{u}$ and C as a sum of superficial average (instead of intrinsic average) and deviations. This is justified because regional boundaries are not distinct in many stochastic geologic medium, so the identification of exact volume fraction of each region is not feasible rendering the calculation of intrinsic quantities difficult. Another assumption would be rendering the effective dispersion coefficient a scalar $\mathbf{D}^* = \mathbf{D}_\eta = \mathbf{D}_\varpi = D$. Alternatively, the effective dispersion coefficient could be derived from the averaging process at the pore scale. The averaged equation becomes:

$$\frac{\partial\left\langle C_{\beta}\right\rangle}{\partial t}+\nabla\cdot\left\langle \mathbf{u}'_{\beta}C'_{\beta}\right\rangle+\left\langle \mathbf{u}_{\beta}\right\rangle\cdot\nabla\left\langle C_{\beta}\right\rangle=$$
$$\nabla\cdot\left[D\left(\nabla\left\langle C_{\beta}\right\rangle+\frac{1}{V}\int_{A_{\beta\gamma}}\mathbf{n}_{\beta\gamma}C'_{\beta}dA+\frac{1}{V}\int_{A_{\beta\sigma}}\mathbf{n}_{\beta\sigma}C'_{\beta}dA\right)\right] \tag{4-22}$$
$$+\frac{1}{V}\int_{A_{\beta\gamma}}\mathbf{n}_{\beta\gamma}\cdot D\nabla C'_{\beta}dA+\frac{1}{V}\int_{A_{\beta\sigma}}\mathbf{n}_{\beta\sigma}\cdot D\nabla C'_{\beta}dA$$

$$\frac{\partial\left\langle C_{\beta}\right\rangle}{\partial t}+\left\langle \mathbf{u}_{\beta}\right\rangle\cdot\nabla\left\langle C_{\beta}\right\rangle=K_{eff}\left(C_{\max}-\left\langle C_{\beta}\right\rangle\right) \tag{4-23}$$

Second, recall that the internal boundary conditions are imposed in the case of volume averaging methods because the solution of closure variables (deviation quantities) without knowledge of averaged quantities must ensure continuity at internal regional/interfacial boundaries. Since continuity of fluxes and concentrations at grid block boundaries are automatically satisfied from reservoir simulations, internal boundary conditions within the averaging volume are no longer necessary and should be removed. However, external boundary conditions around the entire integration volume are required, and for this a no-flow boundary is assumed.

Furthermore, the coarse-scale equation is evaluated under quasi-steady state conditions, so the accumulation term will be ignored (this term could be significant if there are non-equilibrium reactions of solute species or fluid-rock interactions taking place). The terms $\frac{\partial\left\langle C_{\beta}\right\rangle}{\partial t}$ and $\frac{\partial C'_{\beta}}{\partial t}$ are therefore neglected. This assumption will need to be re-visited when adsorption becomes important. In that case, adsorption effects can be modeled as mass transfer between a moving fluid phase and a non-moving solid phase.

A note on the physical meaning of effective mass transfer coefficient

Before we proceed to the discussion of implementation details, it would be beneficial to gain some insight regarding the physical meaning of the effective mass transfer coefficient K_{eff}, defined in equation (4-23), by looking at some widely studied transport processes such as Taylor's dispersion in stratified porous media (Lake and Hirasaki, 1981). In their study, the authors derived an effective longitudinal dispersion coefficient for a two-layer porous medium as a function of average velocity, system transverse thickness, transverse dispersion coefficient, and various measures of the contrast of permeability, porosity, and thickness of the two layers. They explained that stratification tends to increase the effective dispersion for the two adjacent layers because the difference in the velocity of the two layers causes a solute to travel with a different velocity in each layer. They subsequently demonstrated that as the permeability-porosity contrast $(k_1\phi_2)/(k_2\phi_1)$ increases, the effective longitudinal dispersion coefficient also increases.

Consider three layered models in Figure 4-2 with different amount of permeability contrast. If a solute concentration of 1mg/m^3 is injected at the left end of the medium with a fluid velocity of 0.5m/day, the resulting concentration profiles are shown in Figure 4-4. Also shown in Figure 4-4 are the corresponding K_{eff} values for an averaging length scale of 2x2 grid blocks. It is observed that high values of K_{eff} are localized at the solution front. The mean and variance of K_{eff} can be computed as a spatial average and variance. Higher mean and variability in K_{eff} values are observed as the permeability contrast increases. This observation agrees with Lake and Hirasaki's study showing that effective longitudinal dispersion coefficient increases with permeability contrast (Figure 4-3).

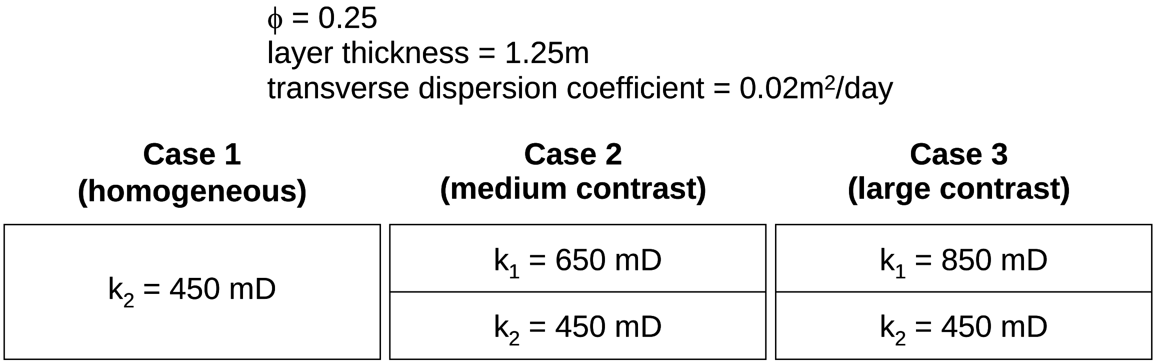

Figure 4-2: Taylor's dispersion in a two-layer porous medium.

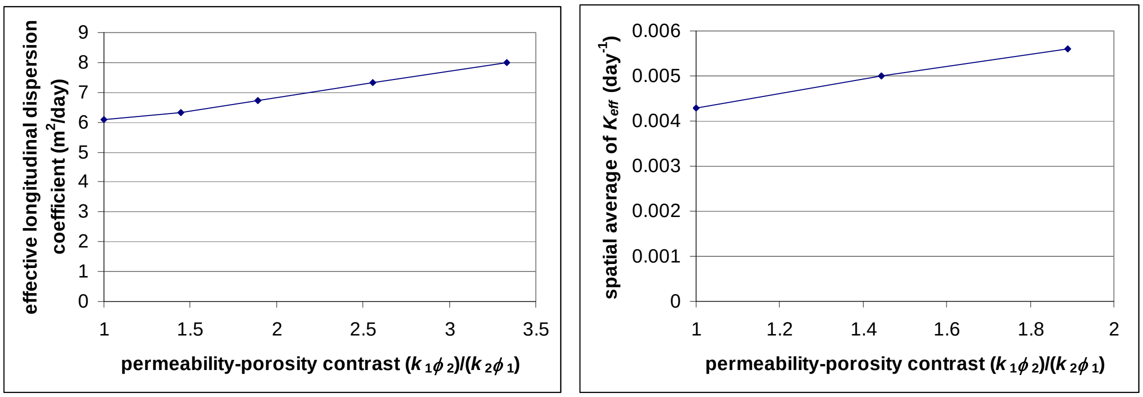

Figure 4-3: Comparison of effective longitudinal dispersion coefficient (prediction according to formulation in Lake and Hirasaki (1981)) in the left and mean of K_{eff} in the right as a function of permeability-porosity contrast.

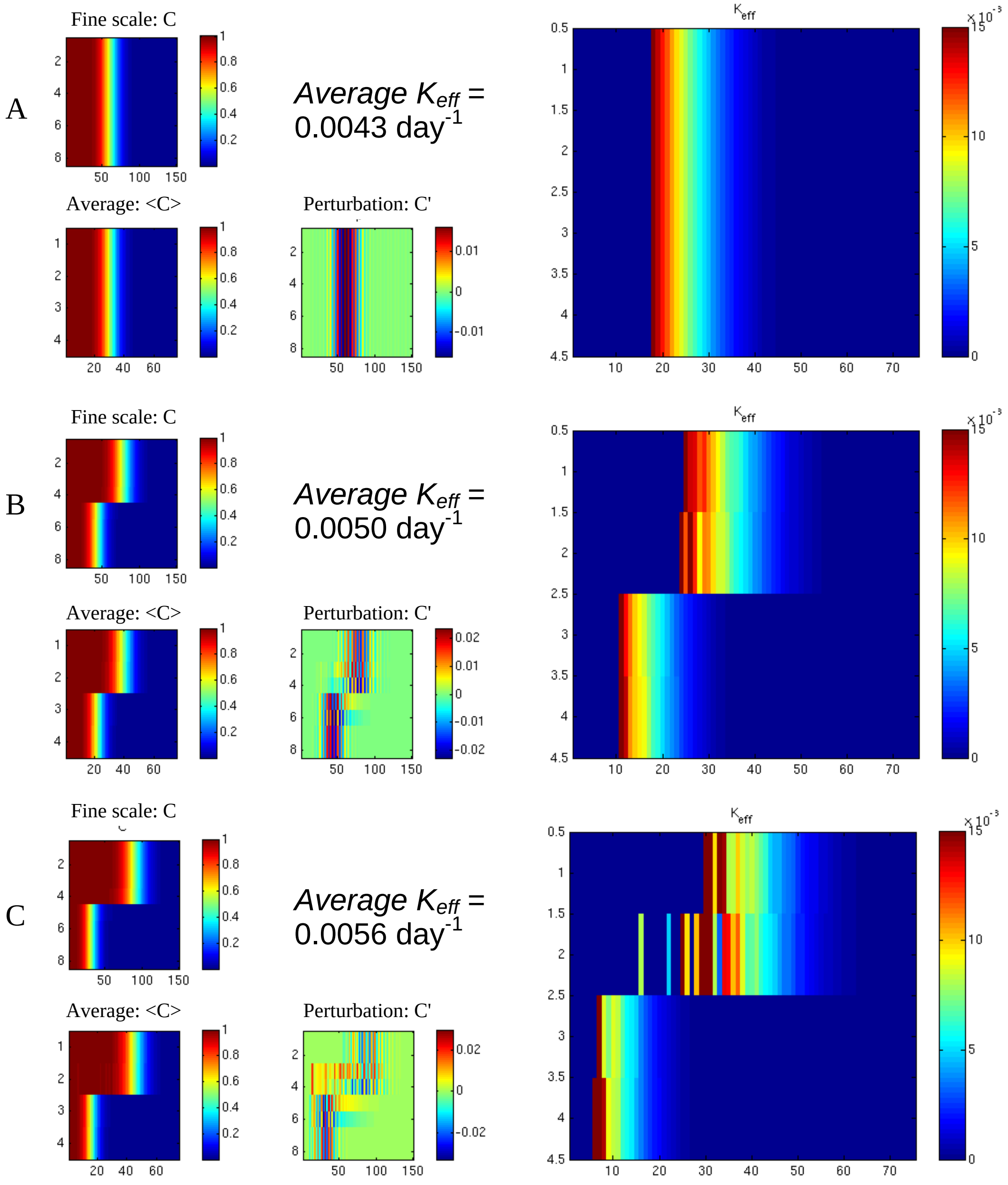

Figure 4-4: Concentration profiles and spatial distribution of K_{eff} for all three cases. It is observed that both average K_{eff} values and effective longitudinal dispersion coefficient increase with permeability contrast.

4.2.2 Implementation Details

The strategy is to incorporate heterogeneity effects directly into the velocity calculations with the use of a flow simulator, while averages $\left\langle C_\beta \right\rangle$ and closure variable s_β are obtained from the closure equation and the known fine-scale concentrations (also obtained from the flow simulation). Exact contribution of each dominant transport mechanisms and relevant scaled-up transport coefficients can be computed directly once $\left\langle C_\beta \right\rangle$ and s_β are known. Based on the derivations from the previous section:

Closure PDE:

$$
\begin{aligned}
&\left[\mathbf{u}_\beta - 2D\frac{\nabla\left(C_{eq}-\left\langle C_\beta\right\rangle\right)}{\left(C_{eq}-\left\langle C_\beta\right\rangle\right)}\right]\cdot\nabla s_\beta = -\mathbf{u}'_\beta\cdot\frac{\nabla\left\langle C_\beta\right\rangle}{\left(C_{eq}-\left\langle C_\beta\right\rangle\right)} + D\nabla^2 s_\beta \\
&+\left[-\mathbf{u}_\beta\cdot\frac{\nabla\left(C_{eq}-\left\langle C_\beta\right\rangle\right)}{\left(C_{eq}-\left\langle C_\beta\right\rangle\right)} + D\frac{\nabla^2\left(C_{eq}-\left\langle C_\beta\right\rangle\right)}{\left(C_{eq}-\left\langle C_\beta\right\rangle\right)}\right]s_\beta - \frac{D}{V\left(C_{eq}-\left\langle C_\beta\right\rangle\right)}\cdot \\
&\left[\begin{array}{l}
\nabla\cdot\int\limits_{A_{\beta\gamma}}\mathbf{n}_{\beta\gamma}s_\beta\left(C_{eq}-\left\langle C_\beta\right\rangle\right)dA + \nabla\cdot\int\limits_{A_{\beta\sigma}}\mathbf{n}_{\beta\sigma}s_\beta\left(C_{eq}-\left\langle C_\beta\right\rangle\right)dA \\
+\int\limits_{A_{\beta\gamma}}\mathbf{n}_{\beta\gamma}\cdot\nabla\left[s_\beta\left(C_{eq}-\left\langle C_\beta\right\rangle\right)\right]dA + \int\limits_{A_{\beta\sigma}}\mathbf{n}_{\beta\sigma}\cdot\nabla\left[s_\beta\left(C_{eq}-\left\langle C_\beta\right\rangle\right)\right]dA \\
+\int\limits_{A_{\beta\gamma}}\mathbf{n}_{\beta\gamma}\cdot\nabla\left\langle C_\beta\right\rangle dA + \int\limits_{A_{\beta\sigma}}\mathbf{n}_{\beta\sigma}\cdot\nabla\left\langle C_\beta\right\rangle dA
\end{array}\right]
\end{aligned}
\tag{4-24}
$$

Constraint – the averaged equation:

$$
\begin{aligned}
&\left\langle \mathbf{u}_\beta \right\rangle \cdot \nabla \left\langle C_\beta \right\rangle = -\nabla \cdot \left\langle \mathbf{u}'_\beta s_\beta \left(C_{eq} - \left\langle C_\beta \right\rangle \right) \right\rangle + D\nabla^2 \left\langle C_\beta \right\rangle \\
&+\frac{D}{V}\nabla \cdot \left[\int\limits_{A_{\beta\gamma}} \mathbf{n}_{\beta\gamma} s_\beta \left(C_{eq} - \left\langle C_\beta \right\rangle \right) dA + \int\limits_{A_{\beta\sigma}} \mathbf{n}_{\beta\sigma} s_\beta \left(C_{eq} - \left\langle C_\beta \right\rangle \right) dA \right] \\
&+\frac{D}{V}\left[\int\limits_{A_{\beta\gamma}} \mathbf{n}_{\beta\gamma} \cdot \nabla \left[s_\beta \left(C_{eq} - \left\langle C_\beta \right\rangle \right) \right] dA + \int\limits_{A_{\beta\sigma}} \mathbf{n}_{\beta\sigma} \cdot \nabla \left[s_\beta \left(C_{eq} - \left\langle C_\beta \right\rangle \right) \right] dA \right] \\
&+\frac{D}{V}\left[\int\limits_{A_{\beta\gamma}} \mathbf{n}_{\beta\gamma} \cdot \nabla \left\langle C_\beta \right\rangle dA + \int\limits_{A_{\beta\sigma}} \mathbf{n}_{\beta\sigma} \cdot \nabla \left\langle C_\beta \right\rangle dA \right]
\end{aligned}
\tag{4-25}
$$

In simplified notation:

PDE: $\mathbf{a} \cdot \nabla s_\beta = b s_\beta - c + D\nabla^2 s_\beta - \alpha$ (4-26)

Constraint: $\alpha = \dfrac{\left\langle \mathbf{u}_\beta \right\rangle \cdot \nabla \left\langle C_\beta \right\rangle + \nabla \cdot \left\langle \mathbf{u}'_\beta s_\beta \left(C_{eq} - \left\langle C_\beta \right\rangle \right) \right\rangle - D\nabla^2 \left\langle C_\beta \right\rangle^\beta}{\left(C_{eq} - \left\langle C_\beta \right\rangle \right)}$ (4-27)

Where:

$$\mathbf{a} = \left[\mathbf{u}_\beta - 2D\mathbf{f} \right] = a_1\mathbf{i} + a_2\mathbf{j} + a_3\mathbf{k} \tag{4-28}$$

$$\mathbf{f} = \frac{\nabla \left(C_{eq} - \left\langle C_\beta \right\rangle^\beta \right)}{\left(C_{eq} - \left\langle C_\beta \right\rangle^\beta \right)} = f_1\mathbf{i} + f_2\mathbf{j} + f_3\mathbf{k} \tag{4-29}$$

$$b = \left[-\mathbf{u}_\beta \cdot \mathbf{f} + D\frac{\nabla^2 \left(C_{eq} - \left\langle C_\beta \right\rangle^\beta \right)}{\left(C_{eq} - \left\langle C_\beta \right\rangle^\beta \right)} \right] \tag{4-30}$$

$$c = \mathbf{u}'_\beta \cdot \frac{\nabla \left\langle C_\beta \right\rangle^\beta}{\left(C_{eq} - \left\langle C_\beta \right\rangle^\beta \right)} \tag{4-31}$$

and

$$\begin{aligned}\alpha = {} & \frac{D}{V\left(C_{eq}-\left\langle C_{\beta}\right\rangle^{\beta}\right)}\nabla\cdot\left[\int\limits_{A_{\beta\gamma}}\mathbf{n}_{\beta\gamma}s_{\beta}\left(C_{eq}-\left\langle C_{\beta}\right\rangle^{\beta}\right)dA+\int\limits_{A_{\beta\sigma}}\mathbf{n}_{\beta\sigma}s_{\beta}\left(C_{eq}-\left\langle C_{\beta}\right\rangle^{\beta}\right)dA\right] \\ & +\frac{D}{V\left(C_{eq}-\left\langle C_{\beta}\right\rangle^{\beta}\right)}\left[\int\limits_{A_{\beta\gamma}}\mathbf{n}_{\beta\gamma}\cdot\nabla\left[s_{\beta}\left(C_{eq}-\left\langle C_{\beta}\right\rangle^{\beta}\right)\right]dA+\int\limits_{A_{\beta\sigma}}\mathbf{n}_{\beta\sigma}\cdot\nabla\left[s_{\beta}\left(C_{eq}-\left\langle C_{\beta}\right\rangle^{\beta}\right)\right]dA\right] \\ & +\frac{D}{V\left(C_{eq}-\left\langle C_{\beta}\right\rangle^{\beta}\right)}\left[\int\limits_{A_{\beta\gamma}}\mathbf{n}_{\beta\gamma}\cdot\nabla\left\langle C_{\beta}\right\rangle dA+\int\limits_{A_{\beta\sigma}}\mathbf{n}_{\beta\sigma}\cdot\nabla\left\langle C_{\beta}\right\rangle dA\right]\end{aligned}\tag{4-32}$$

Note that, since fine-scale concentration is known everywhere from flow simulation, we can modify the closure formulation to $C'_{\beta}=s_{\beta}\left(C_{\beta}-\left\langle C_{\beta}\right\rangle\right)$, which is equivalent to setting $s_{\beta}=1$. This is also equivalent to setting ∇s_{β} and $\nabla^{2}s_{\beta}$ to zero:

$$\begin{aligned}0 = {} & \left[-\mathbf{u}_{\beta}\cdot\frac{\nabla\left(C_{eq}-\left\langle C_{\beta}\right\rangle^{\beta}\right)}{\left(C_{eq}-\left\langle C_{\beta}\right\rangle^{\beta}\right)}+D\frac{\nabla^{2}\left(C_{eq}-\left\langle C_{\beta}\right\rangle^{\beta}\right)}{\left(C_{eq}-\left\langle C_{\beta}\right\rangle^{\beta}\right)}\right]-\mathbf{u}'_{\beta}\cdot\frac{\nabla\left\langle C_{\beta}\right\rangle^{\beta}}{\left(C_{eq}-\left\langle C_{\beta}\right\rangle^{\beta}\right)} \\ & -\frac{D}{V\left(C_{eq}-\left\langle C_{\beta}\right\rangle^{\beta}\right)}\left[\nabla\cdot\int\limits_{A_{\beta\gamma}}\mathbf{n}_{\beta\gamma}\left(C_{eq}-\left\langle C_{\beta}\right\rangle^{\beta}\right)dA+\nabla\cdot\int\limits_{A_{\beta\sigma}}\mathbf{n}_{\beta\sigma}\left(C_{eq}-\left\langle C_{\beta}\right\rangle^{\beta}\right)dA\right] \\ & -\frac{D}{V\left(C_{eq}-\left\langle C_{\beta}\right\rangle^{\beta}\right)}\left[\begin{aligned}&\int\limits_{A_{\beta\gamma}}\mathbf{n}_{\beta\gamma}\cdot\nabla\left[\left(C_{eq}-\left\langle C_{\beta}\right\rangle^{\beta}\right)\right]dA+\int\limits_{A_{\beta\sigma}}\mathbf{n}_{\beta\sigma}\cdot\nabla\left[\left(C_{eq}-\left\langle C_{\beta}\right\rangle^{\beta}\right)\right]dA \\ &+\int\limits_{A_{\beta\gamma}}\mathbf{n}_{\beta\gamma}\cdot\nabla\left\langle C_{\beta}\right\rangle^{\beta}dA+\int\limits_{A_{\beta\sigma}}\mathbf{n}_{\beta\sigma}\cdot\nabla\left\langle C_{\beta}\right\rangle^{\beta}dA\end{aligned}\right]\end{aligned}\tag{4-33}$$

Since fine-scale quantities are themselves coming from the simulation, there will be consistency between the perturbation and the average quantities; as a result, there is really no need for a closure condition. Hence, one can use either equation (4-24) or equation (4-6) directly. In this research, equation (4-24) is used, but for completeness, equation (4-6) in simplified notation is also presented here:

$$
\begin{aligned}
&\mathbf{u}_\beta \cdot \nabla C'_\beta + \mathbf{u}'_\beta \cdot \nabla \left\langle C_\beta \right\rangle = \nabla \cdot \left(D \nabla C'_\beta \right) \\
&-\nabla \cdot \left[D \left(\frac{1}{V} \int\limits_{A_{\beta\gamma}} \mathbf{n}_{\beta\gamma} C'_\beta dA + \frac{1}{V} \int\limits_{A_{\beta\sigma}} \mathbf{n}_{\beta\sigma} C'_\beta dA \right) \right] \\
&-\frac{1}{V} \left(\begin{array}{l} \displaystyle\int\limits_{A_{\beta\gamma}} \mathbf{n}_{\beta\gamma} \cdot D \nabla C'_\beta dA + \frac{1}{V} \int\limits_{A_{\beta\sigma}} \mathbf{n}_{\beta\sigma} \cdot D \nabla C'_\beta dA \\ \displaystyle + \int\limits_{A_{\beta\gamma}} \mathbf{n}_{\beta\gamma} \cdot D \nabla \left\langle C_\beta \right\rangle dA + \int\limits_{A_{\beta\sigma}} \mathbf{n}_{\beta\sigma} \cdot D \nabla \left\langle C_\beta \right\rangle dA \end{array} \right)
\end{aligned}
\tag{4-34}
$$

PDE: $\mathbf{a} \cdot \nabla C'_\beta = -c + D \nabla^2 C'_\beta - \alpha$ (4-35)

Constraint: $\alpha = \left\langle \mathbf{u}_\beta \right\rangle \cdot \nabla \left\langle C_\beta \right\rangle + \nabla \cdot \left\langle \mathbf{u}'_\beta C'_\beta \right\rangle - D \nabla^2 \left\langle C_\beta \right\rangle$ (4-36)

Where:

$$\mathbf{a} = \mathbf{u}_\beta = a_1 \mathbf{i} + a_2 \mathbf{j} + a_3 \mathbf{k} \tag{4-37}$$

$$c = \mathbf{u}'_\beta \cdot \nabla \left\langle C_\beta \right\rangle \tag{4-38}$$

$$
\begin{aligned}
&\alpha = \frac{D}{V} \nabla \cdot \left[\int\limits_{A_{\beta\gamma}} \mathbf{n}_{\beta\gamma} C'_\beta dA + \int\limits_{A_{\beta\sigma}} \mathbf{n}_{\beta\sigma} C'_\beta dA \right] \\
&+ \frac{D}{V} \left[\int\limits_{A_{\beta\gamma}} \mathbf{n}_{\beta\gamma} \cdot \nabla C'_\beta dA + \int\limits_{A_{\beta\sigma}} \mathbf{n}_{\beta\sigma} \cdot \nabla C'_\beta dA + \int\limits_{A_{\beta\gamma}} \mathbf{n}_{\beta\gamma} \cdot D \nabla \left\langle C_\beta \right\rangle dA + \int\limits_{A_{\beta\sigma}} \mathbf{n}_{\beta\sigma} \cdot D \nabla \left\langle C_\beta \right\rangle dA \right]
\end{aligned}
\tag{4-39}
$$

Boundary conditions:

$$\mathbf{n}_{\beta\sigma} \cdot \nabla C'_\beta + \mathbf{n}_{\beta\sigma} \cdot \nabla \left\langle C_\beta \right\rangle = 0 \tag{4-40}$$

$$\mathbf{n} \cdot \nabla C'_\beta + \mathbf{n} \cdot \mathbf{g} = 0 \tag{4-41}$$

$$\mathbf{g} = \nabla \left\langle C_\beta \right\rangle \tag{4-42}$$

4.2.3 Numerical Scheme

1. Generate a fine-scale heterogeneous reservoir model (porosity and permeability) for a section of the reservoir and subject to flow simulation to obtain $\mathbf{u}_\beta$ and C_β. This is referred to as the simulation domain in Figure 4-5.
2. Perform flow-based upscaling of reservoir permeability at various coarse scales and subject each to flow simulation to obtain $\langle \mathbf{u}_\beta \rangle$ and initial estimates of $\langle C_\beta \rangle$ at different coarse scales. Note that these are termed initial estimate since the boundary conditions employed for the flow based upscaling procedure may not exactly match the global boundary conditions employed in order to obtain the fine scale $\mathbf{u}_\beta$ and C_β.
3. Choose a sub-domain for volume averaging calculations to avoid boundary effects due to wells (Figure 4-5).
4. At each averaging scale, make small adjustments to $\langle C_\beta \rangle$ using a simulated annealing scheme such that the left and right hand sides of equations (4-35) and (4-36) are matched. First, the two equations can be rearranged into the following simplified form:

   Closure PDE: $\mathbf{a} \cdot \nabla s_\beta = b s_\beta - c + D\nabla^2 s_\beta - \alpha$ (4-43)

   Averaged equation: $\alpha = \dfrac{\langle \mathbf{u}_\beta \rangle \cdot \nabla \langle C_\beta \rangle + \nabla \cdot \left\langle \mathbf{u}'_\beta s_\beta \left(C_\beta - \langle C_\beta \rangle \right) \right\rangle - D\nabla^2 \langle C_\beta \rangle}{\left(C_\beta - \langle C_\beta \rangle \right)}$ (4-44)

   Procedure for simulated annealing:

   a. Initialize with $\langle C_\beta \rangle$ from coarse-scale simulations
   b. $C'_\beta = C_\beta - \langle C_\beta \rangle$ and $s_\beta = 1$
   c. Compute α from equation (4-44)
   d. Compute error $\varepsilon = D\nabla^2 s_\beta + b s_\beta - \mathbf{a} \cdot \nabla s_\beta - c - \alpha$

   e. If ε is more than tolerance update the guess of $\langle C_\beta \rangle$ randomly with $\langle C_\beta \rangle^{new} = \langle C_\beta \rangle \pm 0.5\% \langle C_\beta \rangle$ and repeat steps b) – d)
   f. Accept or reject the new guess → if accepted: $\langle C_\beta \rangle = \langle C_\beta \rangle^{new}$

5. Repeat Step 4 for all averaging length scales

6. Evaluate the following as a function of averaging scale:
   a. Mass transfer due to convection: $\langle \mathbf{u}_\beta \rangle \cdot \nabla \langle C_\beta \rangle$
   b. Mass transfer due to dispersion: $\nabla \cdot \left\langle \mathbf{u}'_\beta s_\beta \left(C_\beta - \langle C_\beta \rangle \right) \right\rangle$
   c. Mass transfer due to diffusion: $D \nabla^2 \langle C_\beta \rangle$
   d. Mass transfer across the β–γ, β–σ, and γ–σ interfaces: $\alpha \left(C_\beta - \langle C_\beta \rangle \right)$
   e. Effective mass transfer coefficient: K_{eff}

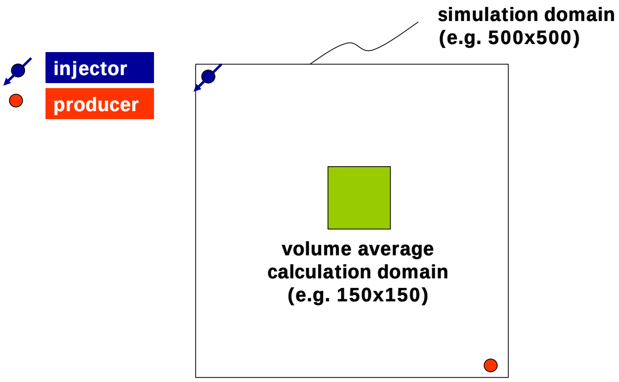

Figure 4-5: Illustration of simulation and volume average calculation domains.

4.2.4 Finite Difference Discretization of the Closure Equation

The closure PDE, equation (4-43), can be discretized by finite difference; for convenience, dropping the subscript β, the closure equation can be written as:

$$D\nabla^2 s + bs - \mathbf{a}\cdot\nabla s = c + \alpha \tag{4-45}$$

$$D\left(\frac{\partial^2 s}{\partial x^2} + \frac{\partial^2 s}{\partial y^2} + \frac{\partial^2 s}{\partial z^2}\right) + bs - \left(a_1\frac{\partial s}{\partial x} + a_2\frac{\partial s}{\partial y} + a_3\frac{\partial s}{\partial z}\right) = c + \alpha \tag{4-46}$$

Finite central differencing of PDE:

$$\begin{aligned}&D\left(\frac{s_{i+1,j,k} - 2s_{i,j,k} + s_{i-1,j,k}}{\Delta x^2} + \frac{s_{i,j+1,k} - 2s_{i,j,k} + s_{i,j-1,k}}{\Delta y^2} + \frac{s_{i,j,k+1} - 2s_{i,j,k} + s_{i-1,j,k-1}}{\Delta z^2}\right) + b_{i,j,k}s_{i,j,k}\\ &-\left(a_1\frac{s_{i+1,j,k} - s_{i-1,j,k}}{2\Delta x} + a_2\frac{s_{i,j+1,k} - s_{i,j-1,k}}{2\Delta y} + a_3\frac{s_{i,j,k+1} - s_{i,j,k-1}}{2\Delta z}\right) = c_{i,j,k} + \alpha_{i,j,k}\end{aligned} \tag{4-47}$$

$$\begin{aligned}&\left(\frac{D}{\Delta x^2} - \frac{a_1}{2\Delta x}\right)s_{i+1,j,k} + \left(\frac{D}{\Delta x^2} + \frac{a_1}{2\Delta x}\right)s_{i-1,j,k} + \left(\frac{D}{\Delta y^2} - \frac{a_2}{2\Delta y}\right)s_{i,j+1,k} + \left(\frac{D}{\Delta y^2} + \frac{a_2}{2\Delta y}\right)s_{i,j-1,k}\\ &+\left(\frac{D}{\Delta z^2} - \frac{a_3}{2\Delta z}\right)s_{i,j,k+1} + \left(\frac{D}{\Delta z^2} + \frac{a_3}{2\Delta z}\right)s_{i,j,k-1} + \left(b_{i,j,k} - \frac{2D}{\Delta x^2} - \frac{2D}{\Delta y^2} - \frac{2D}{\Delta z^2}\right)s_{i,j,k}\\ &= c_{i,j,k} + \alpha_{i,j,k}\end{aligned} \tag{4-48}$$

Finite central differencing of external no-flow boundary conditions, which can be written in terms of *s* as:

$$\mathbf{n}_{\beta\sigma}\cdot\nabla s_\beta + \frac{\mathbf{n}_{\beta\sigma}s_\beta\cdot\nabla\left(C_{eq} - \left\langle C_\beta\right\rangle^\beta\right)}{C_{eq} - \left\langle C_\beta\right\rangle^\beta} + \frac{\mathbf{n}_{\beta\sigma}\cdot\nabla\left\langle C_\beta\right\rangle}{C_{eq} - \left\langle C_\beta\right\rangle^\beta} = 0 \tag{4-49}$$

$$\mathbf{n}\cdot\nabla s + s\mathbf{n}\cdot\mathbf{f} + \mathbf{n}\cdot\mathbf{g} = 0 \tag{4-50}$$

$$\mathbf{g} = \frac{\nabla\left\langle C_\beta\right\rangle}{C_{eq} - \left\langle C_\beta\right\rangle^\beta} \tag{4-51}$$

The numbers of grid blocks in the x-, y-, and z- directions are denoted by nx, ny, and nz, respectively. The above boundary conditions in finite difference notation become:

For *j* = 1:ny, *k* = 1:nz,

$$-\frac{s_{2,j,k}-s_{0,j,k}}{2\Delta x}-f_1 s_{1,j,k}-g_1=0\rightarrow s_{0,j,k}=2\Delta x f_1 s_{1,j,k}+2\Delta x g_1+s_{2,j,k} \tag{4-52}$$

$$+\frac{s_{n+1,j,k}-s_{n-1,j,k}}{2\Delta x}+f_1 s_{n,j,k1}+g_1=0\rightarrow s_{n+1,j,k}=-2\Delta x f_1 s_{n,j,k}-2\Delta x g_1+s_{n-1,j,k} \tag{4-53}$$

For *i* = 1:nx, *k* = 1:nz,

$$s_{i,0,k}=2\Delta y f_2 s_{i,1,k}+2\Delta y g_2+s_{i,2,k} \tag{4-54}$$

$$s_{n+1,j,k}=-2\Delta y f_2 s_{i,n,k}-2\Delta y g_2+s_{i,n-1,k} \tag{4-55}$$

For i = 1:nx, *j* = 1:ny,

$$s_{i,j,0}=2\Delta z f_3 s_{i,j,1}+2\Delta z g_3+s_{i,j,2} \tag{4-56}$$

$$s_{i,j,n+1}=-2\Delta z f_3 s_{i,j,n}-2\Delta z g_3+s_{i,j,n-1} \tag{4-57}$$

Combining equations (4-52) – (4-57) and the original discretized equation (4-48), we get the matrix equation: $[\mathbf{A}][\mathbf{s}]=[\mathbf{b}]$. The elements of **A** and **b** are as follow:

i = 1 → *j* = 1:ny, *k* = 1:nz,

Element of **A** for $s_{2,j,k}$ becomes $\left(\frac{D}{\Delta x^2}-\frac{a_1}{2\Delta x}\right)+\left(\frac{D}{\Delta x^2}+\frac{a_1}{2\Delta x}\right)$

Element of **A** for $s_{1,j,k}$ becomes $\left(b_{1,j,k}-\frac{2D}{\Delta x^2}-\frac{2D}{\Delta y^2}-\frac{2D}{\Delta z^2}\right)+\left(\frac{D}{\Delta x^2}+\frac{a_1}{2\Delta x}\right)\left(2\Delta x f_1\right)$

Element of **b** becomes $c_{1,j,k}+e_{1,j,k}\alpha_{1,j,k}+\left(\frac{D}{\Delta x^2}+\frac{a_1}{2\Delta x}\right)\left(2\Delta x g_1\right)$

i = nx → *j* = 1:ny, *k* = 1:nz,

Element of **A** for $s_{n-1,j,k}$ becomes $\left(\frac{D}{\Delta x^2}+\frac{a_1}{2\Delta x}\right)+\left(\frac{D}{\Delta x^2}-\frac{a_1}{2\Delta x}\right)$

Element of **A** for $s_{n,j,k}$ becomes $\left(b_{n,j,k}-\frac{2D}{\Delta x^2}-\frac{2D}{\Delta y^2}-\frac{2D}{\Delta z^2}\right)+\left(\frac{D}{\Delta x^2}-\frac{a_1}{2\Delta x}\right)\left(-2\Delta x f_1\right)$

Element of **b** becomes $c_{n,j,k}+e_{n,j,k}\alpha_{n,j,k}-\left(\frac{D}{\Delta x^2}-\frac{a_1}{2\Delta x}\right)\left(2\Delta x g_1\right)$

j = 1 → *i* =1:nx, *k* = 1:nz,

Element of **A** for $s_{i,2,k}$ becomes $\left(\frac{D}{\Delta y^2}-\frac{a_2}{2\Delta y}\right)+\left(\frac{D}{\Delta y^2}+\frac{a_2}{2\Delta y}\right)$

Element of **A** $s_{i,1,k}$ becomes $\left(b_{i,1,k}-\frac{2D}{\Delta x^2}-\frac{2D}{\Delta y^2}-\frac{2D}{\Delta z^2}\right)+\left(\frac{D}{\Delta y^2}+\frac{a_2}{2\Delta y}\right)\left(2\Delta y f_2\right)$

Element of **b** becomes $c_{i,1,k}+e_{i,1,k}\alpha_{i,1,k}+\left(\frac{D}{\Delta y^2}+\frac{a_2}{2\Delta y}\right)\left(2\Delta y g_2\right)$

j = ny → *i* = 1:nx, *k* = 1:nz,

Element of **A** for $s_{i,n-1,k}$ becomes $\left(\frac{D}{\Delta y^2}+\frac{a_2}{2\Delta y}\right)+\left(\frac{D}{\Delta y^2}-\frac{a_2}{2\Delta y}\right)$

Element of **A** for $s_{i,n,k}$ becomes $\left(b_{i,n,k}-\frac{2D}{\Delta x^2}-\frac{2D}{\Delta y^2}-\frac{2D}{\Delta z^2}\right)+\left(\frac{D}{\Delta y^2}-\frac{a_2}{2\Delta y}\right)\left(-2\Delta y f_2\right)$

Element of **b** becomes $c_{i,n,k}+e_{i,n,k}\alpha_{i,n,k}-\left(\frac{D}{\Delta y^2}-\frac{a_2}{2\Delta y}\right)\left(2\Delta y g_2\right)$

k = 1 → *i* =1:nx, *j* =1:ny,

Element of **A** for $s_{i,j,2}$ becomes $\left(\frac{D}{\Delta z^2}-\frac{a_3}{2\Delta z}\right)+\left(\frac{D}{\Delta z^2}+\frac{a_3}{2\Delta z}\right)$

Element of **A** for $s_{i,j,1}$ becomes $\left(b_{i,j,1}-\frac{2D}{\Delta x^2}-\frac{2D}{\Delta y^2}-\frac{2D}{\Delta z^2}\right)+\left(\frac{D}{\Delta z^2}+\frac{a_3}{2\Delta z}\right)\left(2\Delta z f_3\right)$

Element of **b** becomes $c_{i,j,1}+e_{i,j,1}\alpha_{i,j,1}+\left(\frac{D}{\Delta z^2}+\frac{a_3}{2\Delta z}\right)\left(2\Delta z g_3\right)$

k = nz → *i* = 1:nx, *j* = 1:ny,

Element of **A** for $s_{i,j,n-1}$ becomes $\left(\frac{D}{\Delta z^2}+\frac{a_3}{2\Delta z}\right)+\left(\frac{D}{\Delta z^2}-\frac{a_3}{2\Delta z}\right)$

Element of **A** for $s_{i,j,n}$ becomes $\left(b_{i,j,n}-\frac{2D}{\Delta x^2}-\frac{2D}{\Delta y^2}-\frac{2D}{\Delta z^2}\right)+\left(\frac{D}{\Delta z^2}-\frac{a_3}{2\Delta z}\right)\left(-2\Delta z f_3\right)$

Element of **b** becomes $c_{i,j,n}+e_{i,j,n}\alpha_{i,j,n}-\left(\frac{D}{\Delta z^2}-\frac{a_3}{2\Delta z}\right)\left(2\Delta z g_3\right)$

It should be noted that central differencing might cause oscillations, especially at high Peclet numbers; one alternative is to apply upwind differencing for the convection terms. An error analysis using the Taylor series expansion method shows that the discretization method is second-order accurate and consistent. Regarding the solution stability, since the equations are evaluated assuming quasi-steady state, errors do not propagate with time. However, numerical errors coming from fine-scale simulations might still accumulate over time; by evaluating the closure and average equations assuming quasi-steady state, accumulation of error would manifest itself by altering the scaling statistics with time. For example, the scaling characteristics of K_{eff} would appear to vary depending on the concentration front location in an injection process. Finally, it should be noted that as in most optimization methods, simulated annealing used to decompose C_β into $\left\langle C_\beta \right\rangle$ and C'_β does not provide a unique solution; the statistics of $\left\langle C_\beta \right\rangle$ and K_{eff}, however, should remain stationary.

4.3 SUMMARY

Detailed derivations of the volume averaged solute transport equations for single phase flow are presented. In order to apply these methods to real geological systems exhibiting complex heterogeneity, a new procedure is described where results from a fine-scale numerical flow simulation reflecting the full physics of the transport process albeit over a small sub-volume of the reservoir can be integrated with the volume averaging technique. A detailed discussion of the implementation, numerical scheme, and finite difference discretization of the governing equations is presented. Numerous case studies illustrating the implementation of the volume averaging calculations for single phase flow will be presented in Chapter 5. Derivations presented in this chapter will serve as the basis for subsequent development of the volume averaging equations for multiphase transport in Chapter 6.

Chapter 5: A Numerical Approach to Scale-Up of Mass Transfer Equations in Single-Phase Flow Using Volume Averaging (Case Studies)

5.1 OVERVIEW

The mathematical formulations and practical implementation of volume averaging for scale-up analyses of single-phase flow in heterogeneous media are described in Chapter 4. In this chapter, several case examples are presented that illustrate the methods and the resultant scale-up results will be discussed. First, the effect of heterogeneity on scaling of flow response and recovery are investigated for both convection-dispersion controlled and diffusion controlled processes. Results from volume average calculations are compared with recovery results from numerical simulations for different size of models. Impacts of flow orientation in relation to the direction of anisotropy will also be investigated. Next, a dispersion controlled process in a fractal medium is presented where results are compared to scaling characteristics of dispersivity for fractal media in literature. Finally, effects of non-stationarity of the underlying permeability field on scaling characteristics of flow are also studied.

5.2 EFFECTS OF HETEROGENEITY

5.2.1 Convection-Dispersion Controlled (Base Case)

Consider a tracer injection process in a 500x500 2-D fine grid model. The grid blocks are of uniform size ($\Delta x = \Delta y = 10$m) with a thickness of 10m. An injector is placed at the top left corner and a producer is located at the bottom right corner. Injection and production rates are held constant at 1000 sm^3/day. A passive tracer is added to the injection stream at a concentration of 1mg/m^3.

D = 1e-6 m^2/day (fine-scale diffusion)
P = 280 bar (4060 psi) (Initial average reservoir pressure)
Q = 1000 sm^3/day

To investigate the effects of heterogeneity, four cases with different correlation lengths for porosity were considered (Figure 5-1 – Figure 5-4):

Case A (short correlation length) – isotropic:

- A model described by two spherical structures (Journel and Hujbregts, 1978) was assumed.
- $0.7 * Spherical(a_{\max} = a_{\min} = 2) + 0.3 * Spherical(a_{\max} = a_{\min} = 30)$

Case B (long correlation length) – anisotropic:

- A model characterized by one spherical structure was assumed.
- $1.0 * Spherical(a_{\max} = 50, a_{\min} = 10)$

Case C (uncorrelated) – isotropic:

- A very short range structure was assumed.
- $1.0 * Spherical(a_{\max} = a_{\min} = 2)$

Case D (local varying mean):

- A trend in the underlying permeability model, specified by means of an external trend map, was assumed.
- External trend + $0.5 * Spherical(a_{\max} = a_{\min} = 2) + 0.5 * Spherical(a_{\max} = a_{\min} = 50)$

Permeability (in mD) is related to porosity as $6000\phi^2$ and ranges from 15 to 1215mD (mean = 420mD), while ϕ ranges from 0.05 to 0.45 (mean = 0.23). Average velocity from the fine-scale simulation is approximately 0.27 m/day. The relative importance of convective and diffusion mechanisms affecting flow can be assessed through the dimensionless measure uD_p/D. A value greater than 6 indicates that miscible flow process is controlled by convection and dispersion instead of diffusion (Lake, 1989). A quick calculation assuming a typical grain size (D_p) of 1e-4m (100 μm) shows that the dimensionless group uD_p/D = (0.27)(1e-4)/(1e-6) ~ 27. Thus convective effects are dominant in the current flow scenario.

In order to test how sensitive are our calculations to choice of the location for the volume average calculation domain, we considered two locations as shown in Figure 5-5: region 1 is near the middle while region 2 is closer to the producer – representing the characteristics of the displacement process at a later time. To ensure there are similar amount of tracer in each region at the snap-shot of time where the calculations are performed, we will look at results from calculations at 30000 days and 50000 days for regions 1 and 2, respectively.

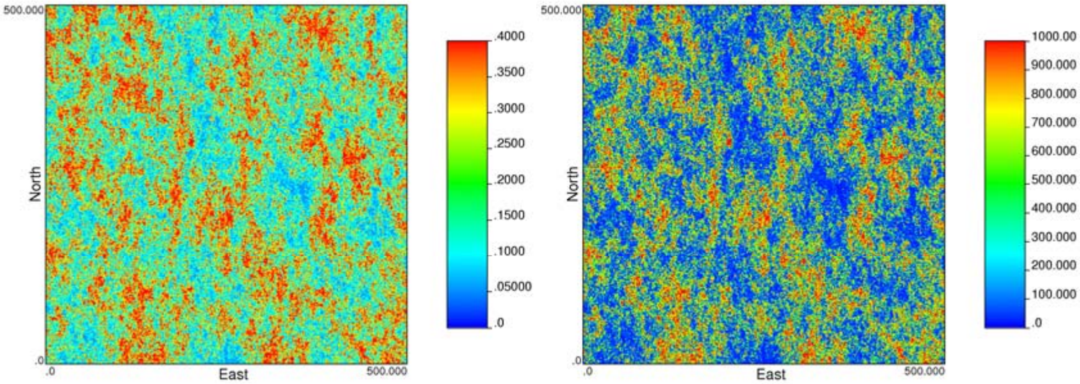

Figure 5-1: Porosity and permeability models for Case A (short correlation length).

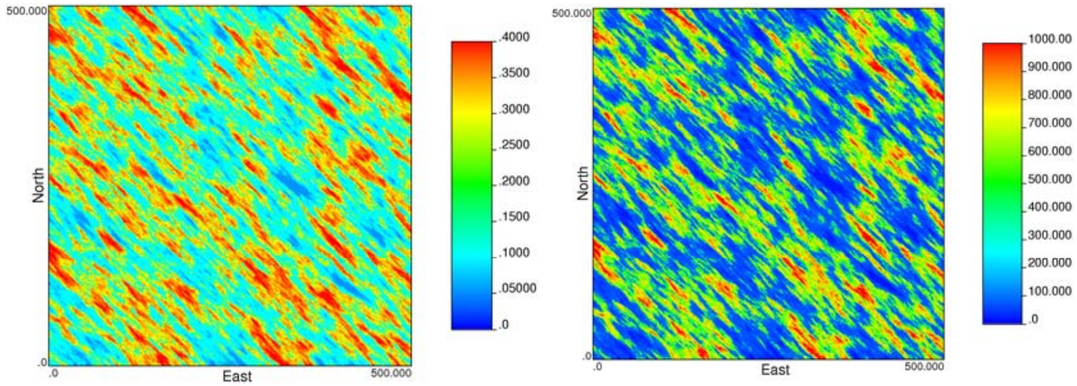

Figure 5-2: Porosity and permeability models for Case B (long correlation length).

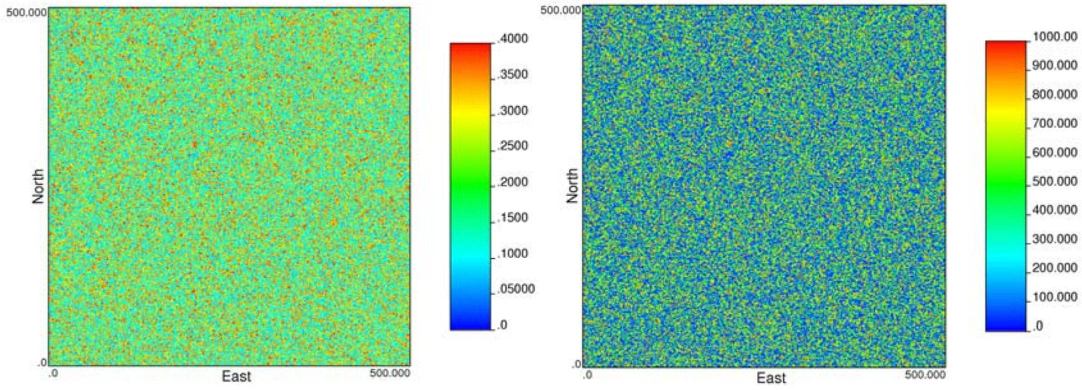

Figure 5-3: Porosity and permeability models for Case C (uncorrelated or very short correlation length).

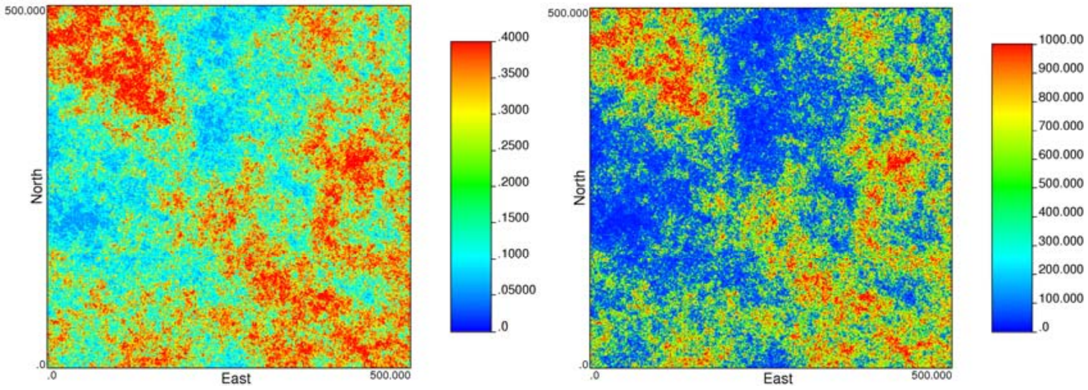

Figure 5-4: Porosity and permeability models for Case D (a non-stationary trend modeled using a local varying mean).

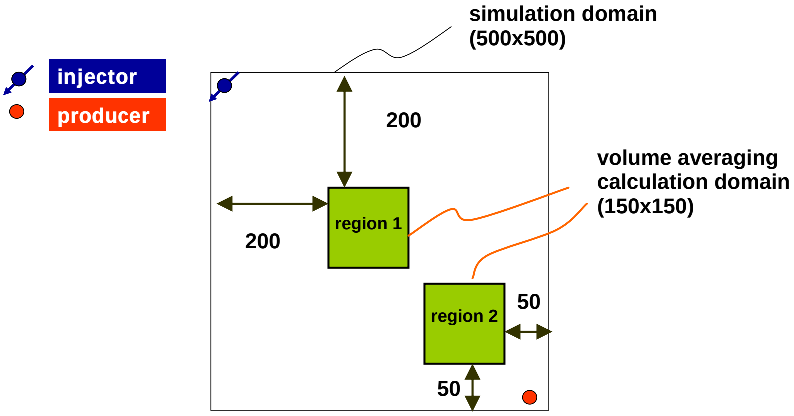

Figure 5-5: Set-up of simulation and volume averaging calculation domains. Regions 1 and 2 are used to calculate the scaling characteristics at two snap shots in time (when the leading edge of the tracer front has moved from region 1 to region 2).

Results for Region 1

Figure 5-6 shows the maps of permeability and velocity magnitude over the volume averaging domain for a coarse grid size of 10x10. Significant smoothing is observed comparing the average velocity $||\langle \mathbf{u}_\beta \rangle||$ to the fine-scale velocity $||\mathbf{u}_\beta||$. Figure 5-7 shows the corresponding concentration maps. Once again, the average concentration maps, both before and after simulated annealing adjustments, look much smoother than the original fine-scale concentration. The figures also show the spatial distribution of the perturbed quantities: $||\mathbf{u}'_\beta||$ and C'_β. For cases where reservoir properties are uncorrelated or exhibit short correlation length, summation of the concentration deviations over the entire volume averaging domain is close to zero. This is because in the case of short correlation length, a relatively uniform tracer front is observed. It is interesting to note that highest concentration deviations (C'_β) are localized at the front.

The reduction of error (ε, mismatch between the LHS and RHS of the closure equation as defined in Chapter 4) during the simulated annealing procedure is shown in Figure 5-8; it can be observed that only small adjustments to the average concentrations are required to reduce the error by 35-45%.

Figure 5-9 shows the spatial distribution of absolute value of K_{eff}. Recall from Chapter 4 that K_{eff} is defined as: $K_{eff} = \left(\left\langle \mathbf{u}_\beta \right\rangle \cdot \nabla \left\langle C_\beta \right\rangle\right) \Big/ \left(C_{\max} - \left\langle C_\beta \right\rangle\right)$. Hence, K_{eff} is the highest in regions that are swept by the tracer front and is close to zero ahead of the front. This is because the maximum amount of mass transfer between the injection fluid and the in-situ fluid occurs at regions that have already been swept by the tracer front, while no mass transfer occurs at regions ahead of the front. This observation suggests that K_{eff} can be used as an indication of recovery; high values of K_{eff} reflect an increase in areas contacted by the concentration front. Higher magnitude of K_{eff} are observed in the case of long correlation length because in this case, heterogeneity (and hence the direction of convective transport) is oriented along the flow direction. Higher values of variance of K_{eff} are also observed for the long correlation length case because a strong contrast in concentration values is maintained between the high permeability (high velocity) areas and low permeability areas. In uncorrelated media, there is more mixing leading to lower variability in K_{eff}.

As we repeat the volume averaging calculations at different coarse grid sizes, we can study the scaling relationships of K_{eff} as well as of all the different transport mechanisms (interfacial flux, convection, diffusion, dispersion etc.). Figure 5-10 and Figure 5-11 show the scaling relationship (spatial mean and standard deviation) of the absolute values of K_{eff}, convection, upscaled permeability, diffusion, and dispersion as a function of averaging scale for all four models. More correlated models exhibit higher mean and variability. Just as expected in a convection-dispersion dominant system, mass transfer due to convection and dispersion dominate the transport process; they are about five orders of magnitude higher than diffusion.

It is interesting to compare the results for scaling of dispersion to measured values of dispersivity in literature and other studies related to large-scale dispersion as discussed in Chapter 2. However, it should be noted that the effective dispersion in Figure 5-11 represents the rate of mass transfer due to dispersion effects and has the units of mass/time; therefore, it does not necessarily follow the scaling characteristics of dispersivity directly. Nonetheless, in the cases with larger correlation lengths (Case B and Case D), effective dispersion is the highest. In particular, the model in Case D exhibits a nested structure with local varying mean, representing a system with correlation length much larger than the size of the reservoir model. This results in a monotonically increasing profile of effective dispersion continues with length. On the other hand, in the uncorrelated case (Case C), effective dispersion is the lowest and begins to decrease and stabilize at smaller length scales.

The spatial variability of K_{eff} can be quantified in terms of the semi-variogram. Figure 5-12 shows the range of the experimental semi-variogram of K_{eff}. Along the direction of flow, the variogram range of K_{eff} in all cases appears to be infinite (non-stationarity introduced by the directionality of flow); therefore, the experimental variogram is plotted in the direction perpendicular to flow. Certain important features can be observed: 1) range of K_{eff} increases with scale – this implies increased mixing with volume averaging; 2) at large scales, the range tends to stabilize to about 50 units, which is approximately the extent or size of the region swept by the tracer front; 3) models with larger correlation lengths (i.e. Case B and Case D) show a sharper increase in correlation length of K_{eff} with L than models with smaller correlation lengths.

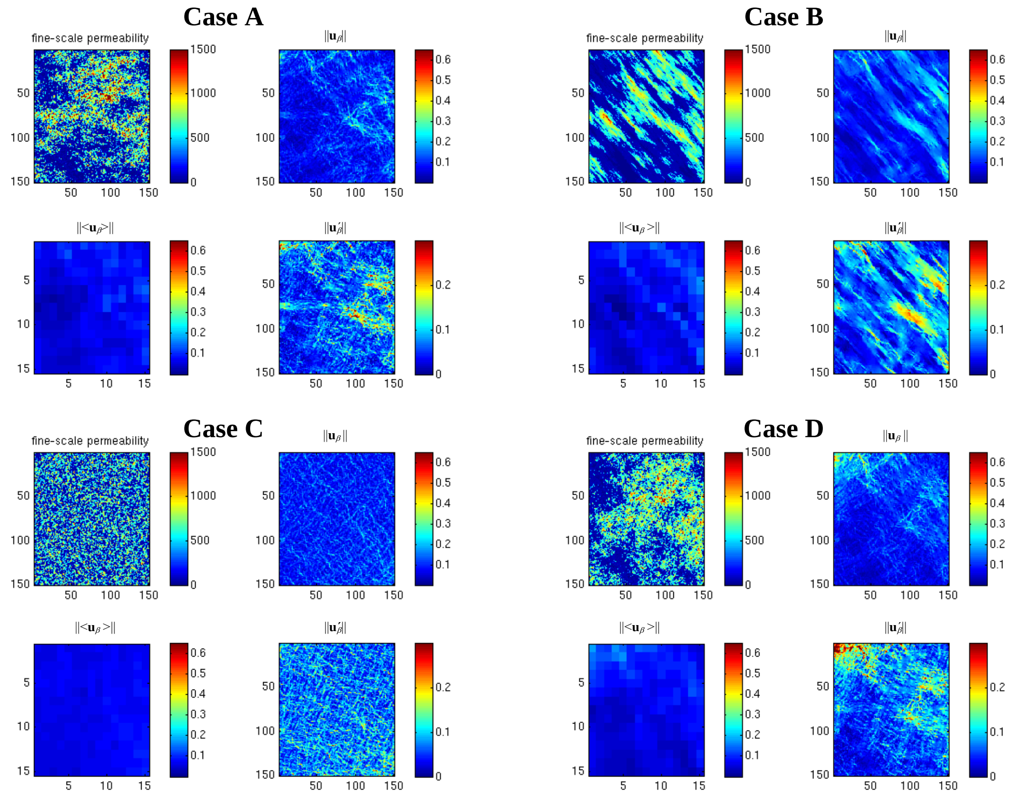

Figure 5-6: (From top left to bottom right) permeability, velocity $\mathbf{u}_\beta$, and its decomposition into average velocity $<\mathbf{u}_\beta>$ and $\mathbf{u}'_\beta$ for a coarse grid size of 10x10 (top left: Case A; top right: Case B; bottom left: Case C; bottom right: Case D).

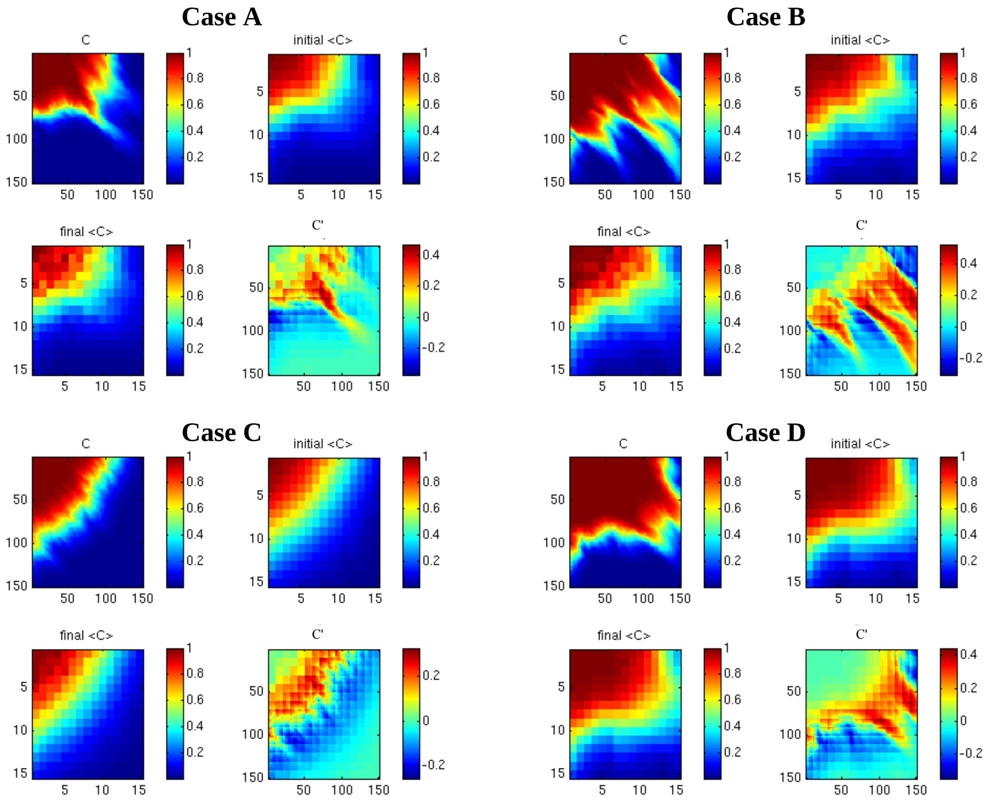

Figure 5-7: (From top left to bottom right) fine-scale concentration, average concentration <C> from coarse-scale simulation (initial guess before simulated annealing), final average concentration <*C*> after simulated annealing and the corresponding deviations *C'* for a coarse grid size of 10x10 (top left: Case A; top right: Case B; bottom left: Case C; bottom right: Case D).

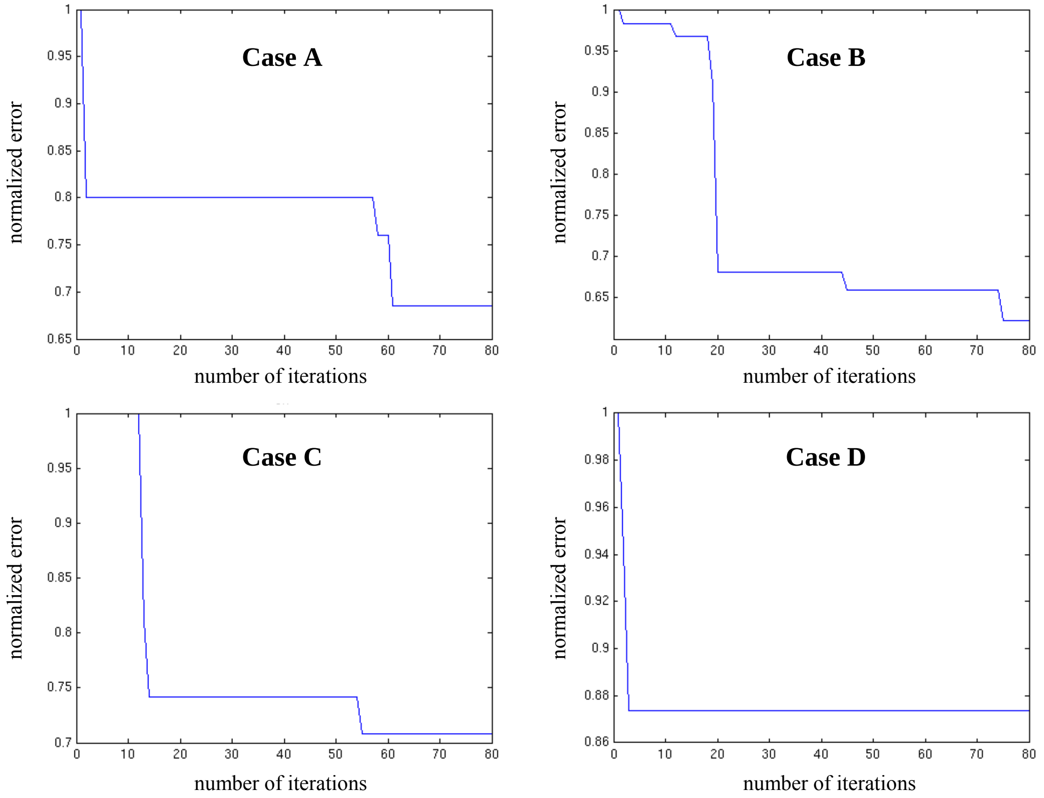

Figure 5-8: Error (mismatch between LHS and RHS of the closure equation (4-43)) reduction during simulated annealing (top left: Case A; top right: Case B; bottom left: Case C; bottom right: Case D).

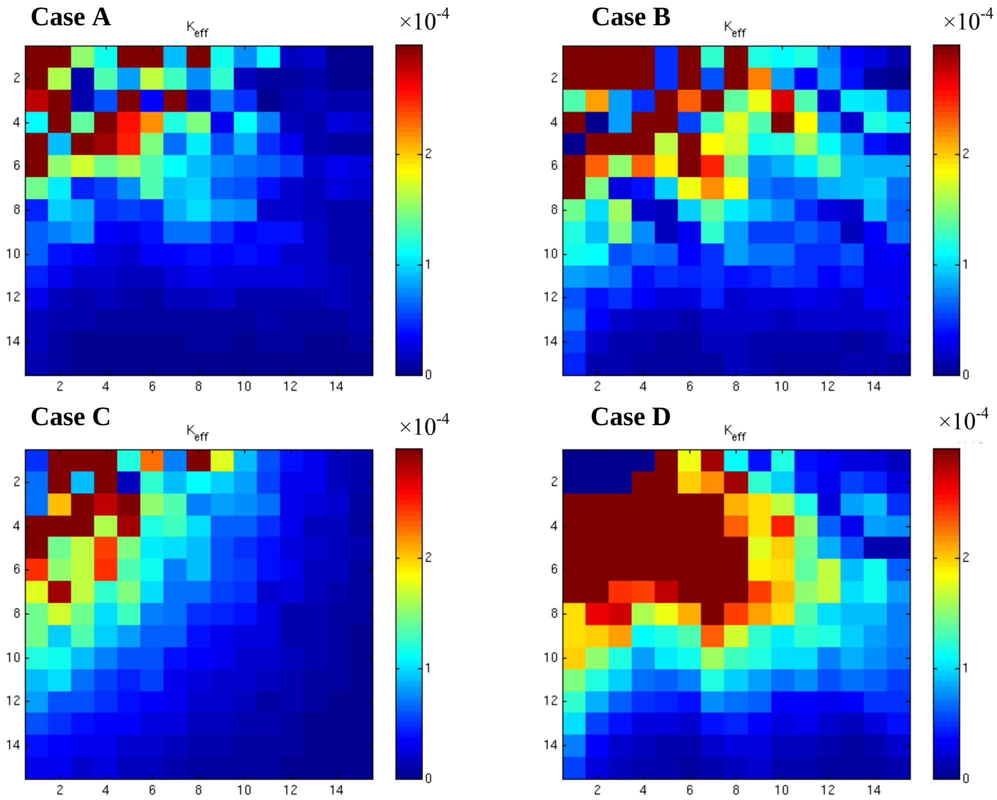

Case A

Case B

Case C

Case D

Figure 5-9: Spatial distribution of K_{eff} for a coarse grid size of 10x10 (top left: Case A; top right: Case B; bottom left: Case C; bottom right: Case D).

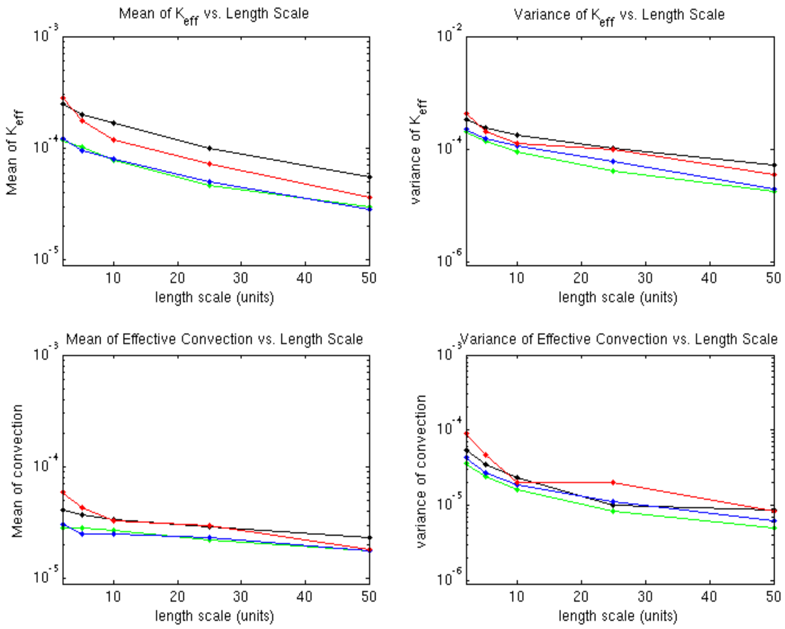

Figure 5-10: Mean and variance of K_{eff} and mass transfer due to convection as a function of length scale (blue: Case A; red: Case B; green: Case C; black: Case D).

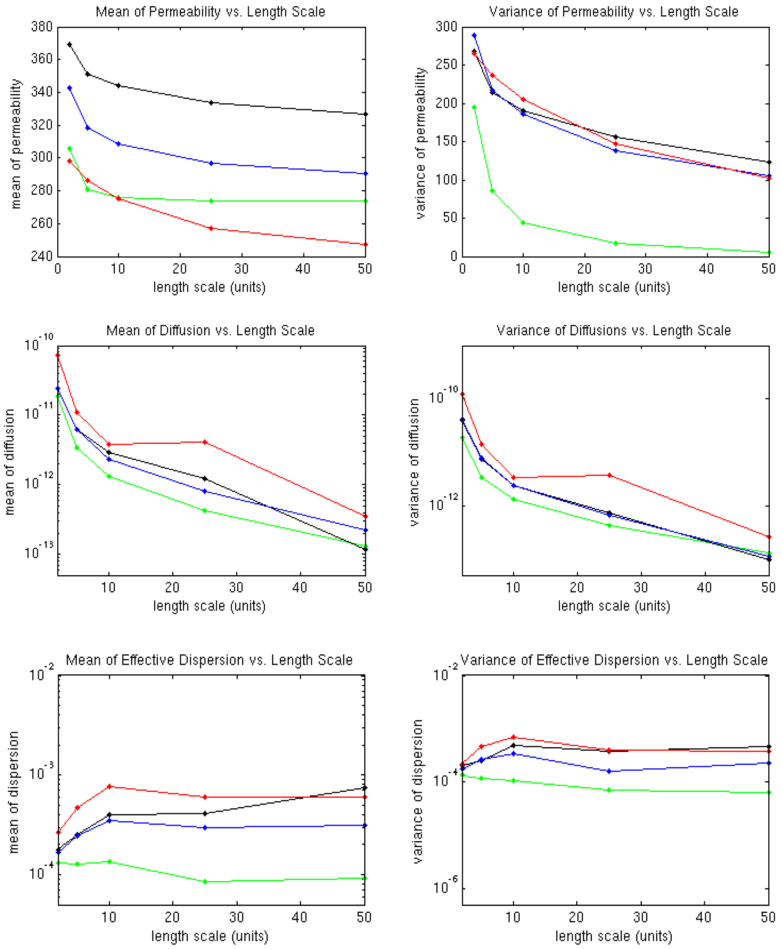

Figure 5-11: Mean and variance of permeability (top 2 figures); mass transfer due to diffusion (middle 2 figures); and mass transfer due to dispersion (bottom 2 figures) as a function of length scale (blue: Case A; red: Case B; green: Case C; black: Case D).

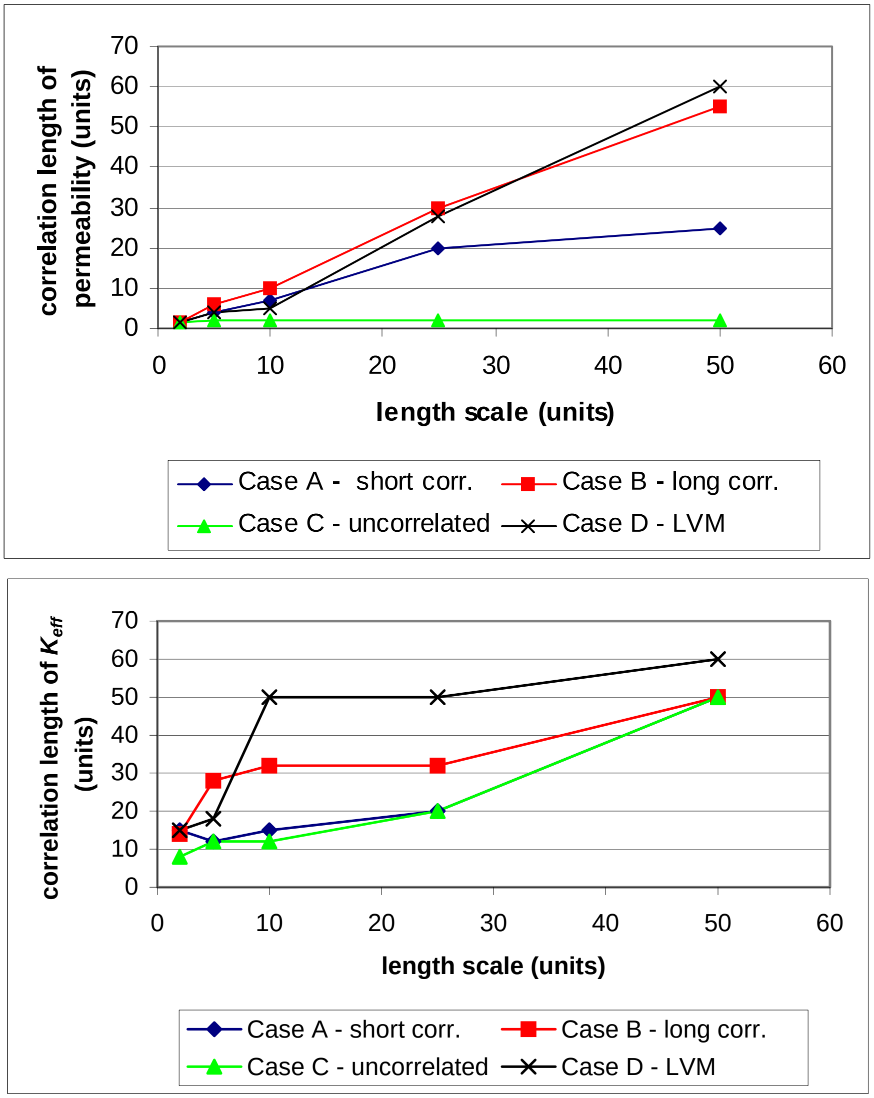

Figure 5-12: The top figure is the range of semi-variogram of permeability along major direction of anisotropy (45°). The bottom figure is the semi-variogram range of K_{eff} in the direction perpendicular to flow.

Results for Region 2

Compared to region 1, region 2 is located much closer to the producer; therefore, higher velocity can be observed (Figure 5-13), especially in areas close to the bottom right corner near the producer, where some radial artifact is also evident. Nevertheless, similar characteristics of the velocity and concentration maps (fine scale, average, and perturbation) in Figure 5-6 and Figure 5-7 are observed in Figure 5-13 and Figure 5-14. The convergence characteristics of the error shown in Figure 5-15 are also similar to that for region 1. The spatial distribution of absolute value of K_{eff} shown in Figure 5-16 shows an even higher contrast between short and long correlation lengths, as compared to that in Figure 5-9.

Comparing Figure 5-10 and Figure 5-11 to Figure 5-17 and Figure 5-18, it is reasonable to conclude that similar scaling relationships of transport mechanisms (in terms of both magnitude and trend) are observed, regardless of the location of the averaging volume. Slightly higher values for convection, dispersion, and K_{eff} are observed in region 2 because it is located closer to the well with higher fluxes than the rest of the reservoir and hence is more influenced by boundary effects. Once again, the effective dispersion for the uncorrelated case is the lowest and decreases slowly with scale, whereas all the other models show a gradual increase in dispersion with scale. Dispersive flux captures the combined effects of molecular diffusion and velocity variations. It is evident in both Figure 5-6 and Figure 5-13 that the velocities are fairly uniformly distributed spatially when the correlation length is shortest (Case A); this means that velocity variations do not differ significantly with averaging scale. On the other hand, as the correlation length increases, contrasts in velocity variations between low and high permeability zones increase with scale, causing the dispersive flux to exhibit a gradual increase.

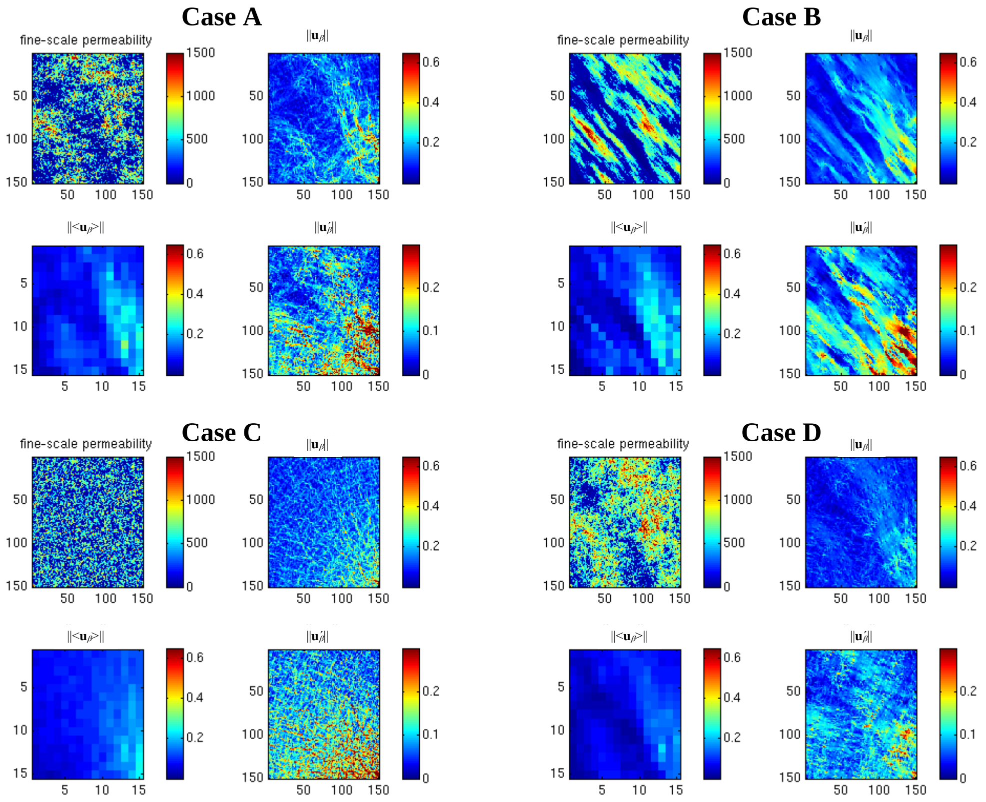

Figure 5-13: (From top left to bottom right) permeability, velocity $\mathbf{u}_\beta$, and its decomposition into average velocity $<\mathbf{u}_\beta>$ and $\mathbf{u}'_\beta$ for a coarse grid size of 10x10 (top left: Case A; top right: Case B; bottom left: Case C; bottom right: Case D).

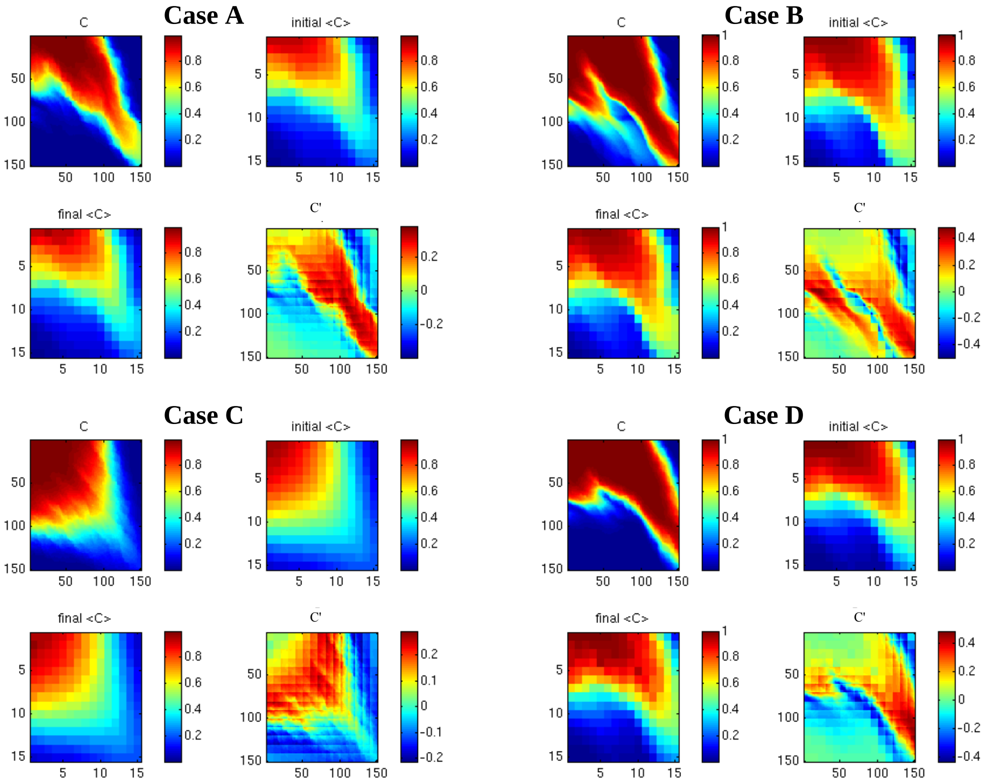

Figure 5-14: (From top left to bottom right) fine-scale concentration, average concentration <*C*> from coarse-scale simulation (initial guess before simulated annealing), final average concentration <*C*> after simulated annealing and the corresponding deviations *C'* for a coarse grid size of 10x10 (top left: Case A; top right: Case B; bottom left: Case C; bottom right: Case D).

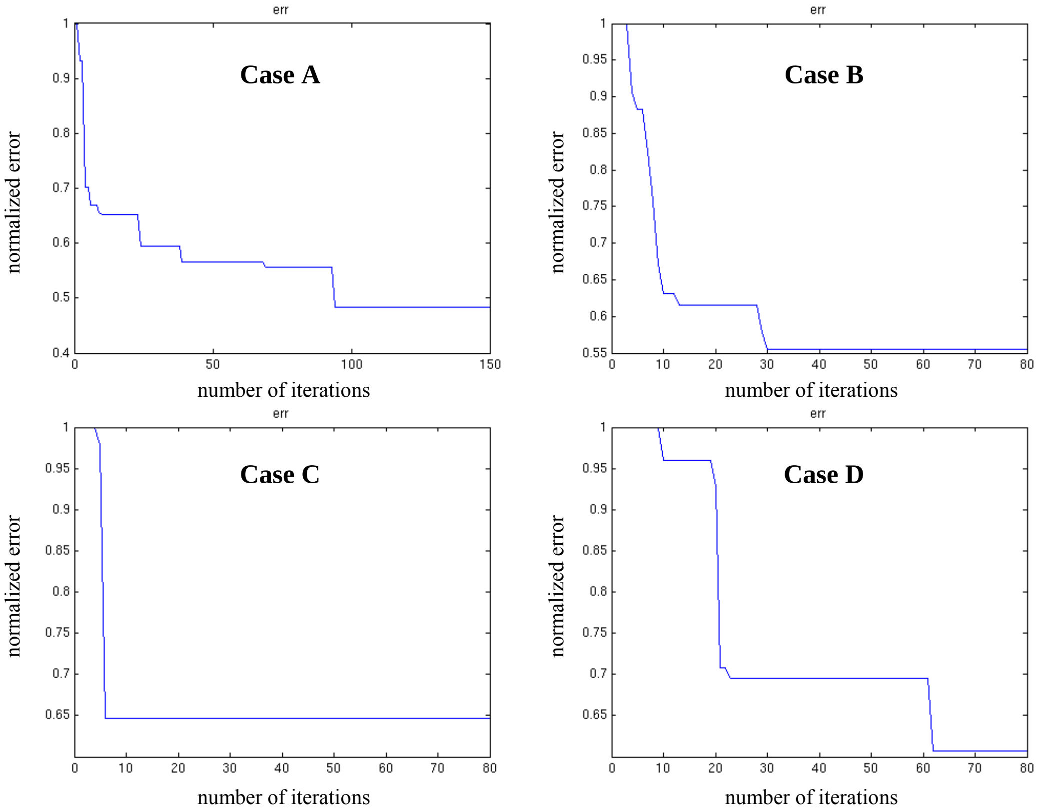

Figure 5-15: Error reduction during simulated annealing (top left: Case A; top right: Case B; bottom left: Case C; bottom right: Case D).

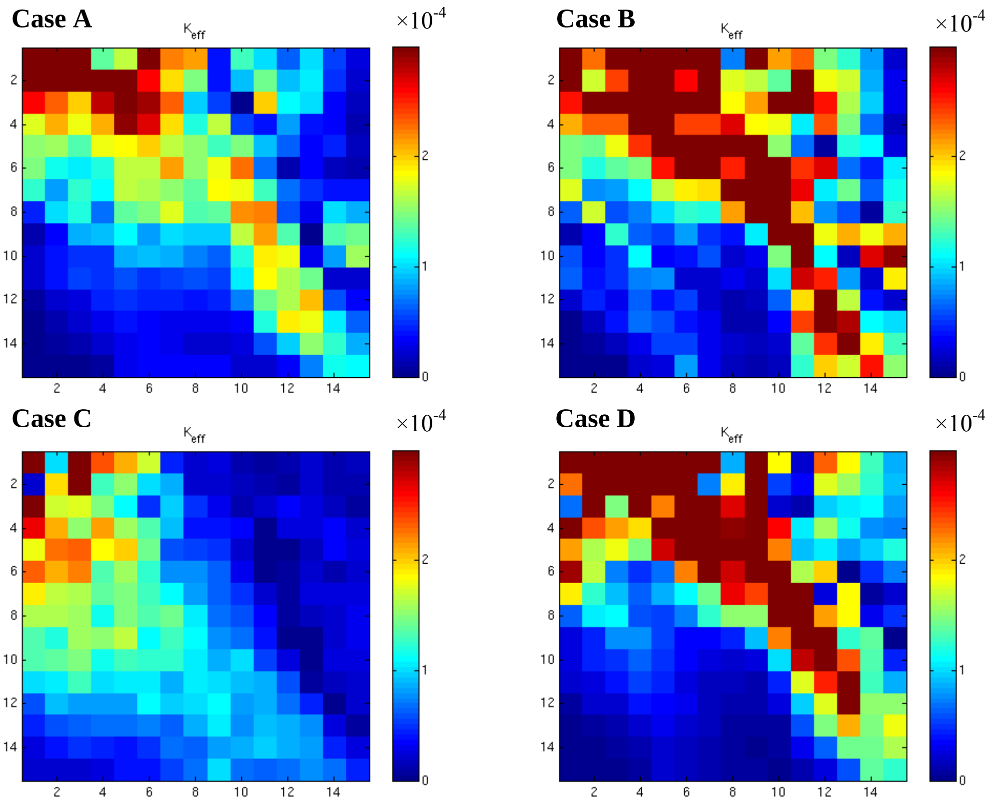
Case A

Case B

Case C

Case D

Figure 5-16: Spatial distribution of K_{eff} for a coarse grid size of 10x10 (top left: Case A; top right: Case B; bottom left: Case C; bottom right: Case D).

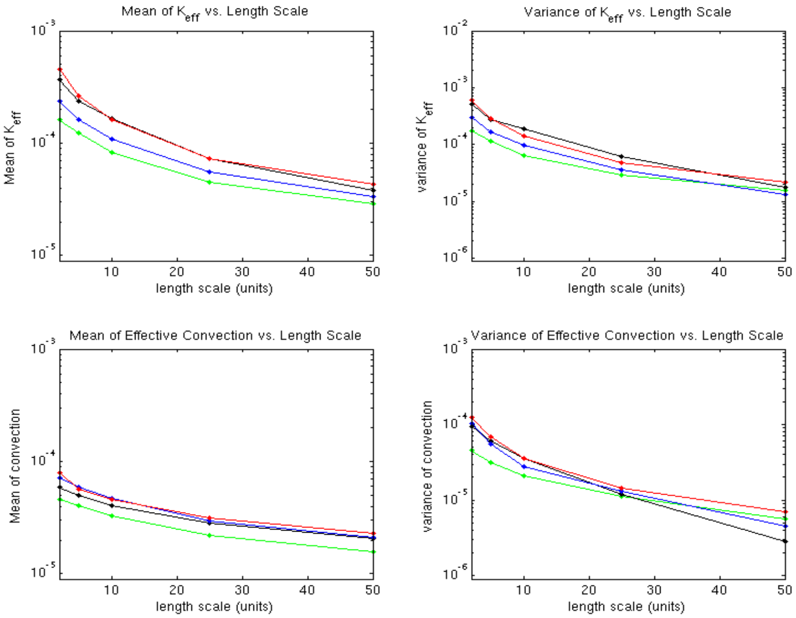

Figure 5-17: Mean and variance of K_{eff} and mass transfer due to convection as a function of length scale (blue: Case A; red: Case B; green: Case C; black: Case D).

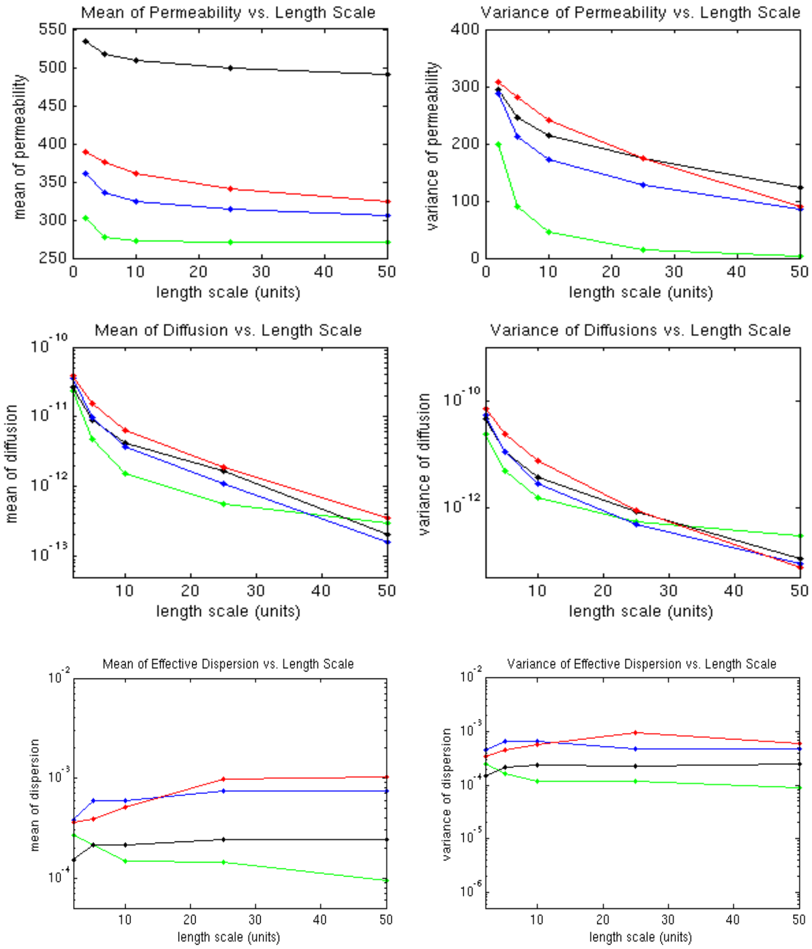

Figure 5-18: Mean and variance of permeability (top 2 figures); mass transfer due to diffusion (middle 2 figures); and mass transfer due to dispersion (bottom 2 figures) as a function of length scale (blue: Case A; red: Case B; green: Case C; black: Case D).

Scaling of Recovery

Based on the observations in the case study, we might postulate the following: 1) recovery scales similar to K_{eff}, which contains information from different dominating recovery mechanisms; 2) higher recovery and variability in recovery can be expected in models with longer correlated features oriented along the direction of flow. In the case where flow direction is oriented along the direction of anisotropy, recovery is related to the size of the total area that is swept by the tracer front where the maximum amount of mass transfer between the injection fluid and the in-situ fluid occurs. In the long correlation length case, a strong contrast in concentration values is maintained between the high permeability (high velocity) areas and low permeability (low velocity) areas. As a result, large variation in regions that are swept by the tracer front is expected. This causes an increased variability in recovery when the correlation length is long.

In order to test these hypotheses, we can perform the following experiment. Consider the two original reservoir models in Figure 5-1 and Figure 5-2 representative of short and long correlation length, we randomly draw 50 sub-models of size 5 fine cells x 5 fine cells from each of these original models (similar to Figure 3-12). Each sub-model is then subjected to flow simulation with an injector-producer pair located at the top left and bottom right corners. From each simulation, the breakthrough time and tracer recovery after a fixed amount of injected volume can be obtained; we can also compute the corresponding mean and variance over all 50 sub-models, representing the recovery statistics for that particular sub-model size. This exercise was repeated with sub-models of bigger and bigger sizes (e.g., 10x10, 50x50). Figure 5-19 is a plot of the recovery statistics as a function of sub-model size or length scale and verifies our hypothesis that higher mean and variance in recovery is observed for the case of long correlation length. More importantly, recovery decreases as length scale increases because effective transport coefficient decreases with scale. As shown earlier, the mean and variance of K_{eff} decreases with scale, which is consistent with the decrease in mean and variance of recovery. The mean of breakthrough time appears relatively constant for the case of long correlation length but increases gradually in the case of short correlation length. This is because in a convection dominant process, the fluid would always follow the fastest streamline to breakthrough regardless of domain size, and this is evident when long correlated features are oriented in the flow direction. On the other hand, when the correlation length is short, the fluid front is increasingly smeared as the domain size increases and that delays breakthrough. However, it is important to remember that breakthrough statistics reveal only information about the fastest fluid pathway, but they cannot be used to make general statement about scaling of recovery.

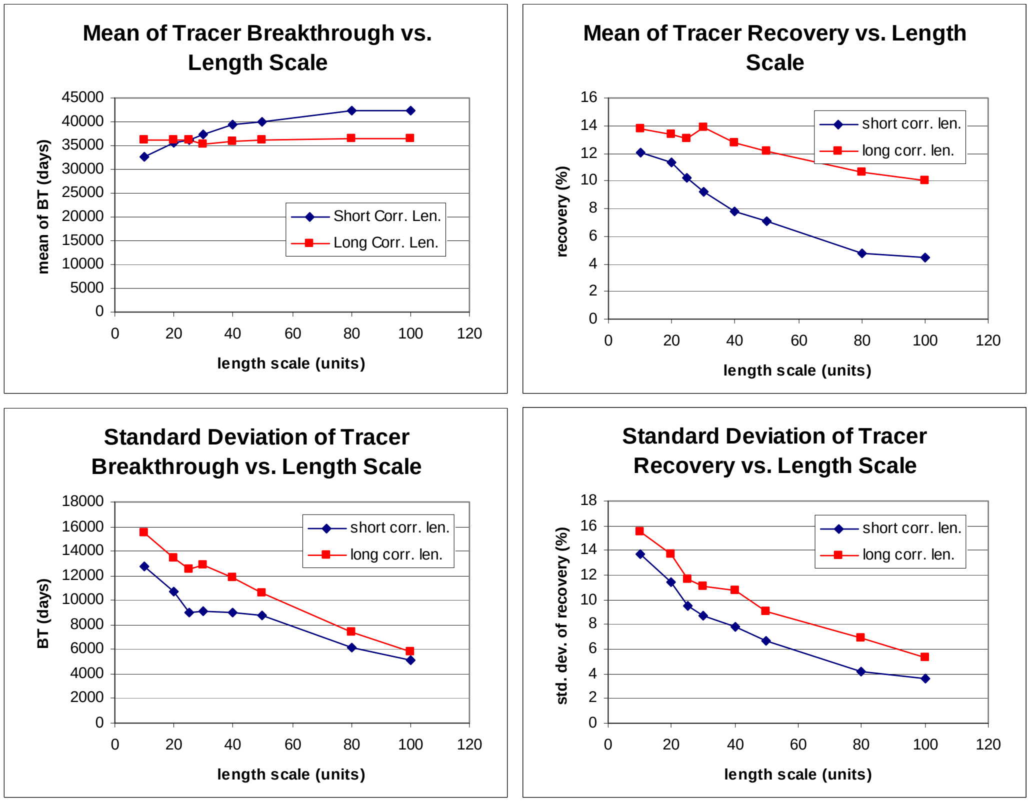
Mean of Tracer Breakthrough vs. Length Scale

Mean of Tracer Recovery vs. Length Scale

Standard Deviation of Tracer Breakthrough vs. Length Scale

Standard Deviation of Tracer Recovery vs. Length Scale

Figure 5-19: Scaling characteristics of breakthrough time (BT) and tracer recovery with length scale when convection-dispersion is the dominant transport mechanism.

5.2.2 Flow Perpendicular to the Direction of Anisotropy

In the previous examples, the flow is oriented along the direction of anisotropy, and significant differences in the scaling characteristics of K_{eff} and recovery statistics can be observed between different heterogeneity models. In the next example, the flow direction will be oriented opposite to the direction of anisotropy as shown in Figure 5-20. All other parameters remain the same as in the previous section, but we will focus on only Case A and Case B in this study. Figure 5-21 shows the maps of permeability and velocity magnitude over the volume averaging domain for a coarse grid size of 10x10, while Figure 5-22 shows the corresponding concentration maps. Figure 5-23 shows the spatial distribution of K_{eff} for the two heterogeneity models.

The scaling characteristics of K_{eff} are shown in Figure 5-24. This result can be compared against the tracer recovery statistics shown in Figure 5-26 obtained by flow simulation as described earlier for the case when the flow was parallel to the direction of anisotropy. Since flow direction is no longer aligned with the underlying anisotropy, the effect of heterogeneity on scaling characteristics of recovery is reduced. Compared to the results for the previous case when the flow was in the direction of anisotropy, the scaling characteristics of effective transport (K_{eff}, mass transfer due to convection, dispersion, and diffusion) also become less dependent on the underlying heterogeneity. In particular, slightly higher mean and variance in both K_{eff} and recovery are observed for the longer correlation model at smaller length scales; as the length scale increases, the differences are minimized and beyond a certain scale, the shorter correlation model exhibits a higher mean and variance of recovery and K_{eff} again due to the smearing of the injection front. As opposed to the previous example where breakthrough time remains constant with domain size for the long correlation length model, breakthrough time increases in this case, indicating that front smearing is significant when the flow is perpendicular to the direction of heterogeneity.

These observations suggest the following: 1) differences in scaling characteristics due to heterogeneity are most prominent when the flow direction is aligned with the direction of anisotropy, at least in the case of convection-dispersion dominant transport; 2) uncertainty in direction of anisotropy introduces additional uncertainty in scaling characteristics of transport mechanisms and recovery; and 3) the volume averaging framework proposed in this research provides a promising tool to characterize that uncertainty by integrating numerical simulation results corresponding to arbitrary flow configurations.

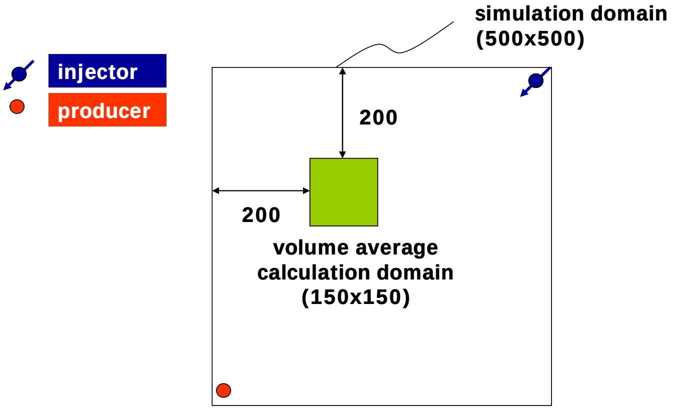

Figure 5-20: Set-up of simulation and volume averaging calculation domains for the case when the flow is perpendicular to the direction of anisotropy.

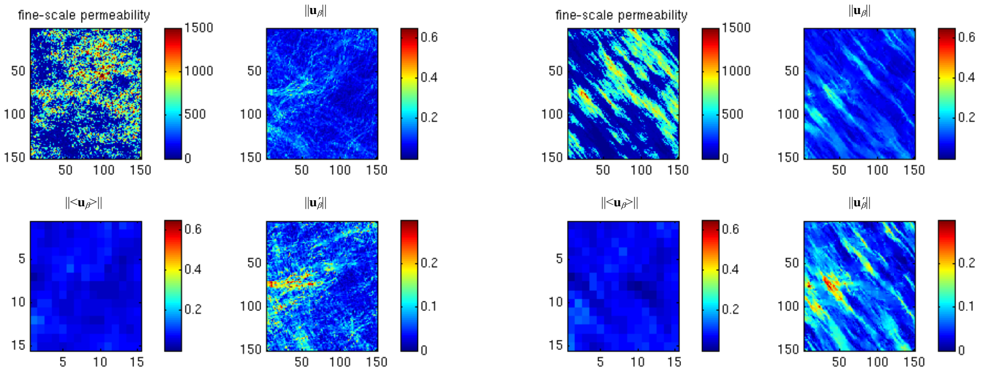

Figure 5-21: (From top left to bottom right) permeability, velocity $\mathbf{u}_\beta$, and its decomposition into average velocity $<\mathbf{u}_\beta>$ and $\mathbf{u}'_\beta$ for a coarse grid size of 10x10 (left: Case A; right: Case B). These results are for the case when the flow is counter to the direction of anisotropy.

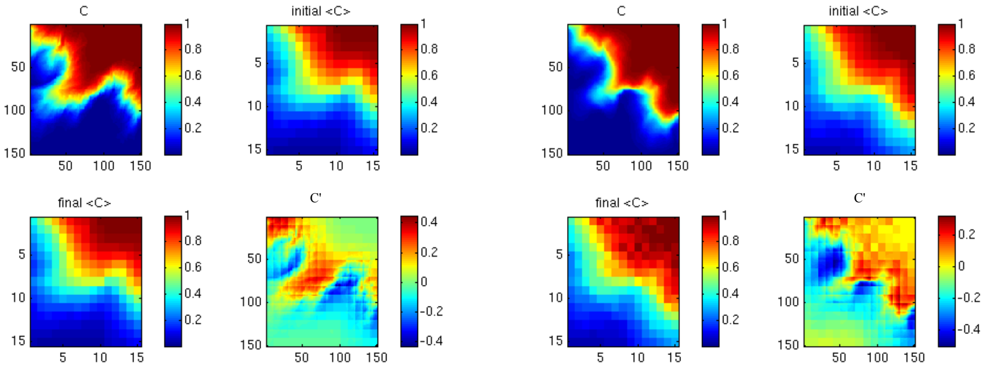

Figure 5-22: (From top left to bottom right) fine-scale concentration, average concentration $<C>$ from coarse-scale simulation (initial guess before simulated annealing), final average concentration $<C>$ after simulated annealing and the corresponding deviations C' for a coarse grid size of 10x10 (left: Case A; right: Case B). These results are for the case when the flow is counter to the direction of anisotropy.

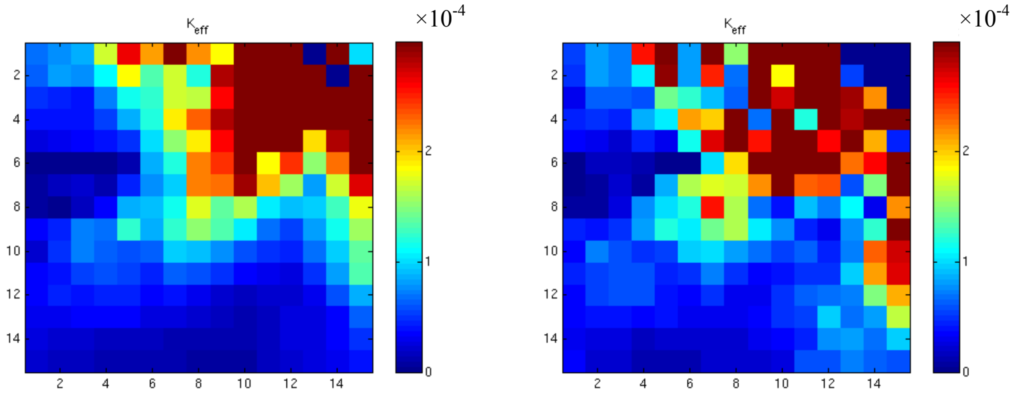

Figure 5-23: Spatial distribution of K_{eff} for a coarse grid size of 10x10 (left: Case A; right: Case B) for the case when the flow is counter to the direction of anisotropy.

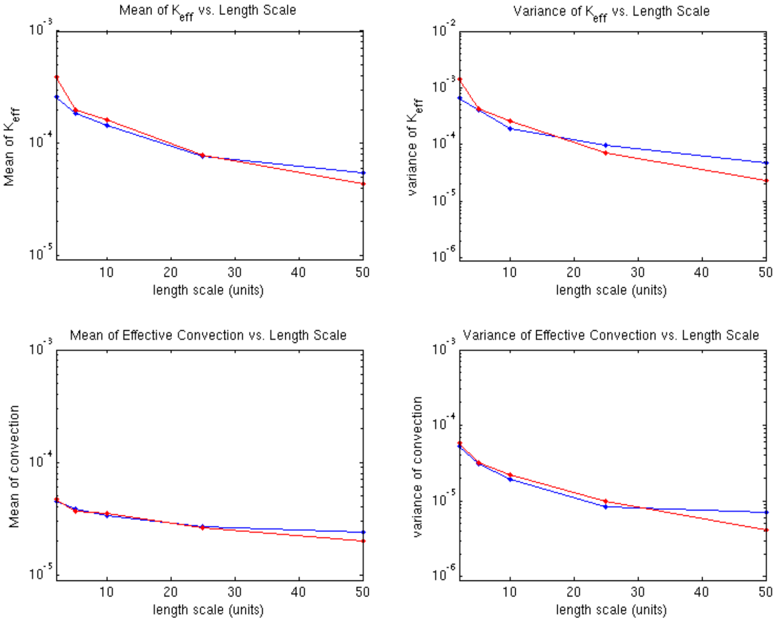

Figure 5-24: Mean and variance of K_{eff} and mass transfer due to convection as a function of length scale for the case when the flow is counter to the direction of anisotropy (blue: Case A; red: Case B).

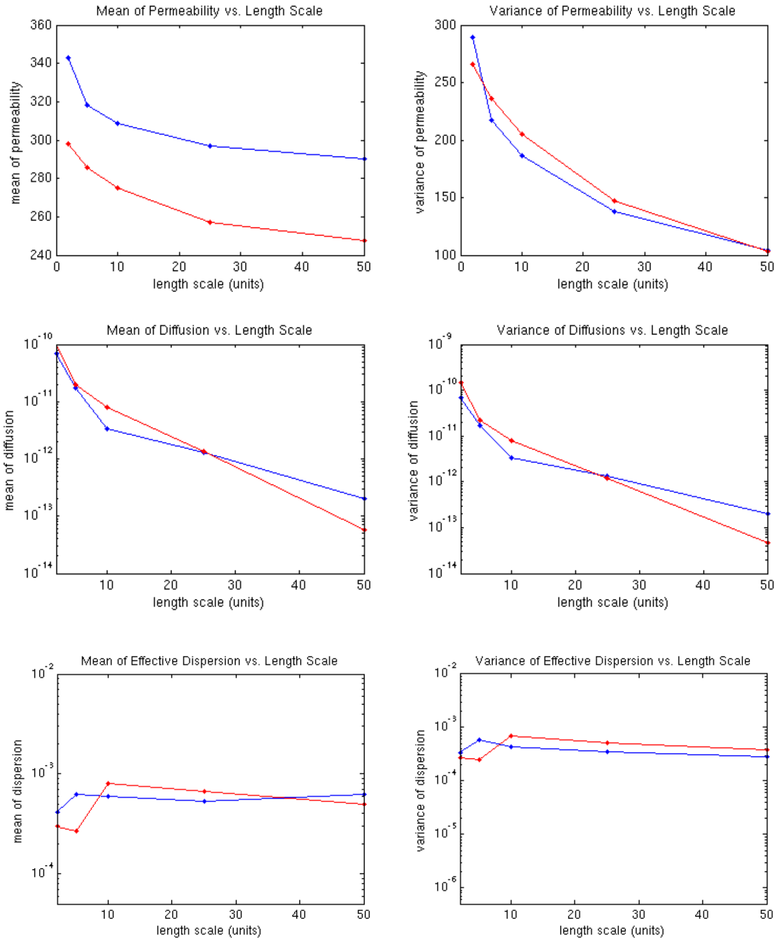

Figure 5-25: Mean and variance of permeability; mass transfer due to diffusion; and mass transfer due to dispersion as a function of length scale for the case when the flow is counter to the direction of anisotropy (blue: Case A; red: Case B).

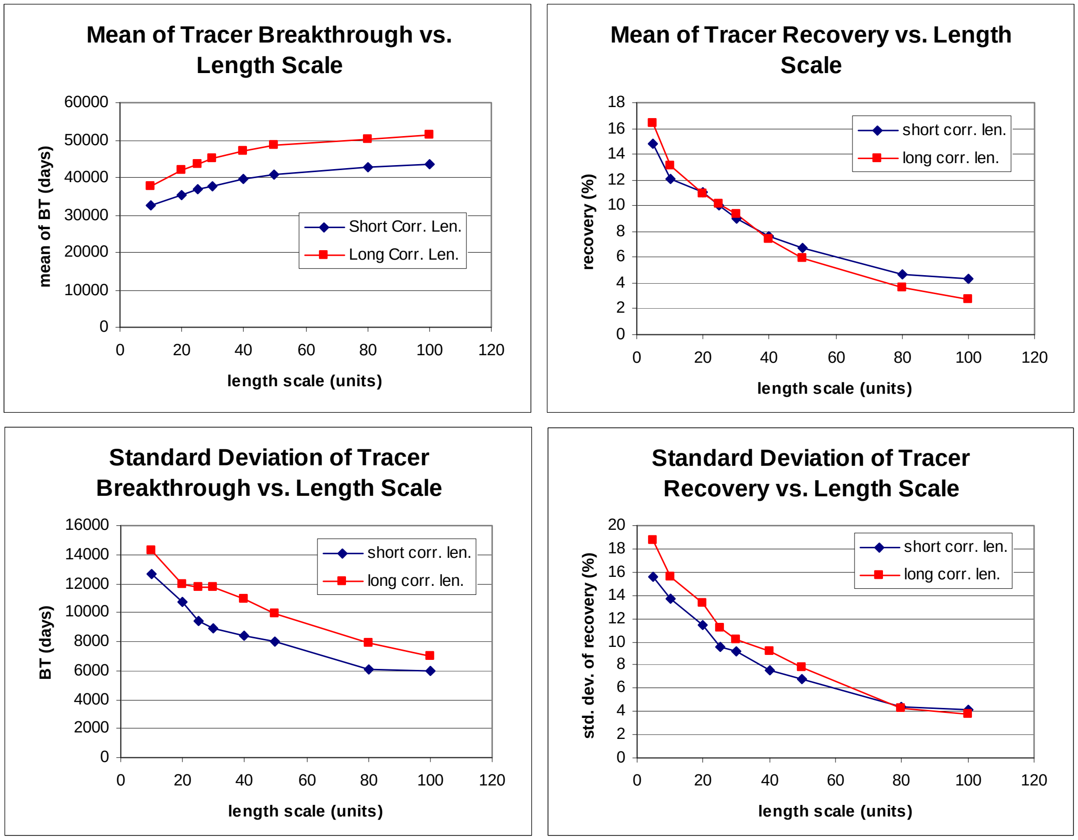

Figure 5-26: Scaling characteristics of breakthrough time (BT) and tracer recovery when the flow is counter to the direction of anisotropy.

5.2.3 Increasing the Role of Diffusion

All the previous examples in this chapter illustrate the scaling characteristics in flow scenarios where convection and dispersion dominate; in the next example, the scaling of effective mass transfer coefficient and recovery are studied for a slow transport process where the role of diffusion is emphasized. Once again, the same parameters as in the base case will be used together with heterogeneity models for Cases A and B. In order to simulate a system where diffusion dominates, the flow rate is reduced and the diffusion coefficient is increased.

Q = 100 sm^3/day (reduced from 1000 sm^3/day in the base case)

D = 1e-3 m^2/day (fine-scale diffusion, increased from 1e-6 m^2/day in the base case)

Average velocity from the fine-scale simulation is approximately 0.021 m/day. A quick calculation assuming a typical grain size of 1e-4m shows that the dimensionless group uD_p/D = (0.021)(1e-4)/(1e-3) ~ 0.0021. A value less than 0.02 indicate process is controlled by diffusion (Lake, 1989). Results for region 1 after 250000 days are presented in Figure 5-27 – Figure 5-32. Similar to the scenario where convection and dispersion control the mass transfer, mean and variance of K_{eff} decrease with scale.

The velocity and concentration maps are shown in Figure 5-27 and Figure 5-28. Comparing to the results in the base case where process is convection controlled, all the velocity quantities ($\mathbf{u}$, $\langle \mathbf{u} \rangle$, $\mathbf{u}'$) are much lower. In the previous case, significant differences are observed in the concentration deviation (C') maps between the two correlation length models (Figure 5-7); however, when diffusion controls, these differences are no longer evident.

Furthermore, the spatial distribution of K_{eff} is shown in Figure 5-29, and the scaling characteristics of K_{eff}, mass transfer due to convection, diffusion, and dispersion are shown in Figure 5-30 and Figure 5-31. The most important observation from Figure 5-29 and Figure 5-30 is that the differences in scaling characteristics of K_{eff} between long and short correlation lengths are much less significant; the values of K_{eff} are an order of magnitude less than that for the convection controlled case. In other words, the scaling characteristics of K_{eff} are essentially insensitive to heterogeneity when diffusion dominates. It should also be noted that the scaling characteristics of mass transfer due to diffusion appears to be insensitive to the correlation lengths of the underlying heterogeneity, even when the process is diffusion controlled..

The scaling characteristics of tracer recovery are shown in Figure 5-32. It illustrates similar scaling characteristics as K_{eff}. The mean of breakthrough time increases gradually for both cases of different correlation length. This is because in a diffusion dominant process, there is no concept of a fastest streamline to breakthrough. Instead, the fluid would have a tendency to smear away from the injection point as the domain size increases (due to the averaging process) and delay breakthrough in a way similar to the short correlation case when convection dominates.

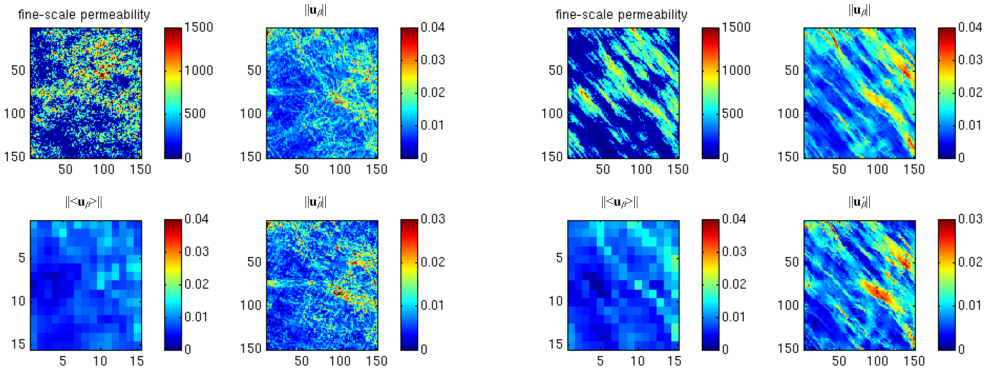

Figure 5-27: (From top left to bottom right) permeability, velocity $\mathbf{u}_\beta$, and its decomposition into average velocity $<\mathbf{u}_\beta>$ and $\mathbf{u}'_\beta$ for a coarse grid size of 10x10 (left: Case A; right: Case B). These results are for the case where diffusion is the dominant mass transfer mechanism.

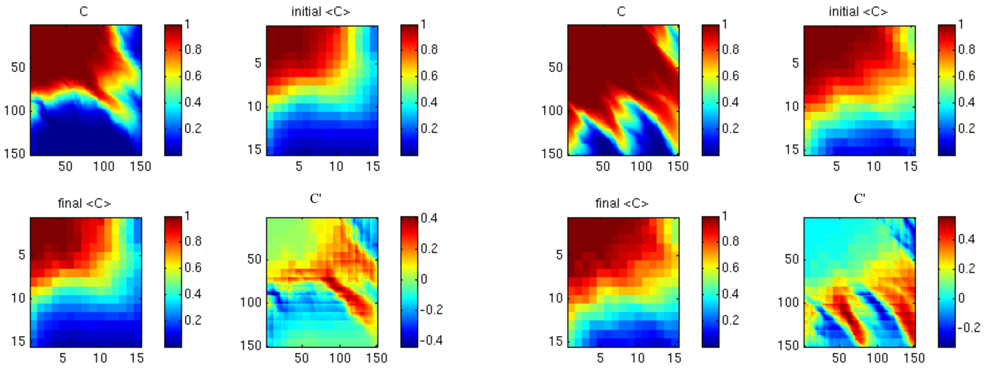

Figure 5-28: (From top left to bottom right) fine-scale concentration, average concentration <*C*> from coarse-scale simulation (initial guess before simulated annealing), final average concentration <*C*> after simulated annealing and the corresponding deviations *C'* for a coarse grid size of 10x10 (left: Case A; right: Case B). These results are for the case where diffusion is the dominant mass transfer mechanism.

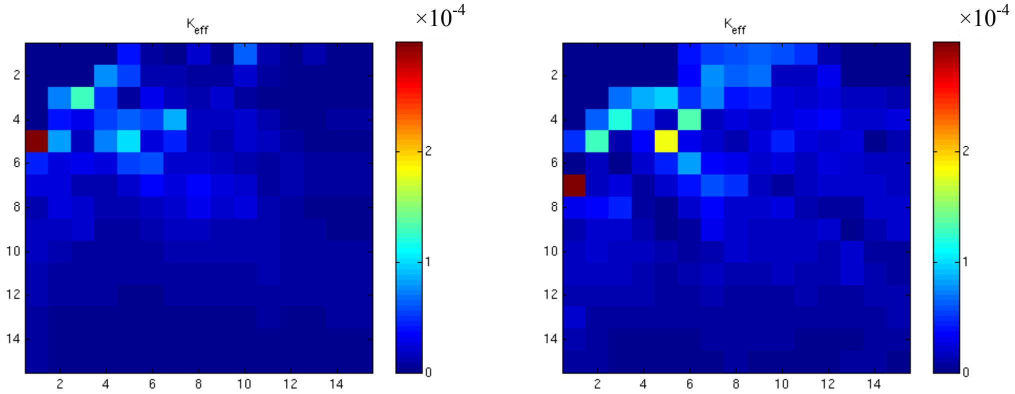

Figure 5-29: Spatial distribution of K_{eff} for a coarse grid size of 10x10 for the case where diffusion is the dominant mass transfer mechanism (left: Case A; right: Case B).

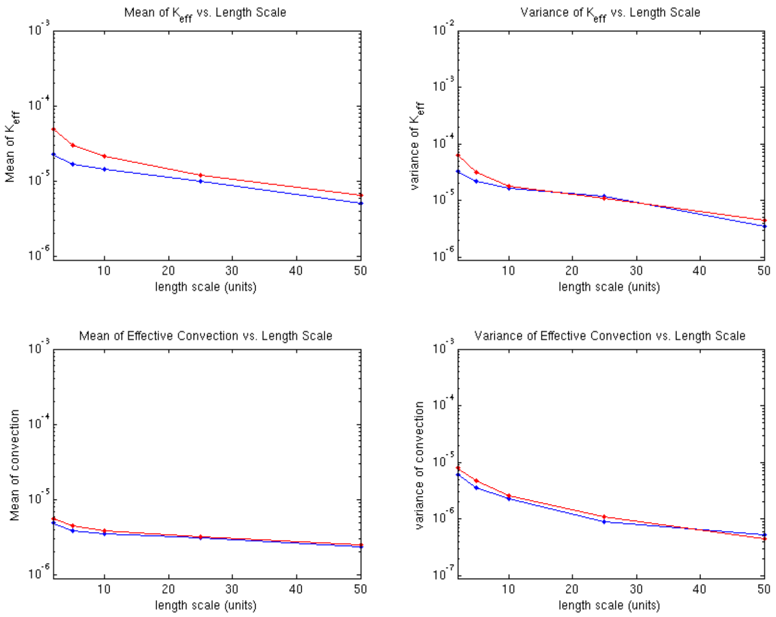

Figure 5-30: Mean and variance of K_{eff} and mass transfer due to convection as a function of length scale for the case where diffusion is the dominant mass transfer mechanism (blue: Case A; red: Case B).

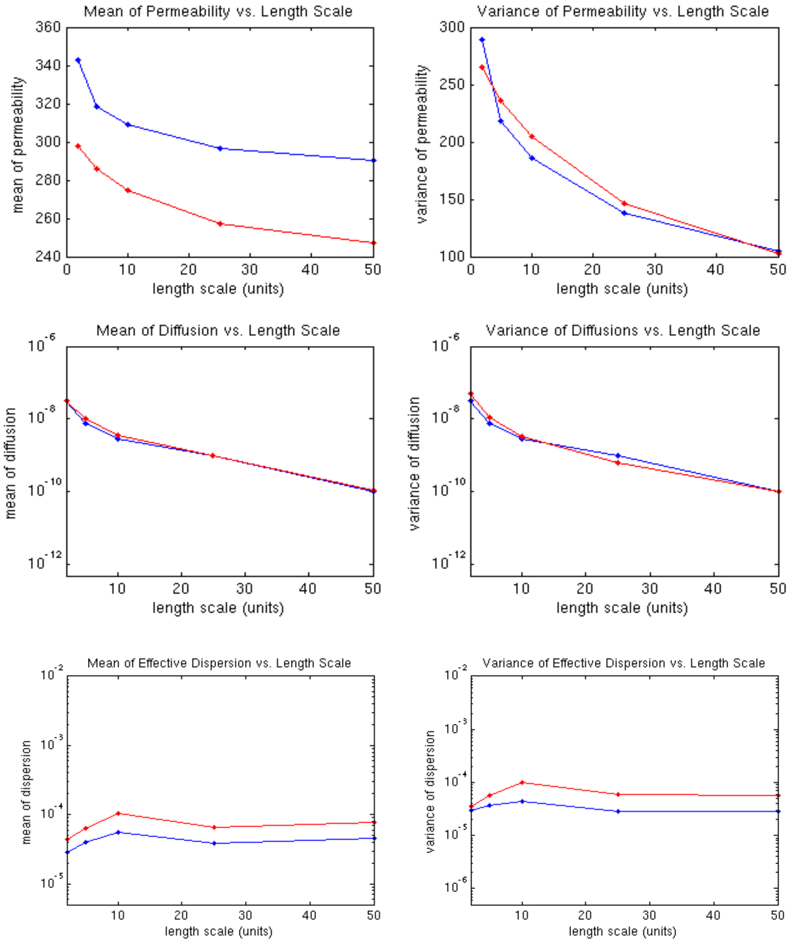

Figure 5-31: Mean and variance of permeability; mass transfer due to dispersion; mass transfer due to dispersion as a function of length scale for the case where diffusion is the dominant mass transfer mechanism (blue: Case A; red: Case B).

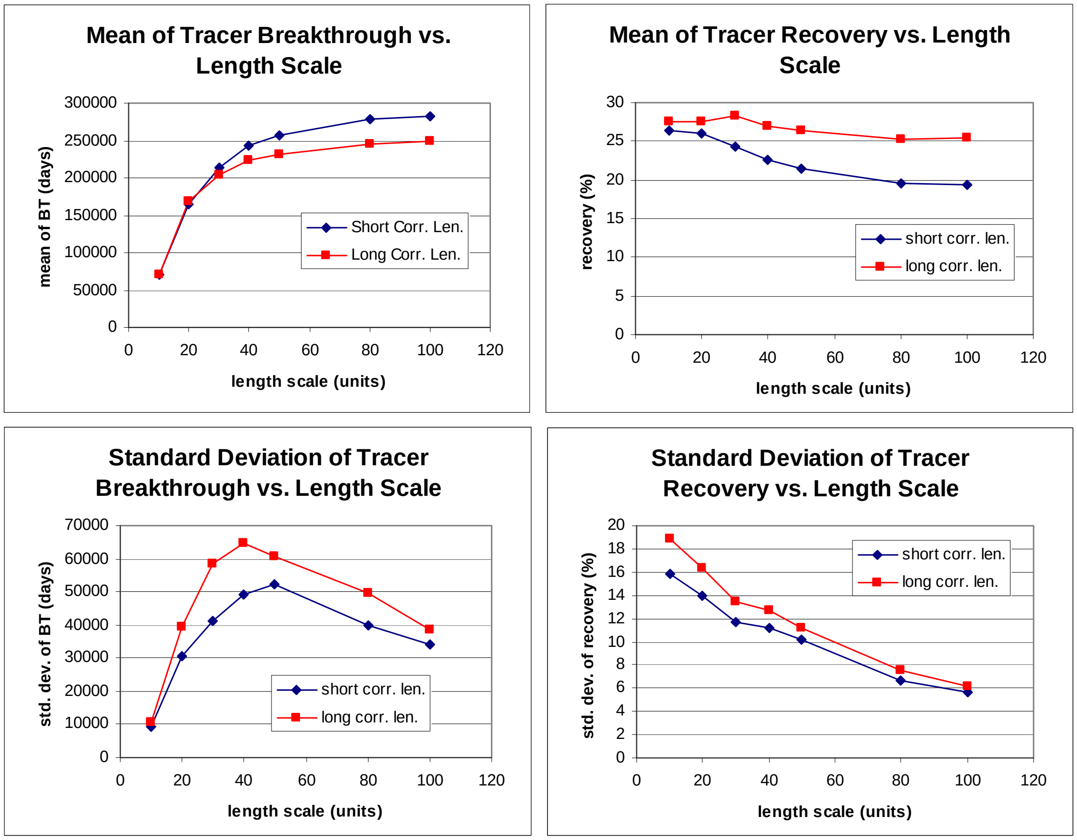
Mean of Tracer Breakthrough vs. Length Scale

Mean of Tracer Recovery vs. Length Scale

Standard Deviation of Tracer Breakthrough vs. Length Scale

Standard Deviation of Tracer Recovery vs. Length Scale

Figure 5-32: Scaling characteristics of breakthrough time (BT) and tracer recovery when diffusion is the dominant mass transfer mechanism.

5.2.4 Efficacy of the Volume Averaging Process for Deriving Scale-Up Relations

Obtaining scaling characteristics of recovery via repeated flow simulations with multiple realizations could be a computationally expensive task. Table 5-1 demonstrates how the computing time required for the volume averaging approach is significantly less than that for the repeated flow simulations procedure. All the flow simulations are performed with a Desktop workstation consisting of a Dell Optiplex GX745 Intel® Core™2 2.13 GHz processor and 2 GB of RAM. The volume averaging calculations are implemented in MATLAB and executed with a Linux cluster: front-end is a Dell

Poweredge 2650 with four (4) Intel Xeon 2.40 GHz processors and 2 GB of memory, and each of the eight (8) computer node is a Dell Poweredge 2650s with four (4) Intel Xeon 2.40 GHz processors and 2 GB of memory.

In the case of repeated flow simulations, as the length scale increases, the computing time increases drastically. In the volume averaging approach, obtaining the fine-scale solution is the most expensive step, but this solution can be used again for all length scales in the volume averaging step. Although coarse-scale simulations are also performed in order to obtain initial estimates of average velocities and concentration at each length scale, only one realization is actually needed. Moreover, cheaper proxy transfer functions such as streamline simulations can be used in lieu of these coarse-scale simulations to further reduce the cost.

Table 5-1: Comparison of computation time between the volume averaging approach and repeated flow simulations

			computing time (minutes)
volume averaging approach	one fine-scale 500x500 flow simulation		31
	coarse-scale simulation at each length scale (*L*)	*L* (unit)	
		5	4
		10	2
		25	1
		50	1
	volume averaging calculations at each length scale (*L*)	*L* (unit)	
		5	4
		10	6
		25	5
		50	5
	total computing time:		**59**
repeated flow simulations	flow simulations with 50 realizations at each length scale (*L*)	*L* (unit)	
		5	20
		10	24
		25	25
		50	32
	total computing time:		**101**

5.3 APPLICATION TO FRACTAL MEDIA

In this section, we are interested in comparing the scaling relationships of transport mechanisms obtained with the volume averaging approach to analytical results for fractal media. Figure 5-33 shows a fractal image obtained from Moisy (2009); fractal dimension is determined to be approximately 1.5 by box-counting. Although this image is a reconstruction of a tree, it has been transformed into a map of rock type indicator for this study by setting the black and white pixels to facies 0 and 1, respectively. The porosity and permeability values are populated according to:

$$facies = 0 \rightarrow \begin{Bmatrix} \phi = 0.1 \\ k = 60mD \end{Bmatrix}$$

$$facies = 1 \rightarrow \begin{Bmatrix} \phi = 0.35 \\ k = 735mD \end{Bmatrix}$$

In this example, a tracer injection process is implemented on the 500x500 2-D fine grid fractal medium. Once again, the grid sizes are uniform ($\Delta x = \Delta y = 10m$) with a thickness of 10m. An injector is placed at the top left corner and a producer is located at the bottom right corner. Injection and production rates are held constant at 1000 sm^3/day. A passive tracer is added to the injection stream at a concentration of 1mg/m^3. Figure 5-34 illustrates the simulation and volume average calculation configuration. All parameters are set to be the same in section 5.2.1.

This injection rate was already shown to correspond to a process controlled by convection and dispersion. For a fractal media, dispersivity (α_L) increases with scale of observation in the following manner (Wheatcraft and Tyler; 1988; Sahimi, 1993):

$$\alpha_L = L^{DF-1} = L^{1-H} \tag{5-1}$$

Where H is the Hurst dimension and is related to the fractal dimension (DF) as:

$$\mathrm{DF} = 2 - H \tag{5-2}$$

Since the dominant mechanism is dispersion, it is reasonable to expect that K_{eff} (with units of time^{-1}) would scale with $\alpha_L/L = L^{-H}$ (dimensionless) instead of α_L that has a dimension of L:

$$K_{eff}\Delta C \propto \frac{D^*}{L^2}\Delta C \propto \frac{\alpha_L u}{L^2}\Delta C \propto \left(\frac{\alpha_L}{L}\right)\left(\frac{u}{L}\right)\Delta C$$
$$\therefore K_{eff} \propto \frac{\alpha_L}{L} \tag{5-3}$$

where D^* is the dispersion coefficient. Using the method of box counting, the fractal dimension of the volume average calculation domain is estimated to be 1.5, giving a Hurst dimension of approximately 0.5.

The fine scale concentrations, average and perturbation concentration after 25000 days are shown in Figure 5-35. The spatial variations in K_{eff} obtained by volume average calculations are shown in Figure 5-36. Since mass transfer is controlled by convection-dispersion, the maximum values of K_{eff} are concentrated along the high permeability features. Figure 5-37 shows that K_{eff} scales as approximately $L^{-0.6}$ (obtained by fitting a power function), which is equivalent to DF = 1.4 or H = 0.6. Figure 5-38 shows that dispersion scales as $L^{0.4}$, which in this case appears to be approximately the same as the scaling relationship of dispersivity $\alpha_L = L^{1-0.6} = L^{0.4}$. Since a fractal medium is infinitely correlated at all scales, dispersion grows with scale indefinitely without stabilizing at a plateau value.

The scaling characteristics of K_{eff} and dispersion obtained with the volume averaging approach are in excellent agreement with the analytical predictions based on the fractal theory. These results demonstrate that the volume averaging technique can be used as a reliable tool to derive scaling relationships of effective transport that accounting for sub-scale heterogeneities reliably captures the effect of permeability heterogeneity underlying the flow models.

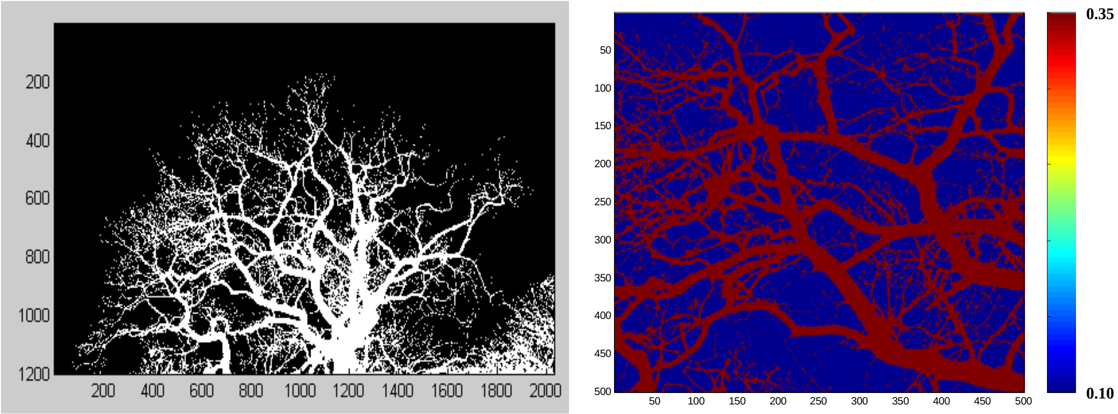

Figure 5-33: A fractal image of a tree (left) and an extracted porosity map (right). Fractal dimension is determined to be approximately 1.5 by box-counting (Moisy, 2009).

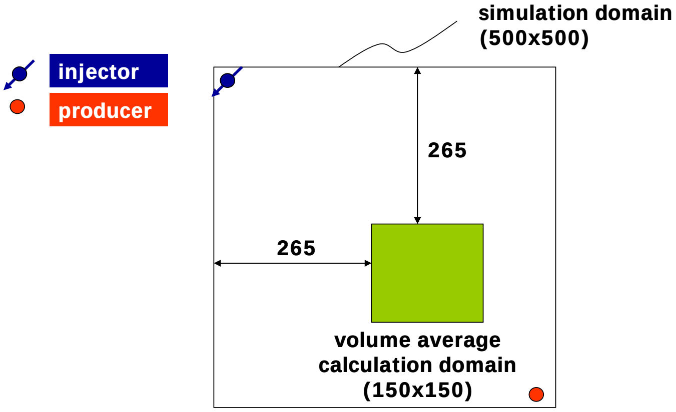

Figure 5-34: Well configuration and location of the volume average calculation domain for the fractal example.

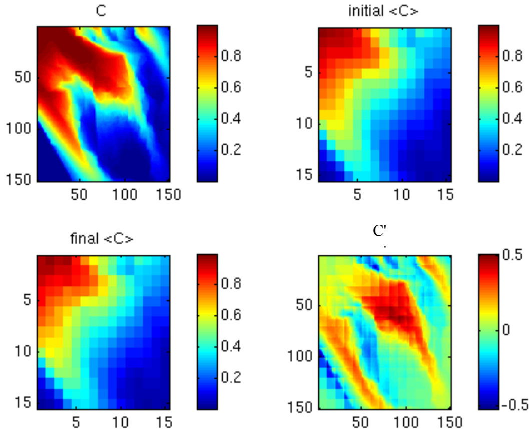

Figure 5-35: (From top left to bottom right) fine-scale concentration, average concentration <*C*> from coarse-scale simulation (initial guess before simulated annealing), final average concentration <*C*> after simulated annealing and the corresponding deviations *C'* for a coarse grid size of 10x10. These results are for the fractal permeability field shown in Figure 5-33.

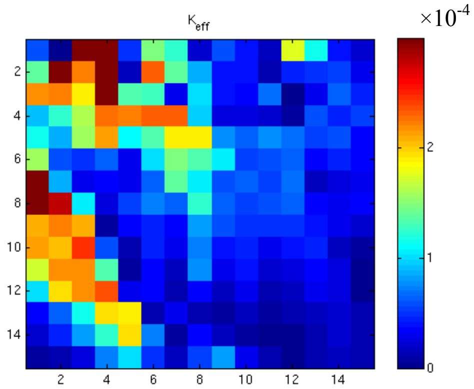

Figure 5-36: Spatial distribution of K_{eff} for a coarse grid size of 10x10 corresponding to the fractal example.

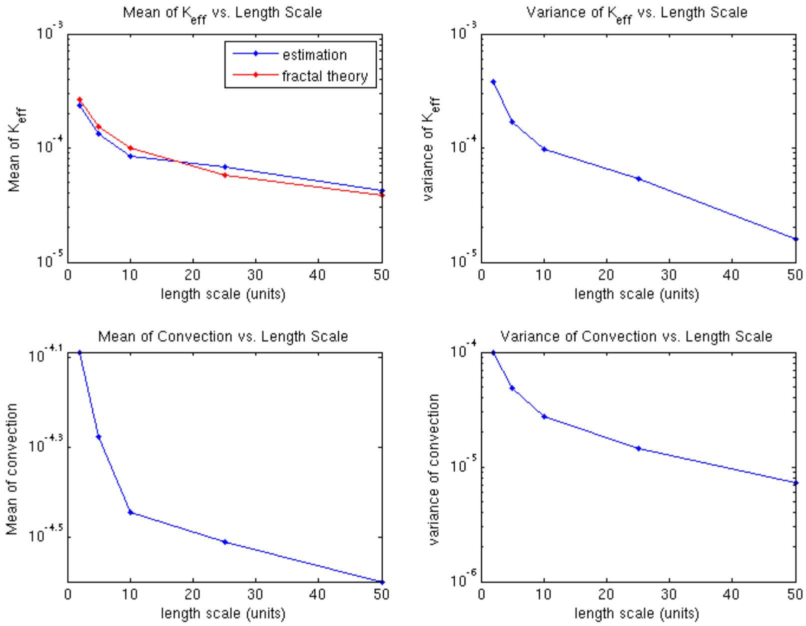

Figure 5-37: The mean and variance of K_{eff} and mass transfer due to convection as a function of length scale for the fractal example.

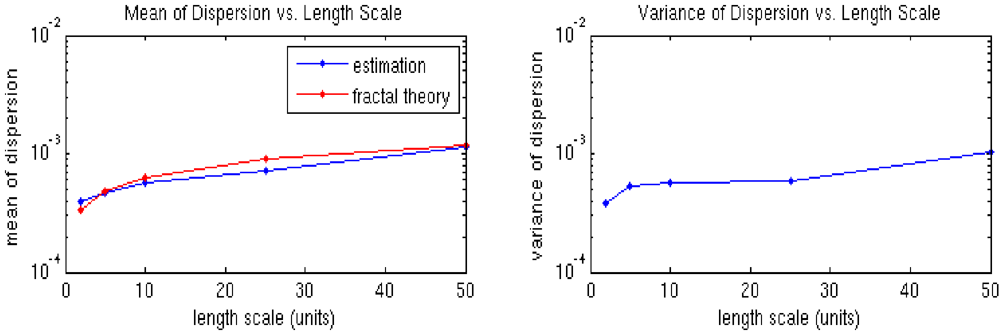

Figure 5-38: Scaling characteristics of dispersion. For comparison purposes, the scaling result obtained by applying fractal theory is also shown in red.

5.4 EFFECTS OF COMPLEX GEOLOGIC CONNECTIVITY ON SCALING CHARACTERISTICS

The reservoir models we have studied in section 5.2 are generated using geostatistical techniques when the assumption of second-order stationarity is valid. Examples of such techniques are Sequential Gaussian Simulation (SGSIM) or Sequential Indicator Simulation (SISIM) (Deutsch and Journel, 1998). In such cases, geological features are considered to be fully described using only the first and second order moments of the random function describing the reservoir properties (e.g., porosity, permeability, or rock types). Unfortunately, many realistic geological features exhibit connectivity characteristics that cannot be captured by 2-point (second order) statistics; a common example could be a river-channel systems. In order to ensure these higher-order connectivity features are reproduced in the reservoir models, many multiple-point statistics (MPS) algorithms have been developed and widely used (Strebelle, 2000; Arpat, 2003; Eskandari and Srinivasan, 2008). Instead of using a variogram or two-point statistic to summarize spatial correlation, multiple-point statistics are calibrated from a training image directly. These statistics are used subsequently in a sequential simulation framework to generate stochastic models that reproduce the higher-order moments of the random function as depicted in the training image.

In this section, effects of complex connectivity of the geologic model on scale-up of transport mechanisms will be studied. Using a training image, we generated a facies map depicting a channel system using a common MPS algorithm called *filtersim* that is implemented in the public-domain software SGeMS (Remy et al., 2009). We then create a second model using *sisim* with the variogram calculated from the *filtersim* model directly (Figure 5-41). As a result, both the MPS and SISIM models exhibit the same statistics up to the second order moments. The resultant facies models are illustrated in Figure 5-40.

Consider a tracer injection process on these 500x500 2-D fine grid models. Once again, the grid sizes are uniform ($\Delta x = \Delta y = 10$m) with a thickness of 10m. An injector is placed at the top in the middle and a producer is located at the bottom in the middle. Injection and production rates are held constant at 1000 sm^3/day. A passive tracer is added to the injection stream at a concentration of 1mg/m^3. Figure 5-39 illustrates the simulation and volume average calculation configuration. All parameters are set to be the same in section 5.2.1.

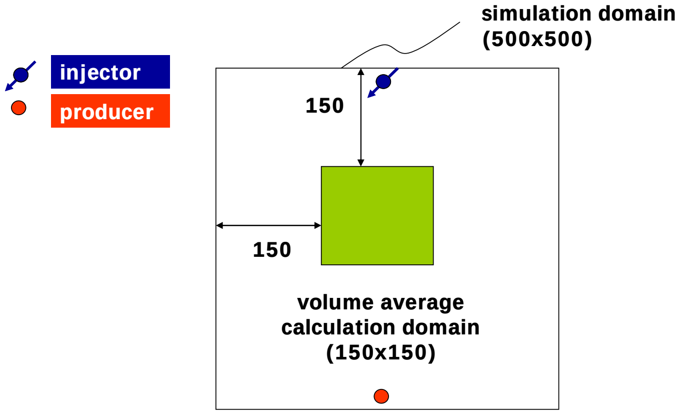

Figure 5-39: Well configuration and volume averaging domain used to study the effect of reservoir connectivity.

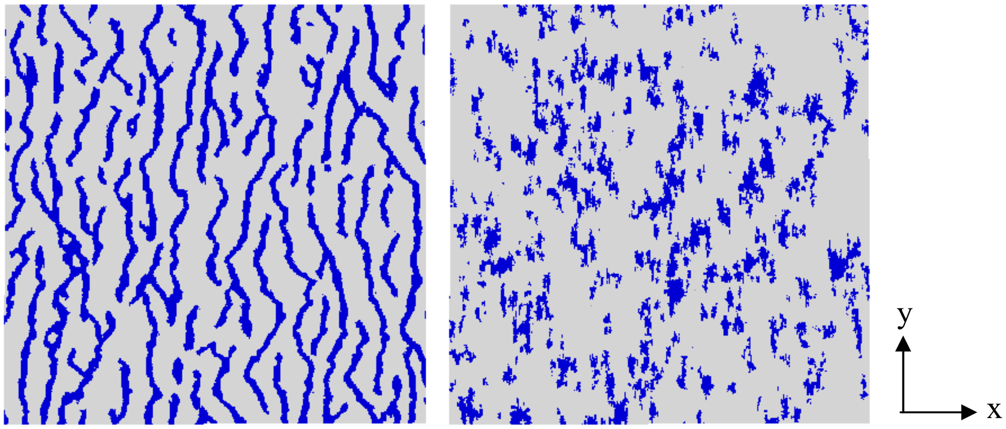

Figure 5-40: Facies maps generated using *filtersim* (left) and *sisim* (right). Grey represents facie 0, while blue represents facie 1.

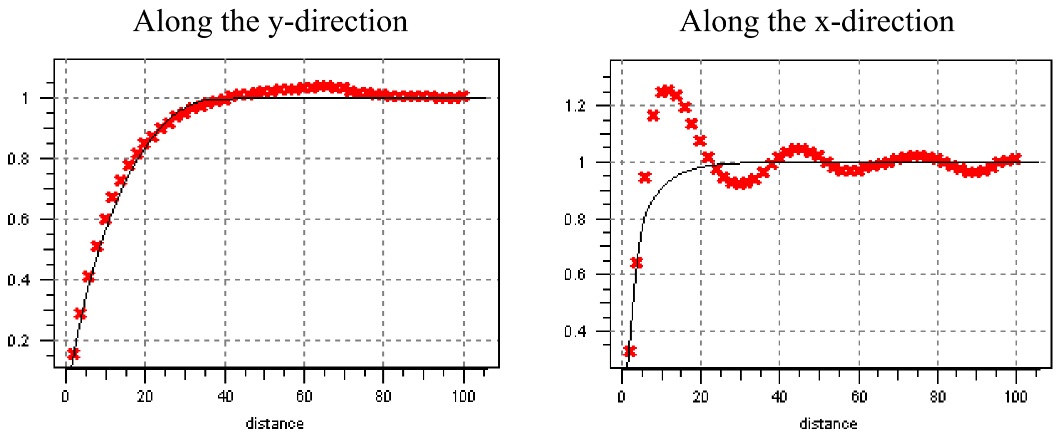

Figure 5-41: Experimental semi-variograms computed using the *filtersim* realization in Figure 5-40. An analytical variogram model is fitted and used to generate the *sisim* realization as shown in Figure 5-40.

$$0.5 * Spherical(a_{\max} = 36;\ a_{\min} = 6) + 0.5 * Exponential(a_{\max} = 24;\ a_{\min} = 18).$$

5.4.1 Moderate Contrast between Facies

Porosity (ϕ) and permeability (k) values are populated according to the facies distribution, and they are shown in Figure 5-42:

$$facies = 0 \rightarrow \begin{Bmatrix} \phi = 0.15 \\ k = 135mD \end{Bmatrix}$$

$$facies = 1 \rightarrow \begin{Bmatrix} \phi = 0.35 \\ k = 735mD \end{Bmatrix}$$

Average velocity from the fine-scale simulation is approximately 0.1 m/day. A quick calculation assuming a typical grain size of 1e-4m shows that the dimensionless group uD_p/D = (0.1)(1e-4)/(1e-6) ~ 10, indicating the process is controlled by convection and dispersion. Results after 15000 days are shown in Figure 5-42 – Figure 5-46.

The velocity and concentration maps for both models are shown in Figure 5-42 and Figure 5-43. Although the velocity and concentration deviations look quite different for the two cases, their corresponding spatial maps of K_{eff} (Figure 5-44) look alike. This is because the average velocity and concentration maps are, in fact, fairly similar for the two cases, and K_{eff} depends on the deviation quantities as well as the spatial averages. Nevertheless, similar "finger-like" patterns can be seen in both the spatial maps of C' and K_{eff} for the MPS case. Figure 5-45 and Figure 5-46 illustrate the scaling characteristics of K_{eff}, mass transfer due to convection, dispersion, and diffusion. It is interesting to note that the two models exhibit significant differences in the scaling of dispersion and diffusion (Figure 5-46). In particular, a larger amount of diffusion and dispersion can be expected when effects of complex geologic connectivity are included in the MPS model. On the other hand, mass transfer due to convection is slightly higher for the SISIM model (Figure 5-45). The combined effects of convection, diffusion, and dispersion manifest themselves in the resultant scaling of K_{eff}, which exhibit similar characteristics for both models (Figure 5-45).

The results indicate that despite the complex connectivity exhibited by the geologic model, if the contrast in flow properties between the different facies is not significant, the impact of connectivity on the scaling characteristics of different mass transfer mechanisms is subdued. In such cases, the use of sophisticated mp statistics based algorithms to represent reservoir heterogeneity might not be warranted.

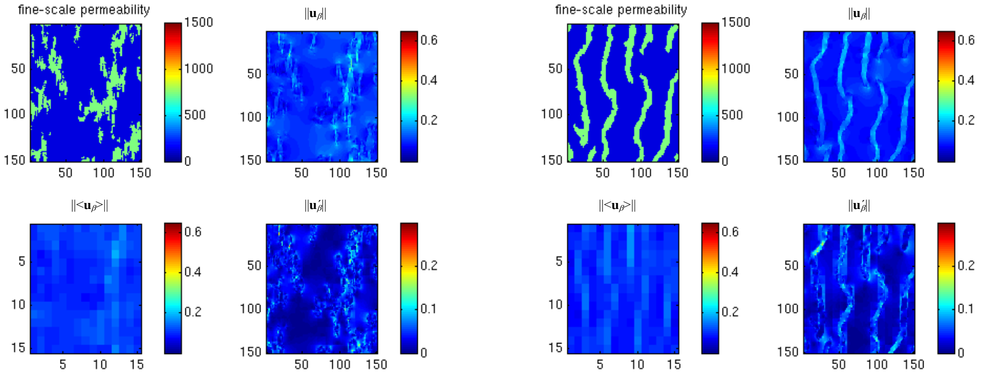

Figure 5-42: (From top left to bottom right) permeability, velocity $\mathbf{u}_\beta$, and its decomposition into average velocity $<\mathbf{u}_\beta>$ and $\mathbf{u}'_\beta$ for a coarse grid size of 10x10 (left: SISIM; right: MPS).

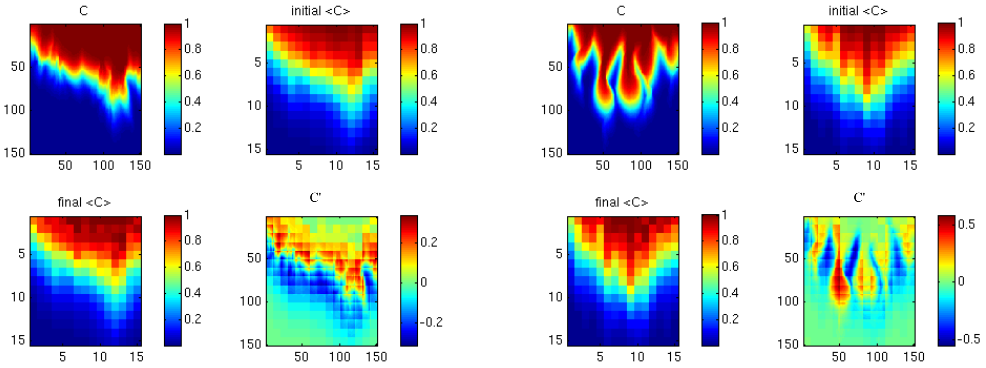

Figure 5-43: (From top left to bottom right) fine-scale concentration, average concentration <*C*> from coarse-scale simulation (initial guess before simulated annealing), final average concentration <*C*> after simulated annealing and the corresponding deviations C' for a coarse grid size of 10x10 (left: SISIM; right: MPS).

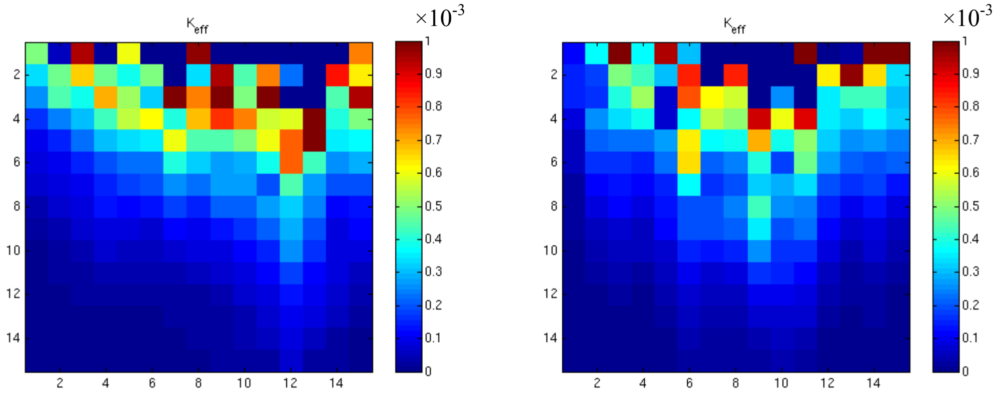

Figure 5-44: Spatial distribution of K_{eff} for a coarse grid size of 10x10 (left: SISIM; right: MPS).

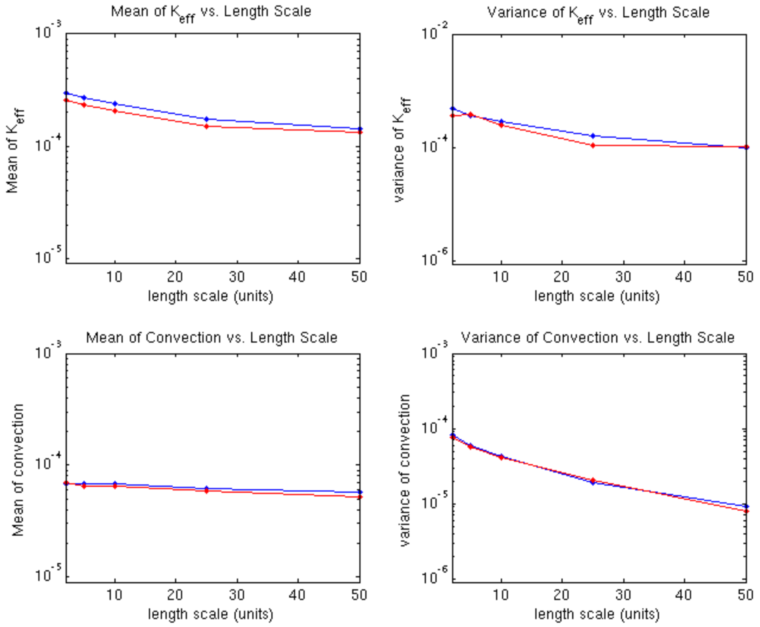

Figure 5-45: Mean and variance of K_{eff} and mass transfer due to convection as a function of length scale (blue: SISIM; red: MPS).

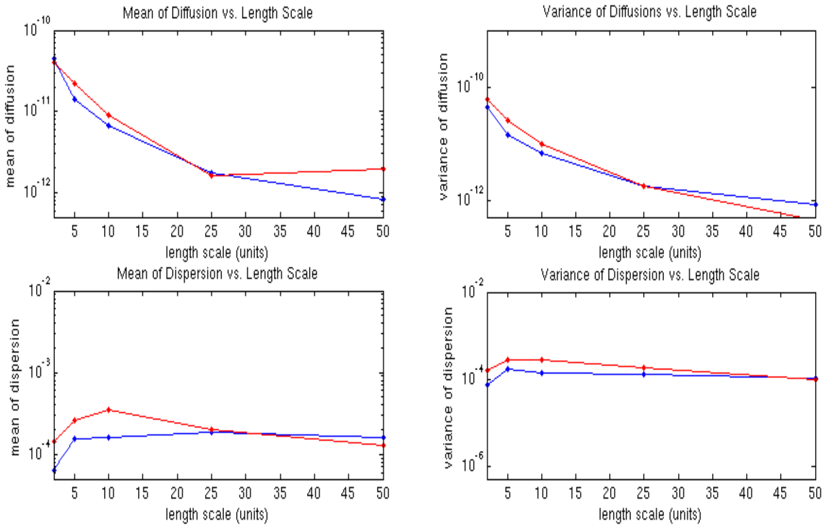

Figure 5-46: Mean and variance of mass transfer due to diffusion and dispersion as a function of length scale (blue: SISIM; red: MPS).

5.4.2 Large Contrast between Facies

In this example, a larger contrast in flow properties for the two facies will be assumed. The porosity and permeability values are populated according to:

$$facies = 0 \rightarrow \begin{Bmatrix} \phi = 0.05 \\ k = 15mD \end{Bmatrix}$$

$$facies = 1 \rightarrow \begin{Bmatrix} \phi = 0.45 \\ k = 1215mD \end{Bmatrix}$$

The facies models are the same as those shown in Figure 5-40. Average velocity from the fine-scale simulation is approximately 0.17 m/day. A quick calculation assuming a typical grain size of 1e-4m shows that the dimensionless group uD_p/D = (0.17)(1e-4)/(1e-6) ~ 17, indicating the process is controlled by convection and dispersion. Results after 10000 days are shown in Figure 5-47 – Figure 5-51. With such sharp contrasts between the two facies, more significant differences between the SISIM and MPS models become evident as observed in the velocity and concentration fields shown in Figure 5-47 and Figure 5-48. The concentration perturbation C' is more neatly organized along connected pathways in the case of the MPS model. The spatial maps of K_{eff} for the two models in Figure 5-49 also look much different as compared to the previous results (Figure 5-44). As in Figure 5-46, significant differences in scaling characteristics of dispersion and diffusion can be seen in Figure 5-51. However, as opposed to the results shown in Figure 5-45, the scaling characteristics of K_{eff} and convection shown in Figure 5-50 for the case with severe contrast between the two facies demonstrate considerable differences.

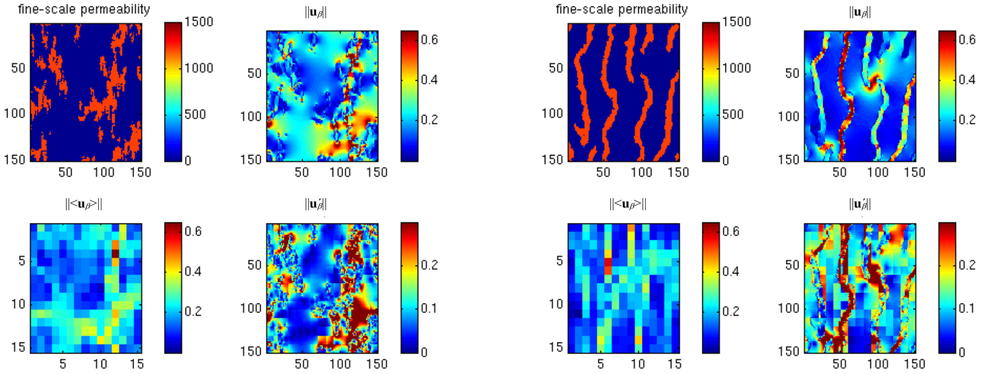

Figure 5-47: (From top left to bottom right) permeability, velocity $\mathbf{u}_\beta$, and its decomposition into average velocity $<\mathbf{u}_\beta>$ and $\mathbf{u}'_\beta$ for a coarse grid size of 10x10 (left: SISIM; right: MPS). These results are for the case with severe contrast in permeability and porosity between the two facies.

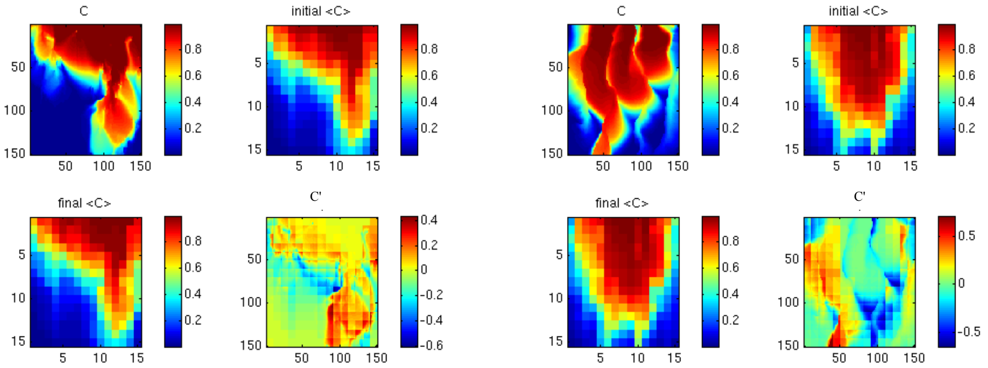

Figure 5-48: (From top left to bottom right) fine-scale concentration, average concentration <*C*> from coarse-scale simulation (initial guess before simulated annealing), final average concentration <*C*> after simulated annealing and the corresponding deviations *C'* for a coarse grid size of 10x10 (left: SISIM; right: MPS). These results are for the case with severe contrast in permeability and porosity between the two facies.

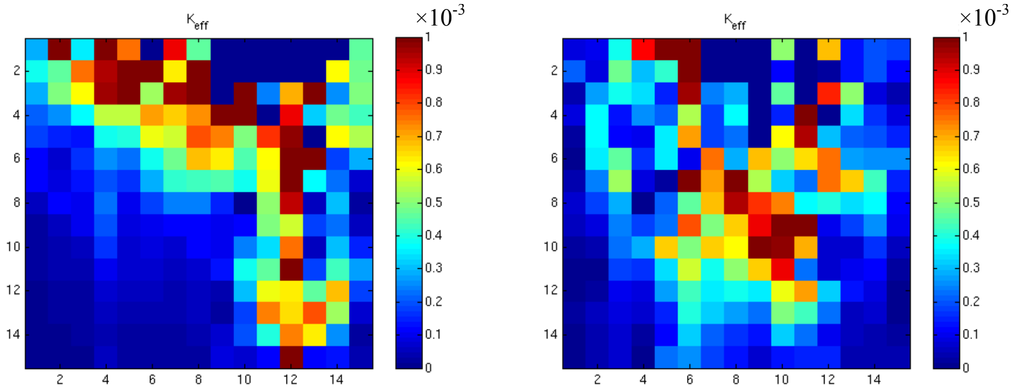

Figure 5-49: Spatial distribution of K_{eff} for a coarse grid size of 10x10 for the case with severe contrast in permeability and porosity between the two facies (left: SISIM; right: MPS).

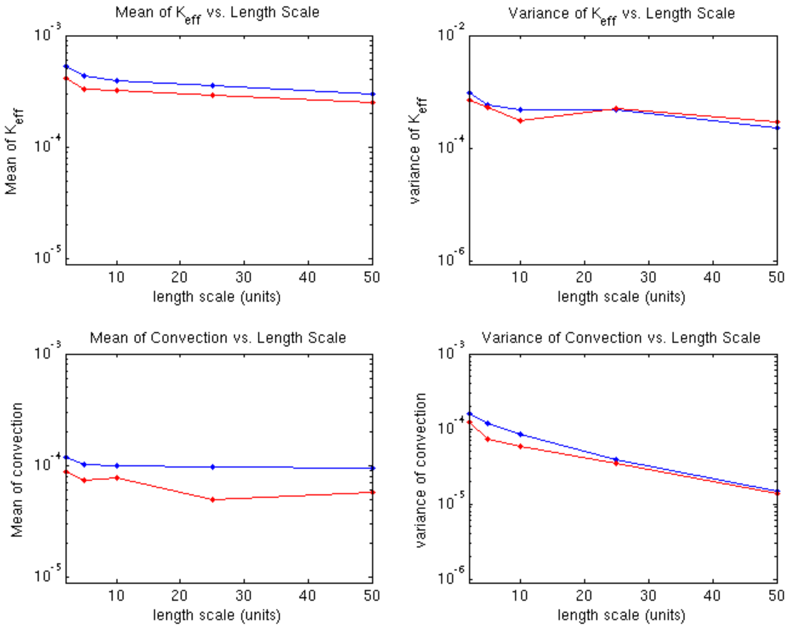

Figure 5-50: Mean and variance of K_{eff} and mass transfer due to convection as a function of length scale for the case with severe contrast in permeability and porosity between the two facies (blue: SISIM; red: MPS).

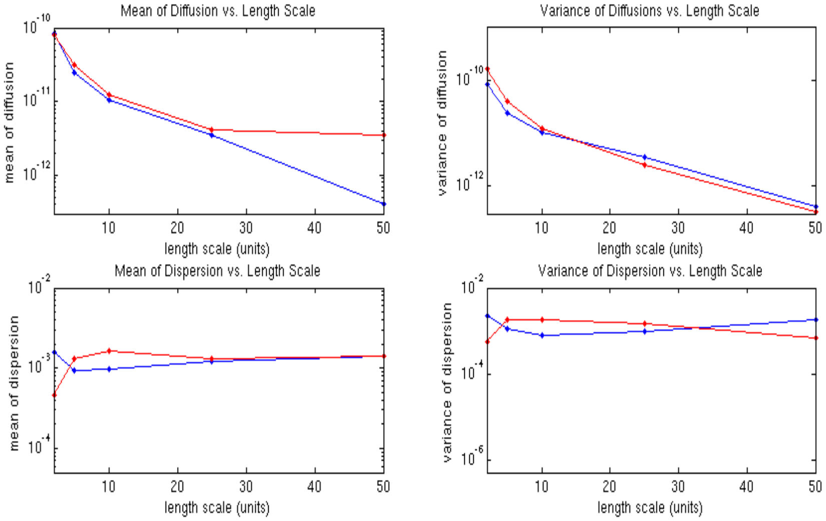

Figure 5-51: Mean and variance of mass transfer due to diffusion and dispersion for the case with severe contrast in permeability and porosity between the two facies (blue: SISIM; red: MPS).

Based on this case study, one might conclude that flow and transport tend to smooth out the effect of moderate contrasts in flow properties between reservoir facies depicting complex connectivity.

5.5 SUMMARY

Differences in scaling characteristics of effective mass transfer coefficients become apparent when scale of heterogeneity increases (e.g., longer correlation lengths or multiple-point connectivity). Scaling characteristics of K_{eff} is shown to be closely correlated to the scaling characteristics of recovery statistics. High values of K_{eff} correspond to zones that exhibit high velocity. The impacts of heterogeneity are also sensitive to the flow direction in relation to the orientation of anisotropy. In the example shown, when flow and anisotropy are oriented perpendicular to one another, the length scale of heterogeneity does not play as significant a role in the scaling characteristics of recovery. These observations suggest that scaling characteristics are functions of heterogeneity and flow patterns, meaning that additional uncertainty is introduced due to uncertainty in both the magnitude (e.g., correlation length) and orientation (e.g., direction of anisotropy) of heterogeneity. Finally, the reliability of the proposed approach is verified by comparing scaling characteristics of effective transport predicted via volume averaging to those obtained from fractal theory.

Chapter 6: A Numerical Approach to Scale-Up of Mass Transfer Equations in Multiphase Flow Using Volume Averaging

6.1 OVERVIEW

This chapter extends the mathematical formulations and concepts for scale-up of mass transfer in single-phase flow to multiphase flow. Detailed derivations of volume averaged equations accounting for dispersion, diffusion, convection, rock-fluid interactions, reactions, and inter-phase exchange are presented. Employing similar arguments as in the case of single-phase flow, we can extend the formulations to model field scale phenomena. We devise a set of volume averaged equations that can be used to integrate numerical simulation results. A detailed outline of the numerical scheme to solve the closure problems is also discussed. We demonstrate that adsorption effects in a tracer injection process can be studied using the two-phase formulation (representing rock and fluid as two phases). Another example of an active tracer partitioning between two phases is also studied.

6.2 MATHEMATICAL FORMULATION

6.2.1 Scale-Up of Transport Equations

We will begin with the pore scale formulation of the solute transport equation. Here are the major assumptions:

1. β = aqueous; σ = solid; γ = non-aqueous
2. Constant temperature
3. σ phase is rigid (not moving): $\mathbf{u}_\sigma = 0$ ($\mathbf{u}$ indicates velocity) is zero.

4. Incompressible aqueous and non-aqueous phases with no-slip $\mathbf{u}_\beta = 0$ at $A_{\beta\sigma}$ and $\mathbf{u}_\gamma = 0$ at $A_{\gamma\sigma}$ (A_{ij} represents the interface between phases i and j)
5. Concentrations in β and γ phases are coupled via the partition coefficient ($K_{\beta\gamma}$).

The governing equations for chemical species i in each phase become:

$$\begin{aligned} &\frac{\partial C_{i\beta}}{\partial t} + \nabla \cdot \left(\mathbf{u}_\beta C_{i\beta} \right) = \nabla \cdot \left(\overline{\overline{D}} \nabla C_{i\beta} \right) \\ &\frac{\partial C_{i\gamma}}{\partial t} + \nabla \cdot \left(\mathbf{u}_\beta C_{i\gamma} \right) = \nabla \cdot \left(\overline{\overline{D}} \nabla C_{i\gamma} \right) \end{aligned} \tag{6-1}$$

B.C.: $C_{i\gamma} = K_{\beta\gamma} C_{i\beta}$ at $A_{\beta\gamma}$

$\mathbf{n}_{\beta\gamma} \cdot D_\beta \nabla C_{i\beta} = \mathbf{n}_{\beta\gamma} \cdot D_\gamma \nabla C_{i\gamma}$ at $A_{\beta\gamma}$

$\mathbf{n}_{\beta\sigma} \cdot D \nabla C_{i\beta} = 0$ at $A_{\beta\sigma}$

$\mathbf{n}_{\gamma\sigma} \cdot D \nabla C_{i\gamma} = 0$ at $A_{\gamma\sigma}$

I.C: $C_{i\beta} = C_{i\beta o}(\mathbf{x})$ and $C_{i\gamma} = C_{i\gamma o}(\mathbf{x})$ at $t = 0$ and $\mathbf{x} \in \Omega$

It is important to note that $K_{\beta\gamma}$ is the partition coefficient, which couples the two governing equations at the β-γ interface. Dropping the subscript i and assuming isotropic D, we can write:

$$\begin{aligned} &\frac{\partial C_\beta}{\partial t} + \nabla \cdot \left(\mathbf{u}_\beta C_\beta \right) = \nabla \cdot \left(D_\beta \nabla C_\beta \right) \\ &\frac{\partial C_\gamma}{\partial t} + \nabla \cdot \left(\mathbf{u}_\gamma C_\gamma \right) = \nabla \cdot \left(D_\gamma \nabla C_\gamma \right) \end{aligned} \tag{6-2}$$

Equations for β and γ are exactly similar; we will therefore focus on the β equation and then write the equivalent formulations for γ directly. Following the same derivations as in single phase, we obtained the **averaged equation** and the **deviation equation**.

$$\underbrace{\varepsilon_\beta \frac{\partial \left\langle C_\beta \right\rangle^\beta}{\partial t}}_{\text{accum}} + \underbrace{\nabla \cdot \left\langle \mathbf{u}'_\beta C'_\beta \right\rangle}_{\text{dispersion}} + \underbrace{\varepsilon_\beta \left\langle \mathbf{u}_\beta \right\rangle^\beta \cdot \nabla \left\langle C_\beta \right\rangle^\beta}_{\text{convection}} =$$

$$\underbrace{\nabla \cdot \left[D_\beta \left(\varepsilon_\beta \nabla \left\langle C_\beta \right\rangle^\beta + \frac{1}{V} \int_{A_{\beta\gamma}} \mathbf{n}_{\beta\gamma} C'_\beta dA + \frac{1}{V} \int_{A_{\beta\sigma}} \mathbf{n}_{\beta\sigma} C'_\beta dA \right) \right]}_{\text{diffusion}} \tag{6-3}$$

$$\underbrace{\begin{aligned} &+\frac{1}{V} \int_{A_{\beta\gamma}} \mathbf{n}_{\beta\gamma} \cdot D \nabla C'_\beta dA + \frac{1}{V} \int_{A_{\beta\gamma}} \mathbf{n}_{\beta\gamma} \cdot \left(-\left\langle \mathbf{u}_\beta \right\rangle \left\langle C_\beta \right\rangle^\beta + D \nabla \left\langle C_\beta \right\rangle^\beta \right) dA \\ &+\frac{1}{V} \int_{A_{\beta\sigma}} \mathbf{n}_{\beta\sigma} \cdot D \nabla C'_\beta dA + \frac{1}{V} \int_{A_{\beta\sigma}} \mathbf{n}_{\beta\sigma} \cdot D \nabla \left\langle C_\beta \right\rangle^\beta dA \end{aligned}}_{\text{interfacial flux}}$$

$$\begin{aligned} &\frac{\partial C'_\beta}{\partial t} - \varepsilon_\beta^{-1} \nabla \cdot \left\langle \mathbf{u}'_\beta C'_\beta \right\rangle + \mathbf{u}_\beta \cdot \nabla C'_\beta + \mathbf{u}'_\beta \cdot \nabla \left\langle C_\beta \right\rangle^\beta = \nabla \cdot \left(D_\beta \nabla C'_\beta \right) \\ &-\varepsilon_\beta^{-1} \nabla \cdot \left[D_\beta \left(\frac{1}{V} \int_{A_{\beta\gamma}} \mathbf{n}_{\beta\gamma} C'_\beta dA + \frac{1}{V} \int_{A_{\beta\sigma}} \mathbf{n}_{\beta\sigma} C'_\beta dA \right) \right] \\ &-\varepsilon_\beta^{-1} \left(\frac{1}{V} \int_{A_{\beta\gamma}} \mathbf{n}_{\beta\gamma} \cdot D \nabla C'_\beta dA + \frac{1}{V} \int_{A_{\beta\gamma}} \mathbf{n}_{\beta\gamma} \cdot \left(-\left\langle \mathbf{u}_\beta \right\rangle \left\langle C_\beta \right\rangle^\beta + D \nabla \left\langle C_\beta \right\rangle^\beta \right) dA \right) \\ &-\varepsilon_\beta^{-1} \left(\frac{1}{V} \int_{A_{\beta\sigma}} \mathbf{n}_{\beta\sigma} \cdot D \nabla C'_\beta dA + \frac{1}{V} \int_{A_{\beta\sigma}} \mathbf{n}_{\beta\sigma} \cdot D \nabla \left\langle C_\beta \right\rangle^\beta dA \right) \end{aligned} \tag{6-4}$$

The averaged equation and the deviation equation are identical to the ones derived for the single phase case. The only difference is an additional integral because the no-slip condition no longer applies at $A_{\beta\gamma}$. An analogous equation can be written for the γ phase. The same steps as described for the single-phase case can now be implemented for the closure formulation. Defining the perturbation quantity for concentration of species in each phase in terms of the respective average concentration:

$$C'_\beta = s_\beta \left(C_\beta - \left\langle C_\beta \right\rangle^\beta \right) \text{ and } C'_\gamma = s_\gamma \left(C_\gamma - \left\langle C_\gamma \right\rangle^\gamma \right) \tag{6-5}$$

in which s_β and s_γ are two closure variables. We know that $\left\langle C_\beta \right\rangle^\beta$ and $\left\langle C_\gamma \right\rangle^\gamma$ are related through $K_{\beta\gamma}$. Assuming the accumulation term $\frac{\partial C'_\beta}{\partial t}$ is small, we can substitute expressions for C'_β and C'_γ into the deviation equation of each phase. The final form of the closure equation is:

$$\begin{aligned}
&\left[\mathbf{u}_\beta - 2D \frac{\nabla\left(C_\beta - \left\langle C_\beta \right\rangle^\beta \right)}{\left(C_\beta - \left\langle C_\beta \right\rangle^\beta \right)} \right] \cdot \nabla s_\beta = -\mathbf{u}'_\beta \cdot \frac{\nabla \left\langle C_\beta \right\rangle^\beta}{\left(C_\beta - \left\langle C_\beta \right\rangle^\beta \right)} + D \nabla^2 s_\beta \\
&+ \left[-\mathbf{u}_\beta \cdot \frac{\nabla\left(C_\beta - \left\langle C_\beta \right\rangle^\beta \right)}{\left(C_\beta - \left\langle C_\beta \right\rangle^\beta \right)} + D \frac{\nabla^2\left(C_\beta - \left\langle C_\beta \right\rangle^\beta \right)}{\left(C_\beta - \left\langle C_\beta \right\rangle^\beta \right)} \right] s_\beta \\
&- \varepsilon_\beta^{-1} \frac{D}{V\left(C_\beta - \left\langle C_\beta \right\rangle^\beta \right)} \left[\nabla \cdot \int_{A_{\beta\gamma}} \mathbf{n}_{\beta\gamma} s_\beta \left(C_\beta - \left\langle C_\beta \right\rangle^\beta \right) dA + \nabla \cdot \int_{A_{\beta\sigma}} \mathbf{n}_{\beta\sigma} s_\beta \left(C_\beta - \left\langle C_\beta \right\rangle^\beta \right) dA \right] \\
&- \varepsilon_\beta^{-1} \frac{D}{V\left(C_\beta - \left\langle C_\beta \right\rangle^\beta \right)} \left[\int_{A_{\beta\gamma}} \mathbf{n}_{\beta\gamma} \cdot \nabla \left[s_\beta \left(C_\beta - \left\langle C_\beta \right\rangle^\beta \right) \right] dA + \int_{A_{\beta\sigma}} \mathbf{n}_{\beta\sigma} \cdot \nabla \left[s_\beta \left(C_\beta - \left\langle C_\beta \right\rangle^\beta \right) \right] dA \right] \\
&- \varepsilon_\beta^{-1} \frac{D}{V\left(C_\beta - \left\langle C_\beta \right\rangle^\beta \right)} \left[\int_{A_{\beta\gamma}} \mathbf{n}_{\beta\gamma} \cdot \left(\frac{-\left\langle \mathbf{u}_\beta \right\rangle \left\langle C_\beta \right\rangle^\beta}{D} + \nabla \left\langle C_\beta \right\rangle^\beta \right) dA + \int_{A_{\beta\sigma}} \mathbf{n}_{\beta\sigma} \cdot \nabla \left\langle C_\beta \right\rangle^\beta dA \right]
\end{aligned} \tag{6-6}$$

As in the single phase case, if we ignore the accumulation term, the averaged equation can be written as:

$$\begin{aligned}
&\underbrace{\left\langle \mathbf{u}_\beta \right\rangle \cdot \nabla \left\langle C_\beta \right\rangle^\beta}_{\text{convection}} = \underbrace{-\nabla \cdot \left\langle \mathbf{u}'_\beta s_\beta \left(C_\beta - \left\langle C_\beta \right\rangle^\beta \right) \right\rangle}_{\text{velocity-dependent dispersion}} + \underbrace{D\varepsilon_\beta \nabla^2 \left\langle C_\beta \right\rangle^\beta}_{\text{diffusion}} \\
&\underbrace{\begin{aligned}
&+\nabla \cdot \left[\frac{D}{V} \int_{A_{\beta\gamma}} \mathbf{n}_{\beta\gamma} s_\beta \left(C_\beta - \left\langle C_\beta \right\rangle^\beta \right) dA + \frac{D}{V} \int_{A_{\beta\sigma}} \mathbf{n}_{\beta\sigma} s_\beta \left(C_\beta - \left\langle C_\beta \right\rangle^\beta \right) dA \right] \\
&+\frac{D}{V} \left[\int_{A_{\beta\gamma}} \mathbf{n}_{\beta\gamma} \cdot \nabla \left[s_\beta \left(C_\beta - \left\langle C_\beta \right\rangle^\beta \right) \right] dA + \int_{A_{\beta\sigma}} \mathbf{n}_{\beta\sigma} \cdot \nabla \left[s_\beta \left(C_\beta - \left\langle C_\beta \right\rangle^\beta \right) \right] dA \right] \\
&+\frac{D}{V} \left[\int_{A_{\beta\gamma}} \mathbf{n}_{\beta\gamma} \cdot \left(\frac{-\left\langle \mathbf{u}_\beta \right\rangle \left\langle C_\beta \right\rangle^\beta}{D} + \nabla \left\langle C_\beta \right\rangle^\beta \right) dA + \int_{A_{\beta\sigma}} \mathbf{n}_{\beta\sigma} \cdot \nabla \left\langle C_\beta \right\rangle^\beta dA \right]
\end{aligned}}_{\text{interfacial mass exchange}}
\end{aligned} \qquad (6\text{-}7)$$

A similar averaged equation is written for the γ phase. It should be reminded equations for β and γ phases are coupled because C_β and C_γ are in equilibrium with each other based on the partition coefficient $K_{\beta\gamma}$.

6.2.2 Implementation Details

The strategy for multiphase scale-up is also to incorporate heterogeneity effects directly into the velocity calculations with the use of a flow simulator. Similar to the single phase case, $\left\langle C_\beta \right\rangle$, $\left\langle C_\gamma \right\rangle$, s_β, and s_γ are obtained from the closure equation and the known fine-scale concentrations (also obtained from flow simulation). Based on the derivations from the previous section, the equations for β-phase are implemented as follow (exactly the same equations are written for the γ-phase):

Closure PDE:

$$\begin{aligned}
&\left[\mathbf{u}_{\beta}-2D\frac{\nabla\left(C_{\beta}-\left\langle C_{\beta}\right\rangle\right)}{\left(C_{\beta}-\left\langle C_{\beta}\right\rangle\right)}\right]\cdot\nabla s_{\beta}=-\mathbf{u}'_{\beta}\cdot\frac{\nabla\left\langle C_{\beta}\right\rangle}{\left(C_{\beta}-\left\langle C_{\beta}\right\rangle\right)}+D\nabla^{2}s_{\beta}\\
&+\left[-\mathbf{u}_{\beta}\cdot\frac{\nabla\left(C_{\beta}-\left\langle C_{\beta}\right\rangle\right)}{\left(C_{\beta}-\left\langle C_{\beta}\right\rangle\right)}+D\frac{\nabla^{2}\left(C_{\beta}-\left\langle C_{\beta}\right\rangle\right)}{\left(C_{\beta}-\left\langle C_{\beta}\right\rangle\right)}\right]s_{\beta}\\
&-\frac{D}{V\left(C_{\beta}-\left\langle C_{\beta}\right\rangle\right)}\left[\nabla\cdot\int_{A_{\beta\gamma}}\mathbf{n}_{\beta\gamma}s_{\beta}\left(C_{\beta}-\left\langle C_{\beta}\right\rangle\right)dA+\nabla\cdot\int_{A_{\beta\sigma}}\mathbf{n}_{\beta\sigma}s_{\beta}\left(C_{\beta}-\left\langle C_{\beta}\right\rangle\right)dA\right]\\
&-\frac{D}{V\left(C_{\beta}-\left\langle C_{\beta}\right\rangle\right)}\left[\int_{A_{\beta\gamma}}\mathbf{n}_{\beta\gamma}\cdot\nabla\left[s_{\beta}\left(C_{\beta}-\left\langle C_{\beta}\right\rangle\right)\right]dA+\int_{A_{\beta\sigma}}\mathbf{n}_{\beta\sigma}\cdot\nabla\left[s_{\beta}\left(C_{\beta}-\left\langle C_{\beta}\right\rangle\right)\right]dA\right]\\
&-\frac{D}{V\left(C_{\beta}-\left\langle C_{\beta}\right\rangle\right)}\left[\int_{A_{\beta\gamma}}\mathbf{n}_{\beta\gamma}\cdot\left(\frac{-\left\langle\mathbf{u}_{\beta}\right\rangle\left\langle C_{\beta}\right\rangle}{D}+\nabla\left\langle C_{\beta}\right\rangle\right)dA+\int_{A_{\beta\sigma}}\mathbf{n}_{\beta\sigma}\cdot\nabla\left\langle C_{\beta}\right\rangle dA\right]
\end{aligned}\tag{6-8}$$

Constraint – the averaged equation:

$$\begin{aligned}
&\left\langle\mathbf{u}_{\beta}\right\rangle\cdot\nabla\left\langle C_{\beta}\right\rangle=-\nabla\cdot\left\langle\mathbf{u}'_{\beta}s_{\beta}\left(C_{\beta}-\left\langle C_{\beta}\right\rangle\right)\right\rangle+D\nabla^{2}\left\langle C_{\beta}\right\rangle\\
&+\nabla\cdot\left[\frac{D}{V}\int_{A_{\beta\gamma}}\mathbf{n}_{\beta\gamma}s_{\beta}\left(C_{\beta}-\left\langle C_{\beta}\right\rangle\right)dA+\frac{D}{V}\int_{A_{\beta\sigma}}\mathbf{n}_{\beta\sigma}s_{\beta}\left(C_{\beta}-\left\langle C_{\beta}\right\rangle\right)dA\right]\\
&+\frac{D}{V}\left[\int_{A_{\beta\gamma}}\mathbf{n}_{\beta\gamma}\cdot\nabla\left[s_{\beta}\left(C_{\beta}-\left\langle C_{\beta}\right\rangle\right)\right]dA+\int_{A_{\beta\sigma}}\mathbf{n}_{\beta\sigma}\cdot\nabla\left[s_{\beta}\left(C_{\beta}-\left\langle C_{\beta}\right\rangle\right)\right]dA\right]\\
&+\frac{D}{V}\left[\int_{A_{\beta\gamma}}\mathbf{n}_{\beta\gamma}\cdot\left(\frac{-\left\langle\mathbf{u}_{\beta}\right\rangle\left\langle C_{\beta}\right\rangle}{D}+\nabla\left\langle C_{\beta}\right\rangle\right)dA+\int_{A_{\beta\sigma}}\mathbf{n}_{\beta\sigma}\cdot\nabla\left\langle C_{\beta}\right\rangle dA\right]
\end{aligned}\tag{6-9}$$

In simplified notation:

PDE: $\mathbf{a}_\beta \cdot \nabla s_\beta = b_\beta s_\beta - c_\beta + D_\beta \nabla^2 s_\beta - \alpha_\beta$ (6-10)

Constraint: $\alpha_\beta = \dfrac{\left\langle \mathbf{u}_\beta \right\rangle \cdot \nabla \left\langle C_\beta \right\rangle + \nabla \cdot \left\langle \mathbf{u}'_\beta s_\beta \left(C_\beta - \left\langle C_\beta \right\rangle \right) \right\rangle - D \nabla^2 \left\langle C_\beta \right\rangle}{\left(C_\beta - \left\langle C_\beta \right\rangle \right)}$ (6-11)

Where:

$$\mathbf{a}_\beta = \left[\mathbf{u}_\beta - 2D\mathbf{f}_\beta \right] = a_{1\beta}\mathbf{i} + a_{2\beta}\mathbf{j} + a_{3\beta}\mathbf{k} \tag{6-12}$$

$$\mathbf{f}_\beta = \frac{\nabla \left(C_\beta - \left\langle C_\beta \right\rangle \right)}{\left(C_\beta - \left\langle C_\beta \right\rangle \right)} = f_{1\beta}\mathbf{i} + f_{2\beta}\mathbf{j} + f_{3\beta}\mathbf{k} \tag{6-13}$$

$$b_\beta = \left[-\mathbf{u}_\beta \cdot \mathbf{f}_\beta + D \frac{\nabla^2 \left(C_\beta - \left\langle C_\beta \right\rangle \right)}{\left(C_\beta - \left\langle C_\beta \right\rangle \right)} \right] \tag{6-14}$$

$$c_\beta = \mathbf{u}'_\beta \cdot \frac{\nabla \left\langle C_\beta \right\rangle^\beta}{\left(C_\beta - \left\langle C_\beta \right\rangle^\beta \right)} \tag{6-15}$$

and

$$\begin{aligned}
\alpha_\beta = {} & \frac{D}{V\left(C_\beta - \left\langle C_\beta \right\rangle \right)} \left[\nabla \cdot \int_{A_{\beta\gamma}} \mathbf{n}_{\beta\gamma} s_\beta \left(C_\beta - \left\langle C_\beta \right\rangle \right) dA + \nabla \cdot \int_{A_{\beta\sigma}} \mathbf{n}_{\beta\sigma} s_\beta \left(C_\beta - \left\langle C_\beta \right\rangle \right) dA \right] \\
& + \frac{D}{V\left(C_\beta - \left\langle C_\beta \right\rangle \right)} \left[\int_{A_{\beta\gamma}} \mathbf{n}_{\beta\gamma} \cdot \nabla \left[s_\beta \left(C_\beta - \left\langle C_\beta \right\rangle \right) \right] dA + \int_{A_{\beta\sigma}} \mathbf{n}_{\beta\sigma} \cdot \nabla \left[s_\beta \left(C_\beta - \left\langle C_\beta \right\rangle \right) \right] dA \right] \\
& + \frac{D}{V\left(C_\beta - \left\langle C_\beta \right\rangle \right)} \left[\int_{A_{\beta\gamma}} \mathbf{n}_{\beta\gamma} \cdot \left(\frac{-\left\langle \mathbf{u}_\beta \right\rangle \left\langle C_\beta \right\rangle}{D} + \nabla \left\langle C_\beta \right\rangle \right) dA + \int_{A_{\beta\sigma}} \mathbf{n}_{\beta\sigma} \cdot \nabla \left\langle C_\beta \right\rangle dA \right]
\end{aligned} \tag{6-16}$$

6.2.3 Numerical Scheme

The following procedure was adopted to implement the above formulations:

1. Generate a fine-scale heterogeneous reservoir model (porosity and permeability) for a section of the reservoir and subject to flow simulation to obtain $\mathbf{u}_\beta$, $\mathbf{u}_\gamma$, C_β, and C_γ. This is referred to as the simulation domain.
2. Perform flow-based upscaling of reservoir permeability at various coarse scales and subject each to flow simulation to obtain $\langle \mathbf{u}_\beta \rangle$, $\langle \mathbf{u}_\gamma \rangle$, and initial estimates of $\langle C_\beta \rangle$, and $\langle C_\gamma \rangle$ at different coarse scales.
3. Choose a sub-domain for volume averaging calculations to avoid boundary effects due to wells.
4. At each averaging scale, make small adjustments to $\langle C_\beta \rangle$ and $\langle C_\gamma \rangle$ using a simulated annealing scheme such that the left and right hand sides of equations (6-10) and (6-11) are matched. First, the two equations can be rearranged into the following simplified form:

   Closure PDE: $\mathbf{a}_\beta \cdot \nabla s_\beta = b_\beta s_\beta - c_\beta + D_\beta \nabla^2 s_\beta - \alpha_\beta$ (6-17)

   Averaged equation: $\alpha_\beta = \dfrac{\langle \mathbf{u}_\beta \rangle \cdot \nabla \langle C_\beta \rangle + \nabla \cdot \langle \mathbf{u}'_\beta s_\beta \left(C_\beta - \langle C_\beta \rangle \right) \rangle - D \nabla^2 \langle C_\beta \rangle}{\left(C_\beta - \langle C_\beta \rangle \right)}$ (6-18)

   Procedure for simulated annealing:

   a. Initialize with $\langle C_\beta \rangle$ and $\langle C_\gamma \rangle$ from coarse-scale simulations

   b. $C'_\beta = C_\beta - \langle C_\beta \rangle$ and $C'_\gamma = C_\gamma - \langle C_\gamma \rangle$

      $s_\beta = 1$ and $s_\gamma = 1$

   c. Compute α_β and α_γ

   d. Compute error $\varepsilon = |\varepsilon_\beta| + |\varepsilon_\gamma|$

$\varepsilon_\beta = D\nabla^2 s_\beta + b_\beta s_\beta - \mathbf{a}_\beta \cdot \nabla s_\beta - c_\beta - \alpha_\beta$ – by rearranging equation (6-17)

$\varepsilon_\gamma = D_\gamma \nabla^2 s_\gamma + b_\gamma s_\gamma - \mathbf{a}_\gamma \cdot \nabla s_\gamma - c_\gamma - \alpha_\gamma$

e. If ε is more than tolerance, update $\left\langle C_\beta \right\rangle^{new}$

$\left\langle C_\beta \right\rangle^{new} = \left\langle C_\beta \right\rangle \pm 1\% \left\langle C_\beta \right\rangle$

$\left\langle C_\gamma \right\rangle^{new} = K_{\beta\gamma} \left\langle C_\beta \right\rangle^{new}$

Note that $K_{\beta\gamma}$ is coupling $\left\langle C_\gamma \right\rangle$ and $\left\langle C_\beta \right\rangle$. Repeat steps b) – d)

f. Accept or reject the new guess → if accepted: $\left\langle C_\beta \right\rangle = \left\langle C_\beta \right\rangle^{new}$ and $\left\langle C_\gamma \right\rangle = \left\langle C_\gamma \right\rangle^{new}$

5. Repeat Step 4 for all averaging length scales
6. Evaluate the following as a function of averaging scale:
   a. Mass transfer due to convection: $\left\langle \mathbf{u}_\beta \right\rangle \cdot \nabla \left\langle C_\beta \right\rangle$ and $\left\langle \mathbf{u}_\gamma \right\rangle \cdot \nabla \left\langle C_\gamma \right\rangle$
   b. Mass transfer due to dispersion: $\nabla \cdot \left\langle \mathbf{u}'_\beta s_\beta \left(C_\beta - \left\langle C_\beta \right\rangle \right) \right\rangle$ and $\nabla \cdot \left\langle \mathbf{u}'_\gamma s_\gamma \left(C_\gamma - \left\langle C_\gamma \right\rangle \right) \right\rangle$
   c. Mass transfer due to diffusion: $D\nabla^2 \left\langle C_\beta \right\rangle$ and $D\nabla^2 \left\langle C_\gamma \right\rangle$
   d. Effective mass transfer across the β–γ, β–σ and γ–σ interfaces (given by the integrals in equation (6-16): $\alpha_\beta \left(C_\beta - \left\langle C_\beta \right\rangle \right)$ and $\alpha_\gamma \left(C_\gamma - \left\langle C_\gamma \right\rangle \right)$
   e. Effective mass transfer coefficients in each of β and γ phases: $K_{eff,\beta}$ and $K_{eff,\gamma}$ are defined as follow (recall that C_{max} is the solute concentration at injection conditions):
      $\left\langle \mathbf{u}_\beta \right\rangle \cdot \nabla \left\langle C_\beta \right\rangle = K_{eff\,\beta} \left(C_{\max} - \left\langle C_\beta \right\rangle \right)$ and $\left\langle \mathbf{u}_\gamma \right\rangle \cdot \nabla \left\langle C_\gamma \right\rangle = K_{eff\,\gamma} \left(C_{\max} - \left\langle C_\gamma \right\rangle \right)$

The finite difference discretization of each closure equation is the same as in the single-phase case.

6.3 EXAMPLE 1 – TRANSPORT WITH ADSORPTION

Single-phase flow with adsorption can be formulated as transport between two phases: fluid (β) and solid (σ) (in this case, γ is treated as a residual phase, and the volume averaged equations are formulated for the β and σ phases instead). Since the solid grains are stationary, $\mathbf{u}_{\sigma} = 0$. Consider a tracer injection process in a 500x500 2-D fine grid model. The grid blocks are of uniform size ($\Delta x = \Delta y = 10$m) with a thickness of 10m. An injector is placed at the top left corner and a producer is located at the bottom right corner. Injection and production rates are held constant at 1000 sm^3/day. A passive tracer is added to the injection stream at a concentration of 1mg/m^3.

D = 1e-6 m^2/day (fine-scale diffusion)
P = 280 bar (Initial average reservoir pressure)
Q = 1000 sm^3/day

Figure 6-1 illustrates the simulation and volume average calculation configuration. To investigate the effects of heterogeneity, we will again focus on Case A and Case B from Chapter 5 (Figure 5-1 and Figure 5-2). The adsorption isotherm is shown in Figure 6-2. Average velocity from the fine-scale simulation is approximately 0.15 m/day. A quick calculation assuming a typical grain size of 1e-4m shows that the dimensionless group uD_p/D = (0.15)(1e-4)/(1e-6) ~ 15, indicating the process is controlled by convection, dispersion, and interfacial transport (through the adsorption mechanism).

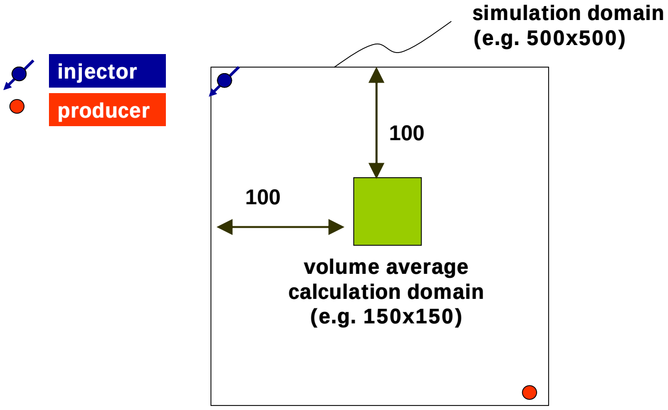

Figure 6-1: Set-up of simulation and volume averaging calculation domains to study the effects of adsorption in single-phase flow.

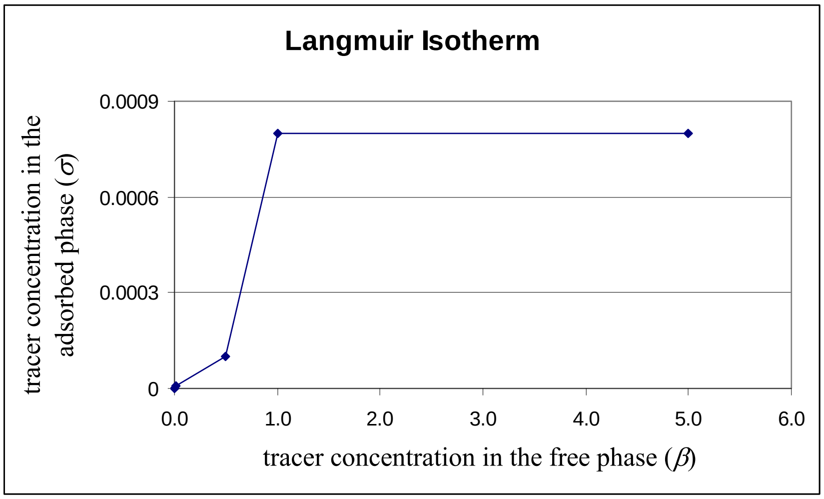

Figure 6-2: Langmuir isotherm for adsorption of tracer (rock density = 2300 kg/m^3).

The fine scale flow simulation was set up with the parameters as above and with the Langmuir adsorption isotherm. Flow based upscaling of permeability was performed at various length scales in order to get the average velocities and concentrations. It is to be noted that in this problem there are only two phases: β and σ. Results after 30000 days are shown in Figure 6-3 – Figure 6-6. Figure 6-3 shows the maps of permeability and velocity magnitude over the volume averaging domain for a coarse grid size of 10x10. Significant smoothing is observed comparing the average velocity $||<\mathbf{u}_\beta>||$ to the fine-scale velocity $||\mathbf{u}_\beta||$. Figure 6-4 shows the corresponding concentration maps. Figure 6-5 shows the spatial distribution of absolute value of K_{eff} for β phase. Since the velocity in σ (solid) phase is zero, K_{eff} is zero for the σ phase.

Adsorption is more in regions of high permeability because of larger flux of adsorbing material β. Consequently, higher values of K_{eff} are observed for the model with longer correlation length and when the flow is aligned with the direction of anisotropy. However, this also causes much less mass of phase β adsorbed in regions of low permeability thereby leading to additional variability in K_{eff}.

By repeating the volume averaging calculations for different coarse grid sizes, we can study the scaling relationships of K_{eff}. Figure 6-6 shows the scaling relationship (spatial mean and standard deviation) of the absolute values of upscaled permeability, $K_{eff\,\beta}$, and mass transfer by convection in the β phase as a function of averaging scale for both the long and short correlation length models (recall that transport is controlled by both convection and adsorption in this case). It should be noted that $K_{eff\,\sigma}$ and mass transfer by convection are zero for the σ phase. The models constrained to longer correlation length exhibit higher mean and variability.

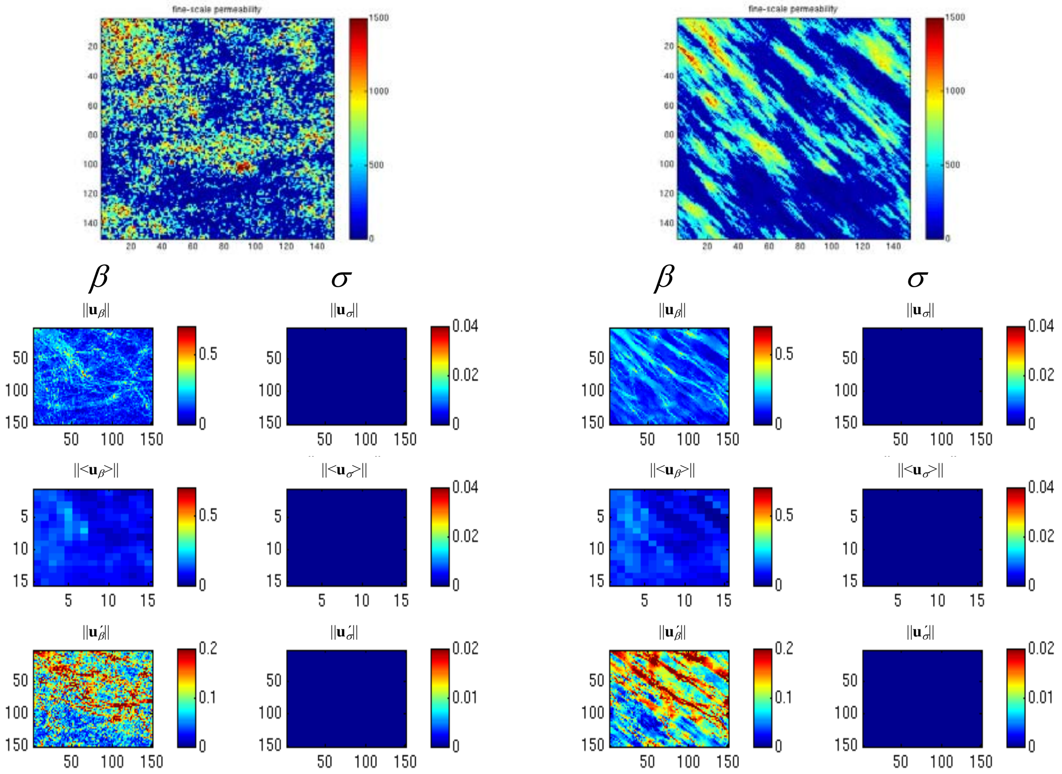

Figure 6-3: (From top to bottom) permeability, velocity **u**, and its decomposition into average velocity <**u**> and **u**' for a coarse grid size of 10x10 (left: Case A; right: Case B). These results are for the case with adsorption effects.

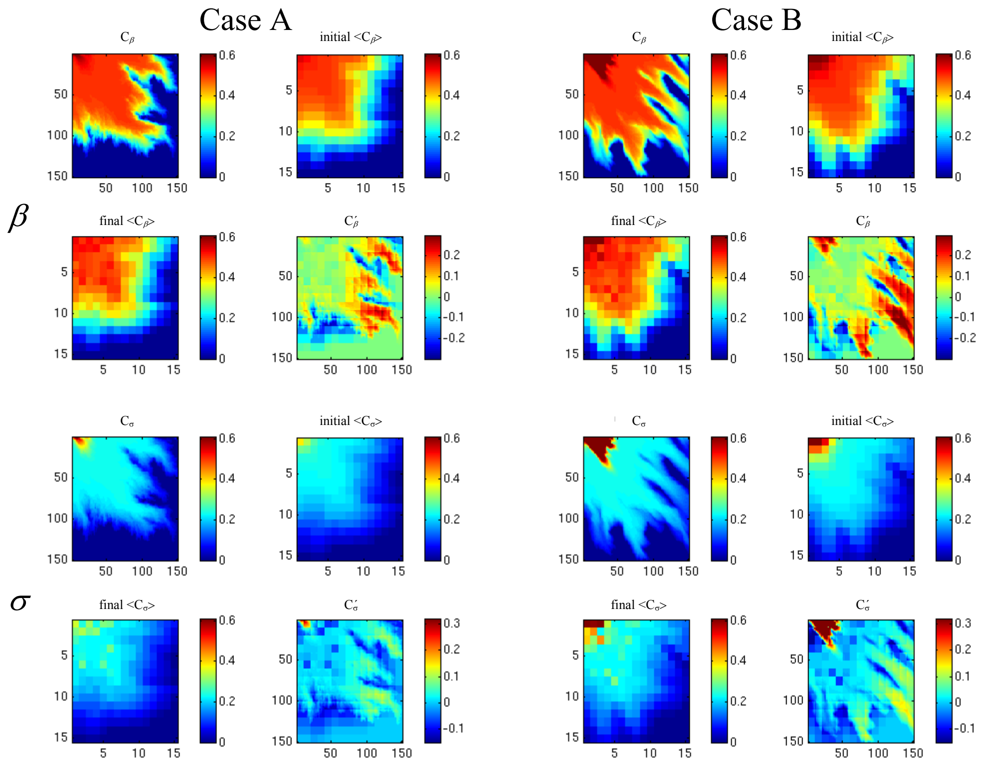

Figure 6-4: (From top left to bottom right) fine-scale concentration *C*, average concentration <*C*> from coarse-scale simulation (initial guess before simulated annealing), final average concentration <*C*> after simulated annealing and the corresponding deviations *C*' for a coarse grid size of 10x10 (left: Case A; right: Case B). These results are for the case with adsorption effects.

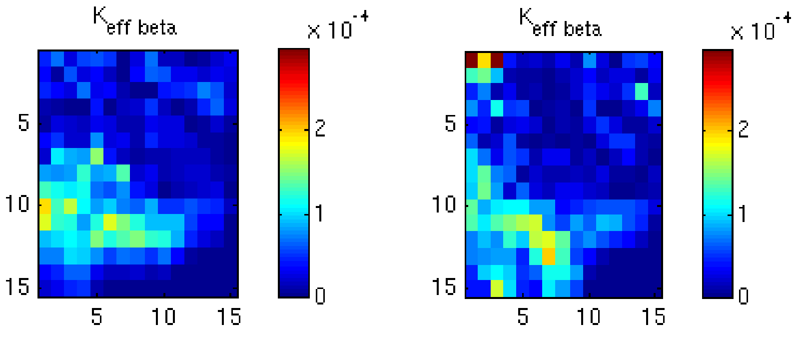

Figure 6-5: Spatial distribution of $K_{eff\,\beta}$ for a coarse grid size of 10x10 (left: Case A; right: Case B) for the case with adsorption effects. Note that $K_{eff\,\sigma}$ is zero everywhere because $\mathbf{u}_\sigma = 0$.

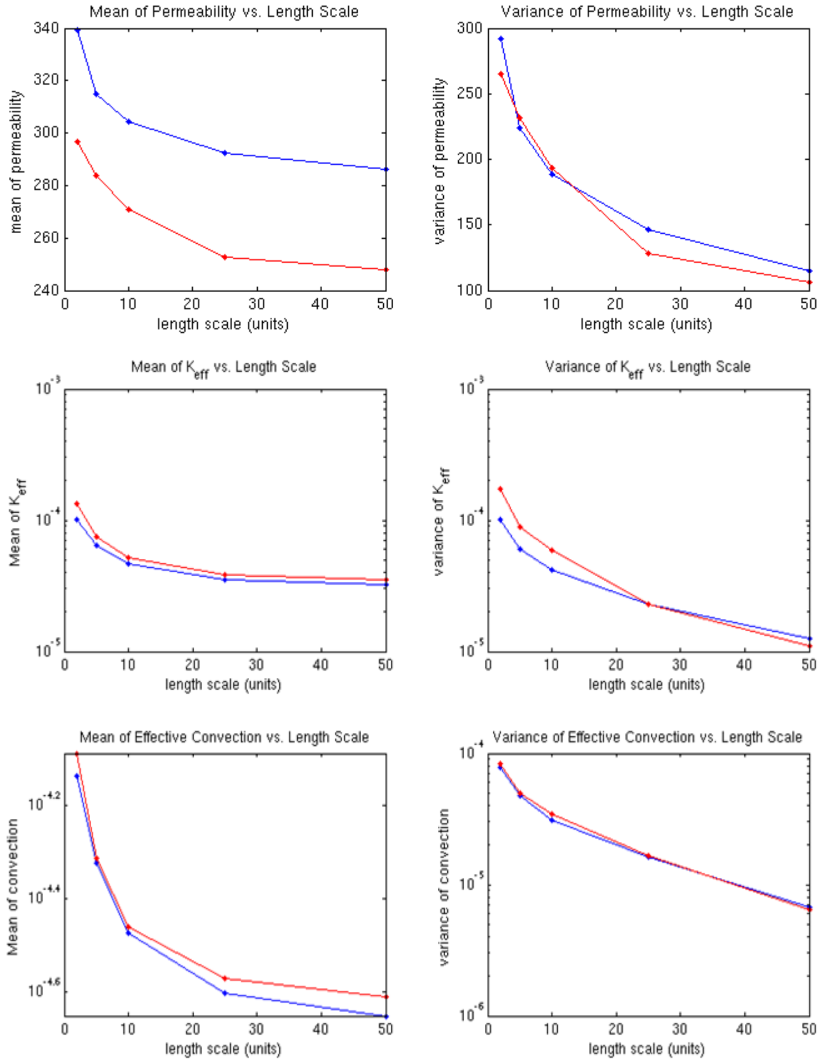

Figure 6-6: Mean and variance of permeability, $K_{eff\,\beta}$, and mass transfer due to convection in β phase (blue: Case A; red: Case B) for the case with adsorption effects.

6.4 EXAMPLE 2 – FLOW OF MULTIPLE FLUID PHASES

In this section, the partitioning of tracer across two fluid phases during an immiscible displacement process is studied: oil (γ) is displaced by water (β). A base case where dispersion controls mass transfer is first described. This is followed by a case where mass transfer is controlled by interfacial transport and diffusion.

6.4.1 Base Case

Consider a tracer injection process in a 500x500 2-D fine grid model. The grid blocks are of uniform size ($\Delta x = \Delta y = 10$m) with a thickness of 10m. A water injector is placed at the top left corner and a producer is located at the bottom right corner. Injection and production rates are held constant at 1000 sm^3/day. A passive tracer is added to the injected water at a concentration of 1mg/m^3. The initial oil and water saturations are above the irreducible saturations (S_{wr} = 0.145 and S_{or} = 0.205), hence both the fluid phases are mobile.

D = 1e-6 m^2/day (fine-scale diffusion)

P = 280 bar (initial average reservoir pressure)

S_{wi} = 0.25 (initial water saturation)

Q = 1000 sm^3/day

Constant $K_{\beta\gamma}(P) = 1$

ρ_w = 1000 kg/m^3 and ρ_o = 850 kg/m^3 (at P = 280 bar)

PVT properties of water:

B_w = 1.0; c_w = 4.6e-5 bar^{-1}; μ_w = 0.34 cp (at P = 280 bar)

PVT properties of oil:

B_o = 1.0; c_o = 1.25e-5 bar^{-1}; μ_o = 0.47 cp (at P = 280 bar)

The water-oil relative permeability (kr) and capillary pressure (Pc) curves are shown in Figure 6-7. Figure 6-8 illustrates the simulation and volume average calculation configuration. To investigate the effects of heterogeneity, we will again focus on two cases, one with long and the other with short correlation length, the same as Case A and Case B from Chapter 5.

To scale-up relative permeability curves, a procedure assuming capillary equilibrium outlined by Pickup and Stephen (2000) is adopted. In their approach, single-phase steady-state simulations are performed separately on the oil and water phase permeabilities (obtained at capillary pressure equilibrium conditions), and then the effective phase permeabilities to each phase are calculated; hence no two-phase flow simulations are required. Since fine-scale two-phase flow solutions are available in our case, the method is slightly modified as follows:

1. Calculate the average saturations in each coarse block, using arithmetic averaging.
2. Obtain fine-scale effective permeability of each phase by multiplying relative permeability with absolute permeability: $k_{eff,j} = k_{rj}\left(S_j\right) \times k$.
3. Perform flow based upscaling of effective permeability of each phase assuming the flow of only that phase.
4. Divide scaled-up effective permeability by scaled-up absolute permeability to obtain scaled-up relative permeability of each phase.

Scaled-up relative permeabilities for a coarse grid size of 10x10 are shown in Figure 6-9. Only one set of fine-scale relative permeability curves is used for all porosity and permeability values (or rock types), the scaled-up relative permeabilities appear to match well with the fine-scale relative permeabilities (indicated by the black curves); same observation is made with other coarse grid sizes. As a result, it is decided that the same set of relative permeability curves would be used for all scales. More rigorous dynamic upscaling methods such as Kyte & Berry and weighted dynamic psuedos (Stone, 1991) might give more accurate results. However, Pickup and Stephen (2000) pointed out that dynamic methods are not general (different pseudos are required for different flow rates and flood directions). Since we are interested in scale-up of mass transfer instead of flow functions in multiphase flow, dynamic upscaling of relative permeabilities was not performed. However, the volume averaging procedure is flexible such that dynamic upscaling techniques can be easily integrated if necessary.

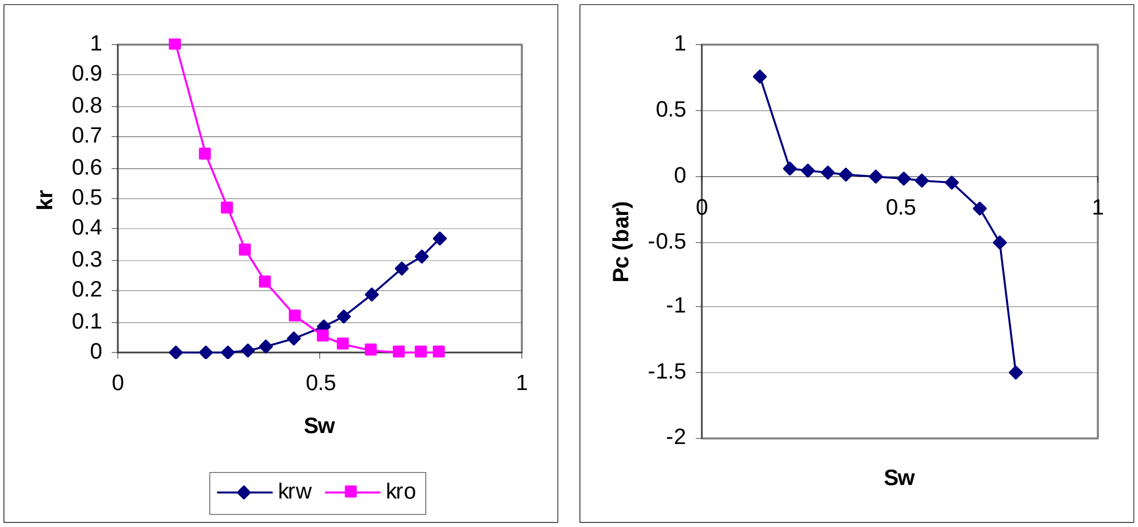

Figure 6-7: Water-oil relative permeability and capillary pressure as a function of water saturation.

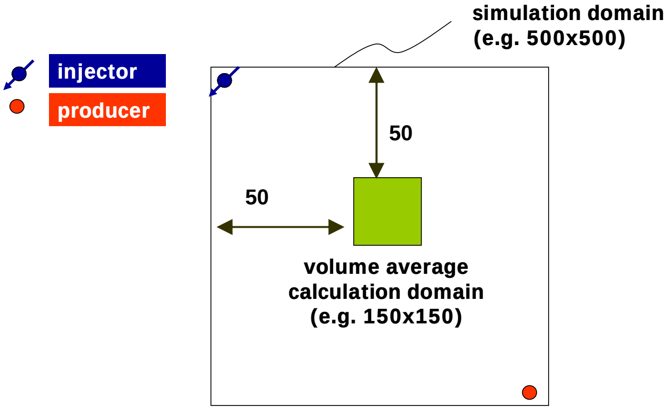

Figure 6-8: Set-up of simulation and volume averaging calculation domains for the case where water immiscibly displaces oil.

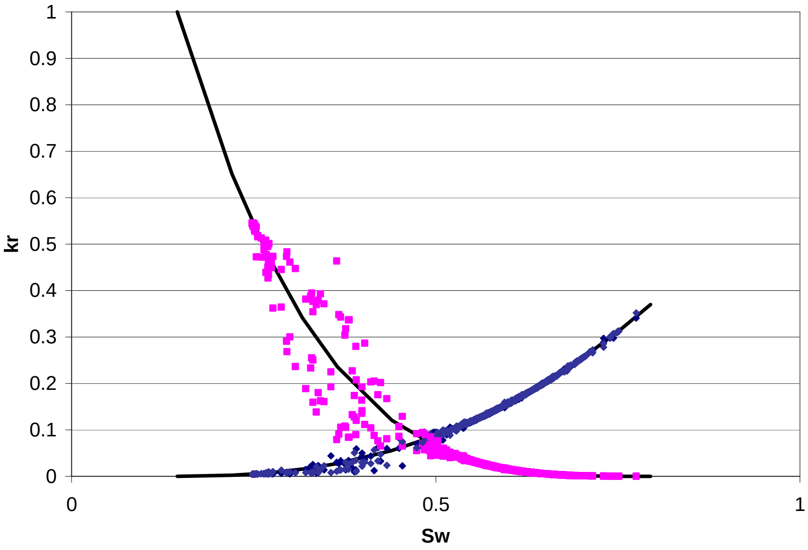

Figure 6-9: Scaled-up water-oil relative permeability for a coarse grid of 10x10 (pink: oil; blue: water). The black curves represent the original fine-scale relative permeabilities.

Average velocity from the fine-scale simulation is approximately 0.3 m/day and 0.02 m/day for u_β and u_γ, respectively. A quick calculation assuming a typical grain size of 1e-4m shows that the dimensionless group $u_\beta D_p/D$ = (0.3)(1e-4)/(1e-6) ~ 30 and

$u_\gamma D_p/D$ = (0.02)(1e-4)/(1e-6) ~ 2, suggesting tracer transport within each phase is dominated by convection and dispersion.

Results after 6000 days are shown in Figure 6-10 – Figure 6-15. Figure 6-10 shows the maps of permeability and velocity magnitude over the volume averaging domain for a coarse grid size of 10x10. Figure 6-10 shows that the displacing phase (water – β) has a much higher velocity compared to the displaced phase (oil – γ). The concentration maps for β and γ phases in Figure 6-11 look identical because the inter-phase partition coefficient ($K_{\beta\gamma}$) equals one. Figure 6-12 shows the spatial distribution of absolute value of K_{eff} for both β and γ phases. Different values of K_{eff} are obtained in β and γ phases because K_{eff} represents the mass transfer of tracer within each phase. Higher magnitude and variability are observed in the case where the permeability field exhibits long correlation length. It should be noted that K_{eff} is not defined at locations close to the injection when ($C_{\max}$ – $<C>$) is approximately zero or at locations far ahead of the displacement front not yet reached by the tracer (C is zero); therefore, highest values of K_{eff} for both phases appear to be localized along the saturation front as shown in the water saturation profile in Figure 6-12. Finally, given that values of $\mathbf{u}_\gamma$ are much smaller than those of $\mathbf{u}_\beta$, absolute values of $K_{eff\,\gamma}$ are much lower than those of $K_{eff\,\beta}$.

As we repeat the volume averaging calculations at different coarse grid sizes, we can study the scaling relationships of K_{eff} as well as all the different transport mechanisms. Figure 6-13 and Figure 6-14 show the scaling relationship (spatial mean and standard deviation) of the absolute values of K_{eff} and mass transfer due to convection for β and γ phase, respectively. More correlated models exhibit higher mean and variability. Figure 6-15 shows the effective mass transfer due to dispersion and interfacial transport as a function of averaging scale for both models. Just as in the single phase case, the contribution of dispersion increases with scale. Significant differences in effective dispersion are observed between the β and γ phases because of the differences in phase velocities.

It is interesting to note that the scaling characteristics of dispersion and inter-phase transport resemble closely each other. From the averaged equation, the inter-phase transport equals $\left\langle \mathbf{u}_\beta \right\rangle \cdot \nabla \left\langle C_\beta \right\rangle + \nabla \cdot \left\langle \mathbf{u}'_\beta s_\beta \left(C_\beta - \left\langle C_\beta \right\rangle \right) \right\rangle - D \nabla^2 \left\langle C_\beta \right\rangle$. When the diffusion term becomes negligible, and if mass transfer due to convection is small compared to the mass transfer due to dispersion, (see Figure 6-13 through Figure 6-15), inter-phase transport would be similar to the dispersion mass transfer. On the other hand, if the diffusion term becomes significant, the inter-phase transport would be much different from the mass transfer due to either diffusion or dispersion.

Figure 6-16 shows the scaling of tracer recovery and breakthrough for the two heterogeneous models. The higher correlation length model exhibits higher mean and variance of K_{eff} and recovery at all length scales investigated. Again, just as in single phase flow, the scaling of tracer recovery closely resembles that of K_{eff}.

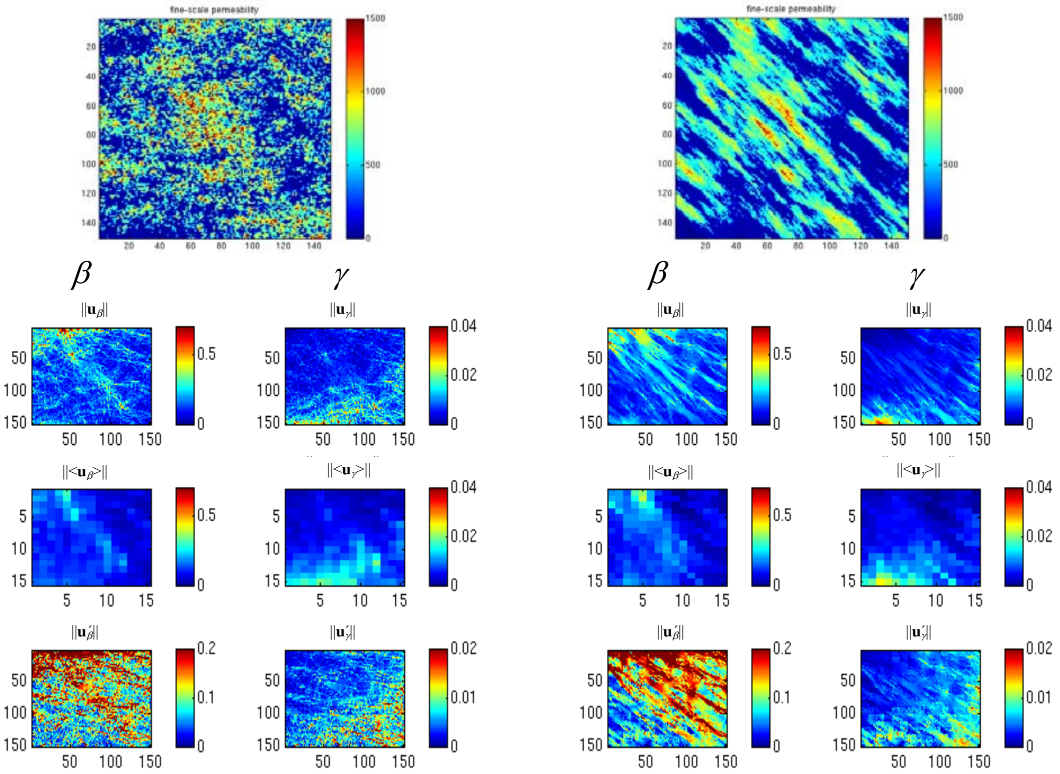

Figure 6-10: (From top to bottom) permeability, velocity **u**, and its decomposition into average velocity <**u**> and **u**' for a coarse grid size of 10x10 (left: Case A; right: Case B). These results are for tracer transport from water phase (β) to oil phase (γ).

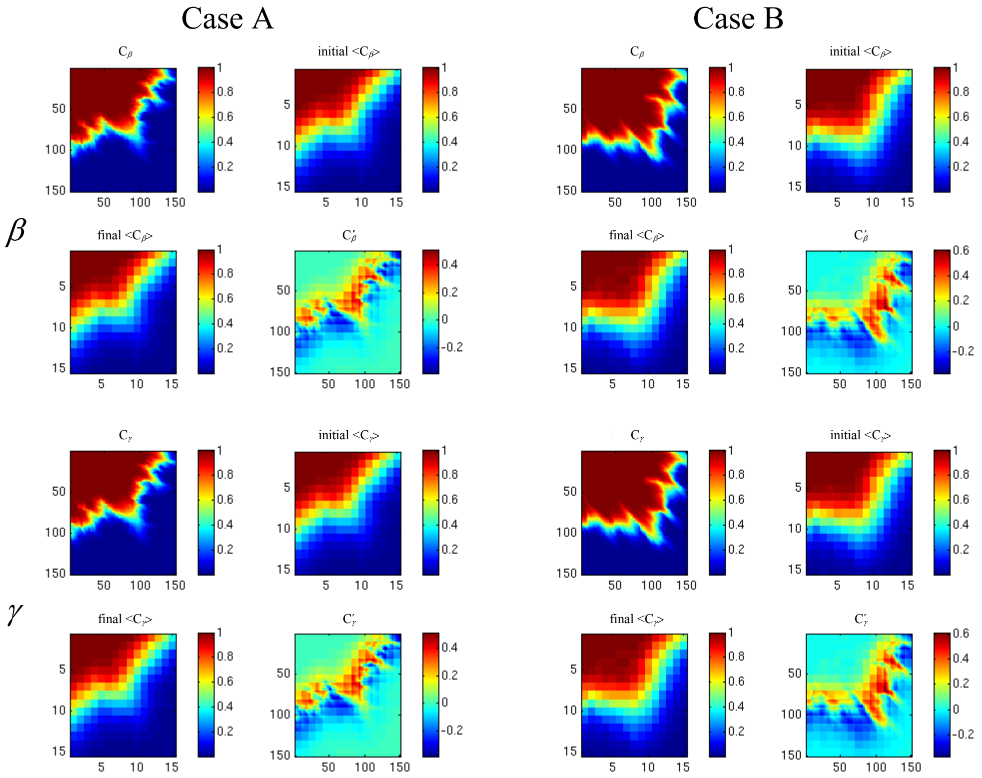

Figure 6-11: (From top left to bottom right) fine-scale concentration *C*, average concentration <*C*> from coarse-scale simulation (initial guess before simulated annealing), final average concentration <*C*> after simulated annealing and the corresponding deviations *C*' for a coarse grid size of 10x10 (left: Case A; right: Case B). These results are for tracer transport from water phase (β) to oil phase (γ).

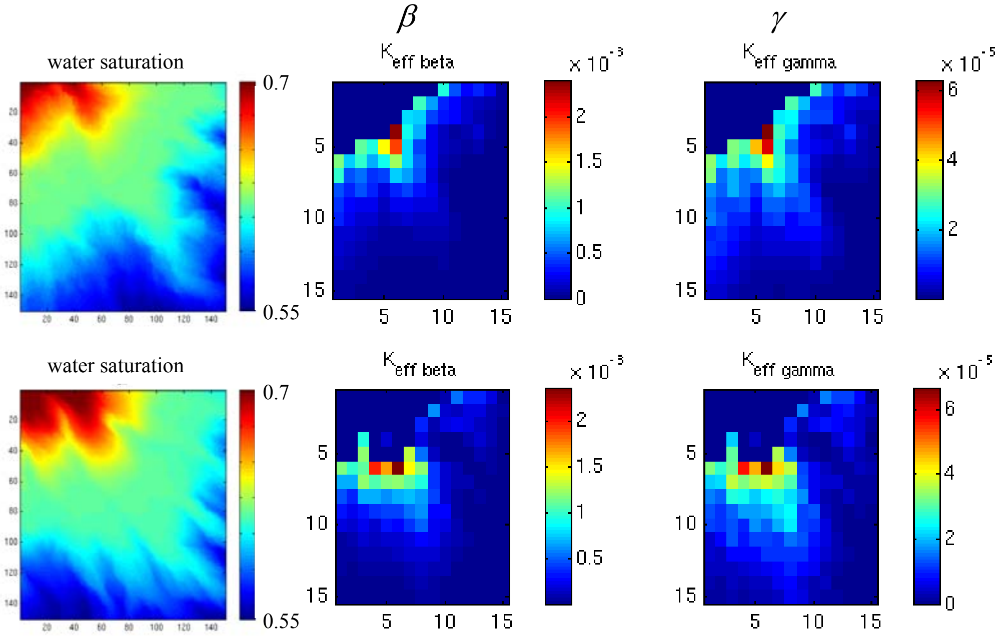

Figure 6-12: Water saturation map and spatial distribution of K_{eff} for a coarse grid size of 10x10 (top: Case A; bottom: Case B) for the case of tracer transport from water phase (β) to oil phase (γ). Note the localization of K_{eff} along the saturation front shown on the left.

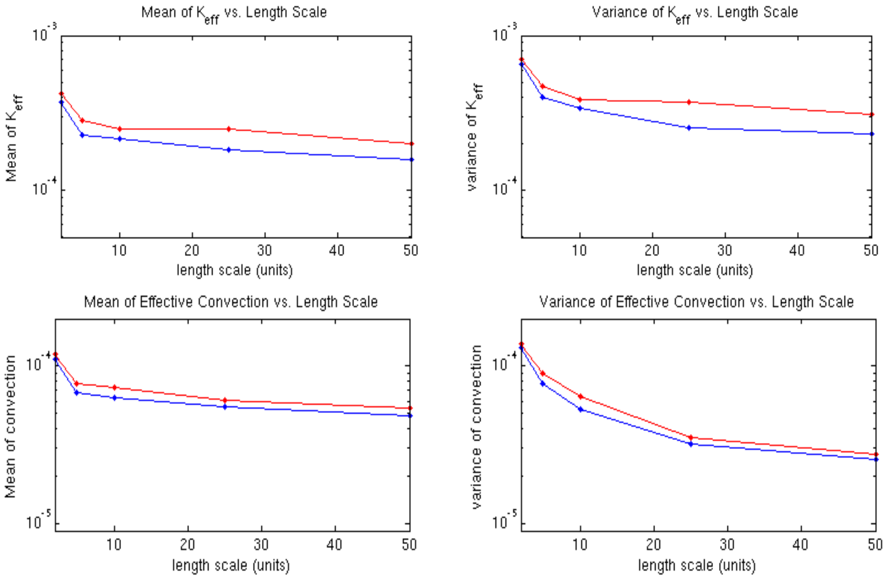

Figure 6-13: Mean and variance of $K_{eff\,\beta}$ and mass transfer due to convection in β phase (blue: Case A; red: Case B) for the case of tracer transport from water phase (β) to oil phase (γ).

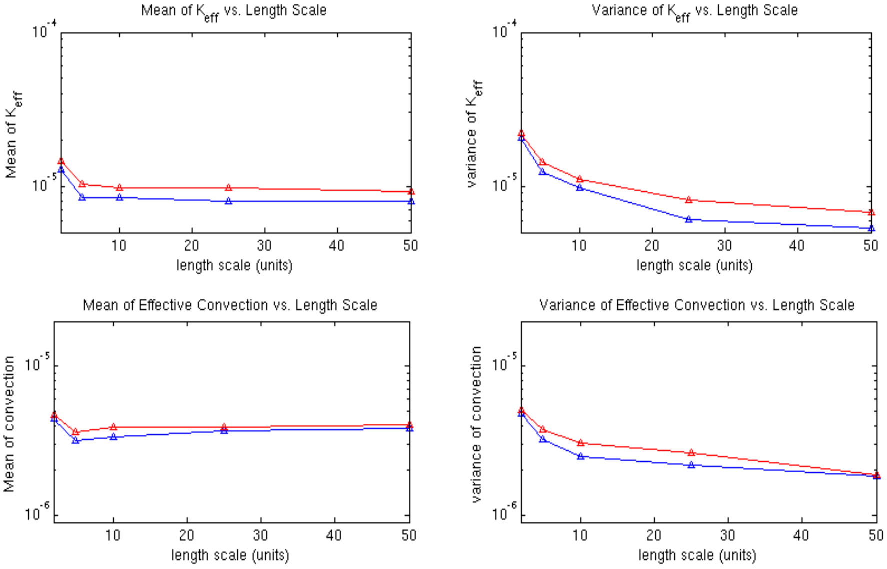

Figure 6-14: Mean and variance of $K_{eff\,\gamma}$ and mass transfer due to convection in γ phase (blue: Case A; red: Case B) for the case of tracer transport from water phase (β) to oil phase (γ).

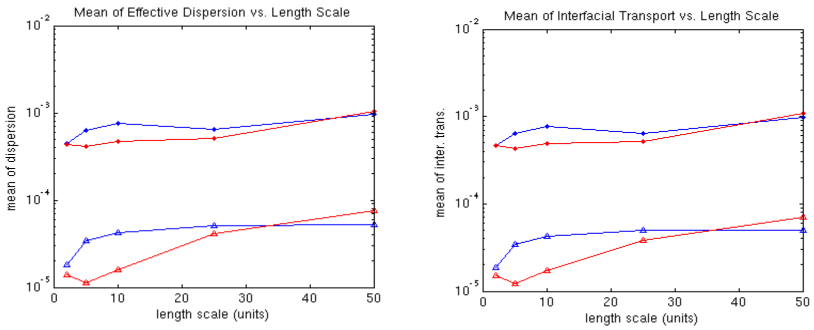

Figure 6-15: Mean of effective dispersion and inter-regional transport (blue: Case A; red: Case B; circle: β phase, triangle: γ phase) for the case of tracer transport from water phase (β) to oil phase (γ).

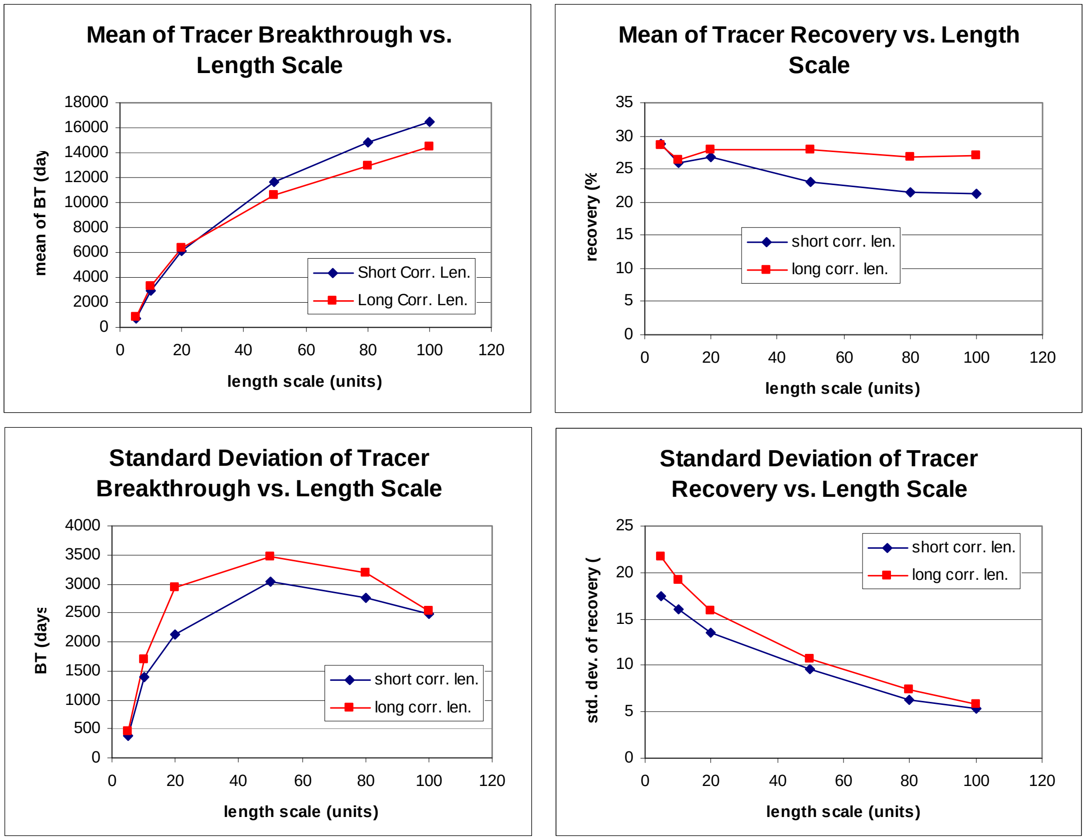

Figure 6-16: Scaling characteristics of breakthrough time (BT) and tracer recovery at base case conditions for the case of tracer transport from water phase (β) to oil phase (γ).

6.4.2 Effects of Inter-Phase Transport

In the next example, the value of $K_{\beta\gamma}(P)$ is reduced to 0.01. This implies that the mass of tracer transferring from the injected phase β to the γ phase will be reduced. Results after 4500 days are shown in Figure 6-17 and Figure 6-18. Results for the β phase appear to be similar to those obtained in the base case, whereas significantly lower values for K_{eff} are obtained for γ phase (Figure 6-17). It should be noted that the results are shown after 4500 days instead of 6000 days for the base case. This is because a reduction of $K_{\beta\gamma}(P)$ decreases the amount of tracers to be transferred from the β phase to γ phase i.e. less smearing, and this helps the tracer front travel faster. The scaling characteristics of K_{eff} are shown in Figure 6-18. Higher mean and variance in K_{eff} of the β phase are observed for the model with longer correlation length.

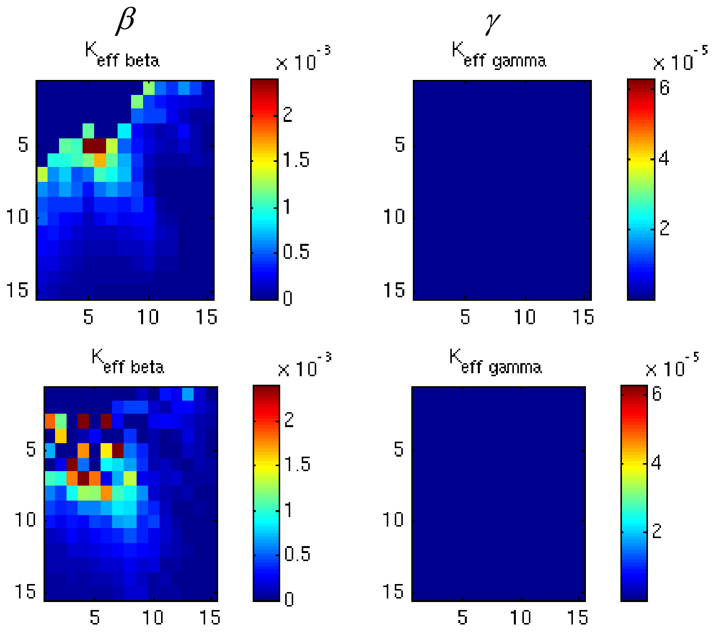

Figure 6-17: Spatial distribution of K_{eff} for a coarse grid size of 10x10 (top: Case A; bottom: Case B) when the tracer partition coefficient is reduced. Plotting with the same color scale as in the base case (Figure 6-12), values of K_{eff} in the γ phase are decreased significantly and become negligible. Note that almost no mass of tracer is transferred into the γ phase.

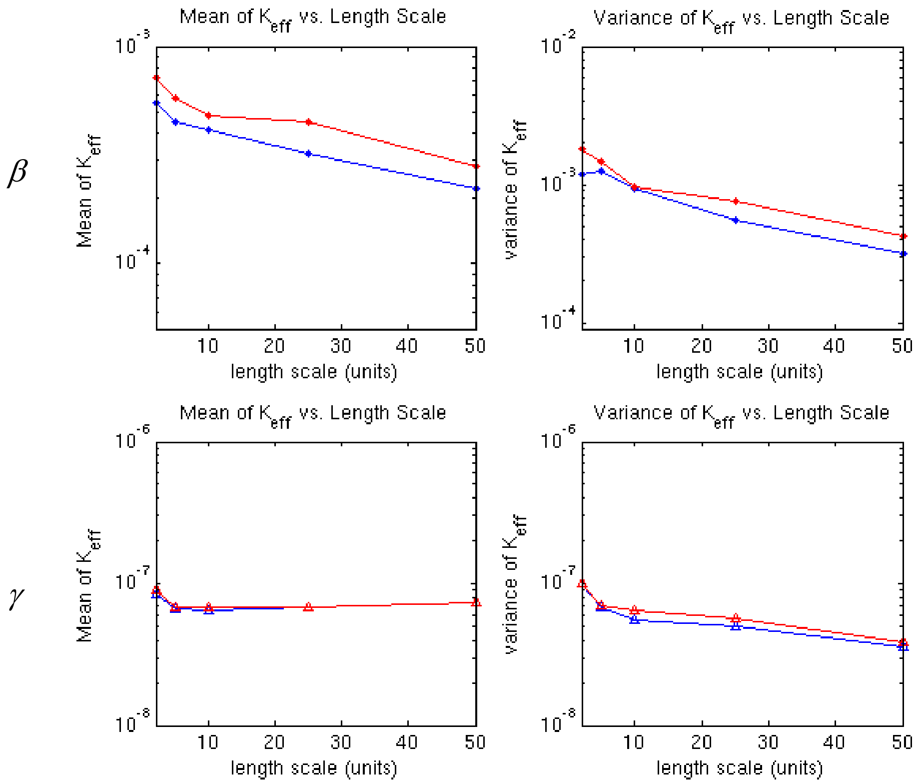

Figure 6-18: Mean and variance of K_{eff} (blue: Case A; red: Case B; circle: β phase, triangle: γ phase) for the case when the tracer partitioning coefficient is reduced.

6.4.3 Effects of Increasing Diffusion

In this example, injection and production rates are reduced to be 100 sm^3/day and the field scale diffusion coefficient D is increased to 0.1 m^2/day from 1e-6 m^2/day. Results after 60000 days are shown in Figure 6-19 – Figure 6-24. Note the longer duration of simulations in this case because the tracer mass transfer process is controlled by diffusion. The velocity and concentration maps are shown in Figure 6-19 and Figure 6-20, respectively. As in the diffusion controlled single phase case, the magnitudes of K_{eff} as shown in Figure 6-21 decrease significantly compared to the dispersion controlled base case; as a result, the differences in scaling characteristics of K_{eff} between different heterogeneity models are significantly diminished (Figure 6-22). In this example where diffusion dominates, the reduced flow rate accompanied by the increase in D leads to a decrease in K_{eff} and suppresses the impacts of heterogeneity. The concentration maps look almost identical to the base case; this is because the spatial distribution of velocities is the same as in the base case, only that the magnitude is smaller.

The scaling characteristics of mass transfer due to diffusion are shown in Figure 6-23. As mentioned earlier, the diffusion term more significantly (especially at small scales) affects the scaling characteristics of inter-phase transport and that profile shown in Figure 6-24 no longer resemble those of dispersion, which remains similar to the base case since the spatial variations of velocity remain unchanged from the base case.

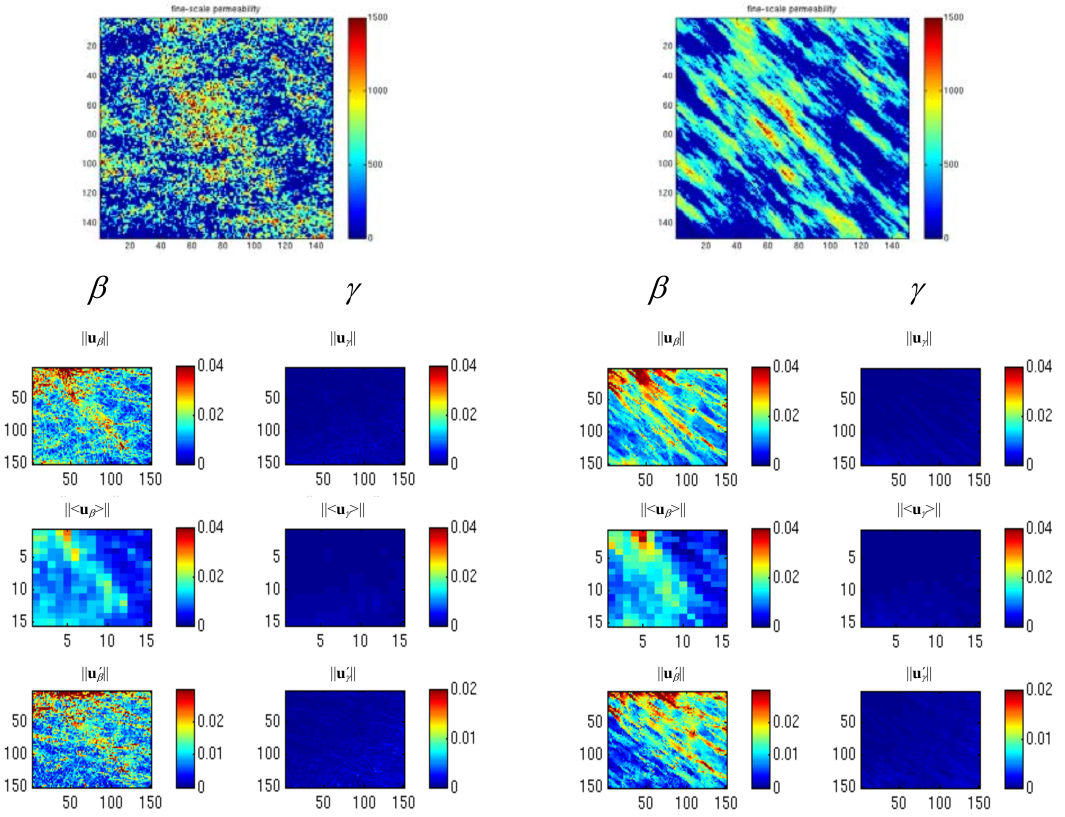

Figure 6-19: (From top to bottom) permeability, velocity **u**, and its decomposition into average velocity <**u**> and **u**' for a coarse grid size of 10x10 (left: Case A; right: Case B). These results are for the case with increased diffusion of tracer.

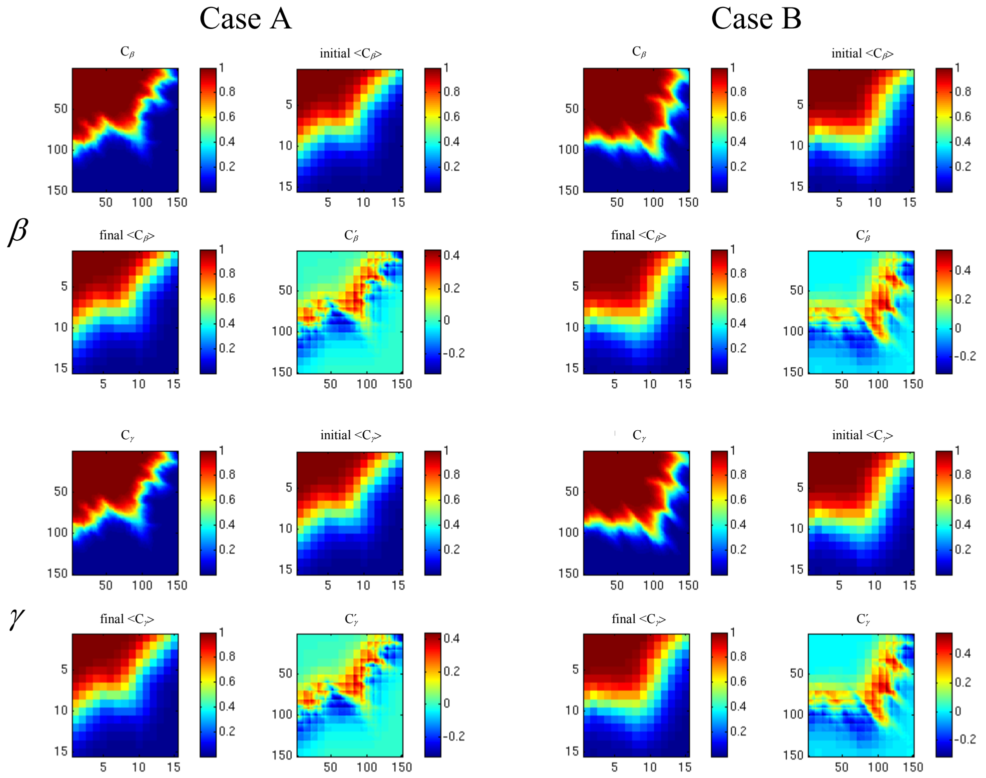

Figure 6-20: (From top left to bottom right) fine-scale concentration *C*, average concentration <*C*> from coarse-scale simulation (initial guess before simulated annealing), final average concentration <*C*> after simulated annealing and the corresponding deviations *C*' for a coarse grid size of 10x10 (left: Case A; right: Case B). These results are for the case with increased diffusion of tracer.

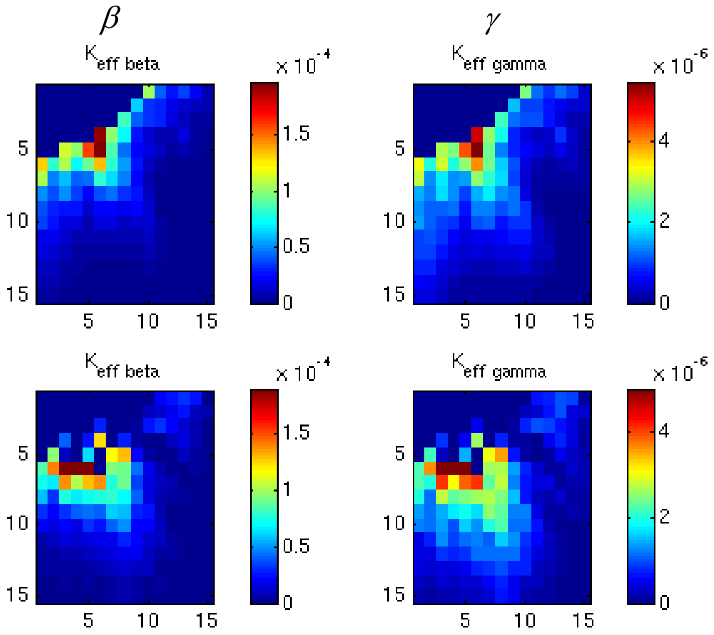

Figure 6-21: Spatial distribution of K_{eff} for a coarse grid size of 10x10 (top: Case A; bottom: Case B). This is for the case with increased diffusion of tracer.

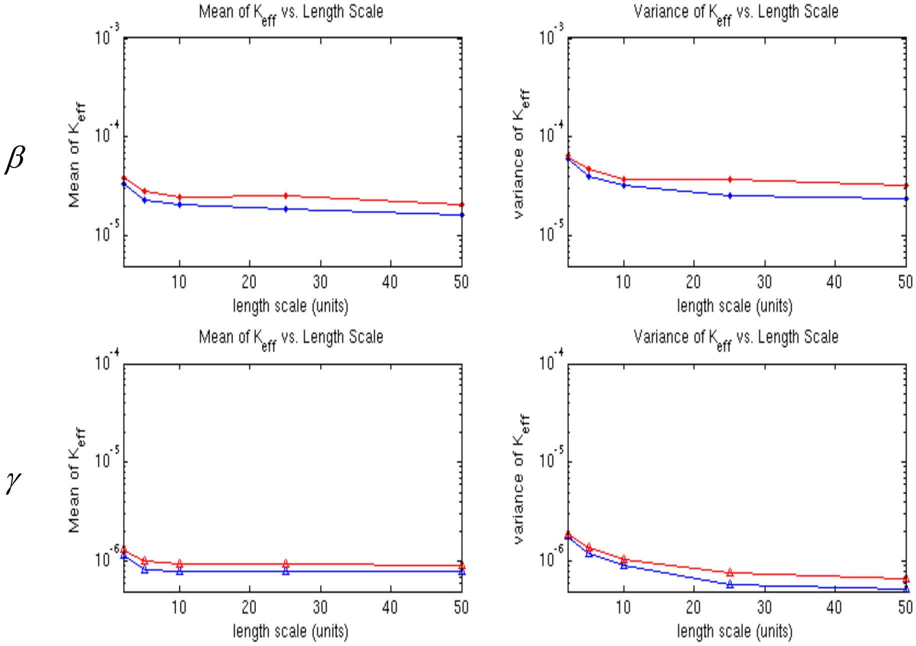

Figure 6-22: Mean and variance of K_{eff} (blue: Case A; red: Case B; circle: β phase, triangle: γ phase) for the case with increased diffusion of tracer.

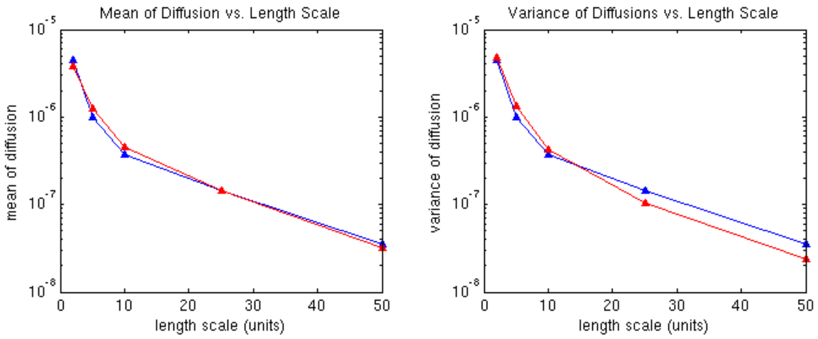

Figure 6-23: Scaling characteristics of mass transfer by diffusion (blue: Case A; red: Case B) for the case with increased diffusion of tracer. Diffusion is the same in both phases because C_β and C_γ are equal for a unit partition coefficient $K_{\beta\gamma}$.

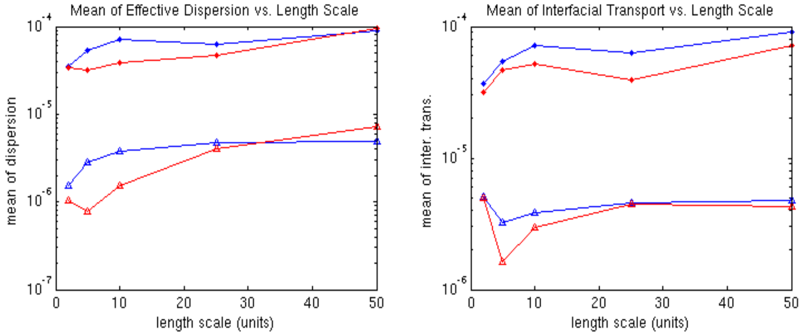

Figure 6-24: Mean of effective dispersion and inter-regional transport (blue: Case A; red: Case B; circle: β phase, triangle: γ phase) for the case with increased diffusion of tracer.

6.4.4 Effects of Scale-Up of Relative Permeability

In this example, the effects of scale-up of relative permeability are investigated by repeating the base case with two sets of relative permeability for two rock types that are defined as follows:

$$\text{rock type} = 1 \rightarrow \phi < 0.2$$
$$\text{rock type} = 2 \rightarrow \phi \geq 0.2$$

The corresponding relative permeability curves for each rock type are shown in Figure 6-25. Less porous and permeable rocks tend to have lower relative permeability end points and higher residual saturations, while rocks with high porosity and permeability would have higher relative permeability end points and lower residual saturations (Lake, 1989).

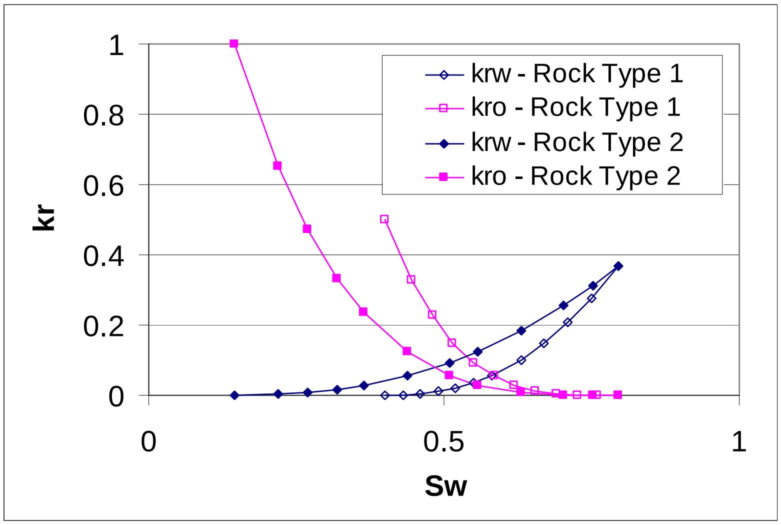

Figure 6-25: Water-oil relative permeability as a function of water saturation for both rock types.

The relative permeability curves are scaled-up and fitted to a model at each coarse grid level. An example of scaled-up relative permeability for a coarse grid size of 10x10 is shown in Figure 6-26. Results after 60000 days are shown in Figure 6-27 through Figure 6-29. The spatial distribution of K_{eff} is shown in Figure 6-27. For comparison purposes, the results from the base case (using fine-scale relative permeability) are repeated here. Slightly lower variability in K_{eff} is observed when scaled-up relative permeabilities are used, particularly for the γ (oil) phase. This seems reasonable given that the oil phase end-point relative permeability in Figure 6-26 is much lower than that in Figure 6-25, hence the variability in $\mathbf{u}_\gamma$ is reduced. The scaling characteristics of K_{eff} for both phases are shown in Figure 6-28 and Figure 6-29. Once again, Figure 6-29 shows that a slightly lower variability in $K_{eff\ \gamma}$ is observed with the use of scaled-up relative permeability.

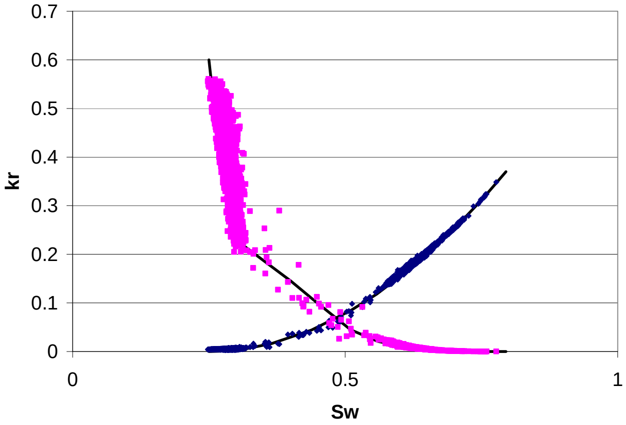

Figure 6-26: Scaled-up water-oil relative permeability corresponding to a two rock type model for a coarse grid of 10x10 (pink: oil; blue: water). The black curves represent the fitted model.

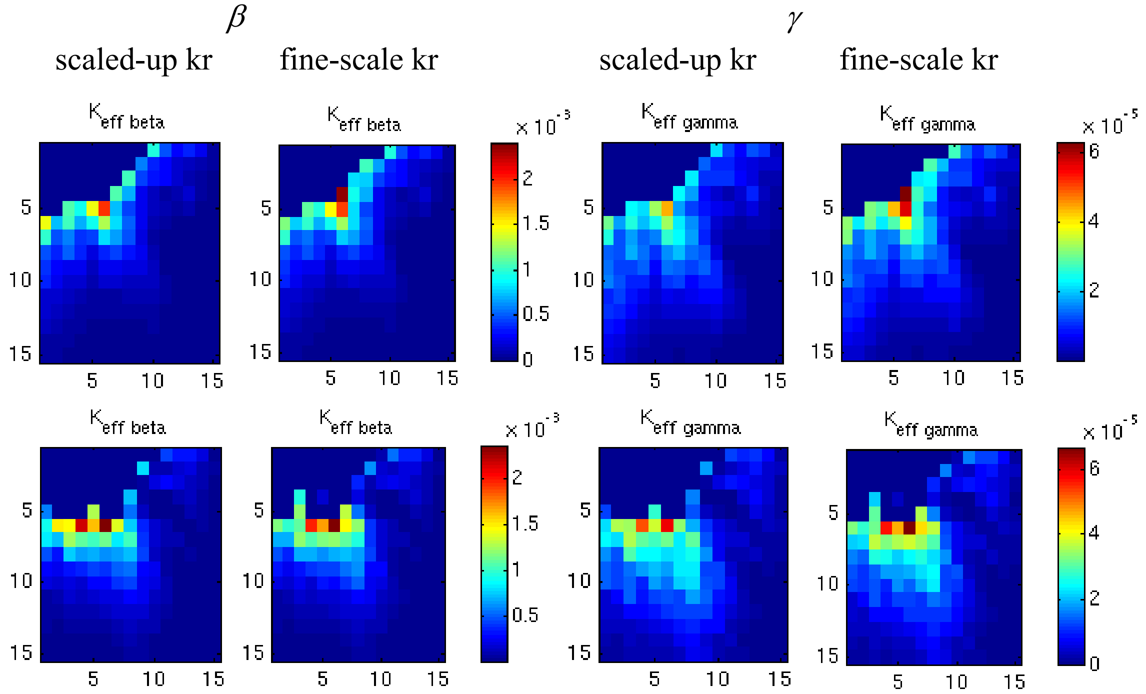

Figure 6-27: Spatial distribution of K_{eff} for a coarse grid size of 10x10 (top: Case A; bottom: Case B).

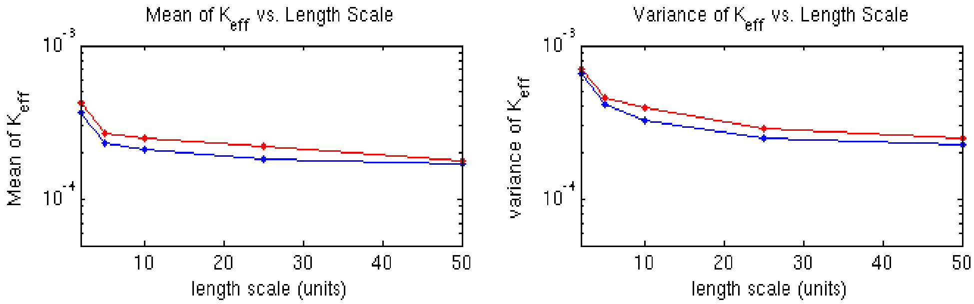

Figure 6-28: Mean and variance of K_{eff} in β phase for the case with scaled-up relative permeability (blue: Case A; red: Case B).

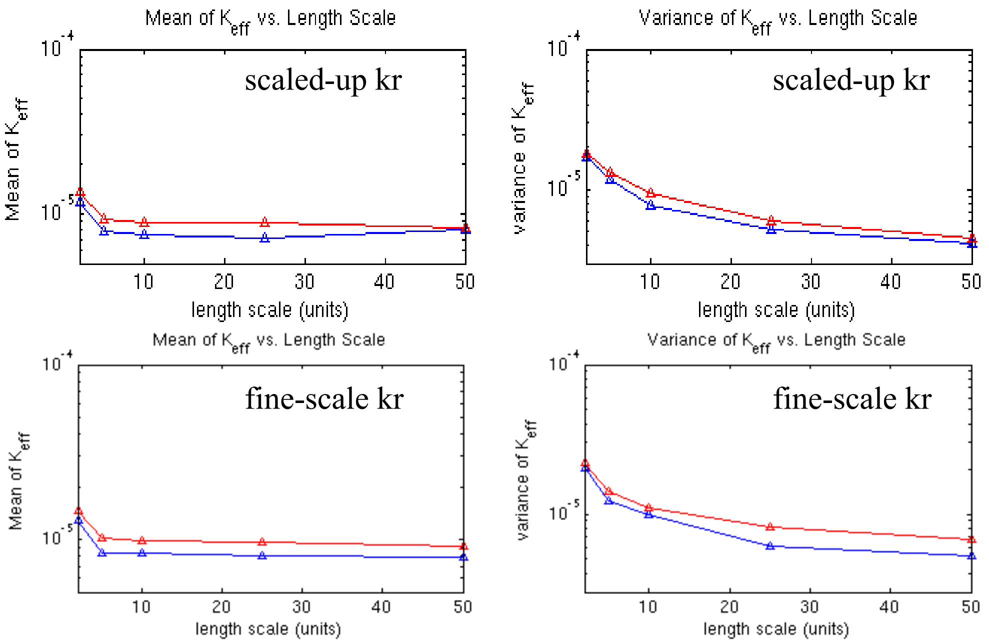

Figure 6-29: Mean and variance of K_{eff} in γ phase (blue: Case A; red: Case B).

6.5 SUMMARY

The chapter extends the volume averaging technique to multiphase systems and applies the methods to study mechanisms involving adsorption and inter-phase transport. It can be seen from the derivations that the formulations are similar to those for the single phase systems. As one might have expected from the single phase results, differences in scaling characteristics of K_{eff} become apparent when the degree of heterogeneity increases (e.g., longer correlation lengths), especially in convection-dispersion dominant processes. When diffusion dominates, the differences in K_{eff} between various heterogeneous models become insignificant.

It should be noted that the absolute value of K_{eff} and the differences in K_{eff} between various heterogeneity models are always higher in the displacing phase because of higher velocities and concentrations. Decrease in velocities and partition coefficient (hence its corresponding concentrations) reduce the magnitude of K_{eff} in the displaced phase, causing its scaling characteristics to be much less dependent on the underlying heterogeneity.

Chapter 7: Scale-Up of Apparent Polymer Viscosity Using Volume Averaging

7.1 OVERVIEW

The application of volume averaging to scale-up apparent viscosity of polymer during single-phase flow was attempted next. This chapter discusses the mathematical formulations and concepts for this procedure. Instead of the transport equations, the volume averaging approach is applied to the momentum balance equations at the continuum scale directly. Employing similar arguments as in the previous chapters, we can compute effective properties at the field scale based on results at the fine scale continuum scale. We devise a set of volume averaged equations appropriate for the scale at which numerical simulation results can be integrated. A detailed outline of the numerical scheme is discussed, and we demonstrate that the scaling characteristics of apparent viscosity and effective shear rate exhibit strong dependency on reservoir heterogeneity.

7.2 SHEAR RATE DEPENDENCY OF POLYMER VISCOSITY

The viscosity of a fluid (μ) can be defined as the resistance to shear; it is the proportionality between shear stress (τ_s) and shear (deformation) rate ($\dot{\gamma}$). For some fluids, this proportionality remains constant over a wide range of shear rates, and they are referred to Newtonian fluids (Sorbie, 1991). For other fluids, viscosity varies as a function of $\dot{\gamma}$, and they are described to exhibit non-Newtonian behavior: $\tau_s = \mu\left(\dot{\gamma}\right)\dot{\gamma}$. If the viscosity function $\mu\left(\dot{\gamma}\right)$ increases with increasing shear rate, the fluid is said to be shear-thickening; on the other hand, if the viscosity function decreases with increasing shear rate, the fluid is said to be shear-thinning. In general, $\mu(\dot{\gamma})$ is a non-linear function of $\dot{\gamma}$, but an *apparent viscosity* μ_{app} can be defined from the slope of τ_s versus $\dot{\gamma}$. Numerous empirical models have been proposed to describe the function form of $\mu(\dot{\gamma})$. An example is the power law model (Bird et al., 1960), which states that $\mu(\dot{\gamma}) \propto \dot{\gamma}^{n-1}$ with *n* being an empirical constant for a particular polymer solution.

7.3 MATHEMATICAL FORMULATION

7.3.1 Derivation of Scaled-Up Equations

In a homogeneous region, the momentum and mass balances for a single-phase, incompressible, steady-state flow can be described as follow:

$$\mathbf{u}_\beta = -\mathbf{M}_\beta \cdot \left(\nabla p_\beta - \rho_\beta \mathbf{g}\right) \tag{7-1}$$

$$\nabla \cdot \mathbf{u}_\beta = 0 \tag{7-2}$$

where β denotes the flowing phase and $\mathbf{M}_\beta = \dfrac{\mathbf{k}}{\mu_\beta}$ is the mobility of phase β. The two equations can be combined:

$$\nabla \cdot \left(\mathbf{M}_\beta \cdot \nabla P_\beta\right) = 0 \tag{7-3}$$

$$\nabla P_\beta = \nabla p_\beta - \rho_\beta \mathbf{g} \tag{7-4}$$

If the scale-up characteristics of the mobility $\mathbf{M}_\beta^*$ can be computed using volume averaging, then the volume averaged apparent viscosity $\mu_{app}{}^*$ can be computed provided the average permeability be available independently:

$$\mathbf{M}_\beta{}^* = \left[\frac{\mathbf{k}}{\mu_{app}}\right]^* = \frac{\overline{\mathbf{k}}}{\mu_{app}{}^*} \tag{7-5}$$

Therefore, our focus is to derive a scheme for computing the effective scaled-up mobility $\mathbf{M}_{\beta}^{*}$. We begin with spatial averaging of the governing equation. The angle brackets indicate spatial averaging. For simplicity of notations, assume that there are only two homogeneous regions (ω, η) (recall Figure 2-9) inside an averaging volume. The equations for the ω region can be derived following the procedure in Whitaker (1999). First, perform the process of spatially smoothing on equation (7-3):

$$\left\langle \nabla \cdot \left(\mathbf{M}_{\beta\varpi} \cdot \nabla P_{\beta\varpi} \right) \right\rangle = 0 \tag{7-6}$$

Applying the spatial averaging equations in equation (4-3) to the above equation gives

$$\nabla \cdot \left\langle \mathbf{M}_{\beta\varpi} \cdot \nabla P_{\beta\varpi} \right\rangle + \frac{1}{V_{\infty}} \int\limits_{A_{\varpi\eta}} \mathbf{n}_{\varpi\eta} \cdot \mathbf{M}_{\beta\varpi} \cdot \nabla P_{\beta\varpi} dA = 0 \tag{7-7}$$

Since $\mathbf{M}_{\beta\varpi}$ exhibits spatial variations within the region ω, assume: $\mathbf{M}_{\beta\varpi} = \left\langle \mathbf{M}_{\beta\varpi} \right\rangle_{\varpi} + \mathbf{M}'_{\beta\varpi}$. Some authors (Quintard and Whitaker, 1998) have performed similar decomposition for the dispersion tensor, so we will assume such decompositions are also valid for phase mobility. The implication is that velocity can be decomposed into an average and a perturbation and since polymer viscosity is dependent on velocity, it can also be expressed as the sum of a average and a perturbation. Substituting this decomposition into Equation (7-7) yields:

$$\nabla \cdot \left\langle \mathbf{M}'_{\beta\varpi} \cdot \nabla P_{\beta\varpi} \right\rangle + \nabla \cdot \left\langle \mathbf{M}_{\beta\varpi} \right\rangle_{\varpi} \cdot \left\langle \nabla P_{\beta\varpi} \right\rangle + \frac{1}{V_{\infty}} \int\limits_{A_{\varpi\eta}} \mathbf{n}_{\varpi\eta} \cdot \mathbf{M}_{\beta\varpi} \cdot \nabla P_{\beta\varpi} dA = 0 \tag{7-8}$$

Expanding the previous equation gives the following:

$$\begin{aligned}&\nabla\cdot\left\langle \mathbf{M}'_{\beta\varpi}\cdot\nabla P_{\beta\varpi}\right\rangle+\nabla\cdot\left\langle \mathbf{M}_{\beta\varpi}\right\rangle_{\varpi}\cdot\left[\nabla\left\langle P_{\beta\varpi}\right\rangle+\frac{1}{V_{\infty}}\int_{A_{\varpi\eta}}\mathbf{n}_{\varpi\eta}P_{\beta\varpi}dA\right]\\&+\frac{1}{V_{\infty}}\int_{A_{\varpi\eta}}\mathbf{n}_{\varpi\eta}\cdot\mathbf{M}_{\beta\varpi}\cdot\nabla P_{\beta\varpi}dA=0\end{aligned}\qquad(7\text{-}9)$$

The pressure terms in the spatially averaged momentum balance equation is similar to the concentration terms in the mass balance equation in the previous chapters. Therefore, we perform the spatial decomposition of pressure, in a way similar to that for concentrations. Spatial decomposition can be performed if the averaged quantities vary smoothly over a distance much larger than the averaging volume:

$$P_{\beta\varpi}=\left\langle P_{\beta\varpi}\right\rangle+P'_{\beta\varpi}\qquad(7\text{-}10)$$

The ***averaged equation*** in equation (7-9) becomes:

$$\begin{aligned}&\nabla\cdot\left\langle \mathbf{M}'_{\beta\varpi}\cdot\nabla P_{\beta\varpi}\right\rangle+\nabla\cdot\left\langle \mathbf{M}_{\beta\varpi}\right\rangle_{\varpi}\cdot\left[\nabla\left\langle P_{\beta\varpi}\right\rangle+\frac{1}{V_{\infty}}\int_{A_{\varpi\eta}}\mathbf{n}_{\varpi\eta}\left(\left\langle P_{\beta\varpi}\right\rangle+P'_{\beta\varpi}\right)dA\right]\\&+\frac{1}{V_{\infty}}\int_{A_{\varpi\eta}}\mathbf{n}_{\varpi\eta}\cdot\mathbf{M}_{\beta\varpi}\cdot\nabla P_{\beta\varpi}dA=0\end{aligned}\qquad(7\text{-}11)$$

The deviation equation is obtained by subtracting the averaged equation from the original equation for each region:

$$\begin{aligned}&\nabla\cdot\left(\mathbf{M}_{\beta\varpi}\cdot\nabla P_{\beta\varpi}\right)-\nabla\cdot\left\langle \mathbf{M}'_{\beta\varpi}\cdot\nabla P_{\beta\varpi}\right\rangle-\frac{1}{V_{\infty}}\int_{A_{\varpi\eta}}\mathbf{n}_{\varpi\eta}\cdot\mathbf{M}_{\beta\varpi}\cdot\nabla P_{\beta\varpi}dA\\&-\nabla\cdot\left\langle \mathbf{M}_{\beta\varpi}\right\rangle_{\varpi}\cdot\left[\nabla\left\langle P_{\beta\varpi}\right\rangle+\frac{1}{V_{\infty}}\int_{A_{\varpi\eta}}\mathbf{n}_{\varpi\eta}\left(\left\langle P_{\beta\varpi}\right\rangle+P'_{\beta\varpi}\right)dA\right]=0\end{aligned}\qquad(7\text{-}12)$$

The previous equation can be written as:

$$\begin{aligned}&\nabla\cdot\left(\mathbf{M}_{\beta\varpi}\cdot\nabla P_{\beta\varpi}\right)-\nabla\cdot\left\langle\mathbf{M}'_{\beta\varpi}\cdot\nabla P_{\beta\varpi}\right\rangle-\nabla\cdot\left(\mathbf{M}_{\beta\varpi}-\mathbf{M}'_{\beta\varpi}\right)\cdot\nabla\left(P_{\beta\varpi}-P'_{\beta\varpi}\right)\\&-\nabla\cdot\left\langle\mathbf{M}_{\beta\varpi}\right\rangle\cdot\frac{1}{V_\infty}\int_{A_{\varpi\eta}}\mathbf{n}_{\varpi\eta}\left(\left\langle P_{\beta\varpi}\right\rangle+P'_{\beta\varpi}\right)dA-\frac{1}{V_\infty}\int_{A_{\varpi\eta}}\mathbf{n}_{\varpi\eta}\cdot\mathbf{M}_{\beta\varpi}\cdot\nabla P_{\beta\varpi}dA=0\end{aligned}\tag{7-13}$$

Equation (7-13) can be further manipulated to yield:

$$\begin{aligned}&-\nabla\cdot\left\langle\mathbf{M}'_{\beta\varpi}\cdot\nabla P_{\beta\varpi}\right\rangle+\nabla\cdot\mathbf{M}'_{\beta\varpi}\cdot\nabla\left(P_{\beta\varpi}-P'_{\beta\varpi}\right)+\nabla\cdot\mathbf{M}_{\beta\varpi}\cdot\nabla P'_{\beta\varpi}\\&\underbrace{-\nabla\cdot\left\langle\mathbf{M}_{\beta\varpi}\right\rangle\cdot\frac{1}{V_\infty}\int_{A_{\varpi\eta}}\mathbf{n}_{\varpi\eta}\left(\left\langle P_{\beta\varpi}\right\rangle+P'_{\beta\varpi}\right)dA-\frac{1}{V_\infty}\int_{A_{\varpi\eta}}\mathbf{n}_{\varpi\eta}\cdot\mathbf{M}_{\beta\varpi}\cdot\nabla P_{\beta\varpi}dA=0}_{\alpha}\end{aligned}\tag{7-14}$$

Finally, the ***deviation equation*** can be written as:

$$\nabla\cdot\left\langle\mathbf{M}'_{\beta\varpi}\cdot\nabla P_{\beta\varpi}\right\rangle-\nabla\cdot\mathbf{M}'_{\beta\varpi}\cdot\nabla\left\langle P_{\beta\varpi}\right\rangle-\nabla\cdot\mathbf{M}_{\beta\varpi}\cdot\nabla P'_{\beta\varpi}-\alpha=0\tag{7-15}$$

Where $\alpha=-\nabla\cdot\left\langle\mathbf{M}_{\beta\varpi}\right\rangle\cdot\frac{1}{V_\infty}\int_{A_{\varpi\eta}}\mathbf{n}_{\varpi\eta}\left(\left\langle P_{\beta\varpi}\right\rangle+P'_{\beta\varpi}\right)dA-\frac{1}{V_\infty}\int_{A_{\varpi\eta}}\mathbf{n}_{\varpi\eta}\cdot\mathbf{M}_{\beta\varpi}\cdot\nabla P_{\beta\varpi}dA$ (7-16)

The α term is indicative of the momentum transfer between the regions ω and η. The ***averaged equation*** can also be written in terms of α:

$$\nabla\cdot\left\langle\mathbf{M}'_{\beta\varpi}\cdot\nabla P_{\beta\varpi}\right\rangle+\nabla\cdot\left\langle\mathbf{M}_{\beta\varpi}\right\rangle_{\varpi}\cdot\nabla\left\langle P_{\beta\varpi}\right\rangle-\alpha=0\tag{7-17}$$

If the first term $\nabla\cdot\left\langle\mathbf{M}'_{\beta\varpi}\cdot\nabla P_{\beta\varpi}\right\rangle$ is small in magnitude compared to the rest of the terms in equation (7-17), we can assume that $\nabla\cdot\left\langle\mathbf{M}_{\beta\varpi}\right\rangle_{\varpi}\cdot\nabla\left\langle P_{\beta\varpi}\right\rangle-\alpha=0$. The effective mobility $\mathbf{M}_{\beta\varpi}{}^{*}$ can now be defined such that the LHS of $\nabla\cdot\left\langle\mathbf{M}_{\beta\varpi}\right\rangle_{\varpi}\cdot\nabla\left\langle P_{\beta\varpi}\right\rangle-\alpha=0$ is the same as the LHS of equation (7-18) and they should be equal to 0.

$$\nabla\cdot\mathbf{M}_{\beta\varpi}{}^{*}\cdot\nabla\left\langle P_{\beta\varpi}\right\rangle=0\tag{7-18}$$

7.3.2 Implementation Details

We start with the deviation equation (7-15) and the averaged equation (7-17). In simplified notation (as in Chapter 4):

Deviation PDE: $\mathbf{a}\cdot\nabla P'_{\beta\varpi} = bP'_{\beta\varpi} - c + D\nabla^2 P'_{\beta\varpi} - \alpha$ (7-19)

The averaged equation: $\alpha = \nabla\cdot\left\langle \mathbf{M}'_{\beta\varpi}\cdot\nabla P_{\beta\varpi}\right\rangle + \nabla\cdot\left\langle \mathbf{M}_{\beta\varpi}\right\rangle_{\varpi}\cdot\nabla\left\langle P_{\beta\varpi}\right\rangle$ (7-20)

$\mathbf{a} = \nabla\cdot\mathbf{M}_{\beta\varpi}$ (7-21)

D = 0 and b = 0 (7-22)

$c = -\nabla\cdot\left\langle \mathbf{M}'_{\beta\varpi}\cdot\nabla P_{\beta\varpi}\right\rangle + \nabla\cdot\mathbf{M}'_{\beta\varpi}\cdot\nabla\left\langle P_{\beta\varpi}\right\rangle$ (7-23)

The boundary conditions are:

$\mathbf{n}\cdot\mathbf{M}\cdot\nabla P_{\beta\varpi} = 0$

$\mathbf{n}_{\beta\sigma}\cdot\nabla P'_{\beta\varpi} + \mathbf{n}_{\beta\sigma}\cdot\nabla\left\langle P_{\beta\varpi}\right\rangle = 0$ (7-24)

$\mathbf{n}\cdot\nabla P'_{\beta\varpi} + \mathbf{n}\cdot\mathbf{g} = 0$ (7-25)

Where $\mathbf{g} = \nabla\left\langle P_{\beta\varpi}\right\rangle$ (7-26)

The following procedure is adopted to solve the deviation PDE subject to the constraint equation and boundary conditions. M^* can be computed once $\left\langle P_{\beta\varpi}\right\rangle$ and $P'_{\beta\varpi}$ are defined.

1. Generate a fine-scale heterogeneous reservoir model (porosity and permeability) for a section of the reservoir and perform flow simulation to obtain velocities and pressure $P_{\beta\omega}$.
2. From the fine-scale model and simulation results, compute a scaled-up permeability field (e.g., harmonic averaging) and initial estimates of $\left\langle \mathbf{u}_{\beta}\right\rangle$ and $\left\langle P_{\beta\varpi}\right\rangle$ (e.g., arithmetic averaging) at different coarse scales. The reason for performing these simple averaging schemes is that permeability, pressure, velocity, and viscosity are all

non-linearly related to each other for the flow of a non-Newtonian fluid. Although arithmetic averaging of velocity and permeability may be inaccurate, these estimates are updated iteratively in the simulated annealing scheme. Finally, note that the permeability used is the effective permeability to polymer solution accounting for permeability reduction R_k

$$\text{effective permeability to polymer} = \frac{\text{effective permeability to water}}{R_k}$$

3. Choose a sub-domain for volume averaging calculations to avoid boundary effects due to wells.
4. At each averaging scale, make small adjustments to $\left\langle P_{\beta\varpi} \right\rangle$ using a simulated annealing scheme such that the left and right hand sides of equations (7-19) and (7-20) are matched. Procedure for simulated annealing:
    a. Initialize with arithmetic averaging of pressure and velocity at various coarse scales to obtain an initial estimates of $\left\langle \mathbf{u}_\beta \right\rangle$ and $\left\langle P_{\beta\varpi} \right\rangle$.
    b. $P'_{\beta\varpi} = P_{\beta\varpi} - \left\langle P_{\beta\varpi} \right\rangle$
    c. Compute α
    d. Compute error ε
    $\varepsilon = D\nabla^2 P'_{\beta\varpi} + bP'_{\beta\varpi} - \mathbf{a} \cdot \nabla P'_{\beta\varpi} - c - \alpha$
    e. If ε is more than tolerance, update $\left\langle P_{\beta\varpi} \right\rangle$; repeat steps b) – d).
        i. Randomly choose 10% of the grid blocks
        ii. Update $\left\langle P_{\beta\varpi} \right\rangle^{new} = \left\langle P_{\beta\varpi} \right\rangle \pm 2\% \left\langle P_{\beta\varpi} \right\rangle$
        iii. If $\operatorname{sgn}\left[\nabla \left\langle P_{\beta\varpi} \right\rangle^{new} \right] \neq \operatorname{sgn}\left[-\left\langle \mathbf{u}_\beta \right\rangle \right]$,
        reject the update and set $\left\langle P_{\beta\varpi} \right\rangle^{new} = \left\langle P_{\beta\varpi} \right\rangle$
    f. Accept or reject the new guess → if accepted: $\left\langle P_{\beta\varpi} \right\rangle = \left\langle P_{\beta\varpi} \right\rangle^{converged}$
5. Compute $\mathbf{M}_\beta *$ from $\left\langle \mathbf{u}_\beta \right\rangle = -\mathbf{M}_\beta * \cdot \nabla \left\langle P_\beta \right\rangle^{converged}$

6. Repeat Steps 4-5 for all averaging length scales
7. Evaluate scaled-up apparent viscosity as a function of averaging scale. Since viscosity is a scalar quantity, and for convenience, $\mu_{app}{}^{*}$ is computed along the direction of flow as follows:

$$\mu_{app}{}^{*} = \langle k_x \rangle_{harmonic} \Big/ M_{\beta x}{}^{*} \tag{27}$$

7.4 RESULTS

Consider a single phase polymer flow in a 250x40 cross sectional (x-z) fine grid model. The simulation is performed with a 3-D compositional flow simulator, UTCHEM, developed by the Center of Petroleum and Geosystems Engineering at the University of Texas at Austin. Details of the simulator can be found in the UTCHEM Technical Documentation (2000). The grid blocks are of uniform size ($\Delta x = \Delta y = \Delta z = 2$ft or 0.61m). An injector is perforated in all the grid blocks along the left edge and a producer is located on the right edge. Injection and production rates are held constant at 60 ft^3/day (1.7 m^3/day) with initial reservoir pressure of 1000 psia (68 bar). A total of 1.5 pore volume (PV) of polymer fluid is injected at the following initial reservoir conditions. It is confirmed that steady state is established much sooner than the end of the injection period.

Initial reservoir conditions:

- C_{polymer} = 0.075wt%
- $C_{\text{monovalent ions}}$ = 0.006096 meq/mL water (e.g., Na$^+$)
- $C_{\text{divalent ions}}$ = 0.004075 meq/mL water (e.g., Ca^{2+}, Mg^{2+})
- μ_{water} = 0.73 cp
- water specific gravity = 0.433 psi/ft (9810Pa/m)

- $k_x = k_y = k_z$

Polymer viscosity is modeled as a function of polymer concentration, salinity, and shear rate and with properties of a high molecular weight Flopaam 3630S that are obtained from a combination of published values (Bhuyan, 1989; Lee et al., 2009). Details of the polymer viscosity, adsorption, and permeability reduction models can be found in Appendix D. Figure 7-1 shows the shear rate dependence of polymer viscosity at injection conditions. Polymer adsorption at the injection concentrations is approximately 36μg/g rock.

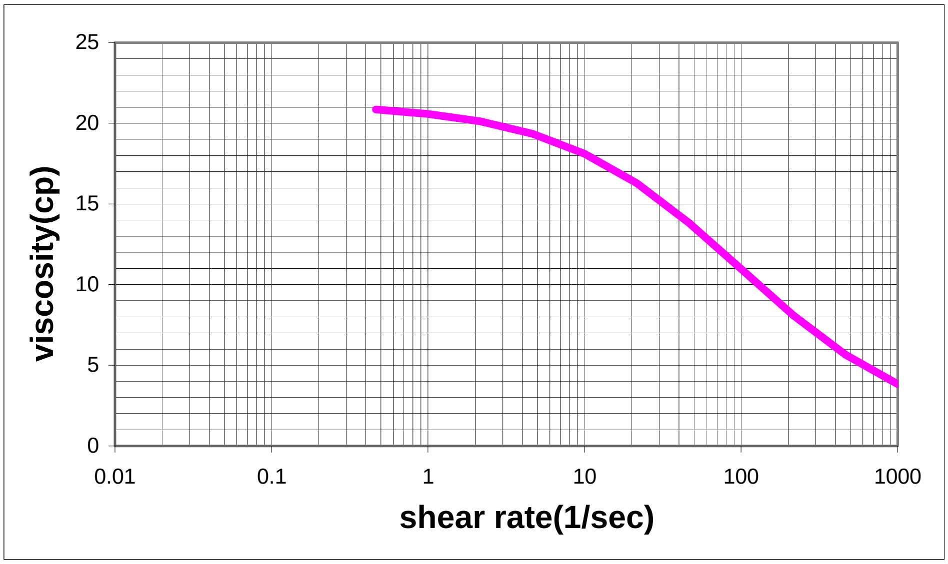

Figure 7-1: Viscosity dependence of polymer on shear rate at injection conditions.

Figure 7-2 illustrates the simulation and volume average calculation configuration. To investigate the effects of heterogeneity, lithofacies models with three different correlation lengths are considered (Figure 7-3). Porosity (ϕ), permeability (k), and permeability reduction (R_k) values are populated according to the rock type at each location as:

$$facies = 1 \rightarrow \begin{Bmatrix} \phi = 0.1 \\ k = 100mD \\ R_k = 1.36 \end{Bmatrix}$$

$$facies = 2 \rightarrow \begin{Bmatrix} \phi = 0.3 \\ k = 2700mD \\ R_k = 3.08 \end{Bmatrix}$$

Case A (short correlation length) – isotropic with the semivariogram model:

- $1.0 * Spherical(a_{horizontal} = a_{vertical} = 5)$

Case B (uncorrelated) – isotropic with the semivariogram model:

- $1.0 * Spherical(a_{horizontal} = a_{vertical} = 1)$

Case C (long correlation length) – anisotropic with the semi-variogram model:

- $1.0 * Spherical(a_{horizontal} = 50;\ a_{vertical} = 5)$

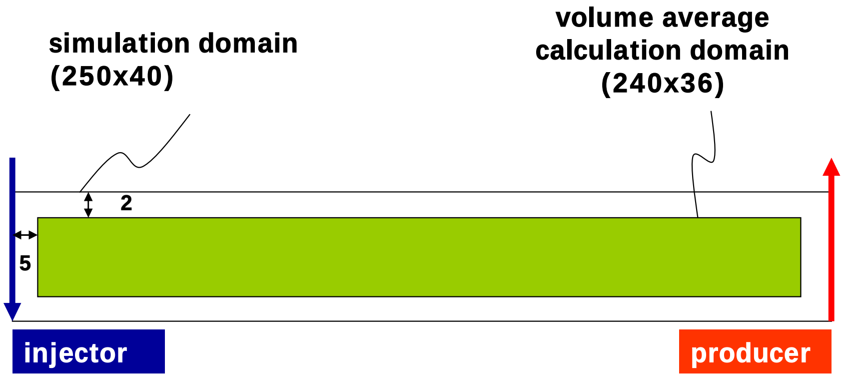

Figure 7-2: Set-up of simulation and volume averaging calculation domains.

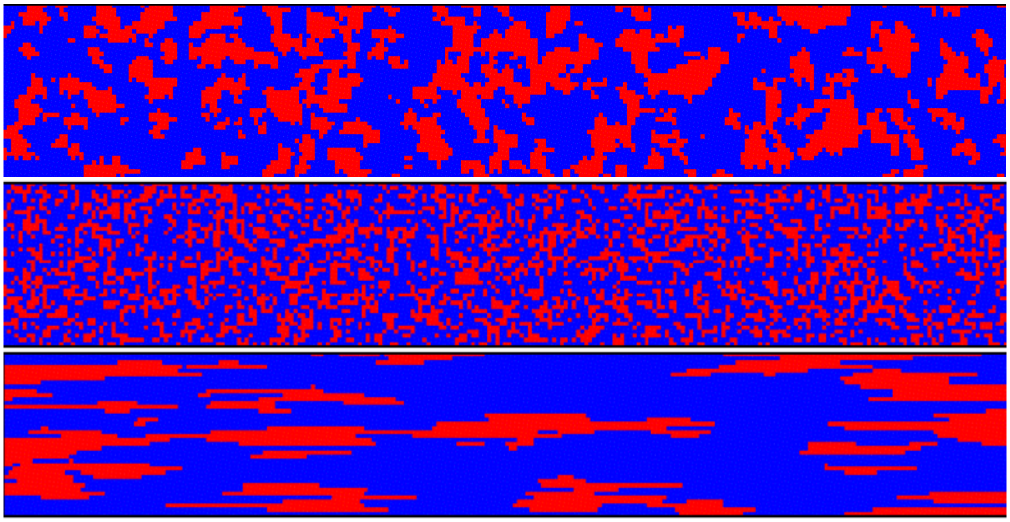

Figure 7-3: Facies model for the three cases (top: Case A; middle: Case B; bottom: Case C; blue – facie #1; red – facie #2).

Selected results from all three cases are presented next. Results of velocity and pressure profiles for Case A are shown in Figure 7-4 and Figure 7-5. Figure 7-6 illustrate that equation (7-18) can be used to define $\mathbf{M}_{\beta\omega}$* if the magnitude of $\nabla \cdot \left\langle \mathbf{M}'_{\beta\varpi} \cdot \nabla P_{\beta\varpi} \right\rangle$ is small. Figure 7-7 and Figure 7-8 shows the spatial distribution of $\mathbf{M}_{\beta\omega}$* and μ_{app}* for each of the three cases. It can be observed that the $\mathbf{M}_{\beta\omega}$* obtained from volume averaging varies smoothly spatially except for Case C (with the most severe heterogeneity). The volume averaged apparent viscosity, on the hand, exhibits a significant amount of noise. This is because in our approach, we have assumed a different averaging scheme for mobility and permeability, the resultant scaled-up apparent viscosity is obtained by dividing the scaled-up permeability by the volume averaged mobility. As a result, noise might be exaggerated around regions with strong permeability contrast.

However, to scale-up apparent viscosity, our intent is not to scale-up individual viscosity values, which are not explicitly specified in flow simulation but are calculated based on correlations with the corresponding grid block effective shear rate (e.g., equations (D-3) and (D-4) in Appendix D). Therefore, our goal is to understand how to make adjustments to the model parameters in these correlations as a function of scale.

This is achieved by first inferring the impacts of heterogeneity models on the scaling characteristics of statistics (mean and variance) of apparent viscosity as shown in Figure 7-9. The figure shows that both mean and variance of apparent viscosity generally decrease with scale. For comparison, the results from conventional approach where apparent viscosity is obtained from arithmetically averaged mobility and permeability are also presented. In the conventional approach, when the correlation length is short (Case A and Case B), mean of scaled-up apparent viscosity remains relatively constant, while its variance continues to decrease with scale. On the other hand, volume averaged apparent viscosity shows a decrease in both mean and variance with scale for all three heterogeneity models; the most drastic decline with scale is observed for the case with long correlation length (Case C).

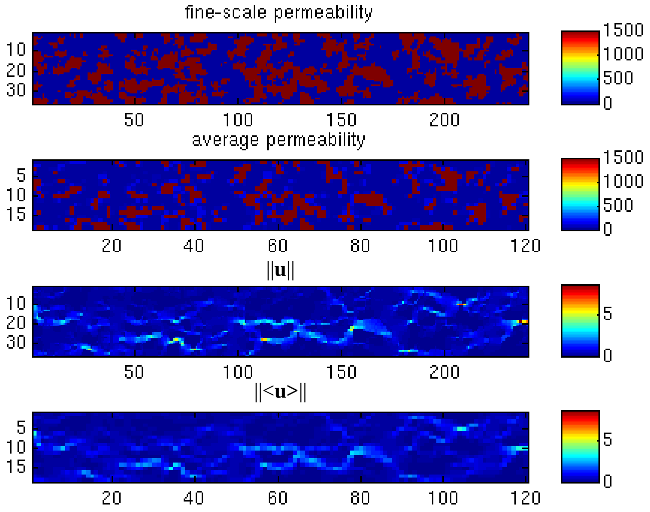

Figure 7-4: (From top to bottom) a) fine-scale permeability, b) upscaled permeability on a 2 x 2 grid, c) magnitude of fine scale velocity, d) magnitude of scaled up velocity for Case A.

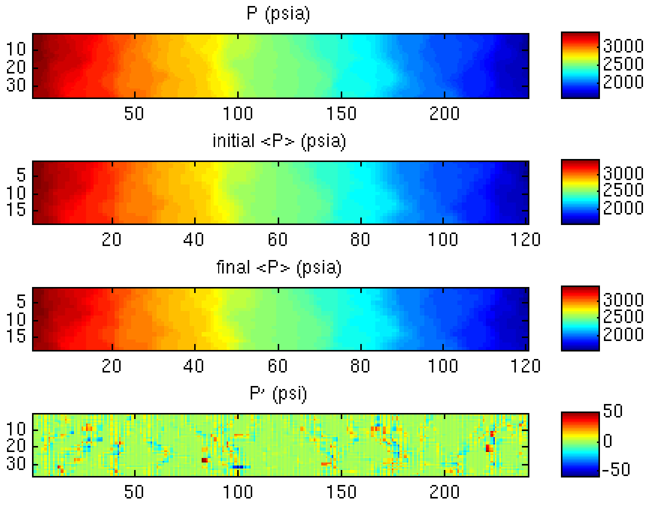

Figure 7-5: (From top to bottom) a) fine-scale pressure, b) initial guess of average pressure <*P*>, c) final average pressure <*P*> after simulated annealing, and d) the corresponding deviations *P*' for a coarse grid size of 2x2 for Case A.

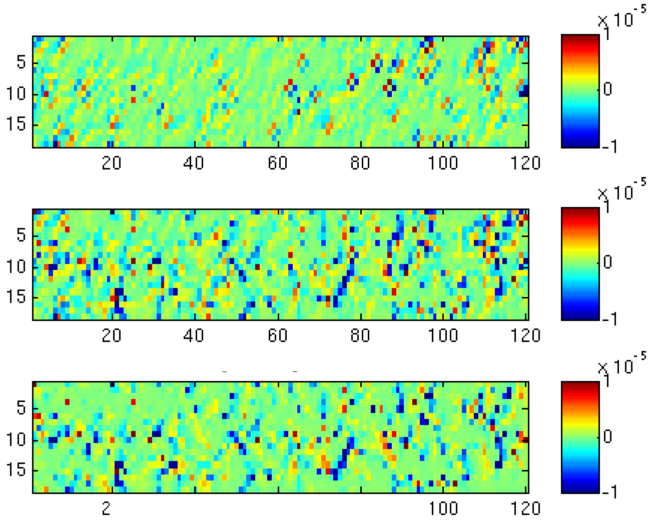

Figure 7-6: (From top to bottom): various terms from the averaged equation for Case A: $\nabla \cdot \left\langle \mathbf{M}'_{\beta\varpi} \cdot \nabla P_{\beta\varpi} \right\rangle$; $\alpha.; \nabla \cdot \left\langle \mathbf{M}_{\beta\varpi} \right\rangle_{\varpi} \cdot \nabla \left\langle P_{\beta\varpi} \right\rangle$ for Case A. This shows that the term on the far left is slightly smaller than the other terms, so $\mathbf{M}_{\beta\omega}*$ can be defined with equation (7-18).

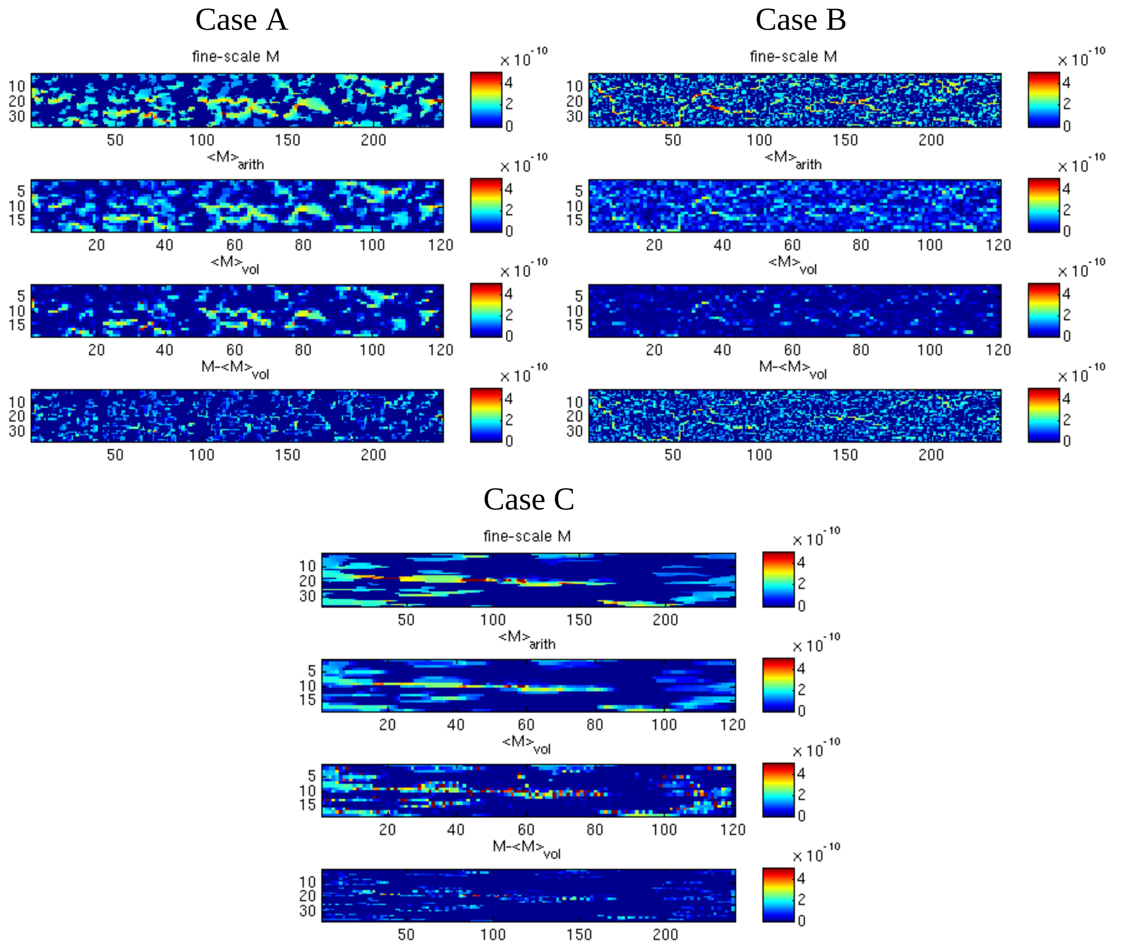

Figure 7-7: (For each case from top to bottom) a) fine-scale mobility *M*, b) arithmetic averaged *M*, b) averaged *M* obtained using the volume averaging procedure, d) deviation of *M* calculated within the volume averaging procedure.

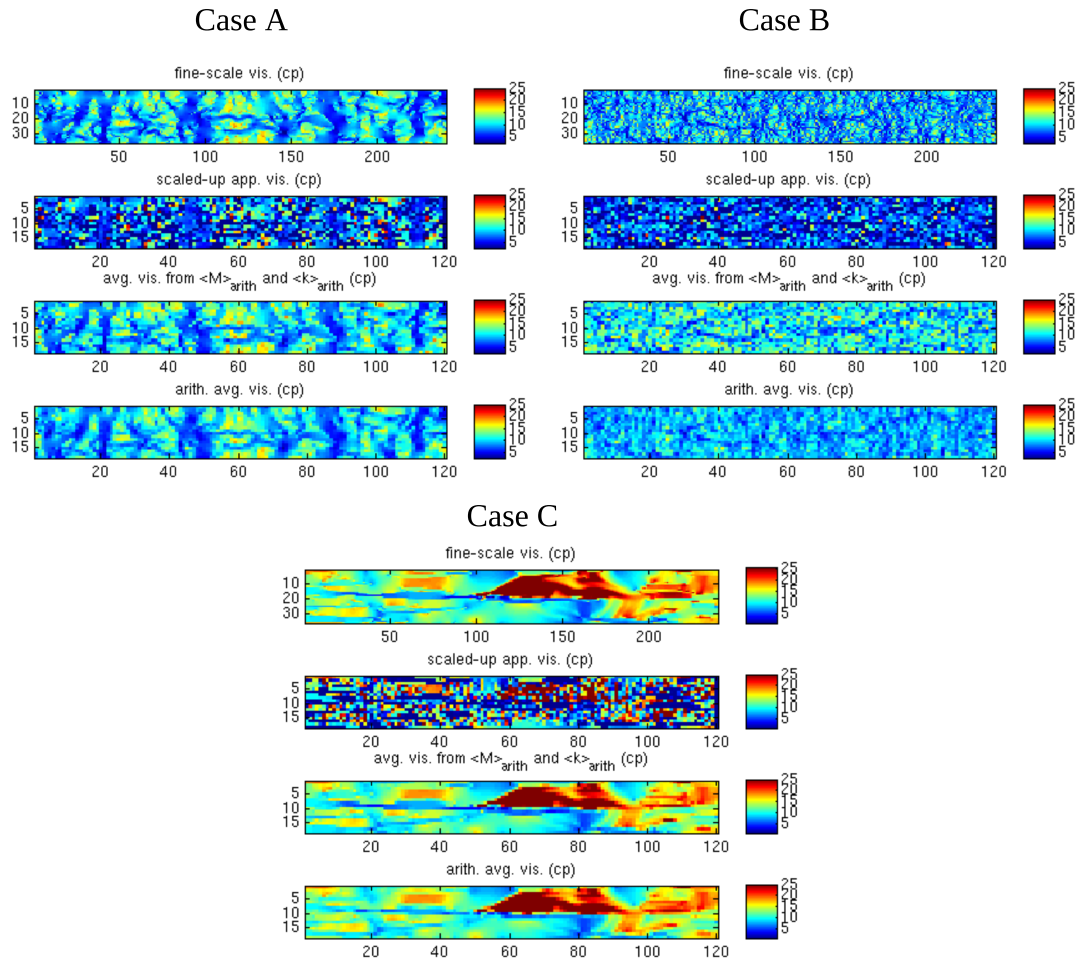

Figure 7-8: (For each case from top to bottom) a) fine-scale viscosity μ_{app} , b) scaled-up viscosity μ_{app}^* from volume averaging, c) for comparison the results are also shown when conventional approach for calculating scaled-up viscosity is implemented $\mu_{app}^* = \langle \mathbf{k} \rangle_{arithmetic} \big/ \langle \mathbf{M}_\beta \rangle_{arithmetic}$, d) result when the fine scale viscosity is directly arithmetically averaged to get the scaled up viscosity for a coarse grid size of 2x2.

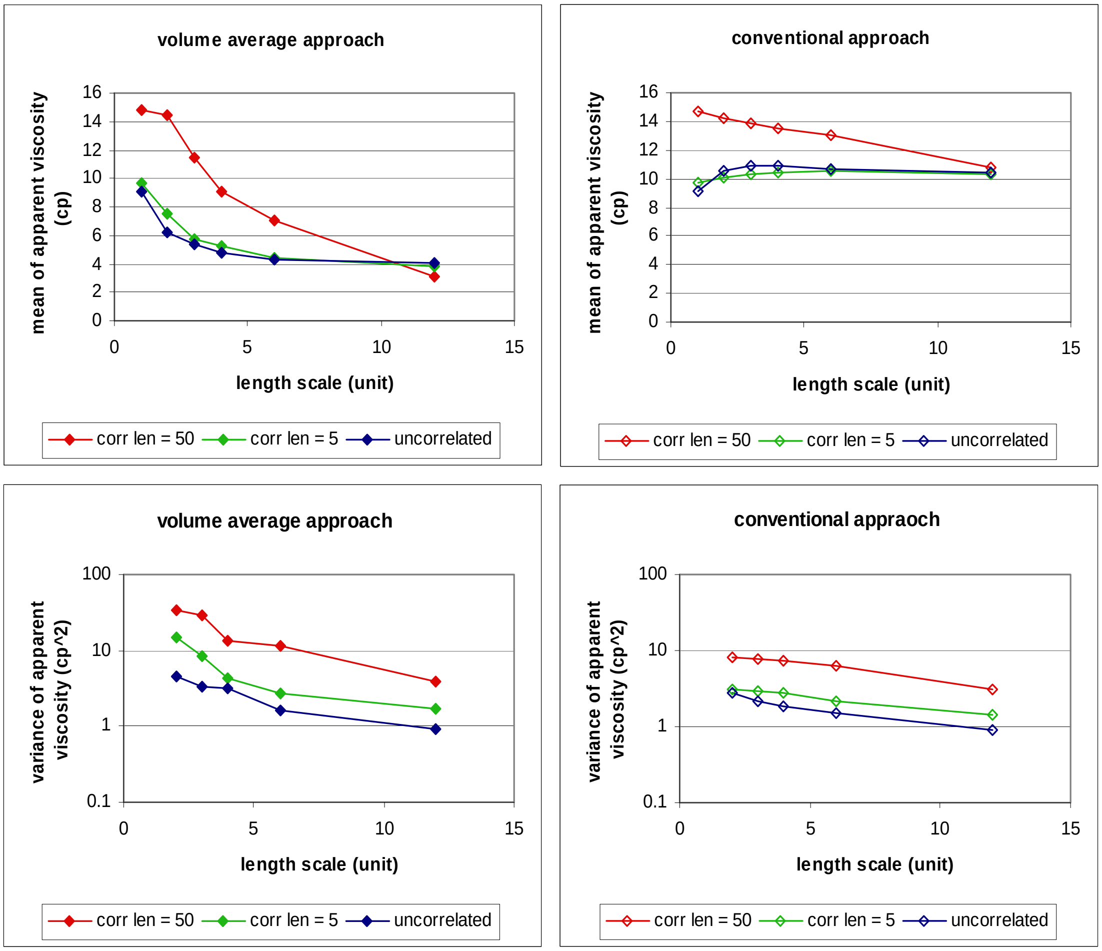

Figure 7-9: Mean and variance of scaled-up apparent viscosity. Left: μ_{app}^{*} from volume averaging; right: conventional approach with $\mu_{app}^{*} = \langle \mathbf{k} \rangle_{arithmetic} \big/ \langle \mathbf{M}_{\beta} \rangle_{arithmetic}$.

If we were to use conventional flow-based upscaling techniques to obtain the averaged permeability field and perform polymer flow simulations, the resultant apparent viscosity map as computed during the flow simulation is shown in Figure 7-10 for Case A using a coarse grid size of 2x2. Note that the apparent viscosities are now direct outputs from UTCHEM. This can be repeated over different coarsening level, and the statistics of the resultant apparent viscosity as a function of coarse grid size is shown in

Figure 7-11. The scaling characteristics agree with those obtained from volume averaging (Figure 7-9). As length scale increases, the mean and variance of viscosity decreases. This decline becomes more drastic when the correlation length is larger, but it is still gentler compared to that obtained from volume averaging.

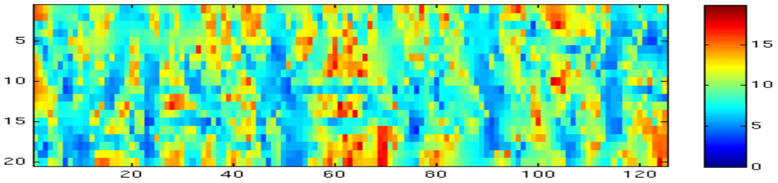

Figure 7-10: Apparent viscosity for a coarse grid size of 2x2 where averaged permeability is obtained directly from flow-based upscaling.

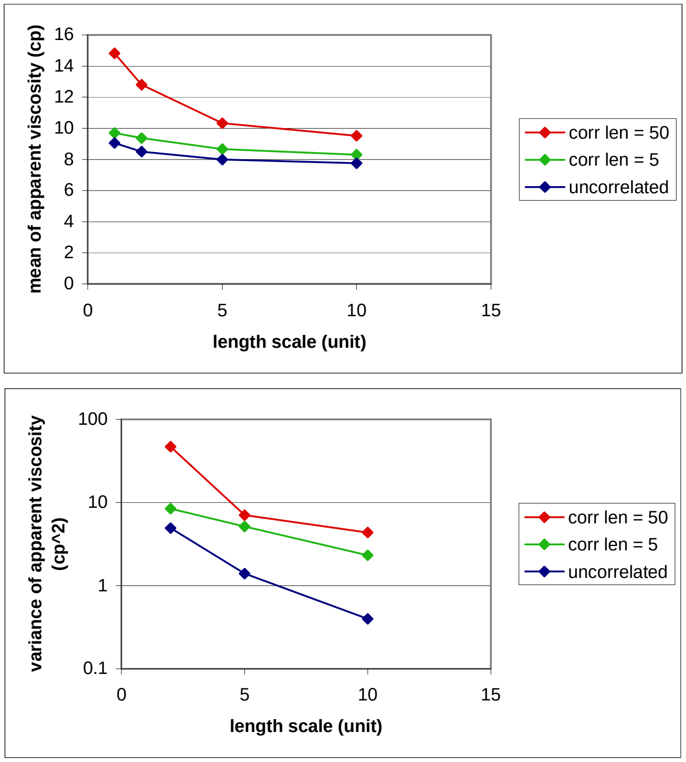

Figure 7-11: Mean and variance of apparent viscosity extracted directly from flow simulations where averaged permeability is obtained from flow-based upscaling.

Understanding the scaling characteristics of apparent viscosity allows us to investigate the scaling characteristics of effective shear rate. In UTCHEM, the relationship between apparent viscosity and shear rate in a porous medium is described as follows (see Appendix D for details):

$$\mu_p = \mu_w + \frac{\mu_p^0 - \mu_w}{1 + \left(\frac{\dot{\gamma}_c \left| u \right|}{\dot{\gamma}_{1/2} \sqrt{\phi k}} \right)^{P_\alpha - 1}} \tag{7-28}$$

In the above equation, $\overline{\left| u \right|}$ denotes average Darcy flux (ft/day); k represent average porosity and permeability (Darcy), respectively; μ_p is the polymer viscosity (cp); the superscript “0” indicates the viscosity at zero shear rate; μ_w is the water viscosity; $\dot{\gamma}_{1/2}$ and P_α are dimensionless fitting parameters that depend on the polymer solution and are generally determined from measurement data. Finally, $\dot{\gamma}_c$ is a model parameter in the units of day*(Darcy)$^{1/2}$/(ft-s) that is assigned empirically as a function of reservoir heterogeneity. Although reservoir property varies spatially, $\dot{\gamma}_c$ is assumed to be a constant. In this study, a constant value of 130 is used for all the simulations.

Since permeability and apparent viscosity vary with scale, it is hypothesized that shear rate and $\dot{\gamma}_c$ would vary with scale as well. Rearranging equation (7-28) and using the averaged values of $\overline{\mu_p}$, $\overline{k}$, and $\overline{\phi}$, we can compute an *effective* $\dot{\gamma}_c$ or $\dot{\gamma}_{c_{eff}}$ as follows:

$$\dot{\gamma}_{c_{eff}} = \frac{\dot{\gamma}_{1/2} \sqrt{\overline{\phi}\,\overline{k}}}{\overline{\left| u \right|}} \left(\frac{\mu_p^0 - \mu_w}{\overline{\mu_p} - \mu_w} - 1 \right)^{\frac{1}{P_\alpha - 1}} \tag{7-29}$$

As mentioned, a base value of 130 is used for $\dot{\gamma}_c$ in all simulations. However, this value is valid at the point scale based on equation (7-28), so we do not necessarily expect $\dot{\gamma}_{ceff}$ to be 130.

If we are interested in finding an equivalent $\dot{\gamma}_c$ such that the apparent viscosity remains constant across all scales, the traditional definition of upscaling, $\dot{\gamma}_{ceff}$ must decrease with scale such that a lower effective shear rate would compensate the decrease in apparent viscosity with scale. This *upscaling* relationship is shown in Figure 7-12 by using a constant $\overline{\mu_p}$ in equation (7-29). However, it is observed that even if $\dot{\gamma}_c$ is kept at the constant value of 130, the resultant pressure gradient remains relatively the same at all coarse scales. This observation suggests that there is no need for decreasing $\dot{\gamma}_{ceff}$ if our objective is to ensure constant rate and pressure gradient in the process of upscaling. This is because as we coarsen up the simulation grid, average permeability decreases, apparent viscosity decreases because shear rate increases. Simultaneous reduction in permeability and apparent viscosity keeps the mobility to be relatively constant; hence the pressure gradient remains unchanged. Therefore, during upscaling of polymer flow, it is the mobility that needs to be kept constant, not the apparent viscosity itself. In polymer flow, since apparent viscosity is a strong function of permeability, as long as permeability is correctly upscaled, upscaling of apparent viscosity will follow the same trend as upscaling of permeability, keeping the mobility relatively constant.

On the other hand, if we are interested in finding a scaled-up $\dot{\gamma}_{ceff}$ such that the apparent viscosity decreases with scale as resulted from the volume averaging calculations, both $\dot{\gamma}_{ceff}$ and effective shear rate must increase with scale. This *scale-up* relationship is shown in Figure 7-13 by substituting the corresponding scaled-up $\overline{\mu_p}$ obtained from volume averaging procedure in equation (7-29). A normalized $\dot{\gamma}_{ceff}$ ($\dot{\gamma}_{ceff}$ divided by $\dot{\gamma}_{ceff}$ at a unit length scale) is also plotted in Figure 7-13. As the system scale increases, both effective permeability in the system and apparent viscosity decrease. However, as opposed to upscaling where the upscaled permeability decreases, individual permeability values in the simulation grid do no change as the system size increases. As a result, higher shear rate can be achieved only by increasing $\dot{\gamma}_{ceff}$. Another interpretation would be that effective mobility needs to be maintained during scale-up (similar to upscaling); if effective permeability decreases with scale, effective apparent viscosity must also decreases; however, if individual grid-block permeability is not reduced, $\dot{\gamma}_c$ must increase to create higher shear rate. Finally, it is noted that when the system is homogeneous and isotropic, $\dot{\gamma}_{ceff}$ increases only slightly with scale; however, as the system becomes more heterogeneous and anisotropic, $\dot{\gamma}_{ceff}$ increases sharply with scale. In either upscaling or scale-up application, higher effective shear rate and $\dot{\gamma}_{ceff}$ are observed for the homogeneous and isotropic systems (Figure 7-12 and Figure 7-13), which is consistent with the lower apparent viscosity observed in Figure 7-9 and Figure 7-11.

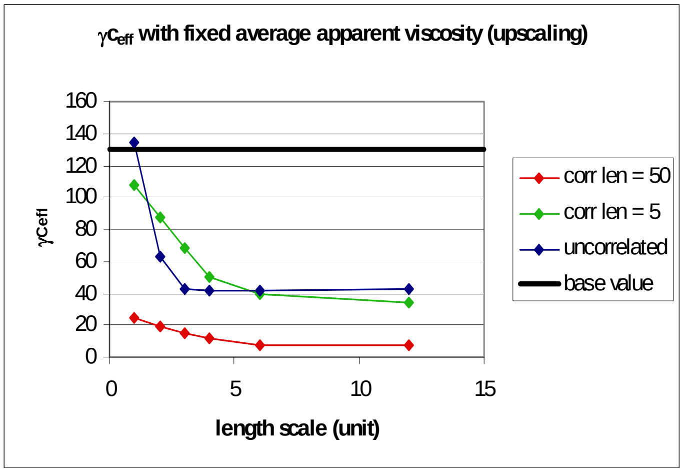

Figure 7-12: Upscaling of $\dot{\gamma}_{ceff}$ in the effective shear rate expression (base value of 130 is indicated by the black line).

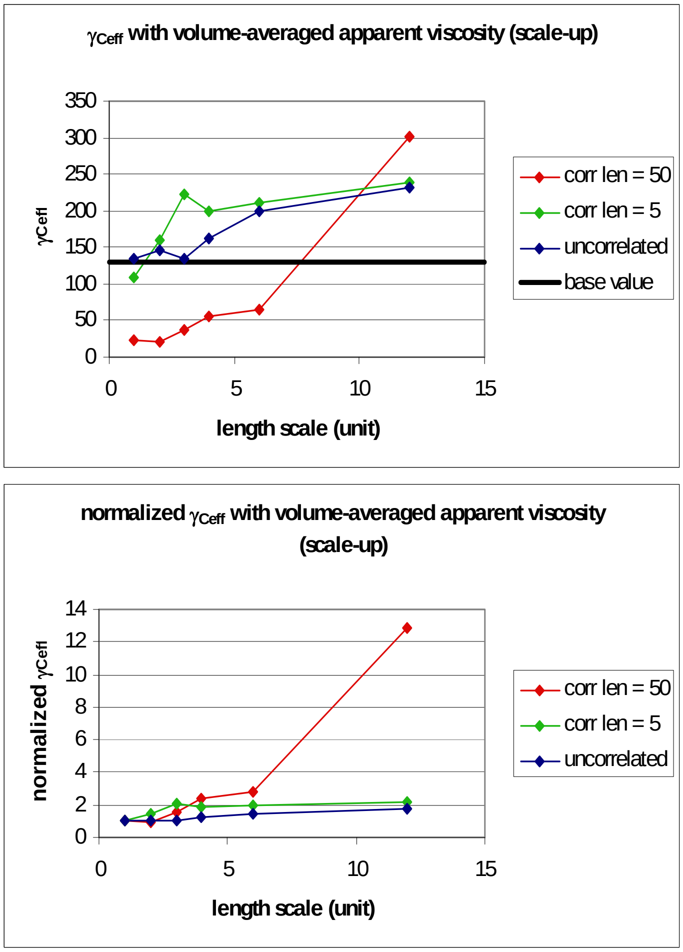

Figure 7-13: Scale-up of $\dot{\gamma}_{ceff}$ in the effective shear rate expression (base value of 130 is indicated by the black line).

In order to verify our results, they are applied in the next example to predict field response. Assume that the field model size is four times (4x) larger than our previous model size: there are a total of 1000 and 40 grid blocks along the x- and z- direction, respectively (so the distance between the injector and producer is 4x larger). The true field response is obtained by running fine-scale simulations on this large field model. All parameters are identical to the ones described previously. In this example, we focus on Case B (uncorrelated) and Case C (long correlation length).

First, we would like to scale-up flow response using our original smaller model (250x40) to predict the response corresponding to the field model. Since both flow rate and cross-sectional area to flow remain the same, if the upscaling procedure is proper then the resulting pressure gradient for the smaller model should match the field pressure gradient. As shown in Table 7-1, for Case B, this is exactly what is observed, while for Case C, $\dot{\gamma}_c$ in the small model (250x40) has to be increased three times (3x) to achieve the same pressure gradient in the field model (1000x40). In other words, $\dot{\gamma}_{ceff}$ is reduced by a factor of 3 as the scale increases in order to achieve the same pressure gradient. We can also interpret the results from a scale-up perspective: if we are asked to predict the pressure gradient observed in the field model from flow experiments performed on the small model, knowing that there is a reduction in apparent viscosity in the field model, we should perform these flow experiments on the small model using a higher value of $\dot{\gamma}_{ceff}$ (or shear rate).

Next, we performed flow-based upscaling of the permeability in the field model and perform flow simulations on the coarsened grid (500x20, 200x8, 100x4, and 50x2). In both Cases B and C, the pressure gradient remains relatively constant for all coarsening levels, confirming that as long as permeability is correctly upscaled, upscaling of apparent viscosity will follow the same trend, keeping mobility relatively constant.

Table 7-1: Scale-up and upscaling of single-phase polymer flow (bolded entry is the true field response)

Case B (uncorrelated)				
system size (ft^3)	no. grid blocks	γ_c	ΔP (psi)	ΔP/ΔL (psi/ft)
80000	250x40	130	2123	4.2
320000	**1000x40**	**130**	**8934**	**4.5**
320000	500x20	130	9215	4.6
320000	200x8	130	9051	4.5
320000	100x4	130	8970	4.5
320000	50x2	130	9015	4.5

Case C (correlation length = 50)				
system size (ft^3)	no. grid blocks	γ_c	ΔP (psi)	ΔP/ΔL (psi/ft)
80000	250x40	130	1445	2.9
80000	250x40	400	927	1.9
320000	**1000x40**	**130**	**3735**	**1.9**
320000	500x20	130	3547	1.8
320000	200x8	130	3638	1.8
320000	100x4	130	3728	1.9
320000	50x2	130	3653	1.8

7.5 SUMMARY

Three averaging schemes have been studied: 1) volume averaging; 2) arithmetic averaging; 3) from simulations using flow-based upscaled permeability field. It is shown that apparent viscosity and its variance decrease with scale. The decline is more drastic as heterogeneity (or correlation length) increases. However, it is also observed that apparent viscosity computed by arithmetic averaging schemes (which is the current practice) does not appear to be sensitive to scale if correlation length is short or the medium is isotropic.

The scaling characteristics of apparent viscosity are used to study the scaling characteristics of effective shear rate and $\dot{\gamma}_c$. In either case of upscaling or scale-up, effective mobility must remain constant. It is shown that since grid-block permeability decreases in the process of upscaling, apparent viscosity decreases accordingly; as a result, mobility would remain relatively constant without adjusting $\dot{\gamma}_c$. On the other hand, individual grid-block permeability does not change during the process of scale-up; a higher value for $\dot{\gamma}_c$ is now required to keep mobility constant. The implication is that if one is to perform polymer flow experiments at core scale to mimic the behavior at field scale, a much higher shear rate should be used.

Chapter 8: Conclusions and Recommendations for Future Work

8.1 KEY CONCLUSIONS

Scale-up of flow performance requires proper representation of sub-scale heterogeneities. The objectives of this research, as stated in Chapter 1, were:

1. Scale-up of flow-related reservoir attributes
2. Scale-up of flow processes in the presence of reservoir heterogeneities using the techniques of volume averaging

For the first objective, a procedure is presented in Chapter 3 where conditioning data is represented in the form of probability distributions to account for uncertainty due to scale-up and subsequently drawing numerous sets of “conditioning data” to perform stochastic simulations. In light of this work, it can be concluded that the notion of “hard” data does not exist when applied to reservoir modeling. Case studies are presented to illustrate the procedure for accounting for uncertainty in hard data in a field application. An extension of the procedure for non-linearly averaged attributes is also presented where a transformation of attributes to linear space is applied. Our results demonstrate that in most cases, the uncertainty distributions obtained by accounting for the scale-up procedure bracket the actual core and log data observed along new wells. The results also demonstrate that accounting for variability due to scale-up can lead to an increase in overall uncertainty, especially in the inter-well regions.

For the second objective, a new framework is proposed where fine-scale flow simulation results are integrated using the volume averaging approach to provide scale-up characteristics of transport parameters accounting for complex heterogeneities. In particular, an effective mass transfer coefficient was defined that could be related to the scaling characteristics of recovery performance. The method is first formulated for the single-phase flow in Chapters 4-5, and is later extended to multi-phase systems in Chapter 6 to account for mass transfer between phases.

The magnitude of the effective transport parameters (e.g., K_{eff}) and their corresponding uncertainty decrease with scale. Results from various case studies demonstrate that these scaling characteristics are strong functions of heterogeneity and the dominating transport mechanisms. It is shown that the scaling characteristics of K_{eff} are correlated to the scaling characteristics of recovery statistics obtained by repeated flow simulations of different domain sizes. In cases where dispersion and convection dominate, there are significant differences in scaling characteristics of K_{eff} for different heterogeneity models. On the other hand, when diffusion dominates, the effects of heterogeneity diminish drastically.

To demonstrate the versatility of the approach, it is applied to study the scaling characteristics of apparent viscosity and effective shear rate in single-phase non-Newtonian polymer flow in Chapter 7. Results indicate 1) mean of apparent viscosity decreases with length scale, and this decline becomes more drastic with increased heterogeneity; 2) at a given length scale, variability in apparent viscosity increases with heterogeneity; 3) effective shear rate increases with scale implying that the shear rate coefficient that affects polymer viscosity in a porous medium also increases with scale. An important implication of these results is that the shear rate coefficient, which is generally assumed to be constant regardless of the modeling scale, actually increases with scale and should be properly represented for accurate prediction of polymer viscosity for simulations with scaled-up reservoir models.

An original contribution of this work is to provide an insight into why the recovery efficiency of several hydrocarbon recovery processes decrease as a function of scale and how this scaling relationship is influenced by heterogeneity. It should be emphasized that this decrease with scale is non-linear and a negative unit slope is not observed in all the cases we studied.

This research also provided a method to scale-up mass transfer that accounts for heterogeneity. The effective transport parameters could be directly used within a new reservoir simulation framework for obtaining reservoir performance predictions that are consistent for the scale at which the modeling is performed. The advantage of using the effective mass transfer coefficient (K_{eff}) directly in a simulation is that instead of scaling each of the transport mechanisms (e.g., dispersion, diffusion, and inter-phase mass transfer) separately, ignoring the potential interactions with one another, the use of K_{eff} allows the total amount of mass transfer to be scaled up in a consistent manner. Most importantly, the values of K_{eff} are shown to vary spatially as a function of both scale and heterogeneity.

This research also illustrates the use of variance of mean concepts for representing sub-scale variability in construction of reservoir models. The proposed method can be implemented to capture field-scale recovery variability from core flood responses by performing numerical flow simulations on several core samples characterizing the sub-scale variability. The corresponding variability in recovery would capture the variability observed in the field-scale.

8.2 RECOMMENDATIONS FOR FUTURE WORK

Based on the results of this dissertation and the aforementioned conclusions, here are some recommendations for future work:

- If there are competing processes that occur at vastly different time scales, it would be useful to investigate the scaling characteristics of K_{eff} as a function time. Slow processes might have significant impacts only at late times. Also, as discussed in Chapter 3, the fine-scale reservoir model used in flow simulation is generally derived from data (e.g., logs) with resolution smaller than the fine-scale grid. Therefore, one can investigate impacts on uncertainty in scaling characteristics of K_{eff} due to sub-scale variability in the reservoir model by generating multiple fine-scale response. It is also interesting to investigate the effects of grid orientation and global boundary conditions (number and locations of wells). In a practical reservoir modeling scenario, global boundary conditions are often complex with large number of wells. Flow orientation with respect to direction of anisotropy in reservoir heterogeneity and large-scale boundary conditions vary around the modeling domain. In order to apply the volume averaging procedure, one approach is to divide the entire domain into various sub-regions and perform the volume averaging calculations within each sub-region. These sub-regions could correspond to different flow pattern (configuration of well groups), and their physical location with respect to the large-scale global boundary conditions must be tracked.

- Heterogeneous features and physical processes in subsurface often occur at vastly different scales; modeling of such systems often requires a multi-scale framework. In many cases, that framework entails the modeling to be broken down into a hierarchy of scales. For example, processes at pore-scale are modeled and scaled-up such that subsequent modeling at the larger scales can be performed. Multi-scale modeling also becomes important in understanding the scaling characteristics of flow performance across all scales (e.g., core scale, inter-well distance, and field scale). Therefore, it would be an interesting idea to adapt this multi-scale framework to the volume averaging methods to derive parameters at coarse-scale. Unresolved issues include how to ensure continuity in parameter values as we transition from one scale to another? Is scale-up from one level to another performed in a consistent manner? A possible way to compute scaled-up transport properties such as dispersivity or effective reaction kinetics parameters for use in flow simulations is to make adjustments to the coarse-scaled values until the corresponding coarse scale response satisfy the averaged and deviation equation. This can be implemented in an optimization procedure. Modeling would continue at the next stage in the hierarchy using the scaled-up properties.

- Another research idea is to develop numerical framework to provide the scaling analysis of specific recovery processes such as migration of carbon dioxide in aquifers, or solvent-based gravity drainage in enhanced oil recovery applications. Many of studies assume a homogeneous, isotropic porous medium and attempt to derive scaling relationships either semi-analytically or empirically. It is well known that heterogeneity plays a significant role in scaling characteristics. For example, researchers who have studied the scaling characteristics of VAPEX (vapor extraction) process would discover that, in most cases, laboratory data suggests much better recovery than expectation scaled from correlation. They generally propose that numerical simulations can be used to develop empirical scaling relationships by matching experimental results via adjusting dispersion coefficients. Since dispersion is directly related to heterogeneity, it is obvious that to correctly capture the scaling characteristics of each process, it is important to incorporate effects of heterogeneity directly in the scale-up of all the contributing mechanisms.
- Although the flow simulations are performed over a sub-volume of the reservoir, less expensive proxy models could be used to reduce the computational effort and make the algorithm more robust. One possible avenue is to use streamline simulations in lieu of flow simulations to obtain coarse-scale velocity and initial estimate of average

concentrations. For example, recall in section 4.2.3 that the second step in the numerical scheme is to perform coarse-scale flow simulations to obtain to obtain $\langle \mathbf{u}_\beta \rangle$ and initial estimates of $\langle C_\beta \rangle$. Streamline simulations can be used to predict $\langle \mathbf{u}_\beta \rangle$ in a fairly accurate and inexpensive manner, particularly in convection-dispersion dominant systems. Although the initial estimates of $\langle C_\beta \rangle$ obtained might be less accurate, but the averaged concentrations are updated subsequently using the volume averaged equations until the error is minimized.

- Finally, another interesting idea is to develop a new generation of simulator that directly uses the mass transfer coefficients to move mass around, as opposed to the conventional simulations that solve the mass transfer problem in terms of fluid displacement followed by mass transfer. Concentration front is marched away from the source using the K_{eff} values directly, and the averaged concentration $\langle C_\beta \rangle$ is governed by the following PDE – equation (4-23):

$$\frac{\partial \langle C_\beta \rangle}{\partial t} + \langle \mathbf{u}_\beta \rangle \cdot \nabla \langle C_\beta \rangle = K_{eff} \left(C_{\max} - \langle C_\beta \rangle \right)$$

The value of K_{eff} at a particular location changes with time (depending on the concentration front position). It is conjectured that the variation of K_{eff} in a grid block versus time is the same as the variation of K_{eff} in space. As a result, at a particular scale, the values of K_{eff} at the concentration front can be assigned as its mean value plus a deviation based on the variance statistics.

Appendix A: Direct Transfer of Uncertainty in Reservoir Models

A.1 OVERVIEW

In a number of subsurface modeling applications, the notion of "hard" conditioning data does not exist. Aside from measurement errors, disparity between the volume support of the measurement and that of the geocellular model introduces additional uncertainty in the conditioning data. In such cases, conditioning data are characterized by probability distributions. One approach to estimate the uncertainty in locations away from the conditioning data would be to repeatedly sample values from the "soft" distributions at conditioning locations and performing repeated conditional simulations. Another approach would be to directly interpolate "soft" probability values. This appendix presents a new approach to directly propagate uncertainty from the soft conditioning data location. This is achieved using the permanence of ratio hypothesis for merging probability distributions. The interpolated uncertainty at an unsampled location due to each "soft" conditioning datum is derived. The aggregated uncertainty distribution due to all the conditioning values is obtained by applying the permanence of ratio hypothesis.

A.2 BACKGROUND

Data available to condition stochastic realizations are, in many cases uncertain - characterized by probability distributions. This may be due to reasons such as non-reproducibility or errors in the data acquisition process. It may also be due to the disparity in scale or support of different measurements and the model grid. As a result, in order to fully capture the uncertainty in reservoir models due to data scarcity and data “uncertainty”, a robust algorithm for propagating uncertainty from conditioning data locations is required.

A simple approach is to sample spatially-correlated values from the “soft” distributions at conditioning locations and perform conditional simulations. Repeated simulations may be performed drawing multiple sets of conditioning data from the probability distributions and estimating the overall uncertainty using numerous realizations over all sets of conditioning data. The major disadvantage is that such a procedure is extremely cumbersome and computationally expensive. The second approach is to directly interpolate “soft” probability values (Sullivan, 1984; Carr and Mao, 1993). Potential pitfall is the possibility of illegitimate probability values and inconsistency between the probability values for adjacent thresholds. The proposed approach is to directly propagate uncertainty from the soft conditioning data location. It involves two major steps: (1) Deriving the interpolated uncertainty at an unsampled location due to each “soft” conditioning datum; (2) The aggregated uncertainty distribution due to all the conditioning values is obtained by applying the permanence of ratio hypothesis.

The interpolation of uncertainty from each soft data location to the unsampled node accounts for the structural distance between the two locations. This is equivalent to the data-to-unknown covariance that regulates the weights in kriging. The merging of uncertainty distributions due to all the conditioning values needs to account for the data-to-data redundancies. The “tau” parameter in the permanence of ratio hypothesis accounts for data-to-data redundancy or data dependence. A unique approach for calibrating the “tau” parameters is presented.

An important application of the approach is to estimate the uncertainty transfer due to sub-scale variance, as described in Chapter 2. Additional variability due to scale-up can be quantified using the variance of block average. The proposed approach can be used to directly transfer this sub-scale variability, in the form of soft conditioning data, to un-sampled locations. Synthetic examples are presented that detail the calculation procedure.

A.3 METHOD

A.3.1 Permanence of Ratio Hypothesis

The permanence of ratio hypothesis proposed by Journel (2002) approximates the joint conditional probability P(A|B,C) as the combination of element probabilities P(A), P(A|B), and P(A|C). P(A|B) represents the probability of the event A happening when B occurs and similarly for P(A|C). For multiple conditioning events, it can be written as follows, where *f* represents the probability density function and $\tilde{f}$ is its negation, i.e. 1-*f*:

$$\frac{\tilde{f}(\mathbf{x}\,|\,D_1, D_2, ..., D_n)}{f(\mathbf{x}\,|\,D_1, D_2, ..., D_n)} = \prod_{i=1}^{n}\left[\frac{\tilde{f}(\mathbf{x}\,|\,D_i)}{f(\mathbf{x}\,|\,D_i)}\right]^{\tau_i} \tag{A-1}$$

The above equation states that the discrimination of an event occurring at location **x** given all the conditioning data can be factorized into a product of discriminations due to each individual event, raised to a power of “tau”. Discrimination here is in terms of the probability of an event not occurring divided by the probability of its occurrence. The “tau” parameters provide a measure of data redundancy (Krishnan, 2004). If “tau” equals exactly one, data events (D_i) are completely not redundant. A value of “tau” not equal to one indicates data redundancy. The use of “tau” parameters allows us to perform probability updating that accounts for data-to-data influence.

A.3.2 Interpolated Uncertainty Due to Each "Soft" Conditioning Datum

Since the interpolation of uncertainty from a soft data location to the unsampled node should account for the structural distance between the two locations (equivalent to the data-to-unknown covariance on the right hand side of the kriging system), a linear weighting factor, λ_α, is used, where **x** = estimation location, and α = conditioning datum location:

$$\lambda_\alpha = C\left(h_{ao}\right):\ f\left(\mathbf{x} \mid D_\alpha\right) = \lambda_\alpha f\left(D_\alpha\right) \tag{A-2}$$

A.3.3 Estimation of τ_α

In kriging, the weights reflect a compromise between data information and redundancy. In effect, redundancy (τ_α) is dependent on both the proximity of the data to the estimation node as well as the correlation to nearby data. A simple postulation is to equate τ_α with ordinary kriging weights. A useful property of such an approach is that data exactitude is already built-in. Thus:

$$\tau_\alpha = \upsilon_{\alpha_{OK}} : \sum_{\alpha=1}^{n} \tau_\alpha = \sum_{\alpha=1}^{n} \upsilon_{\alpha_{OK}} = 1 \tag{A-3}$$

Finally, combining all the above components, the proposed formulation becomes:

$$\frac{1 - P(\mathbf{x} \mid D_1, D_2, ..., D_n)}{P(\mathbf{x} \mid D_1, D_2, ..., D_n)} = \prod_{\alpha=1}^{n} \left[\frac{1 - \lambda_\alpha P(\mathbf{x} \mid D_\alpha)}{\lambda_\alpha P(\mathbf{x} \mid D_\alpha)} \right]^{\tau_\alpha} \tag{A-4}$$

In this approach, probability distributions at data location should reproduce the conditioning data exactly, while at locations far away from data, the uncertainty (hence the variance of estimated) probability distributions increases.

A.4 CASE STUDIES

A.4.1 Synthetic 2-D Case

Consider a synthetic 2-D example with only four conditioning probability distributions as shown in Figure A-1. The sample mean of the four data mean is 8. Numbers in brackets indicate the data mean and standard deviation. Assuming an isotropic variogram with a range of six units, an equal ordinary kriging weight is obtained for each data location to be exactly 0.25. The estimated conditional mean and standard deviation at the unknown location is 8 and 0.8, respectively. Now, in order to verify the validity of formulation, results are compared to those obtained from repeated conditional simulations: drawing 200 sets of spatially-correlated conditioning data from the probability distributions and estimating the overall uncertainty via ordinary kriging on all 200 sets of conditioning data. Two sets of results from repeated conditional simulations are shown in Figure A-1: histograms of kriged means and of random draws from the kriged distributions. Comparison between the proposed approach and random draws from kriged distributions indicate good agreement.

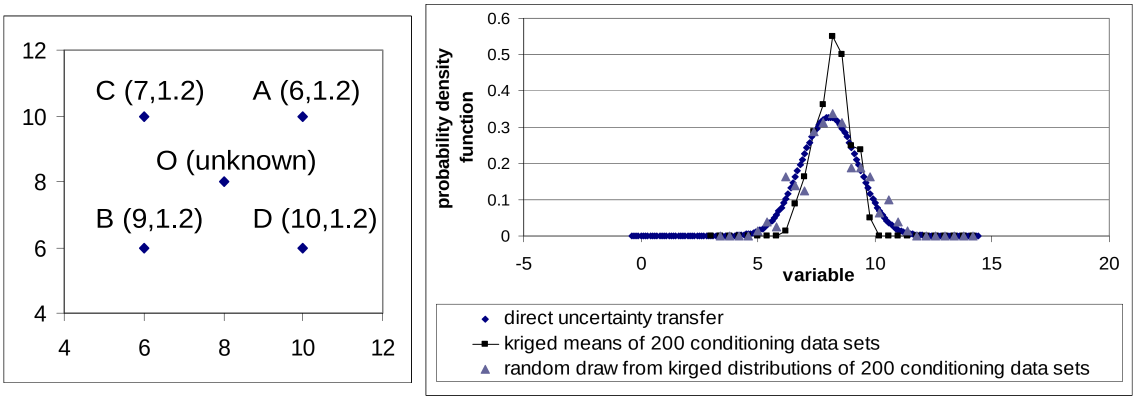

Figure A-1: Configuration of conditioning data and unknown (left). Comparison between results obtained form direct uncertainty transfer and repeated conditioning simulations (right).

Next, a series of cases were constructed to demonstrate the influence of the conditioning data configuration on the uncertainty at the unsampled location. We begin with only one conditioning datum (point A), and we subsequently introduce more data (point B followed by point C). For illustration purposes, we will replace the conditioning data mean at points C and B with 6 and 10, respectively (data symmetry). Results are summarized in Table A-1. As expected, the maximum uncertainty is obtained when there is only one datum. The second datum shifts the conditional mean to be the average of the two data, and the additional data influence reduces the uncertainty at the unknown location. However, as we introduce the third conditioning datum, data redundancy gives a lower kriging weight to point C, hence increasing the estimated uncertainty. This is analogous to kriging, where data redundancy increases the estimation variance. As for the case with all four conditioning data, due to symmetry in both data value and configuration, exact same results are obtained as in the case with two pieces of data.

Table A-1: Results obtained with different configurations of conditioning data

	Sample mean	Estimated Uncertainty at Location O	
		conditional mean	**conditional std. dev.**
1 data (A)	6.00	6.05	1.59
2 data (A,B)	8.00	8.05	1.38
3 data (A,B,C)	7.33	7.45	1.39
4 data (A,B,C,D)	8.00	8.05	1.38

A.4.2 Application to Sub-Scale Variance

Consider database "cluster.dat" available in GSLIB (Deutsch and Journel, 1998). Figure A-2 shows the location map after normal score transformation.

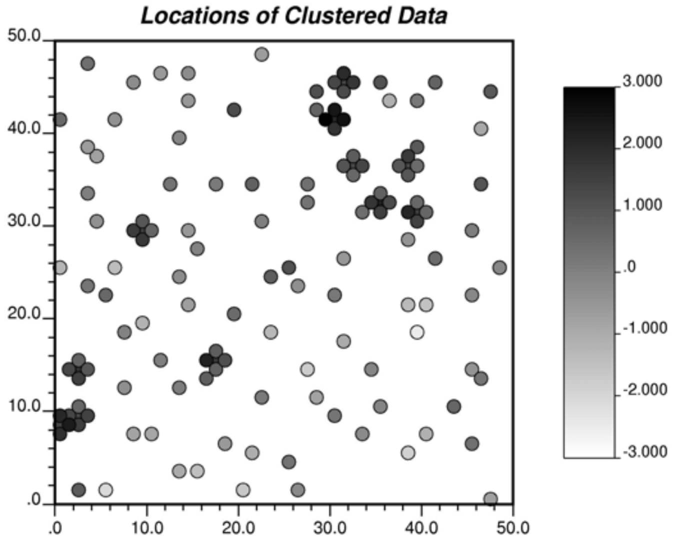

Figure A-2: Configuration of conditioning data in "cluster.dat".

An isotropic spherical variogram $\gamma(\mathbf{h})$ at lag distance **h** can be fitted (Ortiz and Deutsch, 2002). Furthermore, if we scale-up the property to a block size of 5 units x 5 units, a linearly-averaged variogram $\bar{\gamma}(\mathbf{h})$ can also be calculated:

$$\gamma(\mathbf{h}) = 0.1 + 0.9sph(|\mathbf{h}|/15) \text{ and } \bar{\gamma}(\mathbf{h}) = 1.0sph(|\mathbf{h}|/24) \qquad \text{(A-5)}$$

In order to model the effect of additional variability due to scale-up, the variance of block mean is computed using the point-scale variogram model and following the procedure outlined in Chapter 3. This variance (in this case is 0.4, or equivalently, a standard deviation of 0.63) characterizes the uncertainty in property value at each conditioning data location for that particular 5 x 5 length scale. We can now propagate this uncertainty at each conditioning data location to all locations in the coarse grid. The results obtained by directly propagating uncertainty to all locations on the grid are shown in Figure A-3. Alternatively, we can sample from these uncertainty distributions using spatially correlated probability values and generate multiple sets of conditioning data. Using the linearly-averaged scaled-up semi-variogram, conditional simulation is performed on all sets of conditioning data in order to establish the uncertainty estimates at locations away from conditioning data. In this case, we draw 50 sets of conditioning data and generate 30 realizations for each using sequential Gaussian simulations (SGSIM).

Figure A-3 shows the comparison between the two approaches. The mean of the uncertainty distributions obtained by both approaches are similar, but the standard deviation of the distribution obtained by direct propagation of uncertainty is in general higher than those obtained in repeated sampling. Recall the standard deviation in conditioning data (obtained from the variance of mean calculations) in this case is 0.63, which is the minimum uncertainty that should be observed at all locations of the simulation grid. Due to limited sampling, the repeated sampling approach under-estimate this variance at numerous locations, resulting in an estimated standard deviation of less than 0.63. In contrast, the proposed direct uncertainty transfer approach guarantees that the uncertainty at all locations is greater than or equal to this minimum. At conditioning locations, the observed uncertainty is 0.63, but at locations away from conditioning data, the observed uncertainty is greater than 0.63 accounting for both data scarcity and conditioning data configuration.

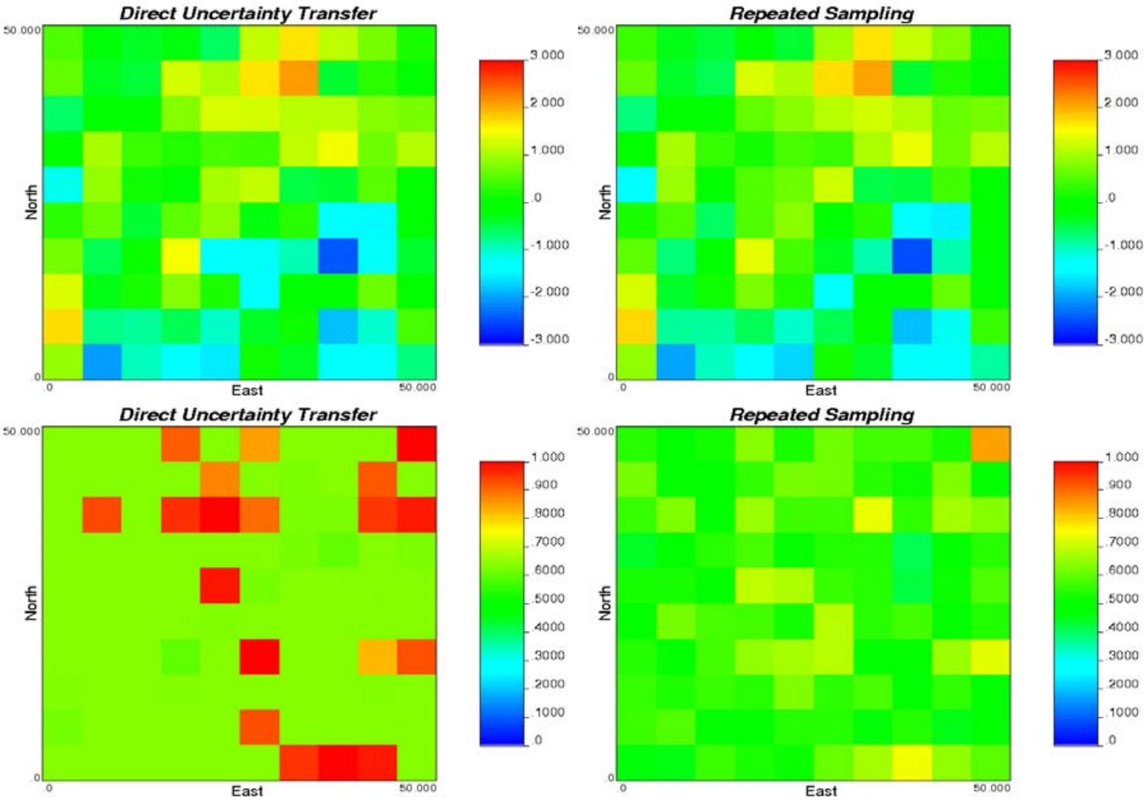

Figure A-3: (Top) Comparison of mean of the uncertainty distribution at each grid node obtained by direct uncertainty transfer (left) and repeated sampling (right). (Bottom) Comparison of the standard deviation of uncertainty distribution obtained by direct uncertainty transfer (left) and repeated sampling (right).

A.5 SUMMARY

The proposed approach has provided an efficient alternative for directly transferring uncertainty in reservoir models. Although other formulations for the “tau” parameters might be feasible, the proposed approach gives a unique estimate with the desired data-exactititude property. Overall uncertainty at an estimated location depends on numerous factors: uncertainty in conditioning datum (variance of conditioning distributions), data redundancy, and physical configuration of data.

An important application of the approach is to transfer the uncertainty due to sub-scale variance recorded at conditioning data locations to other unsampled locations. Additional variability due to scale-up can be quantified using the variance of block average. The proposed approach can be used to directly transfer this sub-scale variability, in the form of soft conditioning data, to un-sampled locations. The efficiency and robustness of this direct approach for propagation of uncertainty is compared against the more traditional approach of repeated sampling from the “soft” conditioning probability distributions and performing a large number of conditional simulations.

Appendix B: Scale-Up of Mass Transfer Equations Using Volume Averaging (Detailed Derivations)

The formulations of volume-averaged transport equations for single phase flow are presented in Chapter 4. This appendix serves to provide additional details regarding the mathematical formulation.

STEP 1: FORMULATION OF GOVERNING EQUATIONS AND BOUNDARY CONDITIONS

Recall from Chapter 4 the assumptions that are invoked in the formulation of the solute transport equation at a scale consisting of an aggregation of pores and fluid distribution among them.

1. Constant temperature
2. β = aqueous phase; σ = solid phase; γ = non-aqueous phase; the σ, γ phases are assumed to be immobile: $\mathbf{u}_\sigma$ & $\mathbf{u}_\gamma = 0$ (**u** indicates velocity). This is equivalent to oil at residual saturation.
3. Incompressible aqueous phase and no-slip $\mathbf{u}_\beta = 0$ at $A_{\beta\gamma}$ and $A_{\beta\sigma}$ (A_{ij} represents the interface between phases i and j).
4. Fast kinetics

The governing equation and boundary conditions become:

$$\frac{\partial C_{i\beta}}{\partial t} + \nabla \cdot \left(\mathbf{u}_\beta C_{i\beta} \right) = \nabla \cdot \left(\overline{\overline{D}} \cdot \nabla C_{i\beta} \right) \qquad \text{(B-1)}$$

B.C. 1: $C_\beta = C_{eq}$ at $A_{\beta\gamma}$

B.C. 2: at $A_{\beta\sigma}$, $\mathbf{n}_{\beta\sigma} \cdot D \nabla C_\beta = 0$ (no diffusion across the solid interface)

Dropping the subscript *i* and assuming isotropic *D*, we can write:

$$\frac{\partial C_\beta}{\partial t}+\nabla\cdot\left(\mathbf{u}_\beta C_\beta\right)=\nabla\cdot\left(D\nabla C_\beta\right) \qquad \text{(B-2)}$$

STEP 2: SPATIAL SMOOTHING AND AVERAGING

We begin the process of spatially smoothing of the governing equation by forming superficial volume average using the spatial averaging theorem (Cushman, 1982; Howes and Whitaker, 1985):

Define:

ψ_j = function value in phase *j*

V_j = volume of phase *j*

V = averaging volume

$\left\langle\psi_j\right\rangle=\varepsilon_j\left\langle\psi_j\right\rangle^j$ and $\varepsilon_j=\dfrac{V_j}{V}$

Superficial volume average: $\left\langle\psi_j\right\rangle=\dfrac{1}{\mathrm{V}}\displaystyle\int_{V_j}\psi_j dV$

Intrinsic volume average: $\left\langle\psi_j\right\rangle^j=\dfrac{1}{\mathrm{V_j}}\displaystyle\int_{V_j}\psi_j dV$

Spatial average of scalar: $\left\langle\nabla\cdot\psi_j\right\rangle=\nabla\cdot\left\langle\psi_j\right\rangle+\dfrac{1}{\mathrm{V}}\displaystyle\sum_{k=1;k\neq j}^{n}\int_{A_{jk}}\mathbf{n}_{jk}\cdot\psi_j dA$

Spatial average of vector: $\left\langle\nabla\psi_j\right\rangle=\nabla\left\langle\psi_j\right\rangle+\dfrac{1}{\mathrm{V}}\displaystyle\sum_{k=1;k\neq j}^{n}\int_{A_{jk}}\mathbf{n}_{jk}\psi_j dA$

n = total number of interfaces (B-3)

Apply spatial average theorem to the governing equation, we get

$$\begin{aligned}&\frac{\partial\left\langle C_\beta\right\rangle}{\partial t}+\nabla\cdot\left\langle\mathbf{u}_\beta C_\beta\right\rangle+\cancelto{}{\frac{1}{V}\int_{A_{\beta\gamma}}\mathbf{n}_{\beta\gamma}\cdot\left(\mathbf{u}_\beta C_\beta\right)dA}+\cancelto{}{\frac{1}{V}\int_{A_{\beta\sigma}}\mathbf{n}_{\beta\sigma}\cdot\left(\mathbf{u}_\beta C_\beta\right)dA}\\&=\nabla\cdot\left\langle D\nabla C_\beta\right\rangle+\frac{1}{V}\int_{A_{\beta\gamma}}\mathbf{n}_{\beta\gamma}\cdot\left(D\nabla C_\beta\right)dA+\frac{1}{V}\int_{A_{\beta\sigma}}\mathbf{n}_{\beta\sigma}\cdot\left(D\nabla C_\beta\right)dA\end{aligned}\tag{B-4}$$

The two terms are zero due to no-slip boundary conditions. We further ignore variations of molecular diffusivity within averaging volume:

$$\left\langle D\nabla C_\beta\right\rangle=D\left\langle\nabla C_\beta\right\rangle=D\left(\nabla\left\langle C_\beta\right\rangle+\frac{1}{V}\int_{A_{\beta\gamma}}\mathbf{n}_{\beta\gamma}C_\beta dA+\frac{1}{V}\int_{A_{\beta\sigma}}\mathbf{n}_{\beta\sigma}C_\beta dA\right)\tag{B-5}$$

The spatially-averaged equation becomes

$$\begin{aligned}&\underbrace{\frac{\partial\left\langle C_\beta\right\rangle}{\partial t}}_{\text{accum}}+\underbrace{\nabla\cdot\left\langle\mathbf{u}_\beta C_\beta\right\rangle}_{\text{convection}}=\underbrace{\nabla\cdot\left[D\left(\nabla\left\langle C_\beta\right\rangle+\frac{1}{V}\int_{A_{\beta\gamma}}\mathbf{n}_{\beta\gamma}C_\beta dA+\frac{1}{V}\int_{A_{\beta\sigma}}\mathbf{n}_{\beta\sigma}C_\beta dA\right)\right]}_{\text{diffusion}}\\&\underbrace{+\frac{1}{V}\int_{A_{\beta\gamma}}\mathbf{n}_{\beta\gamma}\cdot\left(D\nabla C_\beta\right)dA+\frac{1}{V}\int_{A_{\beta\sigma}}\mathbf{n}_{\beta\sigma}\cdot\left(D\nabla C_\beta\right)dA}_{\text{interfacial flux}}\end{aligned}\tag{B-6}$$

STEP 3: SPATIAL DECOMPOSITION

Macroscopic quantity of interests, such as concentrations and velocities, can be represented as a sum of its coarse-scale intrinsic average and a fine-scale deviation.

$$C_\beta=\left\langle C_\beta\right\rangle^\beta+C'_\beta\text{, where }\left\langle C_\beta\right\rangle=\varepsilon_\beta\left\langle C_\beta\right\rangle^\beta\tag{B-7}$$

$$\mathbf{u}_\beta=\left\langle\mathbf{u}_\beta\right\rangle^\beta+\mathbf{u}'_\beta\tag{B-8}$$

Substitute equations (B-7) and (B-8) into the LHS of equation (B-6), we obtain the following:

$$
\begin{aligned}
&\varepsilon_\beta \frac{\partial \left\langle C_\beta \right\rangle^\beta}{\partial t} + \left\langle C_\beta \right\rangle^\beta \frac{\partial \varepsilon_\beta}{\partial t} + \nabla \cdot \left[\left(\left\langle \mathbf{u}_\beta \right\rangle^\beta + \mathbf{u}'_\beta \right) \left(\left\langle C_\beta \right\rangle^\beta + C'_\beta \right) \right] = \\
&\varepsilon_\beta \frac{\partial \left\langle C_\beta \right\rangle^\beta}{\partial t} + \left\langle C_\beta \right\rangle^\beta \left(\frac{\partial \varepsilon_\beta}{\partial t} + \nabla \cdot \left\langle \mathbf{u}_\beta \right\rangle^\beta + \nabla \cdot \mathbf{u}'_\beta \right) + C'_\beta \left(\nabla \cdot \left\langle \mathbf{u}_\beta \right\rangle^\beta + \nabla \cdot \mathbf{u}'_\beta \right) \qquad \text{(B-9)} \\
&+ \left\langle \mathbf{u}_\beta \right\rangle^\beta \cdot \left(\varepsilon_\beta \nabla \left\langle C_\beta \right\rangle^\beta \right) + \mathbf{u}'_\beta \cdot \left(\nabla \left\langle C_\beta \right\rangle + C'_\beta \right)
\end{aligned}
$$

The following approximations are made:

$$
\begin{aligned}
&\left\langle C'_\beta \right\rangle \approx 0 \\
&\left\langle \mathbf{u}'_\beta \right\rangle \approx 0
\end{aligned}
\qquad \text{(B-10)}
$$

As a result, these terms become negligible:

$$
\begin{aligned}
&\left\langle C_\beta \right\rangle^\beta \nabla \cdot \mathbf{u}'_\beta \approx 0 \\
&C'_\beta \nabla \cdot \left\langle \mathbf{u}_\beta \right\rangle^\beta \approx 0 \\
&\left\langle \mathbf{u}_\beta \right\rangle^\beta \cdot \nabla C'_\beta \approx 0 \\
&\mathbf{u}'_\beta \cdot \nabla \left\langle C_\beta \right\rangle^\beta \approx 0
\end{aligned}
\qquad \text{(B-11)}
$$

Moreover, the continuity equation for an incompressible fluid gives

$$
\frac{\partial \varepsilon_\beta}{\partial t} + \nabla \cdot \left\langle \mathbf{u}_\beta \right\rangle^\beta = 0 \qquad \text{(B-12)}
$$

Combing equations (B-10) to (B-12), the LHS of equation (B-6) can be written as:

$$\begin{aligned}&\varepsilon_\beta \frac{\partial\left\langle C_\beta\right\rangle^\beta}{\partial t} + C'_\beta \nabla\cdot\mathbf{u}'_\beta + \varepsilon_\beta \left\langle\mathbf{u}_\beta\right\rangle^\beta\cdot\nabla\left\langle C_\beta\right\rangle^\beta + \mathbf{u}'_\beta\cdot\nabla C'_\beta \\ &= \varepsilon_\beta \frac{\partial\left\langle C_\beta\right\rangle^\beta}{\partial t} + \nabla\cdot\left\langle\mathbf{u}'_\beta C'_\beta\right\rangle + \varepsilon_\beta\left\langle\mathbf{u}_\beta\right\rangle^\beta\cdot\nabla\left\langle C_\beta\right\rangle^\beta\end{aligned} \qquad \text{(B-13)}$$

Similarly, we can substitute equations (B-7) and (B-8) into the RHS of equation (B-6). First, let us focus on the diffusion term:

$$\begin{aligned}&\nabla\cdot\left[D\left(\nabla\left\langle C_\beta\right\rangle + \frac{1}{V}\int_{A_{\beta\gamma}}\mathbf{n}_{\beta\gamma}C_\beta dA + \frac{1}{V}\int_{A_{\beta\sigma}}\mathbf{n}_{\beta\sigma}C_\beta dA\right)\right] \\ &= \nabla\cdot\left[D\left(\begin{aligned}&\varepsilon_\beta\nabla\left\langle C_\beta\right\rangle^\beta + \underline{\left\langle C_\beta\right\rangle^\beta\nabla\varepsilon_\beta} + \frac{1}{V}\int_{A_{\beta\gamma}}\mathbf{n}_{\beta\gamma}C'_\beta dA + \underline{\frac{1}{V}\int_{A_{\beta\gamma}}\mathbf{n}_{\beta\gamma}\left\langle C_\beta\right\rangle^\beta dA} \\ &+\frac{1}{V}\int_{A_{\beta\sigma}}\mathbf{n}_{\beta\sigma}C'_\beta dA + \underline{\frac{1}{V}\int_{A_{\beta\sigma}}\mathbf{n}_{\beta\sigma}\left\langle C_\beta\right\rangle^\beta dA}\end{aligned}\right)\right]\end{aligned} \qquad \text{(B-14)}$$

To show that the summation of the terms underlined in equation (B-14) equals zero, we:

1. Invoke the same approximations as for the LHS and move $\left\langle C_\beta\right\rangle^\beta$ outside of the interfacial area integral.
2. Apply the averaging theorem that gives $\nabla\varepsilon_\beta = -\frac{1}{V}\int_{A_{\beta\gamma}}\mathbf{n}_{\beta\gamma}dA - \frac{1}{V}\int_{A_{\beta\sigma}}\mathbf{n}_{\beta\sigma}dA$

Second, let us focus on the interfacial flux term:

$$\begin{aligned}
&\frac{1}{V}\int_{A_{\beta\gamma}} \mathbf{n}_{\beta\gamma}\cdot\left(D\nabla C_\beta\right)dA+\frac{1}{V}\int_{A_{\beta\sigma}} \mathbf{n}_{\beta\sigma}\cdot\left(D\nabla C_\beta\right)dA\\
&=\frac{1}{V}\int_{A_{\beta\gamma}} \mathbf{n}_{\beta\gamma}\cdot D\nabla\left(\left\langle C_\beta\right\rangle^\beta+C'_\beta\right)dA+\frac{1}{V}\int_{A_{\beta\sigma}} \mathbf{n}_{\beta\sigma}\cdot D\nabla\left(\left\langle C_\beta\right\rangle^\beta+C'_\beta\right)dA\\
&=\frac{1}{V}\int_{A_{\beta\gamma}} \mathbf{n}_{\beta\gamma}\cdot D\nabla C'_\beta dA+\frac{1}{V}\int_{A_{\beta\gamma}} \mathbf{n}_{\beta\gamma}\cdot D\nabla\left\langle C_\beta\right\rangle^\beta dA+\frac{1}{V}\int_{A_{\beta\sigma}} \mathbf{n}_{\beta\sigma}\cdot D\nabla C'_\beta dA\\
&+\frac{1}{V}\int_{A_{\beta\sigma}} \mathbf{n}_{\beta\sigma}\cdot D\nabla\left\langle C_\beta\right\rangle^\beta dA
\end{aligned}\tag{B-15}$$

Combining equations (B-14) and (B-15), the RHS of equation (B-6) can be written as:

$$\begin{aligned}
&=\nabla\cdot\left[D\left(\varepsilon_\beta\nabla\left\langle C_\beta\right\rangle^\beta+\frac{1}{V}\int_{A_{\beta\gamma}}\mathbf{n}_{\beta\gamma}C'_\beta dA+\frac{1}{V}\int_{A_{\beta\sigma}}\mathbf{n}_{\beta\sigma}C'_\beta dA\right)\right]\\
&+\frac{1}{V}\int_{A_{\beta\gamma}} \mathbf{n}_{\beta\gamma}\cdot D\nabla C'_\beta dA+\frac{1}{V}\int_{A_{\beta\gamma}} \mathbf{n}_{\beta\gamma}\cdot D\nabla\left\langle C_\beta\right\rangle^\beta dA+\frac{1}{V}\int_{A_{\beta\sigma}} \mathbf{n}_{\beta\sigma}\cdot D\nabla C'_\beta dA\\
&+\frac{1}{V}\int_{A_{\beta\sigma}} \mathbf{n}_{\beta\sigma}\cdot D\nabla\left\langle C_\beta\right\rangle^\beta dA
\end{aligned}\tag{B-16}$$

Reassembling equations (B-13) and (B-16), the **averaged equation** in (B-6) becomes:

$$\begin{aligned}
&\underbrace{\varepsilon_\beta\frac{\partial\left\langle C_\beta\right\rangle^\beta}{\partial t}}_{\text{accum}}+\underbrace{\nabla\cdot\left\langle\mathbf{u}'_\beta C'_\beta\right\rangle}_{\text{dispersion}}+\underbrace{\varepsilon_\beta\left\langle\mathbf{u}_\beta\right\rangle^\beta\cdot\nabla\left\langle C_\beta\right\rangle^\beta}_{\text{convection}}=\\
&\underbrace{\nabla\cdot\left[D\left(\varepsilon_\beta\nabla\left\langle C_\beta\right\rangle^\beta+\frac{1}{V}\int_{A_{\beta\gamma}}\mathbf{n}_{\beta\gamma}C'_\beta dA+\frac{1}{V}\int_{A_{\beta\sigma}}\mathbf{n}_{\beta\sigma}C'_\beta dA\right)\right]}_{\text{diffusion}}\\
&\underbrace{\begin{aligned}&+\frac{1}{V}\int_{A_{\beta\gamma}} \mathbf{n}_{\beta\gamma}\cdot D\nabla C'_\beta dA+\frac{1}{V}\int_{A_{\beta\gamma}} \mathbf{n}_{\beta\gamma}\cdot D\nabla\left\langle C_\beta\right\rangle^\beta dA+\frac{1}{V}\int_{A_{\beta\sigma}} \mathbf{n}_{\beta\sigma}\cdot D\nabla C'_\beta dA\\
&+\frac{1}{V}\int_{A_{\beta\sigma}} \mathbf{n}_{\beta\sigma}\cdot D\nabla\left\langle C_\beta\right\rangle^\beta dA\end{aligned}}_{\text{interfacial flux}}
\end{aligned}\tag{B-17}$$

The deviation equation is obtained by subtracting the averaged equation from the original point-scale material balance in equation (B-2). First, rearrange the averaged equation:

$$\begin{aligned}
&\frac{\partial \left\langle C_\beta \right\rangle^\beta}{\partial t} + \varepsilon_\beta^{-1} \nabla \cdot \left\langle \mathbf{u}'_\beta C'_\beta \right\rangle + \left\langle \mathbf{u}_\beta \right\rangle^\beta \cdot \nabla \left\langle C_\beta \right\rangle^\beta = \\
&\nabla \cdot \left(D \nabla \left\langle C_\beta \right\rangle^\beta \right) + \varepsilon_\beta^{-1} \nabla \cdot \left[D \left(\frac{1}{V} \int_{A_{\beta\gamma}} \mathbf{n}_{\beta\gamma} C'_\beta dA + \frac{1}{V} \int_{A_{\beta\sigma}} \mathbf{n}_{\beta\sigma} C'_\beta dA \right) \right] \\
&+ \frac{\varepsilon_\beta^{-1}}{V} \int_{A_{\beta\gamma}} \mathbf{n}_{\beta\gamma} \cdot D \nabla C'_\beta dA + \frac{\varepsilon_\beta^{-1}}{V} \int_{A_{\beta\gamma}} \mathbf{n}_{\beta\gamma} \cdot D \nabla \left\langle C_\beta \right\rangle^\beta dA \\
&+ \frac{\varepsilon_\beta^{-1}}{V} \int_{A_{\beta\sigma}} \mathbf{n}_{\beta\sigma} \cdot D \nabla C'_\beta dA + \frac{\varepsilon_\beta^{-1}}{V} \int_{A_{\beta\sigma}} \mathbf{n}_{\beta\sigma} \cdot D \nabla \left\langle C_\beta \right\rangle^\beta dA
\end{aligned} \tag{B-18}$$

The next step is to expand the convection term in equation (B-2).

$$\frac{\partial C_\beta}{\partial t} + \mathbf{u}_\beta \cdot \nabla C_\beta + \underline{C_\beta \cdot \nabla \mathbf{u}_\beta} = \nabla \cdot \left(D \nabla C_\beta \right) \tag{B-19}$$

The term underlined in equation (B-19) is equal to zero because of the incompressibility assumption. We finally subtract equation (B-18) from equation (B-19) to obtain the deviation equation:

$$\begin{aligned}
&\frac{\partial C'_\beta}{\partial t} - \varepsilon_\beta^{-1} \nabla \cdot \left\langle \mathbf{u}'_\beta C'_\beta \right\rangle \underline{- \left\langle \mathbf{u}_\beta \right\rangle^\beta \cdot \nabla \left\langle C_\beta \right\rangle^\beta + \mathbf{u}_\beta \cdot \nabla C_\beta} = \\
&\nabla \cdot \left(D \nabla C'_\beta \right) - \varepsilon_\beta^{-1} \nabla \cdot \left[D \left(\frac{1}{V} \int_{A_{\beta\gamma}} \mathbf{n}_{\beta\gamma} C'_\beta dA + \frac{1}{V} \int_{A_{\beta\sigma}} \mathbf{n}_{\beta\sigma} C'_\beta dA \right) \right] \\
&- \varepsilon_\beta^{-1} \left(\begin{aligned} &\frac{1}{V} \int_{A_{\beta\gamma}} \mathbf{n}_{\beta\gamma} \cdot D \nabla C'_\beta dA + \frac{1}{V} \int_{A_{\beta\gamma}} \mathbf{n}_{\beta\gamma} \cdot D \nabla \left\langle C_\beta \right\rangle^\beta dA \\ &+ \frac{1}{V} \int_{A_{\beta\sigma}} \mathbf{n}_{\beta\sigma} \cdot D \nabla C'_\beta dA + \frac{1}{V} \int_{A_{\beta\sigma}} \mathbf{n}_{\beta\sigma} \cdot D \nabla \left\langle C_\beta \right\rangle^\beta dA \end{aligned} \right)
\end{aligned} \tag{B-20}$$

The terms underlined in equation (B-20) can be simplified as:

$$
\begin{aligned}
&-\left\langle \mathbf{u}_{\beta}\right\rangle^{\beta}\cdot\nabla\left\langle C_{\beta}\right\rangle^{\beta}+\mathbf{u}_{\beta}\cdot\nabla C_{\beta}=-\left(\mathbf{u}_{\beta}-\mathbf{u}'_{\beta}\right)\cdot\nabla\left(C_{\beta}-C'_{\beta}\right)+\mathbf{u}_{\beta}\cdot\nabla C_{\beta}\\
&=-\mathbf{u}_{\beta}\cdot\nabla C_{\beta}+\mathbf{u}_{\beta}\cdot\nabla C'_{\beta}+\mathbf{u}'_{\beta}\cdot\nabla C_{\beta}-\mathbf{u}_{\beta}{}'\cdot\nabla C'_{\beta}+\mathbf{u}_{\beta}\cdot\nabla C_{\beta}\\
&=-\mathbf{u}_{\beta}\cdot\nabla C_{\beta}+\mathbf{u}_{\beta}\cdot\nabla C'_{\beta}+\mathbf{u}'_{\beta}\cdot\nabla\left\langle C_{\beta}\right\rangle^{\beta}+\mathbf{u}_{\beta}\cdot\nabla C_{\beta}\\
&=\mathbf{u}_{\beta}\cdot\nabla C'_{\beta}+\mathbf{u}'_{\beta}\cdot\nabla\left\langle C_{\beta}\right\rangle^{\beta}
\end{aligned}
\tag{B-21}
$$

Substituting equation (B-21) into equation (B-20), the final form for the **deviation equation** can be written as:

$$
\begin{aligned}
&\frac{\partial C'_{\beta}}{\partial t}-\varepsilon_{\beta}{}^{-1}\nabla\cdot\left\langle \mathbf{u}'_{\beta}C'_{\beta}\right\rangle+\mathbf{u}_{\beta}\cdot\nabla C'_{\beta}+\mathbf{u}'_{\beta}\cdot\nabla\left\langle C_{\beta}\right\rangle^{\beta}=\nabla\cdot\left(D\nabla C'_{\beta}\right)\\
&-\varepsilon_{\beta}{}^{-1}\nabla\cdot\left[D\left(\frac{1}{V}\int_{A_{\beta\gamma}}\mathbf{n}_{\beta\gamma}C'_{\beta}dA+\frac{1}{V}\int_{A_{\beta\sigma}}\mathbf{n}_{\beta\sigma}C'_{\beta}dA\right)\right]\\
&-\varepsilon_{\beta}{}^{-1}\left(\begin{aligned}&\frac{1}{V}\int_{A_{\beta\gamma}}\mathbf{n}_{\beta\gamma}\cdot D\nabla C'_{\beta}dA+\frac{1}{V}\int_{A_{\beta\gamma}}\mathbf{n}_{\beta\gamma}\cdot D\nabla\left\langle C_{\beta}\right\rangle^{\beta}dA\\&+\frac{1}{V}\int_{A_{\beta\sigma}}\mathbf{n}_{\beta\sigma}\cdot D\nabla C'_{\beta}dA+\frac{1}{V}\int_{A_{\beta\sigma}}\mathbf{n}_{\beta\sigma}\cdot D\nabla\left\langle C_{\beta}\right\rangle^{\beta}dA\end{aligned}\right)
\end{aligned}
\tag{B-22}
$$

STEP 4: CLOSURE PROCEDURE

The use of a closure procedure to solve for the decomposition of average and deviation concentrations has been discussed in details in Chapter 4. The general steps can be outlined as follows:

1. Identify the sources – generators of the C'_β - field (they are underlined in the following equations).

$$\begin{aligned}
&\frac{\partial C'_\beta}{\partial t} - \varepsilon_\beta^{-1}\nabla\cdot\left\langle \mathbf{u}'_\beta C'_\beta \right\rangle + \mathbf{u}_\beta\cdot\nabla C'_\beta + \underline{\mathbf{u}'_\beta\cdot\nabla\left\langle C_\beta\right\rangle^\beta} = \nabla\cdot\left(D\nabla C'_\beta\right) \\
&-\varepsilon_\beta^{-1}\nabla\cdot\left[D\left(\frac{1}{V}\int_{A_{\beta\gamma}} \mathbf{n}_{\beta\gamma} C'_\beta dA + \frac{1}{V}\int_{A_{\beta\sigma}} \mathbf{n}_{\beta\sigma} C'_\beta dA\right)\right] \qquad \text{(B-23)} \\
&-\varepsilon_\beta^{-1}\left(\begin{aligned}&\frac{1}{V}\int_{A_{\beta\gamma}} \mathbf{n}_{\beta\gamma}\cdot D\nabla C'_\beta dA + \frac{1}{V}\int_{A_{\beta\gamma}} \mathbf{n}_{\beta\gamma}\cdot D\nabla\left\langle C_\beta\right\rangle^\beta dA \\ &+\frac{1}{V}\int_{A_{\beta\sigma}} \mathbf{n}_{\beta\sigma}\cdot D\nabla C'_\beta dA + \frac{1}{V}\int_{A_{\beta\sigma}} \mathbf{n}_{\beta\sigma}\cdot D\nabla\left\langle C_\beta\right\rangle^\beta dA\end{aligned}\right)
\end{aligned}$$

B.C.: $C'_\beta = \underline{C_{eq} - \left\langle C_\beta\right\rangle^\beta}$ at $A_{\beta\gamma}$

$\mathbf{n}_{\beta\sigma}\cdot\nabla C'_\beta = -\mathbf{n}_{\beta\sigma}\cdot\underline{\nabla\left\langle C_\beta\right\rangle^\beta}$ at $A_{\beta\sigma}$

2. Propose a form of solution in terms of closure variables based on the source terms identified in the previous step. Following the discussion in Chapter 4, the closure variable is defined as $C'_\beta = s_\beta\left(C_{eq} - \left\langle C_\beta\right\rangle^\beta\right)$.

3. Simply the problem – in some situations one can perform order of magnitude analysis to eliminate terms that are small. Assuming the transient term is small, we can substitute the closure expression into the deviation equation.

$$\begin{aligned}
&-\varepsilon_\beta{}^{-1}\nabla\cdot\left\langle \mathbf{u}'_\beta s_\beta\left(C_{eq}-\left\langle C_\beta\right\rangle^\beta\right)\right\rangle+\mathbf{u}_\beta\cdot\nabla\left[s_\beta\left(C_{eq}-\left\langle C_\beta\right\rangle^\beta\right)\right]+\mathbf{u}'_\beta\cdot\nabla\left\langle C_\beta\right\rangle^\beta\\
&=\nabla\cdot\left(D\nabla\left[s_\beta\left(C_{eq}-\left\langle C_\beta\right\rangle^\beta\right)\right]\right)\\
&-\varepsilon_\beta{}^{-1}\nabla\cdot\left[D\left(\frac{1}{V}\int\limits_{A_{\beta\gamma}}\mathbf{n}_{\beta\gamma}s_\beta\left(C_{eq}-\left\langle C_\beta\right\rangle^\beta\right)dA+\frac{1}{V}\int\limits_{A_{\beta\sigma}}\mathbf{n}_{\beta\sigma}s_\beta\left(C_{eq}-\left\langle C_\beta\right\rangle^\beta\right)dA\right)\right]\\
&-\varepsilon_\beta{}^{-1}\left(\begin{aligned}&\frac{1}{V}\int\limits_{A_{\beta\gamma}}\mathbf{n}_{\beta\gamma}\cdot D\nabla\left[s_\beta\left(C_{eq}-\left\langle C_\beta\right\rangle^\beta\right)\right]dA+\frac{1}{V}\int\limits_{A_{\beta\sigma}}\mathbf{n}_{\beta\sigma}\cdot D\nabla\left[s_\beta\left(C_{eq}-\left\langle C_\beta\right\rangle^\beta\right)\right]dA\\&+\frac{1}{V}\int\limits_{A_{\beta\gamma}}\mathbf{n}_{\beta\gamma}\cdot D\nabla\left\langle C_\beta\right\rangle^\beta dA+\frac{1}{V}\int\limits_{A_{\beta\sigma}}\mathbf{n}_{\beta\sigma}\cdot D\nabla\left\langle C_\beta\right\rangle^\beta dA\end{aligned}\right)
\end{aligned}\tag{B-24}$$

Simplify the RHS of equation (B-24) as follows:

$$\begin{aligned}
&\underline{-\varepsilon_\beta{}^{-1}\left(C_{eq}-\left\langle C_\beta\right\rangle^\beta\right)s_\beta\nabla\cdot\left\langle\mathbf{u}'_\beta\right\rangle-\varepsilon_\beta{}^{-1}\left(C_{eq}-\left\langle C_\beta\right\rangle^\beta\right)\left\langle\mathbf{u}'_\beta\right\rangle\cdot\nabla s_\beta}\\
&\underline{-\varepsilon_\beta{}^{-1}s_\beta\left\langle\mathbf{u}'_\beta\right\rangle\cdot\nabla\left(C_{eq}-\left\langle C_\beta\right\rangle^\beta\right)}+\mathbf{u}_\beta\cdot\nabla s_\beta\left(C_{eq}-\left\langle C_\beta\right\rangle^\beta\right)\\
&+\mathbf{u}_\beta s_\beta\cdot\nabla\left(C_{eq}-\left\langle C_\beta\right\rangle^\beta\right)+\mathbf{u}'_\beta\cdot\nabla\left\langle C_\beta\right\rangle^\beta=\nabla\cdot\left(D\nabla\left[s_\beta\left(C_{eq}-\left\langle C_\beta\right\rangle^\beta\right)\right]\right)\\
&-\varepsilon_\beta{}^{-1}\frac{D}{V}\left[\nabla\cdot\int\limits_{A_{\beta\gamma}}\mathbf{n}_{\beta\gamma}s_\beta\left(C_{eq}-\left\langle C_\beta\right\rangle^\beta\right)dA+\nabla\cdot\int\limits_{A_{\beta\sigma}}\mathbf{n}_{\beta\sigma}s_\beta\left(C_{eq}-\left\langle C_\beta\right\rangle^\beta\right)dA\right]\\
&-\varepsilon_\beta{}^{-1}\frac{D}{V}\left[\int\limits_{A_{\beta\gamma}}\mathbf{n}_{\beta\gamma}\cdot\nabla\left[s_\beta\left(C_{eq}-\left\langle C_\beta\right\rangle^\beta\right)\right]dA+\int\limits_{A_{\beta\sigma}}\mathbf{n}_{\beta\sigma}\cdot\nabla\left[s_\beta\left(C_{eq}-\left\langle C_\beta\right\rangle^\beta\right)\right]dA\right]\\
&-\varepsilon_\beta{}^{-1}\frac{D}{V}\left[\int\limits_{A_{\beta\gamma}}\mathbf{n}_{\beta\gamma}\cdot\nabla\left\langle C_\beta\right\rangle^\beta dA+\int\limits_{A_{\beta\sigma}}\mathbf{n}_{\beta\sigma}\cdot\nabla\left\langle C_\beta\right\rangle^\beta dA\right]
\end{aligned}\tag{B-25}$$

The terms underlined in equation (B-25) are equal to zero; the first term is zero due to incompressibility, while the remaining terms are zero because of the assumption that $\left\langle \mathbf{u}'_{\beta} \right\rangle \approx 0$. Finally, expand the diffusion term in equation (B-25):

$$\begin{aligned}
&\nabla \cdot \left(D\nabla\left[s_{\beta}\left(C_{eq} - \left\langle C_{\beta} \right\rangle^{\beta} \right) \right] \right) \\
&= \nabla \cdot \left(D\left(C_{eq} - \left\langle C_{\beta} \right\rangle^{\beta} \right)\nabla s_{\beta} + Ds_{\beta}\nabla\left(C_{eq} - \left\langle C_{\beta} \right\rangle^{\beta} \right) \right) \\
&= D\left(2\nabla\left(C_{eq} - \left\langle C_{\beta} \right\rangle^{\beta} \right) \cdot \nabla s_{\beta} + \left(C_{eq} - \left\langle C_{\beta} \right\rangle^{\beta} \right)\nabla^{2} s_{\beta} + s_{\beta}\nabla^{2}\left(C_{eq} - \left\langle C_{\beta} \right\rangle^{\beta} \right) \right) \\
&= 2D\nabla\left(C_{eq} - \left\langle C_{\beta} \right\rangle^{\beta} \right) \cdot \nabla s_{\beta} + D\left(C_{eq} - \left\langle C_{\beta} \right\rangle^{\beta} \right)\nabla^{2} s_{\beta} + Ds_{\beta}\nabla^{2}\left(C_{eq} - \left\langle C_{\beta} \right\rangle^{\beta} \right)
\end{aligned} \tag{B-26}$$

Utilizing equations (B-25) and (B-26), equation (B-24) becomes:

$$\begin{aligned}
&\mathbf{u}_{\beta} \cdot \nabla s_{\beta}\left(C_{eq} - \left\langle C_{\beta} \right\rangle^{\beta} \right) + \mathbf{u}_{\beta} s_{\beta} \cdot \nabla\left(C_{eq} - \left\langle C_{\beta} \right\rangle^{\beta} \right) + \mathbf{u}'_{\beta} \cdot \nabla\left\langle C_{\beta} \right\rangle^{\beta} \\
&= 2D\nabla\left(C_{eq} - \left\langle C_{\beta} \right\rangle^{\beta} \right) \cdot \nabla s_{\beta} + D\left(C_{eq} - \left\langle C_{\beta} \right\rangle^{\beta} \right)\nabla^{2} s_{\beta} + Ds_{\beta}\nabla^{2}\left(C_{eq} - \left\langle C_{\beta} \right\rangle^{\beta} \right) \\
&-\varepsilon_{\beta}^{-1}\frac{D}{V}\left[\nabla \cdot \int_{A_{\beta\gamma}} \mathbf{n}_{\beta\gamma} s_{\beta}\left(C_{eq} - \left\langle C_{\beta} \right\rangle^{\beta} \right) dA + \nabla \cdot \int_{A_{\beta\sigma}} \mathbf{n}_{\beta\sigma} s_{\beta}\left(C_{eq} - \left\langle C_{\beta} \right\rangle^{\beta} \right) dA \right] \\
&-\varepsilon_{\beta}^{-1}\frac{D}{V}\left[\begin{array}{l} \displaystyle\int_{A_{\beta\gamma}} \mathbf{n}_{\beta\gamma} \cdot \nabla\left[s_{\beta}\left(C_{eq} - \left\langle C_{\beta} \right\rangle^{\beta} \right) \right] dA + \int_{A_{\beta\sigma}} \mathbf{n}_{\beta\sigma} \cdot \nabla\left[s_{\beta}\left(C_{eq} - \left\langle C_{\beta} \right\rangle^{\beta} \right) \right] dA \\ \displaystyle + \int_{A_{\beta\gamma}} \mathbf{n}_{\beta\gamma} \cdot \nabla\left\langle C_{\beta} \right\rangle^{\beta} dA + \int_{A_{\beta\sigma}} \mathbf{n}_{\beta\sigma} \cdot \nabla\left\langle C_{\beta} \right\rangle^{\beta} dA \end{array} \right]
\end{aligned} \tag{B-27}$$

Equation (B-27) can be rearranged to this final form:

$$\begin{aligned}
&\left[\mathbf{u}_\beta - 2D\frac{\nabla\left(C_{eq}-\left\langle C_\beta\right\rangle^\beta\right)}{\left(C_{eq}-\left\langle C_\beta\right\rangle^\beta\right)}\right]\cdot\nabla s_\beta = -\mathbf{u}'_\beta\cdot\frac{\nabla\left\langle C_\beta\right\rangle^\beta}{\left(C_{eq}-\left\langle C_\beta\right\rangle^\beta\right)} + D\nabla^2 s_\beta \\
&+\left[-\mathbf{u}_\beta\cdot\frac{\nabla\left(C_{eq}-\left\langle C_\beta\right\rangle^\beta\right)}{\left(C_{eq}-\left\langle C_\beta\right\rangle^\beta\right)} + D\frac{\nabla^2\left(C_{eq}-\left\langle C_\beta\right\rangle^\beta\right)}{\left(C_{eq}-\left\langle C_\beta\right\rangle^\beta\right)}\right]s_\beta - \varepsilon_\beta^{-1}\frac{D}{V\left(C_{eq}-\left\langle C_\beta\right\rangle^\beta\right)}\cdot \\
&\left[\begin{aligned}
&\nabla\cdot\int_{A_{\beta\gamma}}\mathbf{n}_{\beta\gamma}s_\beta\left(C_{eq}-\left\langle C_\beta\right\rangle^\beta\right)dA + \nabla\cdot\int_{A_{\beta\sigma}}\mathbf{n}_{\beta\sigma}s_\beta\left(C_{eq}-\left\langle C_\beta\right\rangle^\beta\right)dA \\
&+\int_{A_{\beta\gamma}}\mathbf{n}_{\beta\gamma}\cdot\nabla\left[s_\beta\left(C_{eq}-\left\langle C_\beta\right\rangle^\beta\right)\right]dA + \int_{A_{\beta\sigma}}\mathbf{n}_{\beta\sigma}\cdot\nabla\left[s_\beta\left(C_{eq}-\left\langle C_\beta\right\rangle^\beta\right)\right]dA \\
&+\int_{A_{\beta\gamma}}\mathbf{n}_{\beta\gamma}\cdot\nabla\left\langle C_\beta\right\rangle^\beta dA + \int_{A_{\beta\sigma}}\mathbf{n}_{\beta\sigma}\cdot\nabla\left\langle C_\beta\right\rangle^\beta dA
\end{aligned}\right]
\end{aligned} \tag{B-28}$$

Boundary conditions must now be re-written in terms of the closure formulation:

B.C.: $C'_\beta = C_{eq} - \left\langle C_\beta\right\rangle^\beta$ at $A_{\beta\gamma}$

$$\mathbf{n}_{\beta\sigma}\cdot\nabla C'_\beta = -\mathbf{n}_{\beta\sigma}\cdot\nabla\left\langle C_\beta\right\rangle^\beta \text{ at } A_{\beta\sigma} \tag{B-29}$$

This is equivalent to the following written in terms of s_β:

B.C.: $s_\beta = 1$ at $A_{\beta\gamma}$

at $A_{\beta\sigma}$,

$$\mathbf{n}_{\beta\sigma}\cdot\nabla s_\beta\left(C_{eq}-\left\langle C_\beta\right\rangle^\beta\right) + \mathbf{n}_{\beta\sigma}s_\beta\cdot\nabla\left(C_{eq}-\left\langle C_\beta\right\rangle^\beta\right) = -\mathbf{n}_{\beta\sigma}\cdot\nabla\left\langle C_\beta\right\rangle^\beta$$

or

$$\mathbf{n}_{\beta\sigma}\cdot\nabla s_\beta + \frac{\mathbf{n}_{\beta\sigma}s_\beta\cdot\nabla\left(C_{eq}-\left\langle C_\beta\right\rangle^\beta\right)}{C_{eq}-\left\langle C_\beta\right\rangle^\beta} + \frac{\mathbf{n}_{\beta\sigma}\cdot\nabla\left\langle C_\beta\right\rangle}{C_{eq}-\left\langle C_\beta\right\rangle^\beta} = 0 \tag{B-30}$$

STEP 5: EVALUATION OF EFFECTIVE TRANSPORT

The averaged equation is used describe the effective transport. Substitute the closure formulation $C'_\beta = s_\beta\left(C_{eq} - \left\langle C_\beta \right\rangle^\beta\right)$ back into the averaged equation:

$$
\begin{aligned}
&\varepsilon_\beta \frac{\partial \left\langle C_\beta \right\rangle^\beta}{\partial t} + \nabla \cdot \left\langle \mathbf{u}'_\beta s_\beta \left(C_{eq} - \left\langle C_\beta \right\rangle^\beta \right) \right\rangle + \varepsilon_\beta \left\langle \mathbf{u}_\beta \right\rangle^\beta \cdot \nabla \left\langle C_\beta \right\rangle^\beta = \\
&\nabla \cdot \left[D \left(\varepsilon_\beta \nabla \left\langle C_\beta \right\rangle^\beta + \frac{1}{V} \int_{A_{\beta\gamma}} \mathbf{n}_{\beta\gamma} s_\beta \left(C_{eq} - \left\langle C_\beta \right\rangle^\beta \right) dA + \frac{1}{V} \int_{A_{\beta\sigma}} \mathbf{n}_{\beta\sigma} s_\beta \left(C_{eq} - \left\langle C_\beta \right\rangle^\beta \right) dA \right) \right] \\
&+ \frac{1}{V} \int_{A_{\beta\gamma}} \mathbf{n}_{\beta\gamma} \cdot D \nabla \left[s_\beta \left(C_{eq} - \left\langle C_\beta \right\rangle^\beta \right) \right] dA + \frac{1}{V} \int_{A_{\beta\sigma}} \mathbf{n}_{\beta\sigma} \cdot D \nabla \left[s_\beta \left(C_{eq} - \left\langle C_\beta \right\rangle^\beta \right) \right] dA \\
&+ \frac{1}{V} \int_{A_{\beta\gamma}} \mathbf{n}_{\beta\gamma} \cdot D \nabla \left\langle C_\beta \right\rangle^\beta dA + \frac{1}{V} \int_{A_{\beta\sigma}} \mathbf{n}_{\beta\sigma} \cdot D \nabla \left\langle C_\beta \right\rangle^\beta dA
\end{aligned}
\tag{B-31}
$$

Rearranging equation (B-32) gives equation (B-33).

$$
\begin{aligned}
&\varepsilon_\beta \frac{\partial \left\langle C_\beta \right\rangle^\beta}{\partial t} + \nabla \cdot \left\langle \mathbf{u}'_\beta s_\beta \left(C_{eq} - \left\langle C_\beta \right\rangle^\beta \right) \right\rangle + \varepsilon_\beta \left\langle \mathbf{u}_\beta \right\rangle^\beta \cdot \nabla \left\langle C_\beta \right\rangle^\beta = \\
&\nabla \cdot \left[\frac{D}{V} \int_{A_{\beta\gamma}} \mathbf{n}_{\beta\gamma} s_\beta \left(C_{eq} - \left\langle C_\beta \right\rangle^\beta \right) dA + \frac{D}{V} \int_{A_{\beta\sigma}} \mathbf{n}_{\beta\sigma} s_\beta \left(C_{eq} - \left\langle C_\beta \right\rangle^\beta \right) dA \right] \\
&+ \nabla \cdot D \varepsilon_\beta \nabla \left\langle C_\beta \right\rangle^\beta - \nabla \varepsilon_\beta \cdot D \nabla \left\langle C_\beta \right\rangle^\beta \\
&+ \frac{D}{V} \left[\begin{aligned} &\int_{A_{\beta\gamma}} \mathbf{n}_{\beta\gamma} \cdot \nabla \left[s_\beta \left(C_{eq} - \left\langle C_\beta \right\rangle^\beta \right) \right] dA + \int_{A_{\beta\sigma}} \mathbf{n}_{\beta\sigma} \cdot \nabla \left[s_\beta \left(C_{eq} - \left\langle C_\beta \right\rangle^\beta \right) \right] dA \\ &+ \int_{A_{\beta\gamma}} \mathbf{n}_{\beta\gamma} \cdot \nabla \left\langle C_\beta \right\rangle^\beta dA + \int_{A_{\beta\sigma}} \mathbf{n}_{\beta\sigma} \cdot \nabla \left\langle C_\beta \right\rangle^\beta dA \end{aligned} \right]
\end{aligned}
\tag{B-32}
$$

If we assume $\nabla\varepsilon_\beta \approx 0$, equation (B-33) becomes:

$$
\begin{aligned}
&\varepsilon_\beta \frac{\partial \left\langle C_\beta \right\rangle^\beta}{\partial t} + \left\langle \mathbf{u}_\beta \right\rangle \cdot \nabla \left\langle C_\beta \right\rangle^\beta = -\nabla \cdot \left\langle \mathbf{u}'_\beta s_\beta \left(C_{eq} - \left\langle C_\beta \right\rangle^\beta \right) \right\rangle + D\varepsilon_\beta \nabla^2 \left\langle C_\beta \right\rangle^\beta \\
&+\nabla \cdot \left[\frac{D}{V} \int_{A_{\beta\gamma}} \mathbf{n}_{\beta\gamma} s_\beta \left(C_{eq} - \left\langle C_\beta \right\rangle^\beta \right) dA + \frac{D}{V} \int_{A_{\beta\sigma}} \mathbf{n}_{\beta\sigma} s_\beta \left(C_{eq} - \left\langle C_\beta \right\rangle^\beta \right) dA \right] \qquad \text{(B-33)} \\
&+\frac{D}{V} \left[\begin{aligned} &\int_{A_{\beta\gamma}} \mathbf{n}_{\beta\gamma} \cdot \nabla \left[s_\beta \left(C_{eq} - \left\langle C_\beta \right\rangle^\beta \right) \right] dA + \int_{A_{\beta\sigma}} \mathbf{n}_{\beta\sigma} \cdot \nabla \left[s_\beta \left(C_{eq} - \left\langle C_\beta \right\rangle^\beta \right) \right] dA \\ &+ \int_{A_{\beta\gamma}} \mathbf{n}_{\beta\gamma} \cdot \nabla \left\langle C_\beta \right\rangle^\beta dA + \int_{A_{\beta\sigma}} \mathbf{n}_{\beta\sigma} \cdot \nabla \left\langle C_\beta \right\rangle^\beta dA \end{aligned} \right]
\end{aligned}
$$

For quasi steady-state (i.e. ignoring the transient term), the final form of the averaged equation can be written as (same as equation (4-8)):

$$
\begin{aligned}
&\underbrace{\left\langle \mathbf{u}_\beta \right\rangle \cdot \nabla \left\langle C_\beta \right\rangle^\beta}_{\text{convection}} = \underbrace{-\nabla \cdot \left\langle \mathbf{u}'_\beta s_\beta \left(C_{eq} - \left\langle C_\beta \right\rangle^\beta \right) \right\rangle}_{\text{dispersion}} + \underbrace{D\varepsilon_\beta \nabla^2 \left\langle C_\beta \right\rangle^\beta}_{\text{diffusion}} \\
&\underbrace{\begin{aligned} &+\nabla \cdot \left[\frac{D}{V} \int_{A_{\beta\gamma}} \mathbf{n}_{\beta\gamma} s_\beta \left(C_{eq} - \left\langle C_\beta \right\rangle^\beta \right) dA + \frac{D}{V} \int_{A_{\beta\sigma}} \mathbf{n}_{\beta\sigma} s_\beta \left(C_{eq} - \left\langle C_\beta \right\rangle^\beta \right) dA \right] \\ &+\frac{D}{V} \left[\begin{aligned} &\int_{A_{\beta\gamma}} \mathbf{n}_{\beta\gamma} \cdot \nabla \left[s_\beta \left(C_{eq} - \left\langle C_\beta \right\rangle^\beta \right) \right] dA + \int_{A_{\beta\sigma}} \mathbf{n}_{\beta\sigma} \cdot \nabla \left[s_\beta \left(C_{eq} - \left\langle C_\beta \right\rangle^\beta \right) \right] dA \\ &+ \int_{A_{\beta\gamma}} \mathbf{n}_{\beta\gamma} \cdot \nabla \left\langle C_\beta \right\rangle^\beta dA + \int_{A_{\beta\sigma}} \mathbf{n}_{\beta\sigma} \cdot \nabla \left\langle C_\beta \right\rangle^\beta dA \end{aligned} \right] \end{aligned}}_{\substack{\text{mass transfer (reaction,} \\ \text{interfacial transport)}}} \qquad \text{(B-34)}
\end{aligned}
$$

Appendix C: Use of Fine-Scale Solutions in Upscaling and Scale-Up Approaches

In this research, we have proposed to integrate results from fine-scale flow simulations to study scale-up of flow. Fine-scale solutions are commonly used in upscaling procedure; therefore, it is interesting to include a brief discussion regarding the use of fine-scale solutions in traditional upscaling and how those formulations are related to the volume averaging methods. The intent of this appendix is to show that the modeling of sub-grid effects in many upscaling techniques in fact resembles the volume averaging formulations that are adopted for this research.

Durlofsky (1998) and Efendiev et al. (2000) describe an averaging procedure to account for sub-grid effects in the saturation equation for two-phase flow. In their approach, fine-scale quantities are also expressed as the sum of a volume-based average (coarse-grid) and a fluctuation (fine-grid):

$$\Phi = \overline{\Phi} + \Phi' \tag{C-1}$$

where Φ can be quantities such as velocity (**u**), saturation (*S*), or fractional flow (*f*). $\overline{\Phi}$ and Φ' are the averaged and fluctuation quantities, respectively. This decomposition gives rise to the following sets of equations:

Fine-scale equation:

$$\frac{\partial S}{\partial t} + \mathbf{u} \cdot \nabla f\left(S\right) = \frac{\partial \overline{S}}{\partial t} + \frac{\partial S'}{\partial t} + \overline{\mathbf{u}} \cdot \nabla \overline{f} + \overline{\mathbf{u}} \cdot \nabla f' + \mathbf{u}' \cdot \nabla \overline{f} + \mathbf{u}' \cdot \nabla f' = 0 \tag{C-2}$$

Averaged equation:

$$\frac{\partial \overline{S}}{\partial t} + \overline{\mathbf{u}} \cdot \nabla \overline{f} + \overline{\mathbf{u}' \cdot \nabla f'} = 0 \qquad \text{(C-3)}$$

Fluctuation equation (subtracting the averaged equation from fine-scale equation):

$$\frac{\partial S'}{\partial t} + \overline{\mathbf{u}} \cdot \nabla f' + \mathbf{u}' \cdot \nabla \overline{f} + \mathbf{u}' \cdot \nabla f' - \overline{\mathbf{u}' \cdot \nabla f'} = 0 \qquad \text{(C-4)}$$

The fluctuation equation represents sub-grid effects and can be used to generate various moment equations of the fine-scale variables. Another approach is to employ fine-scale solutions to calculate these fluctuation quantities and the averaged equation can be used directly. In many cases, these sub-grid effects can be viewed and computed as correctional diffusive and convective terms (Efendiev and Durlofsky, 2003). Durlofsky (1998) also provided a detailed discussion relating existing upscaling techniques (e.g., flow-based upscaling) to treatment of the volume-averaged equations.

As pointed out by Durlofsky (1998), the volume averaging approach as employed in this research is a “mathematically rigorous technique which provides equations for the coarse scale system,” while their upscaling approach (equations (C-2) to (C-4)) might appear somewhat heuristic (Efendiev and Durlofsky, 2003). The heuristic nature refers to the way the various fluctuation terms are approximated. Furthermore, the interfacial flux terms commonly found in the volume averaging equations are missing explicitly in equations (C-3) and (C-4) but are partially represented by the term $\overline{\mathbf{u}' \cdot \nabla f'}$.

Appendix D: Modeling of Polymer Flow Properties

D.1 OVERVIEW

Scale-up of apparent viscosity and effective shear rate of non-Newtonian polymer flow is discussed in Chapter 7. This appendix serves to provide a brief summary of the important equations needed to model various polymer flow properties in UTCHEHM and the corresponding parameter values used in each equation for generating the results discussed in the chapter. Detailed description of all equations presented in this appendix can be found in UTCHEM Technical Documentation (2000) and UTCHEM User's Guide (2000).

D.2 MODELING OF POLYMER APPARENT VISCOSITY

The viscosity of polymer solution depends on salinity, hardness, and polymer concentration according to the Flory-Huggins equation, as described in UTCHEM Technical Documentation (2000):

$$C_{SEP} = \frac{C_m + \left(\beta_P - 1\right) C_d}{C_w} \tag{D-1}$$

$$\mu_p^0 = \mu_w \left(1 + \left(A_{p1} C_p + A_{p2} C_p{}^2 + A_{p3} C_p{}^3\right) C_{SEP}^{S_p}\right) \tag{D-2}$$

C_{SEP} = effective salinity for polymer (meq/mL)

C_m = concentration of monovalent ions (meq/mL)

C_d = concentration of divalent ions (meq/mL)

C_w = concentration of water (volume fraction)

C_p = concentration of polymer (wt%)

μ_p^0 = polymer viscosity at zero shear rate (cp)

μ_w = water viscosity (cp)

A_{p1} = 35.14

A_{p2} = 1899

A_{p3} = 0

β_P = 20

s_p = -0.3

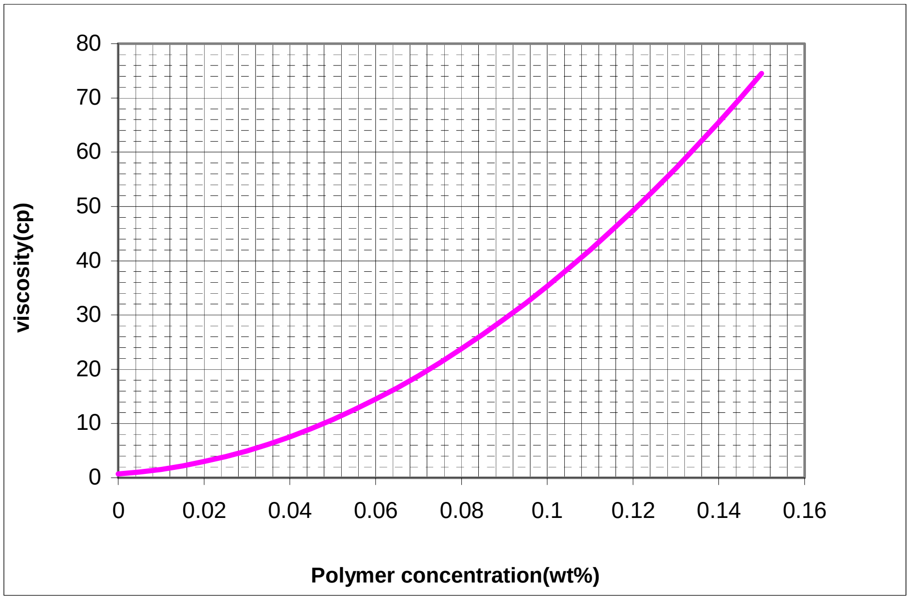

Figure D-1: Viscosity dependence on polymer concentration at injection conditions.

Dependence of shear rate is modeled with the Meter's equation in UTCHEM Technical Documentation (2000):

$$\mu_p = \mu_w + \frac{\mu_p^0 - \mu_w}{1 + \left(\frac{\dot{\gamma}_{eq}}{\dot{\gamma}_{1/2}}\right)^{P_\alpha - 1}} \tag{D-3}$$

$$\dot{\gamma}_{eq} = \frac{\dot{\gamma}_c |u|}{\sqrt{\phi k}} \tag{D-4}$$

$|u|$ = Darcy flux (ft/day)

$\dot{\gamma}_{eq}$ = in-situ shear rate for single phase flow (s^{-1})

k = permeability (Darcy)

μ_p = polymer viscosity (cp)

$\dot{\gamma}_c$ = 130 day*$(\text{Darcy})^{1/2}$/(ft-s)

$\dot{\gamma}_{1/2}$ = 100 s^{-1}

P_α = 1.75 (dimensionless)

Equation (D-3) represents the apparent viscosity dependency on shear rate. However, to apply equation (D-3) for flow in porous media, equation (D-4) is used to compute an *in-situ* or *equivalent* shear rate. Substituting equations (D-3) and (D-4) into the expression for mobility can show its non-linear relationship with porosity, permeability, and velocity.

$$\mathbf{M}_\beta = \frac{\mathbf{k}}{\mu_{app}} \propto \frac{k}{\left(|u|(k\phi)^{-1/2}\right)^{n-1}} \propto \frac{k}{|u|^{n-1}(k\phi)^{-(n-1)/2}} \propto \frac{k^{(n+1)/2}\phi^{(n-1)/2}}{|u|^{n-1}} \tag{D-5}$$

D.3 MODELING OF POLYMER ADSORPTION

Adsorption of polymer is modeled as a function of effective salinity and polymer concentration.

$$\hat{C}_p = \frac{a_4\left(C_p\right)}{1 + b_4 C_p} \qquad \text{(D-6)}$$

$$a_4 = \left(a_{41} + a_{42} C_{SEP}\right) \qquad \text{(D-7)}$$

$\hat{C}_p$ = adsorbed polymer concentration (wt%/pore volume)

a_{41} = 4.33

a_{42} = 0

b_4 = 100

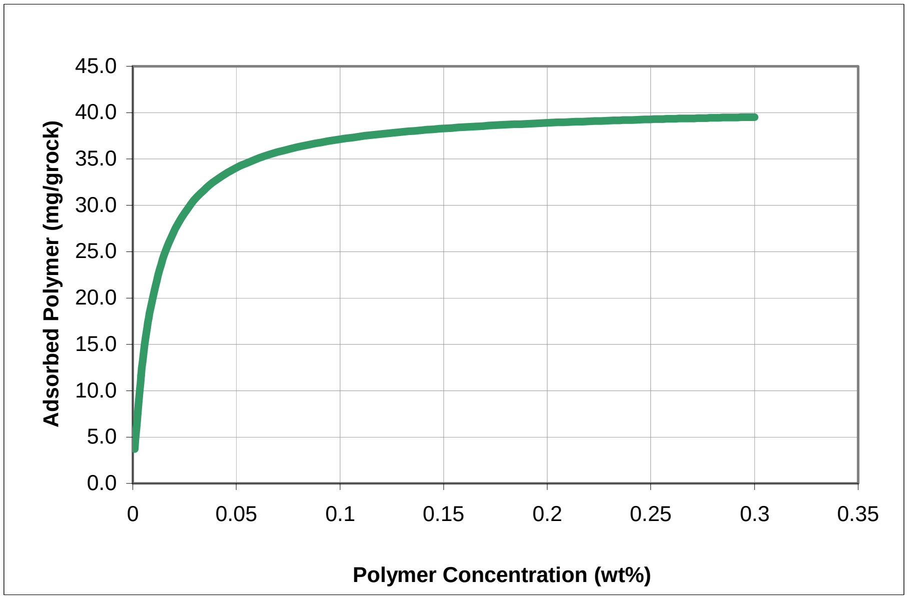

Figure D-2: Polymer adsorption assuming a rock density of 2650g/cc and an average porosity of 0.2.

D.4 MODELING OF PERMEABILITY REDUCTION

Permeability reduction factor is modeled as a function effective salinity, polymer concentration, porosity, and permeability.

$$R_{k,\max} = \min\left\{ \left[1 - \frac{c_{rk}\left(A_{p1} C_{SEP}^{Sp}\right)^{1/3}}{\left(\phi\right)\dfrac{\sqrt{k_x k_y}^{1/2}}{\phi}} \right]^{-4}, 10 \right\} \tag{D-8}$$

$$R_k = 1 + \frac{\left(R_{k\max} - 1\right) b_{rk}\, C_{4\ell}}{1 + b_{rk}\, C_{4\ell}} \tag{D-9}$$

k_x, k_y = permeability in x and y directions (Darcy)

ϕ = porosity (fraction)

R_k = permeability reduction factor

b_{rk} = 4

c_{rk} = 0.15

Appendix E: Simulation Input Files

E.1 OVERVIEW

In this research, numerical flow simulations of the tracer injection processes in Chapters 5 and 6 are performed with ECLISPE 100 (Schlumberger, 2005), while the single-phase polymer flow in Chapter 7 is simulated with UTCHEM (Center for Petroleum and Geosystems Engineering, 2000). In this appendix, sample simulation input files are included for four cases: (1) tracer injection in single phase flow; (2) tracer injection in two phase flow; (3) tracer injection with adsorption for single phase flow; and (4) polymer flow.

E.2 TRACER INJECTION IN SINGLE PHASE FLOW

```
-- =====================================================================
--
--  TRACER INJECTION PROCESS
--  AN INJECTOR IS LOCATED AT (1,1), AND THE PRODUCER IS LOCATED
--  IN THE DIAGONALLY OPPOSITE CORNER GRID CELL (N,N).
--
RUNSPEC
TITLE
   TRACER INJECTION – SINGLE  PHASE

DIMENS
  500   500    1  /

WATER

METRIC

EQLDIMS
   1  400   400    2    2 /

TRACERS
   0    1    0    0  NODIFF /

NOCASC

TABDIMS
   1    1   40   40    2   20 /

REGDIMS
   2    1    0    0  /

WELLDIMS
  10   10    1   10 /
```

```
START
   1 'JAN' 1983  /

FMTOUT

NSTACK
    50 /

GRID      ==============================================================

GRIDFILE
1 /

INIT

DX
  250000*10.0 /

DY
  250000*10.0 /

DZ
  250000*10.0 /

TOPS
  250000*4000.0 /

INCLUDE
'poro.ecl' /

RPTGRID
  'PERMX'  'PERMY' 'PERMZ'  'PORO' /


PROPS     ==============================================================

PVTW
--ref P   Bw                compress   vis             Cv
  1.01325  1.0  4.0E-05  .5  0.0 /

ROCK
--ref P   compress
  1.01325         5.0E-05 /

DENSITY
--oil           water         gas
 600.0  1000.0   1.0 /

-- TRACER NAMES AND THEIR ASSOCIATED STOCK TANK PHASES ARE DEFINED USING
-- THE TRACER KEYWORD

TRACER
 'INJ' 'WAT' 'mg'/
/

TRACTVD

TRDIFINJ
 1e-6  /

RPTPROPS
 8*0 0 1 /

REGIONS    ============================================================

FIPNUM
250000*1
```

```
/

SOLUTION   ==============================================================

PRESSURE
 250000*280.0 /

TBLKFINJ
250000*0 /

RPTSOL
1 1 1 0 0 0 0 4 0 0 0 1 0 0 0 0 0 0 0 0 0 0 0 0 0 0 0 1 0 0 0 1 1 0 0 0 0 0 0 0 0 0 0 0 0 0 0 0 0 0  /

'RESTART=1'
/

SUMMARY    ============================================================

FTPRINJ
FTPTINJ

RUNSUM
RPTSMRY
1 /
SEPARATE


SCHEDULE   ============================================================

RPTRST
VELOCITY
'BASIC=3'
'FREQ=25' /

RPTSCHED
1 1 1 0 0 0 2 2 2 2 2 2 0 1 2 0 0 0 0 0 0 0 0 0 0 0 0 0 0 0 0 2 1 0 0 0 0 0 0 0 0 0 0 0 0 0 0 0 0 0  /


WELSPECS
'I'  'G'  1     1  4000  'WAT'  /
'P3'  'G'  500   500   4000  'WAT'  /
/

COMPDAT
'I'   1  1   1   1 'OPEN'   0  .0   1.0 /
'P3'  500  500   1   1 'OPEN'   0  .0   1.0 /
/

WCONPROD
'P3'            'OPEN' 'WRAT' 1* 1000.0 /
/

WCONINJE
'I' 'WAT' 'OPEN' 'RATE' 1000     /
/

WTRACER
'I' 'INJ' 1  /
/

TSTEP
 800*100.00 /

END
```

E.3 TRACER INJECTION IN TWO PHASE FLOW

```
-- ======================================================================
--
--  TRACER INJECTION PROCESS
--  AN INJECTOR IS LOCATED AT (1,1), AND THE PRODUCER IS LOCATED
--  IN THE DIAGONALLY OPPOSITE CORNER GRID CELL (N,N).
--
RUNSPEC
TITLE
   TRACER INJECTION – TWO  PHASE

DIMENS
  500   500    1  /

OIL

WATER

METRIC

EQLDIMS
   1  400   400    2    2 /

TRACERS
   0    1    0    0  NODIFF /

PARTTRAC
   1            1    30 /

TABDIMS
   1    1   40   40    2   20 /

REGDIMS
   2    1    0    0  /

WELLDIMS
  10   10    1   10 /

START
  1 'JAN' 1983  /

FMTOUT

NSTACK
   50 /

GRID      ===============================================================

GRIDFILE
1 /

INIT

DX
 250000*10.0 /

DY
 250000*10.0 /

DZ
 250000*10.0 /

TOPS
 250000*4000.0 /
```

```
INCLUDE
'poro.ecl' /

RPTGRID
  'PERMX'  'PERMY' 'PERMZ'  'PORO' /


PROPS     ===============================================================
SWFN
    .145 .0000 .75
    .220 .0001 .05
    .270 .0004 1*
    .320 .009  1*
    .365 .018  1*
    .438 .043  1*
    .510 .082  1*
    .558 .118  1*
    .631 .187  -.05
    .703 .270  -.25
    .752 .310  -.50
    .795 .370  -1.50
/
    0.0    0.0   0.0
    1.0    1.0   0.0
/
SOF2       1 TABLES   20 NODES IN EACH           FIELD   13:34  5 MAY 85
    .205 .000
    .250 .00006
    .300 .0009
    .370 .008
    .440 .027
    .490 .052
    .560 .120
    .635 .228
    .683 .334
    .730 .470
    .780 .644
    .855 1.00
/
    0.0    0.0
    1.0    1.0
/
PVTW
  280 1.030 4.6E-5 0.34 0.0  /
PVDO
  200    1.0     0.47
  280    0.999   0.47
  300    0.998   0.47
/
ROCK
--ref P   compress
 280 .3E-5 /
DENSITY
--oil           water         gas
 850. 1000. 10. /

-- TRACER NAMES AND THEIR ASSOCIATED STOCK TANK PHASES ARE DEFINED USING
-- THE TRACER KEYWORD

TRACER
 'INJ' 'WAT' 'mg' 'OIL'  1/
/

TRACERKP
100           1
200           1
400           1
```

```
500           1
600           1 /
/

TRDIFINJ
 1e-6  /

RPTPROPS
    20*0 1 /

REGIONS    ===========================================================

FIPNUM
250000*1
/

TRKPFINJ
250000*1
/

SOLUTION   ==============================================================

SWAT
 250000*0.25 /

PRESSURE
 250000*280.0 /

TBLKFINJ
250000*0 /

RPTSOL
1 1 1 0 0 0 0 4 0 0 0 1 0 0 0 0 0 0 0 0 0 0 0 0 0 0 0 1 0 0 0 1 1 0 0 0 0 0 0 0 0 0 0 0 0 0 0 0 0  /

'RESTART=1'
/

SUMMARY    ===========================================================

FTPRINJ
FTPTINJ

RUNSUM
RPTSMRY
1 /
SEPARATE


SCHEDULE   ===========================================================

RPTRST
VELOCITY
'BASIC=3'
'FREQ=25' /

RPTSCHED
1 1 1 0 0 0 2 2 2 2 2 2 0 1 2 0 0 0 0 0 0 0 0 0 0 0 0 0 0 0 0 2 1 0 0 0 0 0 0 0 0 0 0 0 0 0 0 0 0 0  /

WELSPECS
'I'  'G'  1     1  4000  'WAT'  /
'P3'  'G'  500   500   4000  'OIL'  /
/

COMPDAT
'I'   1  1   1   1 'OPEN'   0  .0   157E-3 /
'P3'  500  500   1   1 'OPEN'   0  .0   157E-3 /
/
```

```
WCONPROD
'P3'           'OPEN' 'RESV' 4* 1000.0 /
/

WCONINJE
'I' 'WAT' 'OPEN' 'RESV' 1* 1000     /
/

WTRACER
'I' 'INJ' 1  /
/

TSTEP
 200*60.00 /

END
```

E.4 TRACER INJECTION IN SINGLE PHASE FLOW WITH ADSORPTION

```
-- =====================================================================
--
--  TRACER INJECTION PROCESS
--  AN INJECTOR IS LOCATED AT (1,1), AND THE PRODUCER IS LOCATED
--  IN THE DIAGONALLY OPPOSITE CORNER GRID CELL (N,N).
--
RUNSPEC
TITLE
   TRACER INJECTION – SINGLE PHASE WITH ADSORPTION

DIMENS
  500   500    1  /

WATER

METRIC

EQLDIMS
   1  400   400    2    2 /

TRACERS
   0    1    0    1  NODIFF /

NOCASC

TABDIMS
   1    1   40   40    2   20 /

REGDIMS
   2    1    0    0  /

WELLDIMS
  10   10    1   10 /

START
  1 'JAN' 1983  /

FMTOUT

NSTACK
   50 /

GRID      ==============================================================
```

```
GRIDFILE
1 /

INIT

DX
  250000*10.0 /

DY
  250000*10.0 /

DZ
  250000*10.0 /

TOPS
  250000*4000.0 /

INCLUDE
'poro.ecl' /

RPTGRID
  'PERMX'  'PERMY' 'PERMZ'  'PORO' /


PROPS     ==============================================================

PVTW
--ref P   Bw                compress   vis             Cv
  1.01325  1.0  4.0E-05  .5  0.0 /

ROCK
--ref P   compress
  1.01325         5.0E-05 /

DENSITY
--oil           water         gas
 600.0  1000.0   1.0 /

-- TRACER NAMES AND THEIR ASSOCIATED STOCK TANK PHASES ARE DEFINED USING
-- THE TRACER KEYWORD

TRACER
 'INJ' 'WAT' 'mg'/
/

TRADSINJ
 0              0
 0.01           0.00001
 0.5            0.0001
 1.0            0.0008
 5.0            0.0008 /
/

TRROCK
 2              2300          1 /

TRACTVD

TRDIFINJ
 1e-6  /

RPTPROPS
 8*0 0 1 /

REGIONS    ===========================================================

FIPNUM
250000*1
```

```
/

SOLUTION   =============================================================

PRESSURE
 250000*280.0 /

TBLKFINJ
250000*0 /

RPTSOL
1 1 1 0 0 0 0 4 0 0 0 1 0 0 0 0 0 0 0 0 0 0 0 0 0 0 0 1 0 0 0 1 1 0 0 0 0 0 0 0 0 0 0 0 0 0 0 0 0 0  /

'RESTART=1'
/

SUMMARY    ============================================================

FTPRINJ
FTPTINJ

RUNSUM
RPTSMRY
1 /
SEPARATE


SCHEDULE   ============================================================

RPTRST
VELOCITY
'BASIC=3'
'FREQ=25' /

RPTSCHED
1 1 1 0 0 0 2 2 2 2 2 2 0 1 2 0 0 0 0 0 0 0 0 0 0 0 0 0 0 0 0 2 1 0 0 0 0 0 0 0 0 0 0 0 0 0 0 0 0 0  /

WELSPECS
'I'  'G'  1     1  4000  'WAT'  /
'P3'  'G'  500   500   4000  'WAT'  /
/

COMPDAT
'I'   1  1   1   1 'OPEN'   0  .0   1.0 /
'P3'  500  500   1   1 'OPEN'   0  .0   1.0 /
/

WCONPROD
'P3'           'OPEN' 'WRAT' 1* 1000.0 /
/

WCONINJE
'I' 'WAT' 'OPEN' 'RATE' 1000     /
/

WTRACER
'I' 'INJ' 1  /
/

TSTEP
 800*100.00 /

END
```

E.5 SINGLE PHASE POLYMER FLOW

```
CC*****************************************************************
CC*                                                               *
CC*    BRIEF DESCRIPTION OF DATA SE : UTCHEM (VERSION 9.9)        *
CC*                                                               *
CC*****************************************************************
CC*                                                               *
CC*                                                               *
CC*                                                               *
CC*   LENGTH (FT):           PROCESS :                            *
CC*   THICKNESS (FT):          INJ RATE (FT3/DAY) :               *
CC*   WIDTH (FT):            COORDINATES : CARTESIAN              *
CC*   POROSITY :                                                  *
CC*   GRID BLOCKS :                                               *
CC*   DATE :                                                      *
CC*                                                               *
CC*****************************************************************
CC*                                                               *
CC*****************************************************************
CC*                                                               *
CC*   RESERVOIR DESCRIPTION                                       *
CC*                                                               *
CC*****************************************************************
CC
CC Run Number
*----RUNNO
FIEL15
CC
CC Title and run description
*----title(i)
POLYMER FLOODING
HETEROGENEOUS CASE
HORIZONTAL DISPLACEMENT
CC
CC SIMULATION FLAGS
*---- IMODE    IMES   IDISCP  ICWM    ICAP    IREACT  IBIO    ICOORD  ITREAC  ITC     IGAS    IENG
        1       2       3       0       0       0       0       1       0       0       0
        0       0       0
CC
CC no. of gridblocks,flag specifies constant or variable grid size,unit
*---- NX   NY   NZ  IDXYZ  IUNIT
        1000    1       40      0       0
CC
CC constant grid block size in x,y,and z
*---- dx1      dy1      dz1
        2       2       2
CC
CC total no. of components,no. of tracers,no. of gel components
*----n   no   ntw   nta   ngc   ng   noth
        6       0       0       0       0       0       0
CC
CC Name of the components
*----spname(i) for i=1 to n
Water
Oil
Surf
Polymer
Chloride
Calcium
CC
CC flag indicating if the component is included in calculations or not
*----icf(kc) for kc=1,n
1       1       0       1       1       1
CC
```

```
CC***********************************************************
CC*                                                         *
CC*   OUTPUT OPTIONS                                        *
CC*                                                         *
CC***********************************************************
CC
CC
CC FLAG TO WRITE TO UNIT 3,FLAG FOR PV OR DAYS TO PRINT OR TO STOP THE RUN
*---- ICUMTM  ISTOP  IOUTGMS
         1        1        0
CC
CC FLAG INDICATING IF THE PROFILE OF KCTH COMPONENT SHOULD BE WRITTEN
*---- IPRFLG(KC),KC=1,N
1        1        0        1        1        1
CC
CC FLAG FOR PRES.,SAT.,TOTAL CONC.,TRACER CONC.,CAP.,GEL, ALKALINE PROFILES
*---- IPPRES IPSAT IPCTOT IPBIO IPCAP IPGEL IPALK IPTEMP IPOBS
         1        1        1        0        0        0        0        0        0
CC
CC FLAG FOR WRITING SEVERAL PROPERTIES TO UNIT 4 (Prof)
*---- ICKL IVIS IPER ICNM ICSE IHYSTP IFOAMP INONEQ
         1        1        1        0        1        0        0        0
CC
CC FLAG  for variables to PROF output file
*---- IADS IVEL IRKF IPHSE
         1        1        1        0
CC
CC***********************************************************
CC*                                                         *
CC*   RESERVOIR PROPERTIES                                  *
CC*                                                         *
CC***********************************************************
CC
CC
CC MAX. SIMULATION TIME ( DAYS)
*---- TMAX
 1.5
CC
CC ROCK COMPRESSIBILITY (1/PSI), STAND. PRESSURE(PSIA)
*---- COMPR              PSTAND
0.000000E+00          1000.000000
CC
CC FLAGS INDICATING CONSTANT OR VARIABLE POROSITY, X,Y,AND Z PERMEABILITY
*---- IPOR1  IPERMX IPERMY IPERMZ IMOD ITRANZ INTG
         2        2        3        3        0        0        0
CC
CC VARIABLE POROSITY OVER RESERVOIR
*---- POR(I),FOR I=1 TO NX*NY*NZ
0.1
0.3
0.3
0.1
0.1
:
:
CC
CC VARIABLE PERMEABILITY OVER RESERVOIR
*---- PERMX(I),FOR I=1 TO NX*NY*NZ
100
2700
2700
100
100
:
:
CC
CC Y DIRECTION PERMEABILITY IS DEPENDENT ON X DIRECTION PERMEABILITY
*---- CONSTANT PERMEABILITY MULTIPLIER FOR Y DIRECTION PERMEABILITY
```

```
1.00
CC
Z DIRECTION PERMEABILITY IS DEPENDENT ON X DIRECTION PERMEABILITY
*---- CONSTANT PERMEABILITY MULTIPLIER FOR Z DIRECTION PERMEABILITY
1.00
CC
CC FLAG FOR CONSTANT OR VARIABLE DEPTH, PRESSURE, WATER SATURATION,INITIAL AQUEOUS PHASE
COMPOSITIONS
*----IDEPTH  IPRESS  ISWI  ICWI
        0         0         0         0
CC
CC CONSTANT DEPTH (FT)
*---- D111
3500.00
CC
CC CONSTANT PRESSURE (PSIA)
*---- PRESS1
1000.00
CC
CC CONSTANT INITIAL WATER SATURATION
*---- SWIC
1.0
CC
CC INITIAL CONCENTRATION OF SPECIES IN THE AQUEOUS PHASE
*---- CWI(KW) FOR KW=1,N(8+NO)
1.00
CC
CC INITIAL CONCENTRATION OF SPECIES IN THE AQUEOUS PHASE
*---- CWI(KW) FOR KW=1,N(8+NO)
0.00
CC
CC INITIAL CONCENTRATION OF SPECIES IN THE AQUEOUS PHASE
*---- CWI(KW) FOR KW=1,N(8+NO)
0.075
CC
CC INITIAL CONCENTRATION OF SPECIES IN THE AQUEOUS PHASE
*---- CWI(KW) FOR KW=1,N(8+NO)
0.006096
CC
CC INITIAL CONCENTRATION OF SPECIES IN THE AQUEOUS PHASE
*---- CWI(KW) FOR KW=1,N(8+NO)
0.004075
CC
CC***************************************************************
CC*                                                             *
CC*   PHYSICAL PROPERTY DATA                                    *
CC*                                                             *
CC***************************************************************
CC
CC
CC OIL CONC. AT PLAIT POINT FOR TYPE II(+)AND TYPE II(-), CMC
*---- c2plc  c2prc   epsme   ihand
0.000000   1.000000   0.000600   0
CC
CC flag indicating type of phase behavior parameters
*---- ifghbn
        0
CC SLOPE AND INTERCEPT OF BINODAL CURVE AT ZERO, OPT., AND 2XOPT SALINITY
CC FOR ALCOHOL 1
*---- hbns70   hbnc70   hbns71   hbnc71   hbns72   hbnc72
0.000000   0.010000   0.000000   0.016000   0.000000   0.100000
CC SLOPE AND INTERCEPT OF BINODAL CURVE AT ZERO, OPT., AND 2XOPT SALINITY
CC FOR ALCOHOL 2
*---- hbns80   hbnc80   hbns81   hbnc81   hbns82   hbnc82
0.000000   0.000000   0.000000   0.000000   0.000000   0.000000
CC
CC LOWER AND UPPER EFFECTIVE SALINITY FOR ALCOHOL 1 AND ALCOHOL 2
*---- csel7   cseu7   csel8   cseu8
```

```
0.550000   0.916000   0.000000   0.000000
CC
CC THE CSE SLOPE PARAMETER FOR CALCIUM AND ALCOHOL 1 AND ALCOHOL 2
*---- beta6    beta7    beta8
0.800000   -2.000000  0.000000
CC
CC FLAG FOR ALCOHOL PART. MODEL AND PARTITION COEFFICIENTS
*---- ialc   opsk7o   opsk7s   opsk8o   opsk8s
0               0.000000   0.000000   0.000000   0.000000
CC
CC NO. OF ITERATIONS, AND TOLERANCE
*---- nalmax     epsalc
20.000000 0.000100
CC
CC ALCOHOL 1 PARTITIONING PARAMETERS IF IALC=1
*---- akwc7     akws7    akm7     ak7      pt7
4.671000   1.790000   48.000000 35.310000 0.222000
CC
CC ALCOHOL 1 PARTITIONING PARAMETERS IF IALC=2
*---- akwc8     akws8    akm8     ak8      pt8
0.000000   0.000000   0.000000   0.000000   0.000000
CC
CC ift model flag
*----  ift
                0
CC
CC INTERFACIAL TENSION PARAMETERS
*----  g11     g12     g13     g21     g22      g23
                13.000000 -14.800000                0.007000   13.000000 -14.500000                0.010000
CC
CC LOG10 OF OIL/WATER INTERFACIAL TENSION
*---- xiftw
                1.300000
CC
CC ORGANIC MASS TRANSFER FLAG
*---- imass icor
                0               0
CC
CC CAPILLARY DESATURATION PARAMETERS FOR PHASE 1, 2, AND 3
*---- itrap      t11      t22      t33
                1               0.000000   0.000000   364.200000
CC
CC  FLAG FOR RELATIVE PERMEABILITY AND CAPILLARY PRESSURE MODEL
*---- iperm irtype
                0               0
CC
CC FLAG FOR CONSTANT OR VARIABLE REL. PERM. PARAMETERS
*---- isrw    iprw    iew
                0               0               0
CC
CC CONSTANT RES. SATURATION OF PHASES 1,2,AND 3 AT LOW CAPILLARY NO.
*---- s1rwc    s2rwc     s3rwc
      0.2      0.2      0.37
CC
CC CONSTANT ENDPOINT REL. PERM. OF PHASES 1,2,AND 3 AT LOW CAPILLARY NO.
*---- p1rwc     p2rwc    p3rwc
      0.2       1      0.2
CC
CC CONSTANT REL. PERM. EXPONENT OF PHASES 1,2,AND 3 AT LOW CAPILLARY NO.
*---- e1wc     e2wc     e3wc
      1.5       2       1.5
CC
CC RES. SATURATION OF PHASES 1,2,AND 3 AT HIGH CAPILLARY NO.
*---- s1rc   s2rc   s3rc
                0.000000   0.000000   0.000000
CC
CC ENDPOINT REL. PERM. OF PHASES 1,2,AND 3 AT HIGH CAPILLARY NO.
*---- p1rc   p2rc   p3rc
```

```
        1.000000   1.000000   0.000000
CC
CC REL. PERM. EXPONENT OF PHASES 1,2,AND 3 AT HIGH CAPILLARY NO.
*---- e13c   e23c   e31c
        1.500000   2.000000   0.000000
CC
CC WATER AND OIL VISCOSITY , RESERVOIR TEMPERATURE
*---- VIS1    VIS2   TSTAND
        0.730000   40.000000 0.000000
CC
CC COMPOSITIONAL PHASE VISCOSITY PARAMETERS
*----   ALPHAV1   ALPHAV2   ALPHAV3   ALPHAV4  ALPHAV5
        2.000000   2.000000   0.000000   0.900000   0.700000
CC
CC PARAMETERS TO CALCULATE POLYMER VISCOSITY AT ZERO SHEAR RATE
*---- AP1      AP2      AP3
        35.140000 1899.000000              0.000000
CC
CC PARAMETER TO COMPUTE CSEP,MIN. CSEP, AND SLOPE OF LOG VIS. VS. LOG CSEP
*---- BETAP    CSE1     SSLOPE
        20.000000 0.010000   -0.300000
CC
CC PARAMETER FOR SHEAR RATE DEPENDENCE OF POLYMER VISCOSITY
*---- GAMMAC   GAMHF   POWN            IPMOD
        130.000000                100.000000                1.750000   0
CC
CC FLAG FOR POLYMER PARTITIONING, PERM. REDUCTION PARAMETERS
*---- IpOLYM    EPHI3    EPHI4    BRK     CRK           RKCUT
        0              1.000000   0.850000   4.000000   0.150000   10.000000
CC
CC SPECIFIC WEIGHT FOR COMPONENTS 1,2,3,7,8 ,Coeffient of oil and GRAVITY FLAG
*---- DEN1     DEN2    DEN23     DEN3    DEN7    DEN8    IDEN
        0.433530   0.385840   0.368000   0.420000   0.346000   0.000000   2
CC
CC FLAG FOR CHOICE OF UNITS ( 0:BOTTOMHOLE CONDITION , 1: STOCK TANK)
*----- ISTB
        0
CC
CC COMPRESSIBILITY FOR VOL. OCCUPYING COMPONENTS 1,2,3,7,AND 8
*---- COMPC(1)  COMPC(2)  COMPC(3)  COMPC(7)  COMPC(8)
        0.00000010                0.00000010                0.00000000                0.00000000                0.00000000
CC
CC CONSTANT OR VARIABLE PC PARAM., WATER-WET OR OIL-WET PC CURVE FLAG
*---- ICPC    IEPC   IOW
        0              0              0
CC
CC CAPILLARY PRESSURE PARAMETER, CPC0
*---- CPC0
        9.000000
CC
CC CAPILLARY PRESSURE PARAMETER, EPC0
*---- EPC0
        2.000000
CC
CC MOLECULAR DIFFUSION COEF. KCTH COMPONENT IN PHASE 1
*---- D(KC,1),KC=1,N
        0.000000   0.000000   0.000000   0.000000   0.000000   0.000000
CC
CC MOLECULAR DIFFUSION COEF. KCTH COMPONENT IN PHASE 2
*---- D(KC,2),KC=1,N
        0.000000   0.000000   0.000000   0.000000   0.000000   0.000000
CC
CC MOLECULAR DIFFUSION COEF. KCTH COMPONENT IN PHASE 3
*---- D(KC,3),KC=1,N
        0.000000   0.000000   0.000000   0.000000   0.000000   0.000000
CC
LONGITUDINAL AND TRANSVERSE DISPERSIVITY OF PHASE 1
*---- ALPHAL(1)     ALPHAT(1)
```

```
          0.160000   0.040000
CC
LONGITUDINAL AND TRANSVERSE DISPERSIVITY OF PHASE 2
*---- ALPHAL(2)     ALPHAT(2)
          0.160000   0.040000
CC
LONGITUDINAL AND TRANSVERSE DISPERSIVITY OF PHASE 3
*---- ALPHAL(3)     ALPHAT(3)
          0.160000   0.040000
CC
CC flag to specify organic adsorption calculation
*---- iadso
          0
CC
CC SURFACTANT AND POLYMER ADSORPTION PARAMETERS
*---- AD31    AD32   B3D    AD41   AD42   B4D   IADK  IADS1   FADS   REFK
          1.500000   0.500000   1000.000000          4.33       0          100        0          0          0          0
CC
CC PARAMETERS FOR CATION EXCHANGE OF CLAY AND SURFACTANT
*---- QV      XKC     XKS     EQW
          0.000000   0.000000   0.000000   804.000000
CC
CC**************************************************************
CC*                                                            *
CC*   WELL DATA                                                *
CC*                                                            *
CC**************************************************************
CC
CC
CC FLAG FOR SPECIFIED BOUNDARY AND ZONE IS MODELED
*---- IBOUND     IZONE
          0          0
CC
CC TOTAL NUMBER OF WELLS, WELL RADIUS FLAG, FLAG FOR TIME OR COURANT NO.
*---- NWELL   IRO    ITIME    NWREL
          2          2          1          2
CC
CC WELL ID,LOCATIONS,AND FLAG FOR SPECIFYING WELL TYPE, WELL RADIUS, SKIN
*---- IDW    IW    JW    IFLAG    RW     SWELL   IDIR   IFIRST    ILAST   IPRF
          1          1          1          1          0.250000   0          3          1          40         0
CC
CC WELL NAME
*----  WELNAM
          INJVH
CC
CC ICHEK , MAX. AND MIN. ALLOWABLE BOTTOMHOLE PRESSURE AND RATE
*---- ICHEK     PWFMIN     PWFMAX    QTMIN    QTMAX
          0          0.000000   9251.000000          0.000000   4000.000000
CC
CC WELL ID,LOCATIONS,AND FLAG FOR SPECIFYING WELL TYPE, WELL RADIUS, SKIN
*---- IDW    IW    JW    IFLAG    RW     SWELL   IDIR   IFIRST    ILAST   IPRF
          2          1000       1          4          0.250000   0.000000   3          1          40         0
CC
CC WELL NAME
*----  WELNAM
          PROD
CC
CC ICHEK , MAX. AND MIN. ALLOWABLE BOTTOMHOLE PRESSURE AND RATE
*---- ICHEK     PWFMIN     PWFMAX    QTMIN    QTMAX
          0          0.000000   9251.000000          0.000000   2807.000000
CC
CC  ID,INJ. RATE AND INJ. COMP. FOR RATE CONS. WELLS FOR EACH PHASE (L=1,3)
*----  ID     QI(M,L)     C(M,KC,L)
          1          60.000000 1.000000   0.000000   0.000000   0.075      0.006096              0.004075
          1          0.000000   0.000000   0.000000   0.000000   0.000000   0.000000   0.000000
          1          0.000000   0.000000   0.000000   0.000000   0.000000   0.000000   0.000000
CC
CC  ID, TOTAL PRODUCTION RATE
```

```
*----  ID    QI(M,1)
             2               -60.000000
CC
CC CUM. INJ. TIME , AND INTERVALS (PV OR DAY) FOR WRITING TO OUTPUT FILES
*---- TINJ     CUMPR1     CUMHI1     WRHPV     WRPRF      RSTC
             10.500000 0.050000   0.050000   0.010000   0.050000   20.000000
CC
CC FOR IMES=2 ,THE INI. TIME STEP,CONC. TOLERANCE,MAX.,MIN. courant numbers
*----  DT      DCLIM     CNMAX      CNMIN
             0.100000   0.003000   0.200000   0.010000
```

Appendix F: MATLAB Implementation of Volume Averaging Procedure

F.1 OVERVIEW

In this research, a volume averaging approach integrating fine-scale numerical flow simulation results has been developed to describe scale-up of various transport problems. Numerical implementations for the single-phase mass transfer application in MATLAB are presented in this appendix.

F.2 IMPLEMENTATION OF VOLUME AVERAGING PROCESS IN SINGLE PHASE TRANSPORT

```
% =====================================================================
% Main File

for bsize=1:5, % bsize_max = total number length scales (represented by blocksize_x)
   tic
   save bsize.mat bsize; % save the length scale size before clearing all the variables
   clear all;
   load bsize.mat; % reload the length scale size
   bsize_max=5; % the maximum number length scales used
   switch bsize
      case 1
         blocksize_x=2;
      case 2
         blocksize_x=5;
      case 3
         blocksize_x=10;
      case 4
         blocksize_x=25;
      case 5
         blocksize_x=50;
       otherwise
   end
   tcount=0; % a dummy column counter

% INPUT SECTION AND DATA ANALYSIS
% Load the fine-scale flow simulation results
load fine_scale.dat; % "fine_scale.dat" containts the fine-scale simulation results in columns ("e.g., permeability in column #1,
                       % porosity in column #2 etc.)
VEL=fine_scale;

% Indicate the volume averaging calculations domain (i_start, j_start, k_start) indicates the (i,j,k) coordinates of the outermost corner
% of the volume averaging domain with respect to the entire simulation domain
i_start=200;
j_start=200;
k_start=0;
avg_code=2; % choice code for AverageVel and AverageC function calls (different choices signifiy options such as reading in average
                % quantities from a file or computing them via arithmetic averaging)
```

```
%User input about model parameters
nx=150;                         % number of fine-grid cells in the x-direction in the volume averaging domain
ny=150;                         % number of fine-grid cells in the y-direction in the volume averaging domain
nz=1;                           % number of fine-grid cells in the z-direction in the volume averaging domain
blocksize_y=blocksize_x;        % setting the averaging length scale in the y-direction
blocksize_z=1;                  % setting the averaging length scale in the z-direction
nbx=nx/blocksize_x;             % number of grid blocks in the x-direction in the scaled-up grid
nby=ny/blocksize_y;             % number of grid blocks in the y-direction in the scaled-up grid
nbz=nz/blocksize_z;             % number of grid blocks in the z-direction in the scaled-up grid
dx=10;                          % grid block size in the x-direction = 10m
dy=10;                          % grid block size in the y-direction = 10m
dz=10;                          % grid block size in the z-direction = 10m
Dx=dx*blocksize_x;              % coarse grid block size in x-direction
Dy=dy*blocksize_y;              % coarse grid block size in y-direction
Dz=dz*blocksize_z;              % coarse grid block size in z-direction
D=1e-6;                         % molecular diffusion or dispersion coefficient in m2/day


%Initialization the grid with zeros (inactive cells)
perm=zeros(nx,ny,nz);           % permeability
poro=zeros(nx,ny,nz);           % 1=active cell 0 = inactive cell (default is 1)
vo_i=zeros(nx,ny,nz);           % velocity in the x-direction
vo_j=zeros(nx,ny,nz);           % velocity in the y-direction
vo_k=zeros(nx,ny,nz);           % velocity in the z-direction
sf=zeros(nx,ny,nz);             % closure variable
poro1=zeros(nx,ny,nz);          % porosity
C=zeros(nx,ny,nz);              % concnetration
ngrid=nx*ny*nz;                 % total number of fine-grid cells in the volume averaging domain
ntotal=500*500;                 % total number of fine-grid cells in the flow simulation domain

%Read in fine-scale simulation results (which are in columns)
for k=1:nz,
   for j=1:ny,
      for i=1:nx,
         n=(k+k_start-1)*ntotal+(j+j_start-1)*500+i+i_start; % n is the row index in the fine-scale simulation results file (which is in
                                                             % columns)
         poro1(i,j,k)=VEL(n,2); %reading in column 2 of the fine-scale simulation file
         poro(i,j,k)=poro1(i,j,k);
         poro(i,j,k)=1;
         vo_i(i,j,k)=VEL(n,3);
         vo_j(i,j,k)=VEL(n,4);
         vo_k(i,j,k)=VEL(n,5);
         perm(i,j,k)=VEL(n,1);
         C(i,j,k)=VEL(n,6);
      end
   end
end

%Compute velocity magnitude
vo=sqrt(vo_i.^2+vo_j.^2+vo_k.^2);

%Generate of plot of permeability
figure(1)
subplot(2,2,1);imagesc(perm);colorbar;caxis([0 1500]);title('fine-scale permeability');

% Calculate <k> and <C>
perm_avg=AveragePerm(blocksize_x,blocksize_y,blocksize_z,nbx,nby,nbz,perm);
poro_avg=AveragePerm(blocksize_x,blocksize_y,blocksize_z,nbx,nby,nbz,poro1);
[avg_C,Cp_var]=AverageC(blocksize_x,blocksize_y,blocksize_z,nbx,nby,nbz,C,poro,avg_code,bsize);

%Compute the minimum and maximum of average concentrations <C>, and the standard deviation of C, C’
for k=1:nbz,
   for j=1:nby,
      for i=1:nbx,
         maxC(i,j,k)=0;
         minC(i,j,k)=1e10;
```

```
            sumC(i,j,k)=0;
            for a=1:blocksize_x,
                for b=1:blocksize_y,
                    for c=1:blocksize_z,
                        %compute the maximum of <C>
                        if C((i-1)*blocksize_x+a,(j-1)*blocksize_y+b,(k-1)*blocksize_z+c)>maxC(i,j,k)
                            maxC(i,j,k)=C((i-1)*blocksize_x+a,(j-1)*blocksize_y+b,(k-1)*blocksize_z+c);
                        end
                        %compute the minimum of <C>
                        if C((i-1)*blocksize_x+a,(j-1)*blocksize_y+b,(k-1)*blocksize_z+c)<minC(i,j,k)
                            minC(i,j,k)=C((i-1)*blocksize_x+a,(j-1)*blocksize_y+b,(k-1)*blocksize_z+c);
                        end
                        sumC(i,j,k)=sumC(i,j,k)+C((i-1)*blocksize_x+a,(j-1)*blocksize_y+b,(k-1)*blocksize_z+c);
                    end
                end
            end
            sumC2(i,j,k)=sumC(i,j,k)/(nbx*nby*nbz);
        end
    end
end
Cp_std=sqrt(var(reshape(C,nx*ny*nz,1))-var(reshape(avg_C,nbx*nby*nbz,1))); %compute the standard deviation of C’

%Set Ceq, in this case, Ceq = C (fine-scale)
Ceq=C;


%Calculate average velocity <u> using the function “AverageVel”
[vo_avg_i,vo_avg_j,vo_avg_k,perm_avg2]=AverageVel(blocksize_x,blocksize_y,blocksize_z,nbx,nby,nbz,vo_i,vo_j,vo_k,
                                        ones(nx,ny,nz),avg_code,bsize);
vo_avg=sqrt(vo_avg_i.^2+vo_avg_j.^2+vo_avg_k.^2); % magnitude of average velocity <u>


%Calculate u' = u - <u> using the function “BackgroundV”
[vo_p_i,vo_p_j,vo_p_k]=BackgroundV(blocksize_x,blocksize_y,blocksize_z,nx,ny,nz,vo_i,vo_j,vo_k,vo_avg_i,vo_avg_j,vo_avg_k);
vo_p_mag=sqrt(vo_p_i.^2+vo_p_j.^2+vo_p_k.^2); %magnitude of deviation velocity  u’

%Generate plots of velocity maps
cmin=0;cmax1=0.65;cmax2=0.3;
subplot(2,2,2);imagesc(vo);caxis([cmin cmax1]);colorbar;title('||v_1||');
subplot(2,2,3);imagesc(vo_avg);caxis([cmin cmax1]);colorbar;title('||<v_1>||');
subplot(2,2,4);imagesc(vo_p_mag);caxis([cmin cmax2]);colorbar;title('||v_1_p||');



%SOLUTION OF CLOSURE VARIABLE
avg_C_old=avg_C; %save the <C> before it is being modified in the optimization (minimization) procedure

%initial guess of the closure variable
[s_s]=BackgroundC(blocksize_x,blocksize_y,blocksize_z,nx,ny,nz,C,avg_C,Ceq,poro1);

% a function call to “SA” (the simulated annealing sub-routine)
[sf,error,al,avg_C,C_p,gradC_old2,err_tr]=SA(blocksize_x,blocksize_y,blocksize_z,nbx,nby,nbz,nx,ny,nz,ngrid,poro,poro_avg,
          vo_p_i,vo_p_j,vo_p_k,vo_i,vo_j,vo_k,vo_avg_i,vo_avg_j,vo_avg_k,avg_C,C,s_s,Ceq,0.15*sqrt(max(max(Cp_var))));


%Compute Keff
%Compute various terms:  u's & <u's> & grad.<u's> & grad<C>
% terms: u's
vps_i=vo_p_i.*sf.^1;
vps_j=vo_p_j.*sf.^1;
vps_k=vo_p_k.*sf.^1;
% terms: <u's>&grad.<u's>&grad<C>&grad2<C>
[vps_i_avg,vps_j_avg,vps_k_avg]=AverageVec(blocksize_x,blocksize_y,blocksize_z,nbx,nby,nbz,vps_i,vps_j,vps_k);
grad_d_vps=graddotEnsemble(Dx,Dy,Dz,nbx,nby,nbz,vps_i_avg,vps_j_avg,vps_k_avg);
[gradC_i,gradC_j,gradC_k]=gradEnsemble(Dx,Dy,Dz,nbx,nby,nbz,avg_C);
grad2C=grad2Ensemble(Dx,Dy,Dz,nbx,nby,nbz,avg_C);
% compute Cmax - <C>
for k=1:nz,
```

```
  for j=1:ny,
    for i=1:nx,
      bi=ceil(i/blocksize_x);
      bj=ceil(j/blocksize_y);
      bk=ceil(k/blocksize_z);
      Cdiff(i,j,k)=Ceq(i,j,k)-avg_C(bi,bj,bk);
      if abs(Cdiff(i,j,k))<1e-4 % this is to avoid dividing by zero for subsequent calculations
        Cdiff(i,j,k)=1e-4;
      end
      maxCdiff(bi,bj,bk)=1-avg_C(bi,bj,bk);
    end
  end
end

% Calculate Keff indicators: if Cmax-<C> is too small, Keff_ind is set to zero. This is to avoid Keff to be infinite in regions where
%<C> is the same as Cmax. Keff values are calculated only for locations where Keff_ind is greater than zero
Keff_ind=ones(nbx,nby,nbz);
for k=1:nbz,
  for j=1:nby,
    for i=1:nbx,
      % if Cmax-<C> is too small, Keff_ind is set to zero
      if (abs(maxCdiff(i,j,k))/mean(reshape(abs(maxCdiff),nbx*nby*nbz,1)))<0.01
        maxCdiff(i,j,k)=0.01*mean(reshape(abs(maxCdiff),nbx*nby*nbz,1));
        Keff_ind(i,j,k)=0;
      end
    end
  end
end
[gradCdiff_i,gradCdiff_j,gradCdiff_k]=gradEnsemble(dx,dy,dz,nx,ny,nz,Cdiff);
grad2Cdiff=grad2Ensemble(dx,dy,dz,nx,ny,nz,Cdiff);

% terms: u'sCdff
vpsCdiff_i=vo_p_i.*sf.^1*Cdiff.^1;
vpsCdiff_j=vo_p_j.*sf.^1*Cdiff.^1;
vpsCdiff_k=vo_p_k.*sf.^1*Cdiff.^1;
% terms: <u'sCdff>&grad.<u's>
[vpsCdiff_i_avg,vpsCdiff_j_avg,vpsCdiff_k_avg]=AverageVec(blocksize_x,blocksize_y,blocksize_z,nbx,nby,nbz,vpsCdiff_i,
                                             vpsCdiff_j,vpsCdiff_k);
grad_d_vpsCdiff=graddotEnsemble(Dx,Dy,Dz,nbx,nby,nbz,vpsCdiff_i_avg,vpsCdiff_j_avg,vpsCdiff_k_avg);

% computing all the effective transport terms:
% convec - convection
% inter - interphase transport
% diffuse - diffusion
% disperse - dispersion
% dispersivity - effective dispersivity
% Pe - block Peclet number
% Re - block Reynolds number
% Keff - effective mass transfer coefficient (Keff)
for k=1:nz,
  for j=1:ny,
    for i=1:nx,
      bi=ceil(i/blocksize_x);
      bj=ceil(j/blocksize_y);
      bk=ceil(k/blocksize_z);
      convec(bi,bj,bk)=vo_avg_i(bi,bj,bk)*gradC_i(bi,bj,bk)+vo_avg_j(bi,bj,bk)*gradC_j(bi,bj,bk)
                              +vo_avg_k(bi,bj,bk)*gradC_k(bi,bj,bk);
      inter(bi,bj,bk)=al(i,j,k)*Cdiff(i,j,k);
      diffuse(bi,bj,bk)=D*grad2C(bi,bj,bk);
      disperse(bi,bj,bk)=grad_d_vpsCdiff(bi,bj,bk);
      dispersivity(bi,bj,bk)=grad_d_vpsCdiff(bi,bj,bk)/vo_avg(bi,bj,bk)/grad2C(bi,bj,bk);
      Pe(bi,bj,bk)=vo_avg(bi,bj,bk)*Dx/D*gradC_old2(bi,bj,bk)/poro_avg(bi,bj,bk);
      Re(bi,bj,bk)=vo_avg(bi,bj,bk)*Keff_ind(bi,bj,bk);
      Keff(bi,bj,bk)=Keff_ind(bi,bj,bk)*convec(bi,bj,bk)/maxCdiff(bi,bj,bk);

      % putting the results in columns (the “2” indicates it’s the results in columns)
      C_p2((k-1)*nx*ny+(j-1)*nx+i,1)=C_p(i,j,k);
      C2((k-1)*nx*ny+(j-1)*nx+i,1)=C(i,j,k);
```

```
            Keff2((bk-1)*nbx*nby+(bj-1)*nbx+bi,1)=Keff(bi,bj,bk);
            Keff2((bk-1)*nbx*nby+(bj-1)*nbx+bi,2)=Keff_ind(bi,bj,bk);
            Keff2((bk-1)*nbx*nby+(bj-1)*nbx+bi,3)=avg_C(bi,bj,bk);
            Keff2((bk-1)*nbx*nby+(bj-1)*nbx+bi,4)=convec(bi,bj,bk);
            Keff2((bk-1)*nbx*nby+(bj-1)*nbx+bi,5)=Ceq(i,j,k)-avg_C(bi,bj,bk);
            avg_C2((bk-1)*nbx*nby+(bj-1)*nbx+bi,1)=avg_C(bi,bj,bk);
            vo_avg_i2((bk-1)*nbx*nby+(bj-1)*nbx+bi,1)=vo_avg_i(bi,bj,bk);
            vo_avg_j2((bk-1)*nbx*nby+(bj-1)*nbx+bi,1)=vo_avg_j(bi,bj,bk);
            vo_avg2((bk-1)*nbx*nby+(bj-1)*nbx+bi,1)=vo_avg(bi,bj,bk);
        end
    end
end

%Generate a spatial map of Keff
figure(5);imagesc(abs(Keff));caxis([0 0.0003]);colorbar;title('K_e_f_f');


tcount=tcount+1;
% COMPUTE THE STATISTICS OF EFFECTIVE TRANSPORT TERMS AND OUTPUT THE RESULTS
% loading various variables that store the statistics (mean and variance) of different parameters as a function of scale
load Keff_var.mat;
load Keff_mean.mat;
load convec_var.mat;
load convec_mean.mat;
load diffuse_var.mat;
load diffuse_mean.mat;
load disperse_var.mat;
load disperse_mean.mat;
load dispersivity_mean.mat;
load dispersivity_var.mat;
load inter_var.mat;
load inter_mean.mat;
load perm_var.mat;
load perm_mean.mat;
% if the size of these variables are different than the number of length scales specified at the beginning of the file, we erase the
% variables and start with some blank variables instead
if size(Keff_var(:,1),1)~=bsize_max,
    clear Keff_var;
    clear Keff_mean;
    clear convec_var;
    clear convec_mean;
    clear diffuse_var;
    clear diffuse_mean;
    clear disperse_var;
    clear disperse_mean;
    clear inter_var;
    clear inter_mean;
    clear perm_var;
    clear perm_mean;
    clear dispersivity_mean;
    clear dispersivity_var;
end

ALL(:,tcount)=abs(Keff2(:,1));
W(:,tcount)=Keff2(:,2);
%compute Keff_mean and Keff_var
[Keff_var(bsize,1),Keff_mean(bsize,1)]=KO(ALL,blocksize_x,tcount,W,nbx,nby);

W2(:,tcount)=ones(nbx*nby*nbz,1);
%compute convec_mean and convec_var
ALL2(:,tcount)=reshape(abs(convec),nbx*nby*nbz,1);
[convec_var(bsize,1),convec_mean(bsize,1)]=KO(ALL2,blocksize_x,tcount,W2,nbx,nby);
%compute diffuse_mean and diffuse_var
ALL2(:,tcount)=reshape(abs(diffuse),nbx*nby*nbz,1);
[diffuse_var(bsize,1),diffuse_mean(bsize,1)]=KO(ALL2,blocksize_x,tcount,W2,nbx,nby);
%compute disperse_mean and disperse_var
ALL2(:,tcount)=reshape(abs(disperse),nbx*nby*nbz,1);
[disperse_var(bsize,1),disperse_mean(bsize,1)]=KO(ALL2,blocksize_x,tcount,W2,nbx,nby);
```

```
%compute dispersivity_mean and dispersivity_var
ALL2(:,tcount)=reshape(abs(dispersivity),nbx*nby*nbz,1);
[dispersivity_var(bsize,1),dispersivity_mean(bsize,1)]=KO(ALL2,blocksize_x,tcount,W2,nbx,nby);
%compute inter_mean and inter_var
ALL2(:,tcount)=reshape(abs(inter),nbx*nby*nbz,1);
[inter_var(bsize,1),inter_mean(bsize,1)]=KO(ALL2,blocksize_x,tcount,W2,nbx,nby);
%compute perm_mean and perm_var
ALL2(:,tcount)=reshape(abs(perm_avg2),nbx*nby*nbz,1);
[perm_var(bsize,1),perm_mean(bsize,1)]=KO(ALL2,blocksize_x,tcount,W2,nbx,nby);
%saving all the values
save Keff_var.mat Keff_var;
save Keff_mean.mat Keff_mean;
save convec_var.mat convec_var;
save convec_mean.mat convec_mean;
save diffuse_var.mat diffuse_var;
save diffuse_mean.mat diffuse_mean;
save disperse_var.mat disperse_var;
save disperse_mean.mat disperse_mean;
save dispersivity_var.mat dispersivity_var;
save dispersivity_mean.mat dispersivity_mean;
save inter_var.mat inter_var;
save inter_mean.mat inter_mean;
save perm_mean.mat perm_mean;
save perm_var.mat perm_var;

% save the mismatch error from the minimization (optimization) step from the function call “SA”
load err_t.mat;
if size(err_tr(:,1),1)~=bsize_max,
   clear err_t;
end
err_t(:,bsize)=err_tr(:,2);
save err_t.mat err_t;
figure(6);plot(err_tr(:,1),err_tr(:,2));title('err'); % generate plot of mismatch error at each iteration step
toc

end

% ===========================================================================
function [x,emod,alpha,avg_C,C_p,gradC_old2,err]=SA(blocksize_x,blocksize_y,blocksize_z,nbx,nby,nbz,
                                    nx,ny,nz,ngrid,poro,poro_avg,vo_p_i,vo_p_j,vo_p_k,vo_i,vo_j,vo_k,
                                    vo_avg_i,vo_avg_j,vo_avg_k,avg_C,C,s_s,Ceq,Cp_var_max)

% This is the function to perform simulated annealing to update <C> and C’. It calls the function object_error to evaluate the
objective % function that is to be minimized


maxtemps =100;              %the number of temperature
nmove = 1;                  %number of random moves per critical temperature
decay = 1;                  %decay factor in the annealing procedure
nparam = ngrid;             %number of parameters to be perturbed
alpha=ones(nx,ny,nz);       %term alpha
altrial=ones(nx,ny,nz);     %trial guess of alpha

%initialize closure variables with s_s (passed from the main file)
x=s_s;                      %closure variable
xtest = s_s;                %trial solution of closure variable

avg_C_old=avg_C;            %initial guess of <C>
avg_C_test=avg_C;           %trial solution of <C>


%Compute the gradient of <C>:
%if gradient of <C> <= threshold --> don't perturb <C> of the cell, mark the cell with '0' (gradC_old2)
%otherwise --> perturb <C> of the cell, mark the cell with '1' (gradC_old2)
%we want to perturb regions where spatial gradient of <C> is the greatest (i.e. close to the tracer front)
[gradC_i,gradC_j,gradC_k]=gradEnsemble(10*blocksize_x,10*blocksize_y,10*blocksize_z,nbx,nby,nbz,avg_C_old);
```

```
gradC_old=sqrt(gradC_i.^2+gradC_j.^2);
maxa=max(max(gradC_old));
for i=1:nbx,
    for j=1:nby,
        for k=1:nbz,
            if abs(gradC_old(i,j,k))<(1e-2*maxa)
                gradC_old2(i,j,k)=0; %mark the cell with ‘0’
            else
                gradC_old2(i,j,k)=1; %mark the cell with’1’
            end
        end
    end
end
%Plot grad<C> and the cell indicators
figure(4);subplot(2,1,1);imagesc(gradC_old);colorbar;title('Arithmetic Grad C');
subplot(2,1,2);imagesc(gradC_old2);colorbar;title('Arithmetic Grad C Indicators');

% To evaluate an initial error estimate
count=0;
[etrial,xtrial,altrial]=object_error(blocksize_x,blocksize_y,blocksize_z,nbx,nby,nbz,nx,ny,nz,ngrid,xtest,poro,vo_p_i,vo_p_j,vo_p_k,
                                  vo_i,vo_j,vo_k,vo_avg_i,vo_avg_j,vo_avg_k,avg_C_test,Ceq,s_s);

t0=etrial*50;                     %start temperature of individual parameter
temp0=t0;                         %start temp for use in acceptance rule
e0=etrial;                        %initial error
emod=1;                           %error ratio (initialized to 1)

% Simulated Annealing Procedure based on the Metropolis sampling techniques
for jtemp=1:maxtemps,
    if (emod>0)
        temp=temp0*exp(-decay*(jtemp-1)^0.5);
        tmp1=t0*exp(-decay*(jtemp-1)^0.5);
        for jmove=1:nmove,
            %Metropolis SA
            [etrial,xtrial,altrial]=object_error(blocksize_x,blocksize_y,blocksize_z,nbx,nby,nbz,nx,ny,nz,ngrid,xtest,poro,vo_p_i,
                                  vo_p_j,vo_p_k,vo_i,vo_j,vo_k,vo_avg_i,vo_avg_j,vo_avg_k,avg_C_test,Ceq,s_s);
            etrial=etrial/e0; %normalized error

            if etrial<emod % if error is less than the error from previous step, accept the new guess
                emod=etrial;
                x=xtrial;
                avg_C=avg_C_test;
                alpha=altrial;
                xtest=x;
            else % if error is greater than the error from previous step, it can still be accepted or rejected as follows
                arg=(etrial-emod)/temp; %argument used to calculate the  probability of acceptance’prob’
                if arg>0.000001
                    prob=0.00001;
                else
                    prob=exp(-arg);
                end
                if prob>rand(1) % if prob > random number drawn from a uniform distribution, accept and update, else, do nothing
                    emod=etrial;
                    x=xtrial;
                    avg_C=avg_C_test;
                    alpha=altrial;
                    xtest=x;
                end
            end
            count=count+1;
            err(count,1)=count;
            err(count,2)=emod;
            disp([count emod e0])
            % to display to the screen the progress of annealing (number of trials, the normalized error, and the original error size)

            %Update avg_C_test with a new guess
            for i=1:nbx,
                for j=1:nby,
```

```
          for k=1:nbz,
            avg_C_test(i,j,k)=avg_C_test(i,j,k)+gradC_old2(i,j,k)*0.02*round(rand(1)*2-1)*avg_C_test(i,j,k);
            if (avg_C_test(i,j,k)<0) %check to make sure that the new guess of <C> is greater than zero
              avg_C_test(i,j,k)=0;
            end
            if (avg_C_test(i,j,k)>1) %check to make sure that the new guess of <C> is not greater than 1 (that's the maximum
                                     %possible value for C, which is the injection concentration in this example)
              avg_C_test(i,j,k)=1;
            end
          end
        end
      end

      [s_s2]=BackgroundC(blocksize_x,blocksize_y,blocksize_z,nx,ny,nz,C,avg_C_test,Ceq,poro);
      xtest=s_s2; %update trial solution of closure variable
    end
  end
end
[C_p,Cout]=Cp(blocksize_x,blocksize_y,blocksize_z,nx,ny,nz,x,avg_C,Ceq); %update C'

emod
if jtemp==maxtemps
%Generate the concentration maps
figure(3)
cmin=min(min(C));
cmax=max(max(C));
[C_p,Cout]=Cp(blocksize_x,blocksize_y,blocksize_z,nx,ny,nz,x,avg_C,Ceq);

subplot(2,2,3);imagesc(avg_C);caxis([cmin cmax]);colorbar;title('final <C>');
subplot(2,2,4);imagesc(C_p);caxis([cmin cmax]);colorbar;title('C_p');
subplot(2,2,1);imagesc(C);caxis([cmin cmax]);colorbar;title('C');
subplot(2,2,2);imagesc(avg_C_old);caxis([cmin cmax]);colorbar;title('initial <C>');
end

% ============================================================================
function [error,s_new,alpha2]=object_error(blocksize_x,blocksize_y,blocksize_z,nbx,nby,nbz,
                                    nx,ny,nz,ngrid,s,poro,vo_p_i,vo_p_j,vo_p_k,vo_i,vo_j,vo_k,vo_avg_i,
                                    vo_avg_j,vo_avg_k,avg_C,Ceq,s_s)


% This is the objective function in the simulated annealing procedure

dx=10;                          % grid block size in x-direction
dy=10;                          % grid block size in y-direction
dz=10;                          % grid block size in z-direction
Dx=dx*blocksize_x;              % coarse grid block size in x-direction
Dy=dy*blocksize_y;              % coarse grid block size in y-direction
Dz=dz*blocksize_z;              % coarse grid block size in z-direction
nxyz=nx*ny*nz;                  %total number of fine-scale grid blocks



%D=1e-6; %molecular diffusion coefficient m2/day
D=1e-6;

%Compute u's & <u's> & grad.<u's> & grad<C> & grad2<C>
% terms: u's
vps_i=vo_p_i.*s.^1;
vps_j=vo_p_j.*s.^1;
vps_k=vo_p_k.*s.^1;
%terms: <u's>&grad.<u's>&grad<C>&grad2<C>
[vps_i_avg,vps_j_avg,vps_k_avg]=AverageVec(blocksize_x,blocksize_y,blocksize_z,nbx,nby,nbz,vps_i,vps_j,vps_k);
grad_d_vps=graddotEnsemble(Dx,Dy,Dz,nbx,nby,nbz,vps_i_avg,vps_j_avg,vps_k_avg);
[gradC_i,gradC_j,gradC_k]=gradEnsemble(Dx,Dy,Dz,nbx,nby,nbz,avg_C);
grad2C=grad2Ensemble(Dx,Dy,Dz,nbx,nby,nbz,avg_C);

%compute Ceq-<C>
```

```
for k=1:nz,
    for j=1:ny,
        for i=1:nx,
            bi=ceil(i/blocksize_x);
            bj=ceil(j/blocksize_y);
            bk=ceil(k/blocksize_z);
            Cdiff(i,j,k)=Ceq(i,j,k)-avg_C(bi,bj,bk);
            if abs(Cdiff(i,j,k))<1e-4
                Cdiff(i,j,k)=1e-4;
            end
        end
    end
end
[gradCdiff_i,gradCdiff_j,gradCdiff_k]=gradEnsemble(dx,dy,dz,nx,ny,nz,Cdiff);
grad2Cdiff=grad2Ensemble(dx,dy,dz,nx,ny,nz,Cdiff);

vpsCdiff_i=vo_p_i.*s.^1*Cdiff.^1;
vpsCdiff_j=vo_p_j.*s.^1*Cdiff.^1;
vpsCdiff_k=vo_p_k.*s.^1*Cdiff.^1;

%<u'sCdff>&grad.<u's>
[vpsCdiff_i_avg,vpsCdiff_j_avg,vpsCdiff_k_avg]=AverageVec(blocksize_x,blocksize_y,blocksize_z,nbx,nby,nbz,vpsCdiff_i,
                                                                        vpsCdiff_j,vpsCdiff_k);
grad_d_vpsCdiff=graddotEnsemble(Dx,Dy,Dz,nbx,nby,nbz,vpsCdiff_i_avg,vpsCdiff_j_avg,vpsCdiff_k_avg);

%Compute constants (see the section “Implementation Details”  in Chapter 4 to see what these constants mean)
for k=1:nz,
    for j=1:ny,
        for i=1:nx,
            bi=ceil(i/blocksize_x);
            bj=ceil(j/blocksize_y);
            bk=ceil(k/blocksize_z);
            fi(i,j,k)=gradCdiff_i(i,j,k)/Cdiff(i,j,k);
            fj(i,j,k)=gradCdiff_j(i,j,k)/Cdiff(i,j,k);
            fk(i,j,k)=gradCdiff_k(i,j,k)/Cdiff(i,j,k);
            gi(bi,bj,bk)=gradC_i(bi,bj,bk)/Cdiff(i,j,k);
            gj(bi,bj,bk)=gradC_j(bi,bj,bk)/Cdiff(i,j,k);
            gk(bi,bj,bk)=gradC_k(bi,bj,bk)/Cdiff(i,j,k);
            b(i,j,k)=-(vo_i(i,j,k)*fi(i,j,k)+vo_j(i,j,k)*fj(i,j,k)+vo_k(i,j,k)*fk(i,j,k))+D*grad2Cdiff(i,j,k)/Cdiff(i,j,k);
            a_i(i,j,k)=vo_i(i,j,k)-2*D*fi(i,j,k);
            a_j(i,j,k)=vo_j(i,j,k)-2*D*fj(i,j,k);
            a_k(i,j,k)=vo_k(i,j,k)-2*D*fk(i,j,k);
            c(i,j,k)=(vo_p_i(i,j,k)*gradC_i(bi,bj,bk)+vo_p_j(i,j,k)*gradC_j(bi,bj,bk)+vo_p_k(i,j,k)*gradC_k(bi,bj,bk))/Cdiff(i,j,k);
            e(i,j,k)=1/poro(i,j,k);
            alpha(i,j,k)=(vo_avg_i(bi,bj,bk)*gradC_i(bi,bj,bk)+vo_avg_j(bi,bj,bk)*gradC_j(bi,bj,bk)
                              +vo_avg_k(bi,bj,bk)*gradC_k(bi,bj,bk)+grad_d_vpsCdiff(bi,bj,bk)-D*grad2C(bi,bj,bk))/Cdiff(i,j,k);
        end
    end
end


%Construct the finite differencing matrix (T) and the RHS (B)
%Initialize T and B
T=zeros(nx*ny*nz,5);
B=zeros(nx*ny*nz,1);

for k=1:nz,
    for j=1:ny,
        for i=1:nx,
            index(i,j,k)=(k-1)*nx*ny+(j-1)*nx+i; %this index is used to construct the elements of T and B
        end
    end
end


%compute elements corresponding to the interior grid nodes
for k=1:nz,
    for j=1:ny,
```

```
        for i=1:nx,
            ind=index(i,j,k);
            bi=ceil(i/blocksize_x);
            bj=ceil(j/blocksize_y);
            bk=ceil(k/blocksize_z);
            s2(ind,1)=s(i,j,k);
            T(ind,3)=-2*D*(1/Dx^2+1/Dy^2+1/Dz^2)+b(i,j,k);
            if i>1
                T(ind,2)=D/Dx^2+a_i(i,j,k)/2/Dx;
            end
            if i<nx
                T(ind,4)=D/Dx^2-a_i(i,j,k)/2/Dx;
            end
            if j>1
                T(ind,1)=D/Dy^2+a_j(i,j,k)/2/Dy;
            end
            if j<ny
                T(ind,5)=D/Dy^2-a_j(i,j,k)/2/Dy;
            end
            B(ind,1)=c(i,j,k)+e(i,j,k)*alpha(bi,bj,bk);
        end
    end
end

%compute elements corresponding to boundary nodes (only if there is more than one layer in each direction)
%for all nodes with i=1
i=1;
for j=1:ny,
    for k=1:nz,
        ind=index(i,j,k);
        bi=ceil(i/blocksize_x);
        bj=ceil(j/blocksize_y);
        bk=ceil(k/blocksize_z);
        factor=D/Dx^2+a_i(i,j,k)/2/Dx;
        T(ind,3)=T(ind,3)+factor*(2*Dx*fi(bi,bj,bk));
        T(ind,4)=T(ind,4)+factor;
        B(ind,1)=B(ind,1)+factor*2*Dx*gi(bi,bj,bk);
    end
end
%for all nodes with i=nx
i=nx;
for j=1:ny,
    for k=1:nz,
        ind=index(i,j,k);
        bi=ceil(i/blocksize_x);
        bj=ceil(j/blocksize_y);
        bk=ceil(k/blocksize_z);
        factor=D/Dx^2-a_i(i,j,k)/2/Dx;
        T(ind,3)=T(ind,3)-factor*(2*Dx*fi(bi,bj,bk));
        T(ind,2)=T(ind,2)+factor;
        B(ind,1)=B(ind,1)-factor*2*Dx*gi(bi,bj,bk);
    end
end
%for all nodes with j=1
j=1;
for k=1:nz,
    for i=1:nx,
        ind=index(i,j,k);
        bi=ceil(i/blocksize_x);
        bj=ceil(j/blocksize_y);
        bk=ceil(k/blocksize_z);
        factor=D/Dy^2+a_j(i,j,k)/2/Dy;
        T(ind,3)=T(ind,3)+factor*(2*Dy*fj(bi,bj,bk));
        T(ind,5)=T(ind,5)+factor;
        B(ind,1)=B(ind,1)+factor*2*Dy*gj(bi,bj,bk);
    end
end
%for all nodes with j=ny
```

```
j=ny;
for k=1:nz,
    for i=1:nx,
        ind=index(i,j,k);
        bi=ceil(i/blocksize_x);
        bj=ceil(j/blocksize_y);
        bk=ceil(k/blocksize_z);
        factor=D/Dy^2-a_j(i,j,k)/2/Dy;
        T(ind,3)=T(ind,3)-factor*(2*Dy*fj(bi,bj,bk));
        T(ind,1)=T(ind,1)+factor;
        B(ind,1)=B(ind,1)-factor*2*Dy*gj(bi,bj,bk);
    end
end

%the following section is needed to rearrange the T and B matrix into an efficient form, since T is a sparse matrix
%this is to save memory usage and allows us to handle larger system
%first, count the number of non-zero elements
ele=0;
for ind=1:nxyz,
    if (ind-nx)>0
            ele=ele+1;
    end
    if (ind-1)>0
            ele=ele+1;
    end
    ele=ele+1;
    if (ind+1)<=ngrid
        ele=ele+1;
    end
    if (ind+nx)<=ngrid
        ele=ele+1;
    end
end
%T is now replaced with the following efficient format: T1 is a column vector containing the row index of each non-zero element of T
%T2 is a column vector containing the column index of each non-zero element of T
%T3 is a column vector containing the value of the non-zero element of T
T1=zeros(ele,1); %initialize T1
T2=zeros(ele,1); %initialize T2
T3=zeros(ele,1); %initialize T3
ele=0;
%start filling in T1, T2, and T3
for ind=1:nxyz,
    if (ind-nx)>0 %neighboring nodes at y-1
            ele=ele+1;
            T1(ele,1)=ind;
            T2(ele,1)=ind-nx;
            T3(ele,1)=T(ind,1);
    end
    if (ind-1)>0 %neighboring nodes at x-1
            ele=ele+1;
            T1(ele,1)=ind;
            T2(ele,1)=ind-1;
            T3(ele,1)=T(ind,2);
    end
    ele=ele+1;
    T1(ele,1)=ind;
    T2(ele,1)=ind;
    T3(ele,1)=T(ind,3);
    if (ind+1)<=ngrid %neighboring nodes at y+1
        ele=ele+1;
        T1(ele,1)=ind;
        T2(ele,1)=ind+1;
        T3(ele,1)=T(ind,4);
    end
    if (ind+nx)<=ngrid %neighboring nodes at x+1
        ele=ele+1;
        T1(ele,1)=ind;
        T2(ele,1)=ind+nx;
```

```
        T3(ele,1)=T(ind,5);
    end
end


error=norm(sparse(T1,T2,T3,nx*ny*nz,nx*ny*nz)*s2-B); %"sparse" is a function call to reconstruct T ; error = T*s-B
s_new=s; %save the updated closure variables
alpha2=alpha; %save the updated alphas

% ==================================================================
function [C_avg,Cp_var]=AverageC(blocksize_x,blocksize_y,blocksize_z,nbx,nby,nbz,C,poro,choice,bsize)

% This function computes average of concentration and its variance
% choice 1: read in average concentration from coarse-scale simulation
% choice 2: compute average concentration via arithmetic averaging
C_avg=zeros(nbx,nby,nbz);

switch choice
    case 1
        switch bsize
            case 1
                load file.dat;
                coarse = file;
            …
            case 5
                load file.dat;
                coarse = file;
            otherwise
        end
        C_avg=reshape(coarse(:,6),nbx,nby,nbz);

    case 2
        for k=1:nbz,
            for j=1:nby,
                for i=1:nbx,
                    sum1=0;
                    sum2=0;
                    for a=1:blocksize_x,
                        for b=1:blocksize_y,
                            for c=1:blocksize_z,
                                sum1=sum1+C((i-1)*blocksize_x+a,(j-1)*blocksize_y+b,(k-1)*blocksize_z+c)*poro((i-1)*blocksize_x+a,(j-1)*blocksize_y+b,(k-1)*blocksize_z+c);
                            end
                        end
                    end
                    C_avg(i,j,k)=sum1/(blocksize_x*blocksize_y*blocksize_z);
                end
            end
        end
    otherwise
end
for k=1:nbz,
    for j=1:nby,
        for i=1:nbx,
            sum1=0;
            sum2=0;
            for a=1:blocksize_x,
                for b=1:blocksize_y,
                    for c=1:blocksize_z,
                        sum1=sum1+(C((i-1)*blocksize_x+a,(j-1)*blocksize_y+b,(k-1)*blocksize_z+c)-C_avg(i,j,k))^2;
                        sum2=sum2+1;
                    end
                end
            end
            Cp_var(i,j,k)=sum1/sum2;
        end
```

```
    end
end

% ===================================================================
function [vo_avg_i,vo_avg_j,vo_avg_k,perm_avg2]=AverageVel(blocksize_x,blocksize_y,
                                             blocksize_z,nbx,nby,nbz,vo_i,vo_j,vo_k,perm,choice,bsize)

% This function computes average of velocity vector
% choice 1: read in average velocity from coarse-scale simulation
% choice 2: compute average velocity via weighted averaging
vo_avg_i=zeros(nbx,nby,nbz);
vo_avg_j=zeros(nbx,nby,nbz);
vo_avg_k=zeros(nbx,nby,nbz);
perm_avg2=zeros(nbx,nby,nbz);
omega=1;

switch choice
    case 1
        switch bsize
            case 1
                load file.dat;
                coarse = file;
            …
            case 5
                load file.dat;
                coarse = file;
            otherwise
        end
        perm_avg2=reshape(coarse(:,1),nbx,nby,nbz);
        vo_avg_i=reshape(coarse(:,3),nbx,nby,nbz);
        vo_avg_j=reshape(coarse(:,4),nbx,nby,nbz);
        vo_avg_k=reshape(coarse(:,5),nbx,nby,nbz);

    case 2
        for k=1:nbz,
            for j=1:nby,
                for i=1:nbx,
                    sum_i=0;
                    sum_j=0;
                    sum_k=0;
                    sum_i2=0;
                    sum_j2=0;
                    sum_k2=0;
                    for a=1:blocksize_x,
                        for b=1:blocksize_y,
                            for c=1:blocksize_z,
                                ii=vo_i((i-1)*blocksize_x+a,(j-1)*blocksize_y+b,(k-1)*blocksize_z+c)*perm((i-1)*blocksize_x+a,(j-
                                            1)*blocksize_y+b,(k-1)*blocksize_z+c);
                                jj=vo_j((i-1)*blocksize_x+a,(j-1)*blocksize_y+b,(k-1)*blocksize_z+c)*perm((i-1)*blocksize_x+a,(j-
                                            1)*blocksize_y+b,(k-1)*blocksize_z+c);
                                kk=vo_k((i-1)*blocksize_x+a,(j-1)*blocksize_y+b,(k-1)*blocksize_z+c)*perm((i-1)*blocksize_x+a,(j-
                                            1)*blocksize_y+b,(k-1)*blocksize_z+c);
                                if abs(ii)>0
                                    sum_i=sum_i+(ii)^omega;
                                    sum_i2=sum_i2+perm((i-1)*blocksize_x+a,(j-1)*blocksize_y+b,(k-1)*blocksize_z+c);
                                end
                                if abs(jj)>0
                                    sum_j=sum_i+(jj)^omega;
                                    sum_j2=sum_j2+perm((i-1)*blocksize_x+a,(j-1)*blocksize_y+b,(k-1)*blocksize_z+c);
                                end
                                if abs(kk)>0
                                    sum_k=sum_k+(kk)^omega;
                                    sum_k2=sum_k2+perm((i-1)*blocksize_x+a,(j-1)*blocksize_y+b,(k-1)*blocksize_z+c);
                                end
                            end
                        end
                    end
```

```
                    if abs(sum_i)>0
                        vo_avg_i(i,j,k)=(sum_i/sum_i2)^(1.0/omega);
                    else
                        vo_avg_i(i,j,k)=0;
                    end
                    if abs(sum_j)>0
                        vo_avg_j(i,j,k)=(sum_j/sum_j2)^(1.0/omega);
                    else
                        vo_avg_j(i,j,k)=0;
                    end
                    if abs(sum_k)>0
                        vo_avg_k(i,j,k)=(sum_k/sum_k2)^(1.0/omega);
                    else
                        vo_avg_k(i,j,k)=0;
                    end

                end
            end
        end
    otherwise
end

% ========================================================================
function [s_s]=BackgroundC(blocksize_x,blocksize_y,blocksize_z,nx,ny,nz,C,avg_C,Ceq,poro)

% This function computes the closure variable given C and <C>
s_s=zeros(nx,ny,nz); %closure variables

for k=1:nz,
    for j=1:ny,
        for i=1:nx,
            s_s(i,j,k)=1; %if closure variables is set to zero in this work because Ceq = C (could be different if the formulation is different)
        end
    end
end

% ========================================================================
function [C_p,Cout]=Cp(blocksize_x,blocksize_y,blocksize_z,nx,ny,nz,s,avg_C,Ceq)

%This funciton computes concentration deviation

C_p=zeros(nx,ny,nz); %deviation concentrations C'
Cout=zeros(nx,ny,nz); %compute Cout = C' + <C> (in this work, Cout = C since fine-scale C is known everywhere)

for k=1:nz,
    for j=1:ny,
        for i=1:nx,
            C_p(i,j,k)=s(i,j,k)*(Ceq(i,j,k)-avg_C(ceil(i/blocksize_x),ceil(j/blocksize_y),ceil(k/blocksize_z)));
            Cout(i,j,k)=avg_C(ceil(i/blocksize_x),ceil(j/blocksize_y),ceil(k/blocksize_z))+C_p(i,j,k);
        end
    end
end

% ========================================================================
function perm_avg=AveragePerm(blocksize_x,blocksize_y,blocksize_z,nbx,nby,nbz,perm)

% This function computes average permeability using arithmetic averaging

perm_avg=zeros(nbx,nby,nbz); %average permeability

for k=1:nbz,
    for j=1:nby,
        for i=1:nbx,
            sum=0;
            for a=1:blocksize_x,
```

```
                for b=1:blocksize_y,
                    for c=1:blocksize_z,
                        %summation over all permeability values in the average volume
                        sum=sum+perm((i-1)*blocksize_x+a,(j-1)*blocksize_y+b,(k-1)*blocksize_z+c);
                    end
                end
            end
            perm_avg(i,j,k)=sum/(blocksize_x*blocksize_y*blocksize_z);
        end
    end
end

% ===========================================================================
function [vo_avg_i,vo_avg_j,vo_avg_k]=AverageVec(blocksize_x,blocksize_y,blocksize_z,nbx,nby,nbz,
                                     vo_i,vo_j,vo_k)

% This function computes average of a vector via arithmetic averaging
vo_avg_i=zeros(nbx,nby,nbz); %average velocity  in the x-direction
vo_avg_j=zeros(nbx,nby,nbz); %average velocity in the y-direction
vo_avg_k=zeros(nbx,nby,nbz); %average velocity in the z-direction

for k=1:nbz,
    for j=1:nby,
        for i=1:nbx,
            sum_i=0;
            sum_j=0;
            sum_k=0;
            for a=1:blocksize_x,
                for b=1:blocksize_y,
                    for c=1:blocksize_z,
                        % summation over the averaging volume
                        sum_i=sum_i+vo_i((i-1)*blocksize_x+a,(j-1)*blocksize_y+b,(k-1)*blocksize_z+c);
                        sum_j=sum_i+vo_j((i-1)*blocksize_x+a,(j-1)*blocksize_y+b,(k-1)*blocksize_z+c);
                        sum_k=sum_k+vo_k((i-1)*blocksize_x+a,(j-1)*blocksize_y+b,(k-1)*blocksize_z+c);
                    end
                end
            end
            vo_avg_i(i,j,k)=sum_i/(blocksize_x*blocksize_y*blocksize_z);
            vo_avg_j(i,j,k)=sum_j/(blocksize_x*blocksize_y*blocksize_z);
            vo_avg_k(i,j,k)=sum_k/(blocksize_x*blocksize_y*blocksize_z);
        end
    end
end

% ===========================================================================
function [vo_p_i,vo_p_j,vo_p_k]=BackgroundV(blocksize_x,blocksize_y,blocksize_z,nx,ny,nz,vo_i,vo_j,
                               vo_k,vo_avg_i,vo_avg_j,vo_avg_k)

% This function computes velocity deviation

vo_p_i=zeros(nx,ny,nz); %velocity deviation u' in the x-direction
vo_p_j=zeros(nx,ny,nz); %velocity deviation u' in the y-direction
vo_p_k=zeros(nx,ny,nz); %velocity deviation u' in the z-direction

for k=1:nz,
    for j=1:ny,
        for i=1:nx,
            vo_p_i(i,j,k)=vo_i(i,j,k)-vo_avg_i(ceil(i/blocksize_x),ceil(j/blocksize_y),ceil(k/blocksize_z));
            vo_p_j(i,j,k)=vo_j(i,j,k)-vo_avg_j(ceil(i/blocksize_x),ceil(j/blocksize_y),ceil(k/blocksize_z));
            vo_p_k(i,j,k)=vo_k(i,j,k)-vo_avg_k(ceil(i/blocksize_x),ceil(j/blocksize_y),ceil(k/blocksize_z));
        end
    end
end

% ===========================================================================
```

```
function [ddx,ddy,ddz]=grad2(blocksize_x,blocksize_y,blocksize_z,nbx,nby,nbz,Evalue)

% This function computes the 2nd derivatives of a vector (d2/dx2, d2/dy2, d2/dz2) using finitie central difference

ddx=zeros(nbx,nby,nbz); %d2/dx2
ddy=zeros(nbx,nby,nbz); %d2/dy2
ddz=zeros(nbx,nby,nbz); %d2/dz2

%Calculate ddx
if nbx>2
    for k=1:nbz,
        for j=1:nby,
            for i=1,
                ddx(i,j,k)=(Evalue(i+2,j,k)+Evalue(i,j,k)-2*Evalue(i+1,j,k))/(blocksize_x^2);
            end
            for i=2:nbx-1,
                ddx(i,j,k)=(Evalue(i+1,j,k)+Evalue(i-1,j,k)-2*Evalue(i,j,k))/(blocksize_x^2);
            end
            for i=nbx,
                ddx(i,j,k)=(Evalue(i,j,k)+Evalue(i-2,j,k)-2*Evalue(i-1,j,k))/(blocksize_x^2);
            end
        end
    end
else
    for k=1:nbz,
        for j=1:nby,
            for i=1:nbx,
              ddx(i,j,k)=0;
            end
        end
    end
end

%Calculate ddy
if nby>2
    for k=1:nbz,
        for i=1:nbx,
            for j=1,
                ddy(i,j,k)=(Evalue(i,j+2,k)+Evalue(i,j,k)-2*Evalue(i,j+1,k))/(blocksize_y^2);
            end
            for j=2:nby-1,
                ddy(i,j,k)=(Evalue(i,j+1,k)+Evalue(i,j-1,k)-2*Evalue(i,j,k))/(blocksize_y^2);
            end
            for j=nby,
                ddy(i,j,k)=(Evalue(i,j,k)+Evalue(i,j-2,k)-2*Evalue(i,j-1,k))/(blocksize_y^2);
            end
        end
    end
else
    for k=1:nbz,
        for j=1:nby,
            for i=1:nbx,
                ddy(i,j,k)=0;
            end
        end
    end
end

%Calculate ddz
if nbz>1
    for i=1:nbx,
        for j=1:nby,
            for k=1,
                ddz(i,j,k)=(Evalue(i,j,k+2)+Evalue(i,j,k)-2*Evalue(i,j,k+1))/(blocksize_z^2);
            end
            if nbz>2
                for k=2:nbz-1,
```

```
                    ddz(i,j,k)=(Evalue(i,j,k+1)+Evalue(i,j,k-1)-2*Evalue(i,j,k))/(blocksize_z^2);
                end
            end
            for k=nbz,
                ddz(i,j,k)=(Evalue(i,j,k)+Evalue(i,j,k-2)-2*Evalue(i,j,k-1))/(blocksize_z^2);
            end
        end
    end
end

% ==========================================================================
function [result]=grad2Ensemble(blocksize_x,blocksize_y,blocksize_z,nbx,nby,nbz,Evalue)

% This function computes the laplacian of an ensemble quantity (Evalue) = d2/dx2 + d2/dy2 + d2/dz2 using finitie central difference

ddx=zeros(nbx,nby,nbz); %d2/dx2
ddy=zeros(nbx,nby,nbz); %d2/dy2
ddz=zeros(nbx,nby,nbz); %d2/dz2

%Calculate ddx
if nbx>2
    for k=1:nbz,
        for j=1:nby,
            for i=1,
                ddx(i,j,k)=(Evalue(i+2,j,k)+Evalue(i,j,k)-2*Evalue(i+1,j,k))/(blocksize_x^2);
            end
            for i=2:nbx-1,
                ddx(i,j,k)=(Evalue(i+1,j,k)+Evalue(i-1,j,k)-2*Evalue(i,j,k))/(blocksize_x^2);
            end
            for i=nbx,
                ddx(i,j,k)=(Evalue(i,j,k)+Evalue(i-2,j,k)-2*Evalue(i-1,j,k))/(blocksize_x^2);
            end
        end
    end
else
    for k=1:nbz,
        for j=1:nby,
            for i=1:nbx,
              ddx(i,j,k)=0;
            end
        end
    end
end

%Calculate ddy
if nby>2
    for k=1:nbz,
        for i=1:nbx,
            for j=1,
                ddy(i,j,k)=(Evalue(i,j+2,k)+Evalue(i,j,k)-2*Evalue(i,j+1,k))/(blocksize_y^2);
            end
            for j=2:nby-1,
                ddy(i,j,k)=(Evalue(i,j+1,k)+Evalue(i,j-1,k)-2*Evalue(i,j,k))/(blocksize_y^2);
            end
            for j=nby,
                ddy(i,j,k)=(Evalue(i,j,k)+Evalue(i,j-2,k)-2*Evalue(i,j-1,k))/(blocksize_y^2);
            end
        end
    end
else
    for k=1:nbz,
        for j=1:nby,
            for i=1:nbx,
                ddy(i,j,k)=0;
            end
        end
    end
```

```
end

%Calculate ddz
if nbz>1
    for i=1:nbx,
        for j=1:nby,
            for k=1,
                ddz(i,j,k)=(Evalue(i,j,k+2)+Evalue(i,j,k)-2*Evalue(i,j,k+1))/(blocksize_z^2);
            end
            if nbz>2
                for k=2:nbz-1,
                    ddz(i,j,k)=(Evalue(i,j,k+1)+Evalue(i,j,k-1)-2*Evalue(i,j,k))/(blocksize_z^2);
                end
            end
            for k=nbz,
                ddz(i,j,k)=(Evalue(i,j,k)+Evalue(i,j,k-2)-2*Evalue(i,j,k-1))/(blocksize_z^2);
            end
        end
    end
end

result=ddx+ddy+ddz; %the laplacian

% ============================================================================
function [gd]=graddotEnsemble(blocksize_x,blocksize_y,blocksize_z,nbx,nby,nbz,Evalue_i,Evalue_j,
                                    Evalue_k)

% This function computes the dot product of gradient and an ensemble vector (Evalue_i, Evalue_j, Evalue_k) using finitie central
% difference

% which is d/dx + d/dy + d/dz

ddx=zeros(nbx,nby,nbz); %d/dx
ddy=zeros(nbx,nby,nbz); %d/dy
ddz=zeros(nbx,nby,nbz); %d/dz

%Calculate ddx
if nbx>1
    for k=1:nbz,
        for j=1:nby,
            for i=1,
                ddx(i,j,k)=(Evalue_i(i+1,j,k)-Evalue_i(i,j,k))/blocksize_x;
            end
            if nbx>2
                for i=2:nbx-1,
                    ddx(i,j,k)=(Evalue_i(i+1,j,k)-Evalue_i(i-1,j,k))/(blocksize_x*2);
                end
            end
            for i=nbx,
                ddx(i,j,k)=(Evalue_i(i,j,k)-Evalue_i(i-1,j,k))/blocksize_x;
            end
        end
    end
end

%Calculate ddy
if nby>1
    for k=1:nbz,
        for i=1:nbx,
            for j=1,
                ddy(i,j,k)=(Evalue_j(i,j+1,k)-Evalue_j(i,j,k))/blocksize_y;
            end
            if nby>2
                for j=2:nby-1,
                    ddy(i,j,k)=(Evalue_j(i,j+1,k)-Evalue_j(i,j-1,k))/(blocksize_y*2);
                end
```

```
            end
            for j=nby,
                ddy(i,j,k)=(Evalue_j(i,j,k)-Evalue_j(i,j-1,k))/blocksize_y;
            end
        end
    end
end

%Calculate ddz
if nbz>1
    for i=1:nbx,
        for j=1:nby,
            for k=1,
                ddz(i,j,k)=(Evalue_k(i,j,k+1)-Evalue_k(i,j,k))/blocksize_z;
            end
            if nbz>2
                for k=2:nbz-1,
                    ddz(i,j,k)=(Evalue_k(i,j,k+1)-Evalue_k(i,j,k-1))/(blocksize_z*2);
                end
            end
            for k=nbz,
                ddz(i,j,k)=(Evalue_k(i,j,k)-Evalue_k(i,j,k-1))/blocksize_z;
            end
        end
    end
end
gd=ddx.^1+ddy.^1+ddz.^1;

% =========================================================================
function [ddx,ddy,ddz]=gradEnsemble(blocksize_x,blocksize_y,blocksize_z,nbx,nby,nbz,Evalue)

% This function computes the gradient of an ensemble quantity (Evalue) using finitie central difference

ddx=zeros(nbx,nby,nbz); %d/dx
ddy=zeros(nbx,nby,nbz); %d/dy
ddz=zeros(nbx,nby,nbz); %d/dz

%Calculate ddx
if nbx>1
    for k=1:nbz,
        for j=1:nby,
            for i=1,
                ddx(i,j,k)=(Evalue(i+1,j,k)-Evalue(i,j,k))/blocksize_x;
            end
            if nbx>2
                for i=2:nbx-1,
                    ddx(i,j,k)=(Evalue(i+1,j,k)-Evalue(i-1,j,k))/(blocksize_x*2);
                end
            end
            for i=nbx,
                ddx(i,j,k)=(Evalue(i,j,k)-Evalue(i-1,j,k))/blocksize_x;
            end
        end
    end
end

%Calculate ddy
if nby>1
    for k=1:nbz,
        for i=1:nbx,
            for j=1,
                ddy(i,j,k)=(Evalue(i,j+1,k)-Evalue(i,j,k))/blocksize_y;
            end
            if nby>2
                for j=2:nby-1,
                    ddy(i,j,k)=(Evalue(i,j+1,k)-Evalue(i,j-1,k))/(blocksize_y*2);
                end
```

```
            end
            for j=nby,
                ddy(i,j,k)=(Evalue(i,j,k)-Evalue(i,j-1,k))/blocksize_y;
            end
        end
    end
end

%Calculate ddz
if nbz>1
    for i=1:nbx,
        for j=1:nby,
            for k=1,
                ddz(i,j,k)=(Evalue(i,j,k+1)-Evalue(i,j,k))/blocksize_z;
            end
            if nbz>2
                for k=2:nbz-1,
                    ddz(i,j,k)=(Evalue(i,j,k+1)-Evalue(i,j,k-1))/(blocksize_z*2);
                end
            end
            for k=nbz,
                ddz(i,j,k)=(Evalue(i,j,k)-Evalue(i,j,k-1))/blocksize_z;
            end
        end
    end
end

% =====================================================================
function [varKeff,meanKeff]=KO(ALL,blocksize,tcount,W,nbx,nby)

% This function computes weighted mean and variance of vectors
% W = weights (>= 0)


n=nbx*nby;
ALL2=reshape(ALL,n*tcount,1);
W2=reshape(W,n*tcount,1);
varKeff = std(ALL2,W2); % weighted variance

%compute weighted mean
m=0; %counter for weights not equation to zero
for i=1:n*tcount,
    if W2(i)>0
        m=m+1;
        ALL3(m,1)=ALL2(i,1);
    end
end
meanKeff = mean(ALL3);

% =====================================================================
```

Glossary

SYMBOLS:

$a_{horizontal}$ = correlation range in the horizontal direction [=] L

a_{max} = correlation range in the major direction of anisotropy [=] L

a_{min} = correlation range in the minor direction of anisotropy [=] L

a_{vert} = correlation range in the vertical direction [=] L

A_{ij} = interfacial area between phase i and j [=] L^2

$\mathbf{b}$ = closure variable [=] L

B_j = formation volume factor for phase j [=] L^3 / standard L^3

c_j compressibility of phase j [=] L^2 / F

C_{eq} = equilibrium concentration [=] amount/volume

C_{ij} = concentration of species i in phase j [=] amount/volume

$\left\langle C_{ij} \right\rangle$ = superficial average of C_{ij} [=] amount/volume

$\left\langle C_{ij} \right\rangle^j$ = intrinsic average of C_{ij} [=] amount/volume

C'_{ij} = spatial deviation of C_{ij} [=] amount/volume

$C_{\max}$ = maximum (or injection) concentration [=] amount/volume

Cov = covariance

$\overline{\overline{D}}$ = diffusion or dispersion tensor [=] L^2 / t

D_p = grain diameter [=] L

f_j = fractional flow of phase j [=] L^3 / L^3

$f(\mathbf{x} \mid D_i)$ = probability density function at location $\mathbf{x}$ given data event D_i

$\mathbf{g}$ = gravitational vector [=] L / t^2

H = Hurst exponent

J = gradient of hydraulic head [=] L/L

$\mathbf{k}$ = permeability tensor [=] L^2

$\mathbf{K}$ = hydraulic conductivity tensor [=] L/t

$K_{\beta\gamma}$ = partition coefficient

K_{eff} = effective mass transfer coefficient [=] t^{-1}

l = length scale associated with small-scale homogeneous regions [=] L

L = length scale associated with large-scale averaged volumes [=] L

m = Archie's exponent

$m(\mathbf{x})$ = trend component of a random variable

$\dot{m}$ = mass flux [=] m/L^2t

$\mathbf{M}_{jk}$ = mobility tensor of phase j in region k [=] L^3t/m

$\left\langle \mathbf{M}_{jk} \right\rangle_k$ = coarse-scale average of $\mathbf{M}_{jk}$ [=] L^3t/m

$\mathbf{M}'_{jk}$ = fine-scale deviation of $\mathbf{M}_{jk}$ [=] L^3t/m

n = total number of homogeneous regions or number of samples

nx, ny, nz = number of grid blocks in the x-,y-,z- directions

$\mathbf{n}$ = unit outward normal vector

N = normal distribution

p = pressure [=] F/L^2

P = fluid potential [=] F/L^2

$\left\langle P \right\rangle$ = coarse-scale average of P [=] F/L^2

P' = fine-scale deviation of P [=] F/L^2

P_α = exponent in Meter's equation

Q = flow rate [=] L^3/t

r = effective radius of averaging volume at small scale [=] L

R = effective radius of averaging volume at large scale [=] L

R_k = permeability reduction

$R(\mathbf{x})$ = residual component of a random variable
s = closure variable
S_j = saturation of phase j [=] L^3 / L^3
t = time [=] t
u = average volumetric flux across a porous medium [=] L / t
$\mathbf{u}_j$ = velocity vector of phase j [=] L / t
$\langle \mathbf{u}_j \rangle$ = superficial average of $\mathbf{u}_j$ [=] L / t
$\langle \mathbf{u}_j \rangle^j$ = intrinsic average of $\mathbf{u}_j$ [=] L / t
$\mathbf{u}'_j$ = spatial deviation of $\mathbf{u}_j$ [=] L / t
V = averaging volume at Darcy Scale [=] L^3
V_j = volume of phase j [=] L^3
V_σ = averaging volume at macropore scale [=] L^3
V_∞ = averaging volume at local heterogeneity scale [=] L^3
Var = variance
$\mathbf{x}$ = position vector
$\overline{X}$ = sample mean
x, y, z = refers to coordinate directions x, y, z
Z = Gaussian random variable

GREEK SYMBOLS:

α = variable in closure formulations
α_L = longitudinal dispersivity [=] L
β = fluid phase
χ = position vector in linear perturbation
Δ = differential

ε = error or mismatch

ε_j = volume fraction of phase j [=] L^3 / L^3

ϕ = porosity [=] L^3 / L^3

ϕ_t = total porosity [=] L^3 / L^3

ϕ_f = secondary (fracture) porosity [=] L^3 / L^3

γ = fluid phase

$\gamma(\mathbf{h})$ = semivariogram or variogram

$\dot{\gamma}$ = shear rate [=] t^{-1}

$\dot{\gamma}_c$ = shear rate coefficient

$\dot{\gamma}_{1/2}$ = parameter in Meter’s equation [=] t^{-1}

η = homogeneous region

φ_k = volume fraction of region k [=] L^3 / L^3

λ = linear weight

μ = population mean

μ_j = viscosity of phase j [=] $F \cdot t$

ν = partitioning coefficient of secondary and total porosities

θ = source/sink function [=] t^{-1}

ρ_{corr} = spatial autocorrelation function

ρ_j = density of phase j [=] m / L^3

σ = solid phase

σ^2 = variance

Σ = specific storage [=] L^{-1}

τ = redundancy measure in the “tau” parameter

τ_s = shear stress [=] F / L^2

ω = homogeneous region or exponent in a power average

ψ = hydraulic head [=] L

NOTATIONS:

$\langle \; \rangle$ = Darcy scale averaging

$\{ \; \}$ = Large-scale averaging

$\bar{}$ = average quantity

$\hat{}$ = adsorbed quantity

SUPERSCRIPTS:

0 = zero shear rate

* = effective parameters

SUBSCRIPTS:

α = conditioning datum

app = apparent

d = divalent ion

D = support over the entire domain

eff = effective

eq = equilibrium or equivalent quantity

i = chemical species index

j = phase index (β, γ, σ)

k = region index (ϖ, η)

L = support over the averaging length scale

m = monovalent ion

max = maximum quantity

O = point support

p = polymer

SEP = effective salinity

w = water

x, y, z = refers to coordinate directions x, y, z (z also represents elevation)

ACRONYMS:

B.C. = boundary conditions

BT = breakthrough

DF = fractal dimension

I.C. = initial conditions

kr = relative permeability

LHS = left-hand side

MPS = multiple point statistics

NPHI = neutron porosity

P = probability

Pc = capillary pressure

PDE = partial differential equation

PV = pore volume

std. dev. = standard deviation

REV = representative elementary volume

RF = recovery factor

RHS = right-hand side

SDE = stochastic differential equation

SISIM = sequential indicator simulation

SGSIM = sequential Gaussian simulation

NOTES:

1. **bolded** quantities refer to vector or matrix
2. [=] means has units of, *L* is a length unit, *F* is force, *m* is mass, *t* is time, *T* is temperature, amount in moles.

Bibliography

Ahmadi, A., Quintard, M., and Whitaker, S. (1998). Transport in chemically and mechanically heterogeneous porous media V: two-equation model for solute transport with adsorption. *Advances in Water Resources*, 22(1), 59-86.

Arpat, B. (2003). A pattern recognition approach to multiple-point simulation. *Technical Report 16*, Stanford Center for Reservoir Forecasting, Stanford University, Stanford, California, USA.

Barker, J.W. and Thibeau, S. (1997). A critical review of the use of pseudo-relative permeabilities for upscaling. *SPE Reservoir Engineering*, September 1997, 138-143.

Bear, J. (1972). *Dynamics of Fluids in Porous Media*. Amsterdam: Elsevier Scientific Publishing Co.

Bhuyan, D. (1989). *Development of an Alkaline/Surfactant/Polymer Compositional Reservoir Simulator*. Ph.D. dissertation, The University of Texas at Austin, Austin, Texas, USA.

Bird, R.B., Stewart, W.E., and Lightfoot, E.N. (2001). *Transport Phenomena*, 2nd Edition. New York: John Wiley & Sons.

Carr, J. and Mao, N. (1993). A general form of probability kriging for estimation of the indicator and uniform transforms. *Mathematical Geology*, 25(4), 425-438.

Center for Petroleum and Geosystems Engineering. (2000). *UTCHEM Volume I: User's Guide for UTCHEM – 9.0*, The University of Texas at Austin.

Center for Petroleum and Geosystems Engineering. (2000). *UTCHEM Volume II: Technical Documentation for UTCHEM – 9.0*, The University of Texas at Austin.

Christie, M.A. (1996). Upscaling for reservoir simulation. *Journal of Petroleum Technology*, 48(11), 1004-1010.

Christie, M.A. (2001). Flow in porous media – scale up of multiphase flow. *Current Opinion in Colloid & Interface Science*, 6(3), 236-241.

Corbett, P.W.M., Good, T.R., Jensen, J.L., Lewis, J.J.M., Pickup, G.E., Ringrose, P.S., and Sorbie, K.S. (1996). Reservoir description in the 1990's: a perspective from the flow simulation through layercake parasequence flow units. In: K. Glennie and A. Hurst (eds.), *AD 1995: NW Europe's Hydrocarbon Industry* (pp. 167-176). The Geological Society, London.

Corbett, P.W.M., Jensen J.L., and Sorbie, K.S. (1998). A review of up-scaling and cross-scaling issues in core and log data interpretation and prediction. *Geological Society, London, Special Publications 1998*, 136, 9-16.

Coutelieris, F.A., Kainourgiakis, M.E., Stubos, A.K., Kikkinides, E.S., and Yortsos, Y.C. (2006). Multiphase mass transport with partitioning and inter-phase transport in porous media. *Chemical Engineering Science*, 61(14), 4650-4661.

Crotti, M.A. and Cobeñas, R.H. (2001). Relative Permeability Curves. An advantageous approach based on realistic average water saturations. *Paper presented at the SPE Latin American and Caribbean Petroleum Engineering Conference*. Buenos Aires, Argentina, Mar. 25-28.

Cushman, J. (1982). Proofs of the volume averaging theorems for multiphase flow, *Advances in Water Resources*, 5(4), 248-253.

Cvetkovic, V., Shapiro, A.M., and Dagan, G. (1992). A solute flux approach to transport in heterogeneous formations 2. uncertainty analysis. *Water Resources Research*, 28(5), 1377-1388.

Cvetkovic, V. and Dagan, G. (1994). Transport of kinetically sorbing solute by steady random velocity in heterogeneous porous formations. *Journal of Fluid Mechanics*, 265, 189-215.

Dagan, G. (1984). Solute transport in heterogeneous porous formations. *Journal of Fluid Mechanics*, 145, 151-177.

Dagan, G. (1987). Theory of solute transport by groundwater. *Annual Review of Fluid Mechanics*, 19, 183-215.

Dagan, G. (1989). *Flow and Transport in Porous Formations*. New York: Springer-Verlag.

Dagan, G. and Cvetkovic, V. (1996). Reactive transport and immiscible flow in geological media. I. General theory. *Proceedings: Mathematical, Physical and Engineering Sciences*, 452(1945), 285-301.

Dagan, G., Cvetkovic, V., and Shapiro, A.M. (1992). A solute flux approach to transport in heterogeneous formations 1. the general framework. *Water Resources Research*, 28(5), 1369-1376.

Deutsch, C. (1992). *Annealing Techniques Applied to Reservoir Modeling and the Integration of Geological and Engineering (Well Test) Data*. Ph.D. Thesis, Stanford University, Stanford, California, USA.

Deutsch, C.V. and Journel, A.G. (1998). *GSLIB: Geostatistical Software Library and User's Guide,* 2nd Edition. New York: Oxford University Press.

Durlofsky, L.J. (1998). Coarse scale models of two phase flow in heterogeneous reservoirs: volume averaged equations and their relationship to existing upscaling techniques. *Computational Geosciences*, 2(2), 73-92.

Durlofsky, L.J. (2003). Upscaling of geocellular models for reservoir flow simulation: A Review of recent progress. *Paper presented at 7th International Forum on Reservoir Simulation*. Buhl/Baden-Baden, Germany, June 23-27.

Efendiev, Y. and Durlofsky, L.J. (2003). A generalized convection-diffusion model for subgrid transport in porous media. *Multiscale Model Simulation*, 1(3), 504-526.

Efendiev, Y., Durlofsky, L.J., and Lee, S.H. (2000). Modeling of subgrid effects in coarse-scale simulations of transport in heterogeneous porous media. *Water Resources Research*, 36(8), 2031-2041.

Elkewidy,T.I. and Tiab, D. (1998). Application of conventional well logs to characterize naturally fractured reservoirs with their hydraulic (flow) units; a novel approach. *Paper presented at the SPE Gas Technology Symposium*. Calgary, Alberta, Canada, Mar. 15-18.

Eskandari, K. and Srinivasan, S. (2008). Reservoir modeling of complex geological systems – a multiple point perspective, *Paper presented at the Canadian International Petroleum Conference/SPE Gas Technology Symposium Joint Conference*. Calgary, Alberta, Canada, June 17-19.

Gelhar, L.W., Gutjahr, A.L., and Naff, R.L. (1979). Stochastic analysis of macrodispersion in a stratified aquifer. *Water Resources Research*, 15(6), 1387-1397.

Gelhar, L.W. and Axness, C.L. (1983). Three-dimensional stochastic analysis of macrodispersion in aquifers. *Water Resources Research*, 19(1), 161-180.

Gelhar, L.W., Welty, C., and Rehfeldt, K.R. (1992). A critical review of data on field-scale dispersion in aquifers. *Water Resources Research*, 28(7), 1955-1974.

Gelhar, L.W. (1993). *Stochastic Subsurface Hydrology*. Englewood Cliffs, NJ: Prentice-Hall.

Howes, F.A. and Whitaker, S. (1985). The spatial averaging theorem revisited. *Chemical Engineering Science*, 40(8), 1387-1392.

John, A.K., Lake, L.W., Bryant, S.L., and Jennings, J.W. (2008). Investigation of field scale dispersion. *Paper presented at the SPE Improved Oil Recovery Symposium*. Tulsa, Oklahoma, USA, Apr. 19-23.

Journel, A.G. (2002). Combining knowledge from diverse sources: An alternative to traditional data independence hypotheses. *Mathematical Geology*, 34(5), 573-596.

Journel, A.G. and Hujbregts, C. (1978). *Mining Geostatistics*. New York City: Academic Press.

Kechagia, P., Tsimpanogiannis, I., Yortsos, Y., and Lichtner, P. (2002).On the upscaling of reaction-transport processes in porous media with fast or finite kinetics, *Chemical Engineering Sciences*, 57(13), 2565-2577.

Kiraly, L. (1975). Rapport sur l'ètat actuel des connaissances dans le domaine des charactères physiques des roches karstiques. In: A. Burger and L. Dubertret (eds.), *Hydrogeology of Karstic Terrains*, Series B, vol. 3 (pp. 53– 67). International Union of Geological Sciences.

Krishnan, S. (2004). *The tau model to integrate prior probabilities*. Ph.D. Thesis, Stanford University, Stanford, California, USA.

Kumar, A.T.A. and Jerauld, G.R. (1996). Impacts of scale-up on fluid flow from plug to gridblock scale in reservoir rock. *Paper presented at the SPE/DOE Improved Oil Recovery Symposium*. Tulsa, Oklahoma, USA, Apr. 21-24.

Lake, L.W. (1989). *Enhanced Oil Recovery*. Englewood Cliffs, NJ: Prentice-Hall.

Lake, L.W. and Hirasaki, G.J. (1981). Taylor's dispersion in stratified porous media, *Society of Petroleum Engineers Journal*, 21(4), 459-468.

Lake, L.W. and Srinivasan, S. (2004). Statistical scale-up of reservoir properties: concepts and applications, *Journal of Petroleum Science and Engineering*, 44(1-2), 27-39.

Lake, L.W., Srinivasan, S., and John, A. (2005). Statistical scale-up: concepts and application to reservoir flow simulation practice. In O. Leuangthong and C.V. Deutsch (eds.), *Geostatistics Banff 2004*, Vol. 1 (pp. 681-690). Netherlands: Springer.

Lee, S., Kim, D.H., Huh, C., and Pope, G.A. (2009). Development of a comprehensive rheological property database for EOR polymers. *Paper presented at the SPE*

Annual Technical Conference and Exhibition, New Orleans, Louisiana, USA, Oct. 4-7.

Leung, J.Y. and Srinivasan, S. (2008). Direct transfer of uncertainty in reservoir models – application to uncertainty estimation due to sub-scale variance. *Paper presented at the Eighth International Geostatistics Congress*. Santiago, Chile, Dec. 1-5.

Leung, J.Y. and Srinivasan, S. (2008). Analysis of uncertainty introduced by scale-up of log-derived porosity in carbonate settings, *Paper presented at the Eighth International Geostatistics Congress*. Santiago, Chile, Dec. 1-5.

Leung, J.Y. and Srinivasan, S. (2009). Scale-up of hydrocarbons recovery processes in heterogeneous reservoirs. *Paper presented at the International Association of Mathematical Geology Annual Conference*. Stanford, California, USA, Aug. 23-28.

Li, D. and Lake, L.W. (1995). Scaling fluid flow through heterogeneous permeable media. *SPE Advanced Technology Series*, 3(1), 188-197.

Mahadevan, J., Lake, L.W., and Johns, R.T. (2003). Estimation of true dispersivity in field scale permeable media. *Society of Petroleum Engineers Journal*, 8(3), 272-279.

Miller, C.T., Christakos, G., Imhoff, P.T., McBride, J.F., Pedit, J.A., and Trangenstein, J.A. (1998). Multiphase flow and transport modeling in heterogeneous porous media: challenges and approaches. *Advances in Water Resources*, 21(2), 77-120.

Moisy, F. (2008). *Computing a fractal dimension with Matlab: 1D, 2D and 3D box-counting*. Retrieved January 13, 2009, from Fluides, Automatique et Systèmes Thermiques, Laboratorie FAST, University Paris-Sud Website: http://www.fast.u-psud.fr/~moisy/ml/boxcount/html/demo.html

Nenniger, J.E. and Dunn, S.G. (2008). How fast is solvent-based drainage? *Paper presented at the Canadian International Petroleum Conference/ SPE Gas Technology Symposium 2008 Joint Conference*. Calgary, Alberta, Canada, June 17-19.

Neuman, S.P., Winter, C.L., and Newman, C.M. (1987). Stochastic theory of field-scale Fickian dispersion in anisotropic porous media. *Water Resources Research*, 23(3), 453-466.

Neuman, S.P. and Orr, S. (1993). Prediction of steady state flow in nonuniform Geologic Media by Conditional Moments: Exact Nonlocal Formalism, Effective Conductivities, and Weak Approximation. *Water Resources Research*, 29(2), 341-364.

Neuman, S.P. (1994). Generalized scaling of permeabilities: Validation and effect of support scale. *Geophysical Research Letters*, 21(5), 349-352.

Ortiz, J. and Deutsch, C. (2002). Calculation of uncertainty in variogram. *Mathematical Geology*, 34(2), 169-183.

Peters, E.J. (1983). Scaling unstable immiscible displacements. *Unsolicited paper SPE 12331*, 1–9.

Pickup, G.E. and Stephen, K.D. (2000). An assessment of steady-state scale-up for small-scale geologic models. *Petroleum Geoscience*, 6, 203-210.

Pickup, G.E., Stephen, K.D., Ma, J., Zhang, P., and Clark, J.D. (2005). Multi-stage upscaling: Selection of suitable methods. *Transport in Porous Media*, 58, 191-216.

Plumb, O.A. and Whitaker, S. (1988). Dispersion in heterogeneous porous media 1. Local volume averaging and large-scale averaging. *Water Resources Research*, 24(7), 913-926.

Qi, D. and Hesketh, T. (2005). An analysis of upscaling techniques for reservoir simulation. *Petroleum Science and Technology*, 23(7), 827 – 842.

Quintard, M. and Whitaker, S. (1988). Two-phase flow in heterogeneous porous media: The method of large-scale averaging. *Transport in Porous Media*, 3(4), 357-413.

Quintard, M. and Whitaker, S. (1994). Convection, dispersion, and interfacial transport of contaminants: Homogeneous porous media. *Advances in Water Resources*, 17(4), 221-239.

Quintard, M. and Whitaker, S. (1996). Transport in chemically and mechanically heterogeneous porous media I: Theoretical development of region-averaged equations for slightly compressible single-phase flow. *Advances in Water Resources*, 19(1), 29-47.

Quintard, M. and Whitaker, S. (1996). Transport in chemically and mechanically heterogeneous porous media II: Comparison with numerical experiments for slightly compressible single-phase flow. *Advances in Water Resources*, 19(1), 49-60.

Quintard, M. and Whitaker, S. (1998). Transport in chemically and mechanically heterogeneous porous media III: Large-scale mechanical equilibrium and the regional form of Darcy's law. *Advances in Water Resources*, 21(7), 617-629.

Quintard, M. and Whitaker, S. (1998). Transport in chemically and mechanically heterogeneous porous media IV: Large-scale mass equilibrium for solute transport with adsorption. *Advances in Water Resources*, 22(1), 35-57.

Remy, N., Boucher, J., and Wu, J. (2009). *Applied Geostatistics with SGeMS: A User's Guide*. Cambridge: Cambridge University Press.

Renard, Ph. and de Marsily, G. (1997). Calculating equivalent permeability: A review. *Advances in Water Resources*, 20(5-6), 253-278.

Ringrose, P.S., Sorbie, K.S., Corbett, P.W.M., and Jensen, J.L. (1993). Immiscible flow behavior in laminated and cross-bedded sandstones. *Journal of Petroleum Science and Engineering*, 9(2), 103-124.

Rovey, C.W. II and Cherkauer, D.S. (1995). Scale dependency of hydraulic conductivity measurements. *Ground Water*, 33(5), 769-780.

Rubin, Y. and Gomez-Hernandez, J.J. (1990). A stochastic approach to the problem of upscaling of conductivity in disordered media: Theory and unconditional numerical simulations. *Water Resources Research*, 26(4), 691-701.

Rubin, Y. and Dagan, G. (1992). A note on head and velocity covariances in three-dimensional flow through heterogeneous anisotropic porous media. *Water Resources Research*, 28(5), 1463-1470.

Rubin, Y., Sun, A., Maxwell, R., and Bellin, A. (1999). The concept of block-effective macrodispersivity and a unified approach for grid-scale- and plume-scale-dependent transport. *Journal of Fluid Mechanics*, 395, 161-180.

Sahimi, M. (1993). Flow phenomena in rocks: From continuum models to fractals, percolation, cellular automata, and simulated annealing. *Reviews of Modern Physics*, 65(4), 1393-1537.

Sauter, M. (1991). Assessment of hydraulic conductivity in a karst aquifer at local and regional scale. *Proceedings of Third Conference on Hydrogeology, Ecology, Monitoring and Management of Ground Water in Karst Terranes. National Ground Water Association*, 39-56.

Schlumberger. (2005). *ECLIPSE Simulation Software Manuals 2005A.*

Sharma, A., Leung, J., Srinivasan, S., and Kim, Y. (2008). An integrated approach to reservoir uncertainty assessment: case study of a Gulf of Mexico reservoir. *Paper presented at the SPE Annual Technical Conference and Exhibition*. Denver, Colorado, USA, Sept. 21-24.

Shook, M., Li, D., and Lake, L.W. (1992). Scaling immiscible flow through permeable media by inspectional analysis. *In Situ*, 16(4), 311–349.

Sorbie, K.S. (1991). *Polymer – improved oil recovery*. Glasgow and London: Blackie and Son Ltd.

Srinivasan, S. and Journel, A.G. (1998). Simulation of permeability field conditioned to well test data. *Paper presented at the SPE Annual Technical Conference and Exhibition*, New Orleans, Louisiana, USA, Sept. 27-30.

Stone, H.L. (1991). Rigorous black oil pseudo functions. *Paper presented at the 11th SPE Symposium on Reservoir Simulation*, Anaheim, California, USA, Feb. 17-20.

Strebelle, S. (2000). *Sequential simulation drawing structure from training images*. Ph.D. dissertation, Stanford University, Stanford, California, USA.

Sullivan, J. (1984). Conditional recovery estimation through probability kriging – Theory and practice. In G. Verly et al. (eds.), *Geostatistics for Natural Resources Characterization*, Vol.1 (pp. 365-384). Dordrecht: Reidel.

Sun, A.Y. and Zhang, D. (2000). Prediction of solute spreading during vertical infiltration in unsaturated, bounded heterogeneous porous media. *Water Resources Research*, 36(3), 715-723.

Vereecken, H., Kasteel, R., Vanderborght, J., and Harter, T. (2007). Upscaling hydraulic properties and soil water flow processes in heterogeneous soils: A review. *Vadose Zone Journal*, 6, 1-28.

Wen, X.H. and Gomez-Hernandez, J.J. (1996). Upscaling hydraulic conductivities in heterogeneous media: An overview. *Journal of Hydrology*, 183(1-2), ix-xxxii.

Wheatcraft, S.W. and Tyler, S.W. (1988). An explanation of scale-dependent dispersivity in heterogeneous aquifers using concepts of fractal geometry. *Water Resources Research*, 24(4), 566-578.

Whitaker, S. (1999). *Theory and applications of transport in porous media: The method of volume averaging*. The Netherlands: Kluwer Academic Publishers.

Wood, B.D., Cherblanc, F., Quintard, M., and Whitaker, S. (2003). Volume averaging for determining the effective dispersion tensor: Closure using periodic unit cells and comparison with ensemble averaging. *Water Resources Research*, 39(8), SBH6.1-SBH6.22.

Wood, D.J., Lake, L.W., Johns, R.T., and Nunez, V. (2006). A screening model for CO_2 flooding and storage in Gulf Coast reservoirs based on dimensionless groups.

Paper presented at the SPE/DOE Symposium on Improved Oil Recovery Symposium. Tulsa, Oklahoma, USA, Apr. 22-26.

Zanotti, F. and Carbonell, R.G. (1984). Development of transport equations for multiphase systems I: General developments for two-phase systems. *Chemical Engineering Science*, 39(2), 263-278.

Zhang, D. and Neuman, S.P. (1995). Eulerian-Lagrangian analysis of transport conditioned on hydraulic data, 1. Analytical-numerical approach. *Water Resources Research*, 31(1), 39-51.

Zhang, D. (1998). Numerical solutions to statistical moment equations of groundwater flow in nonstationary, bounded heterogeneous media. *Water Resources Research*, 34(3), 529-538.

Zhang, D. (1999). Quantification of uncertainty for fluid flow in heterogeneous petroleum reservoirs. *Physica D: Nonlinear Phenomena*, 133(1-4), 488-497.

Zhang, D. and Winter, C.L. (1999). Moment-equation approach to single phase fluid flow in heterogeneous reservoirs. *Society of Petroleum Engineers Journal*, 4(2), 118-127.

Zhang, D., Li, L., and Tchelepi, H. (2000). Stochastic formulation for uncertainty assessment of two-phase flow in heterogeneous reservoirs. *Society of Petroleum Engineers Journal*, 5(1), 60-70.

Vita

Juliana Yuk Wing Leung was born in Hong Kong on October 12, 1980, the daughter of Louis Leung and Cecilia Lee. Her family moved to Canada when she was fourteen. She received her degree of Bachelor of Science in Chemical Engineering with Distinction in June 2002 from the University of Calgary. In August 2004, she graduated from the Department of Petroleum and Geosystems Engineering at the University of Texas at Austin with a Master's degree. She joined Shell Canada Ltd. in Sept 2004 and worked as a reservoir engineer for over 2 years. In January 2007, she entered the Gradual School at the University of Texas at Austin again to pursue her Ph.D. degree. She has other internship experiences with Sandia National Laboratories and ExxonMobil Upstream Research Company. She is also the author of numerous technical papers.

Permanent address: 119 Millview Place, S.W.
Calgary, Alberta
Canada T2Y 2W7

This thesis was typed by the author.